# Transport de particules induit par les Dents-de-Scie dans les palsmas de tokamak

Timothée Nicolas

# Sawtooth driven particle transport in tokamak plasmas

Thèse de doctorat

soutenue publiquement le 09/12/2013 par

**Timothée Nicolas**

en vue d'obtenir le grade de

**Docteur de l'École Polytechnique**

Spécialité : Physique des plasmas

| | |
|---|---|
| Prof. Howard Wilson | Referee – Professor at University of York |
| Prof. Olivier Sauter | Referee – Professor at EPFL |
| Prof. Jean-Marcel Rax | Professor at École Polytechnique |
| Dr. Xavier Garbet | Research Director at CEA |
| Dr. Roland Sabot | Senior Expert at CEA |
| Dr. Hinrich Lütjens | Research Fellow at CNRS |
| Prof. Peter Beyer | Professor at Université Aix-Marseille |

# Abstract

The radial transport of particles in tokamaks is one of the most stringent issues faced by the magnetic confinement fusion community, because the fusion power is proportional to the square of the pressure, and also because accumulation of heavy impurities in the core leads to important power losses which can lead to a "radiative collapse". Sawteeth and the associated periodic redistribution of the core quantities can significantly impact the radial transport of electrons and impurities. In this thesis, we perform numerical simulations of sawteeth using a nonlinear tridimensional magnetohydrodynamic code called XTOR-2F to study the particle transport induced by sawtooth crashes. We show that the code recovers, after the crash, the fine structures of electron density that are observed with fast-sweeping reflectometry on the JET and Tore Supra tokamaks. The presence of these structure may indicate a low efficiency of the sawtooth in expelling the impurities from the core. However, applying the same code to impurity profiles, we show that the redistribution is quantitatively similar to that predicted by Kadomtsev's model, which could not be predicted *a priori*. Hence finally the sawtooth flushing is efficient in expelling impurities from the core.



# Résumé

Le transport radial des particules dans les tokamaks constitue une des questions les plus cruciales pour la communauté de la fusion par confinement magnétique. En effet, d'une part la puissance de fusion est proportionnelle au carré de la pression, d'autre part l'accumulation d'impuretés lourdes dans le coeur du plasma conduit à d'importantes pertes par rayonnement qui peuvent finir par causer un effondrement radiatif du plasma. Les dent de scie et la redistribution périodique de la température et de la densité de coeur qui lui est associée peuvent affecter significativement le transport radial des électrons et des impuretés. Dans cette thèse, nous présentons des simulations numériques de dents de scie utilisant un code tridimensionnel non linéaire de magnétohydrodynamique appelé XTOR-2F, afin d'étudier le transport de particules pendant les dents de scie. Nous montrons que le code est capable de reproduire les structures fines de densité observées après le crash de la dent de scie avec le diagnostic de réflectométrie à balayage rapide sur les tokamaks Tore Supra et JET. La présence de ces structures implique la possibilité que le crash de dent de scie ne soit pas aussi efficace que prévu pour évacuer les impuretés du coeur du plasma. Cependant, en appliquant le code aux impuretés, nous montrons que finalement le taux de redistribution est quantitativement similaire à ce qui est prévu par le modèle de Kadomtsev, un résultat inattendu *a priori*. Nous concluons que la dent de scie est efficace pour évacuer les impuretés du coeur du plasma.

# Acknowledgments

Several persons have proven essential in the completion of this thesis and I would like to sincerely thank them. I apologize in advance for the ones I will forget. First, I would like to thank my two referees, Olivier Sauter and Howard Wilson, who have done a great job in carefully going through the (probably too long) manuscript. I am also grateful to all the other jury members, Jean-Marcel Rax, Peter Beyer, Hinrich Lütjens, as well as my two supervisors Roland Sabot and Xavier Garbet, for their presence and for the stimulating questions during the defence.

Je tiens maintenant à remercier chaleureusement mes encadrants, qui ont permis à cette thèse de se passer dans des conditions idéales. Roland, en plus de tes compétences scientifiques, tes encouragements au début de ma deuxième année ont été vraiment déterminants. A ce moment-là, je ne savais pas trop où j'en étais, si ce que je faisais était bien ou pas, et ce que tu m'as dit m'a réellement beaucoup aidé. Merci ! Xavier, il n'est plus vraiment nécessaire de chanter tes louanges. Je le fais quand même... Ton expertise de physicien a été un phare pour moi pendant 3 ans, et j'ai vite réalisé qu'on pouvait te faire confiance les yeux fermés. Te voir, en plein milieu d'une discussion, exhiber un cahier vieux de 20 ans et en sortir un calcul parfaitement adapté est une expérience assez magique. Merci pour tous les papiers envoyés semaine après semaine, et qui témoignent de ton statut de véritable bibliothèque vivante de l'IRFM. Comme ça ne suffit pas, il faut en plus que tu aies des qualités humaines exceptionnelles, et pour couronner le tout, un sens de l'humour qui m'a permis d'avoir le sourire chaque fois que tu te pointais dans mon bureau. Merci à tous les deux pour cet encadrement irréprochable !

Mais je n'étais pas encadré qu'à l'IRFM. Au Centre de Physique Théorique de l'Ecole Polytechnique, Hinrich Lütjens et Jean-François Luciani, les créateurs du code XTOR que j'ai exploité, n'étaient pas en reste. Merci à tous les deux pour votre souci et votre patience lors de mes quelques passages à Palaiseau. Merci Hinrich de m'avoir initié aux arcanes numériques du code, ça ne va pas tout seul pour quelqu'un qui n'a au préalable presque jamais touché à un langage informatique. Merci Jean-François pour ton expertise sans concession, pour ta rigueur et ton honnêteté intellectuelle implacables. J'aurai encore beaucoup de plaisir à travailler avec vous.

Je remercie ma hiérarchie, en particulier Alain Bécoulet, Xavier Litaudon et Tuong Hoang, dont le suivi attentif des thésards nous permet à tous d'avoir des conditions de travail excellentes. Même au CEA, tout le monde n'a pas la chance d'aller fréquemment à des conférences à l'étranger. Durant ma thèse, j'ai eu l'occasion d'aller dans 5 pays différents, dont le Japon, pour rencontrer et interagir avec des chercheurs de tous horizons. J'insiste particulièrement sur le Japon, car cette conférence m'a permis de confirmer mon intérêt pour ce pays et cette culture, et de rencontrer mon futur encadrant de postdoc. Merci Xavier d'avoir facilité le contact avec les Japonais, merci Alain de m'avoir si bien soutenu dans ma demande de bourse. Merci aussi aux secrétaires du

SCCP, Valérie et Nathalie, qui font un travail formidable pour nous faciliter la tâche à chaque déplacement et pour faire tourner le service en général.

Merci à tous les copains/collègues côtoyés durant ces trois années, d'abord les anciens thésards, déjà aux 4 coins du monde, et qui nous ont appris tant de choses : Antoine (Merle), mon premier co-bureau, que je pense n'avoir jamais entendu dire une bêtise et qui n'a jamais reculé devant mes questions, tant physiques qu'informatiques, Jérémie, pour qui tout semble si facile, David, aux incroyables facultés de concentration, Hugo, toujours zen, Antoine (Strugarek), pour les intéressantes discussions et les moments partagés. Merci d'avoir été de si bons compagnons de soirée et de boulot.

Merci à tous les collègues, anciens et moins anciens, qui créent une si bonne ambiance de travail : Philippe, Yanick et Yves, merci d'abord pour vos cours de master qui m'ont donné envie de continuer, merci Patrick (Maget) d'avoir partagé avec moi le goût de la musique baroque (j'en profite pour remercier à titre posthume Bach, Charpentier, Rameau, Lully, Purcell et tant d'autres), merci Joan pour ton aide et tes conseils, merci Chantal, Virginie, Rémi, Marina pour les bons moments en salle café, Guilhem pour ta vision si personnelle et riche de la physique, Patrick (Tamain) pour ta bonne humeur inaltérable, même pris en otage par la First Great Western !

Merci à tous les thésards et postdocs d'avoir apporté tant de bonne humeur et de fraîcheur, en particulier Greg et son insatiable curiosité, Farah, merci pour ta confiance, François, merci d'être un si bon co-bureau et ami, tu nous réserves plein de (très bonnes) surprises, Thomas (TC) et ta délicate attention aux autres, Hugo (Bobby) et ta joie de vivre, Daminou, toujours tourmenté par le mystérieux NaN, Frozar et Olivier, en communion avec FORTRAN, Clothilde et ta passion si familière pour la bonne chère, Jean-Baptiste si naturellement enthousiaste à l'égard des GAMs, Hue, qu'on aimerait voir encore plus souvent, Olivier et Jae-Heon, merci de reprendre le flambeau d'XTOR...

Et bien sûr merci Didou, collègue et colloc pendant 3 ans. Je te pardonne volontiers les quelques sabotages culinaires, non seulement on en a bien rigolé, mais ce que tu m'as apporté est à des années-lumière au-delà. Merci pour la gentillesse que tu portes naturellement en toi, une bénédiction pour ton entourage, pour les séjours à Mens inoubliables, pour les mails d'invitation à la colloc absolument mythiques, pour ta joie de vivre, ton enthousiasme et ta curiosité insatiable, pour nos longues discussions où je m'énervais de constater que tu avais décidément plus d'arguments que moi ! Bon vent et merci à tous !

En dehors du labo, merci à tous ceux qui ont marqué mon passage à Aix, notamment JB et Céline, Sabine, et Florian qui n'a jamais raté une occasion de squatter notre canapé.

Merci Alexandre pour ton hospitalité lors de mes séjours à Paris, et pour ta fidèle amitié.

Merci Pépé de nous avoir donné le goût des sciences, à mes frères et moi. Merci Mémé pour ta joie de vivre, et merci à tous les deux pour votre amour. Et merci Papa, Maman, Armel, Joseph et Victor d'être une famille aussi adorablement géniale !

# Contents

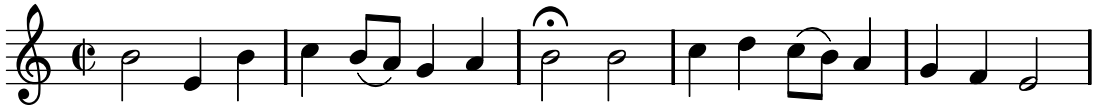

*Aus tiefer Not schrei ich zu dir*
*(BWV 38)*
**Johann-Sebastian Bach**

Chapter 1

# Introduction

## Contents



## 1.1 The challenge of nuclear fusion as an energy source

The middle of the $20^{th}$ century was marked by a widespread enthusiasm regarding the use of nuclear power as a large scale energy source. It was soon clearly identified that nuclear energy could be released either by breaking heavy atoms in lighter ones (fission), or by joining together light atoms to form heavier ones (fusion). However, whereas it took only a couple of decades from the discovery of the neutron by Chadwick in 1932 to the first generation of fission reactors, fusion energy still remains only a potential energy source, despite an intense international collaboration since the middle of the 1950s.

How come it is so difficult to effectively conceive and build a fusion power plant, while the basic principles have been known for more than 50 years ? Why are the time scales of the fusion program so long ?

In this introduction, we will briefly review some aspects of the fusion challenge. Many different devices are developed, which can be classified as inertial confinement fusion or magnetic confinement fusion devices. Among the latter category, the most advanced concept as of today is the tokamak, invented by the Russians in the 50's. This thesis deals only with the physics of tokamaks, even if many tokamak concepts also apply to other magnetic confinement devices. The focus of the thesis is on the so-called sawtooth instability, which will be introduced in section 1.2. Section 1.1.1 presents the stakes of the fusion research program, section 1.1.2 presents the basic principles of nuclear fusion and the functioning of a tokamak, and section 1.1.3 deals with the issues faced by the fusion community.

### 1.1.1 The stakes

The claims of fusion as an energy source are to be clean, intrinsically safe, and almost inexhaustible. In other words, it is the dream of the modern society. We will see in section 1.1.2 why these epithets, and others, are indeed relevant, and suppose so in the remainder of this subsection.

The issue of energy production will be one of the most stringent of the 21st century, and most probably the next as well, as long as the majority of the nations on Earth tend to adopt a western style of life, requiring heavy industries and services, very greedy in energy. Of course mankind will face many other challenges in this century, the most worrying being the sharp increase in the world's population, resource scarcity as a whole, global warming, geopolitical tensions and instabilities or terrorism. Yet these issues reduce, *in fine*, to the energy issue. Indeed energy, because it is such a basic physical concept, accounts for the ability to make things move (heat engine, electrical engine etc.) or transform (agriculture, chemical, petrochemical industries, nuclear engineering, even bit conversion requires energy, etc.) to serve projects forged by humans. Thus it appears as an evidence that energy abundance greatly eases *all* these challenges.

This energy challenge will have for sure to be faced during the 21st century. This affirmation is based on numerous cross-checked projections of the world's population and their energy needs by 2030, 2050 or even, more cautiously, 2100. Projections beyond this date are virtually irrelevant. What is striking in this context is the time scale of the fusion project, with milestones every 10 years approximately: ITER site construction started around 2010, will yield its first plasma around 2020, and first Deuterium Tritium full scale operation is planned at the end of the 2020s, while the core of the DEMO[1] project is optimistically estimated to be in the 2040s or 2050s. On top of that, the first commercial fusion reactors will probably suffer from a lack of competitiveness, because of their inherent operation complexity and fragility. Given these time scales, the objective of the fusion project *cannot* be solving the pressing energy issues of our century. It will simply not be ready. They will have to be dealt with using the already available resources: fossil fuels of all sorts (including uranium for nuclear fission), solar, wind, tidal, hydraulic, geothermal energy sources, in what is now called the "Energy mix", helped by energetic efficiency of industries and homes. Fusion research's objectives apply to a much longer term. If the fusion community is finally able to deliver the plans and reproducible operation guidelines for an efficient, steady-state, long-lived and marginally economically competitive fusion device, then we can expect investors to really take some interest in the project and finance the development of several facilities across the world. If the enterprise is a success, the future of fusion will be on good tracks, and hopefully a new era will start where energy is produced at a large scale with very low waste generation, in safe conditions and abundantly.

We will now progressively introduce the basic concepts of magnetic confinement fusion, and more specifically tokamaks. The claims of fusion as an energy mentioned at the beginning of this subsection will also become clear. Readers already familiar with

[1] DEMO is the possible successor of ITER, an actual fusion demonstrator which should produce electricity out of the 1000 to 4000 MW of fusion power delivered in its core.

tokamaks can jump to section 1.2.

### 1.1.2 The principle and the means

A fusion reaction happens when light nuclei combine to form heavier, more stable nuclei. This does not happen very easily because atoms' nuclei are always positively charged and repel each other with a Coulomb force proportional to their inverse squared distance. The particles inside the nucleus are bound by the strong interaction, which has a finite range contrary to the Coulomb interaction, which has an infinite range[2]. The fusion between the light elements happens when they approach close enough for the strong interaction to take over the Coulomb interaction, that is, when they enter into the range of the strong interaction. When two particles with same mass $m$ and charge $q$ travel towards each other with a relative velocity at infinity $v_0$, conservation of the energy in the centre of mass: $\mathcal{E} = m\frac{v_0^2}{4} - \frac{q^2}{4\pi\varepsilon_0 r}$, yields the distance of minimal approach

$$\lambda = \frac{q^2}{\pi\varepsilon_0 m v_0^2}. \tag{1.1}$$

Thus the faster the particles, the more likely they are to come close enough to react. This simplistic model predicts that a minimum energy of the order of 1 MeV is necessary for the reaction to take place, given the range of the strong interaction of the order of $10^{-15}$ m. This energy is larger than the actual energies required, but it is the right order of magnitude of the energies at stake in nuclear processes. One sees right away that at such energies, matter is in the plasma state. Electron binding to nucleus are in the tens of eV range, so that at temperatures of a few keV, light atoms are already completely stripped.

#### The reaction

The most studied reaction in fusion energy research is the reaction between Deuterium (D) and Tritium (T), which yields a neutron and an $\alpha$ particle:

$$^2_1\mathrm{D} + {}^3_1\mathrm{T} \longrightarrow \alpha + \mathrm{n} \qquad \Delta E_f = +17.6\,\mathrm{MeV}, \tag{1.2}$$

where $\alpha$ denotes $^4_2$He and n is a neutron. There is a mass difference equivalent to an energy of $\Delta E_f = 17.6$ MeV between the fusion reactants and the products. This energy is split between the $\alpha$ particle and the neutron with respect to their masses, in order to conserve momentum. Thus the $\alpha$ takes one fifth of the energy, that is, 3.5 MeV, and the neutron 14.1 MeV. For this D-T reaction, the energy threshold is much lower than what is expected from the simple calculation above because of the quantum nature of interactions at this scale. The energy necessary for the reaction is significantly lowered by the tunnelling effect. At the microscopic scale, the relevant quantity to quantify the

[2] When the force $F$ decreases algebraically, $F \propto r^{-\alpha}$, $\alpha > 0$, the force is said to have an infinite range, while when it is weighted by an exponential term, $F \propto e^{-r/L}$, it is said to have the range $L$

probability of a reaction is the cross-section, which has dimensions of the square of a distance. It is the equivalent of the classical cross-section of an object. For instance a billiard ball of radius $r$ has a cross-section $\sigma = \pi r^2$. This means that if a population of billiard balls with density $n_1$ and velocity $v_1$ targets a population of billiard balls with density $n_2$, the number of collisions in the elementary volume $\mathrm{d}V$ during the time interval $\mathrm{d}t$ will be $\mathrm{d}N = \sigma n_1 v_1 n_2 \mathrm{d}V \mathrm{d}t$. Fig. 1.1 represents the cross-section of reaction 1.2 and of the two following reactions between two D nuclei:

$$ {}^2_1\mathrm{D} + {}^2_1\mathrm{D} \longrightarrow {}^3_1\mathrm{T} + \mathrm{p} \qquad \Delta E = +4.0\,\mathrm{MeV} \tag{1.3} $$

$$ {}^2_1\mathrm{D} + {}^2_1\mathrm{D} \longrightarrow {}^3_2\mathrm{He} + \mathrm{n} \qquad \Delta E = +3.3\,\mathrm{MeV}. \tag{1.4} $$

Here, p is a proton. As we see, not only is the reaction between Deuterium and Tritium by far the most energetic, but the maximum of the cross section arises at an energy two orders of magnitude smaller, and is larger by almost two orders of magnitudes. This is the reason why this reaction is the most promising and has driven so much effort since its discovery.

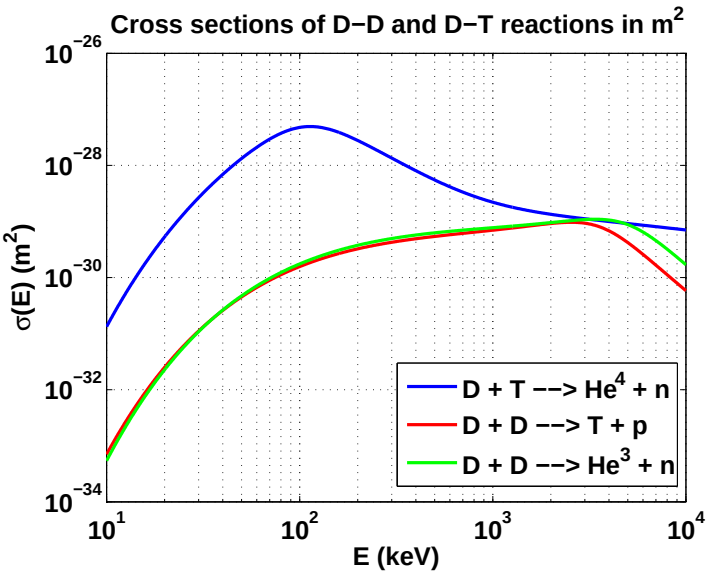


Figure 1.1: Cross sections of the D-T reaction and of the two different D-D reactions in $\mathrm{m}^2$ [Huba 2007].

### The D-T fuel

Deuterium is very abundant on Earth. 0.016% of the Hydrogen atoms are in fact Deuterium. The total volume of water (mainly ocean water) is $V_{\mathrm{Water}} \sim 10^{18}\mathrm{m}^3$. Taking the total number of D nuclei multiplied by the energy of one D-T reaction, one obtains a potential energy of the order of $10^{28}$ J, which represents tens of millions of years of the total world energy consumption in the late 2000s. However the limiting factor is not Deuterium but Tritium. It is a radioactive compound with a short half-life of 12 years, present in nature as traces only because it is dynamically regenerated by cosmic rays.

It must be produced by nuclear reactions. It is usually projected to produce it *in situ*, in Lithium blankets located around the vacuum vessel, using the following exothermic reaction:

$$^{6}_{3}\mathrm{Li} + \mathrm{n} \longrightarrow {}^{4}_{2}\mathrm{He} + {}^{3}_{1}\mathrm{T} \qquad \Delta E = +4.8\,\mathrm{MeV}. \tag{1.5}$$

The neutrons produced by the D-T reactions can be used for this purpose. Thus the actual limiting factor is not Tritium but Lithium. The abundance of $^{6}_{3}\mathrm{Li}$ is 7.5% of the total Lithium, the most common isotope being $^{7}_{3}\mathrm{Li}$. Extracting all the $^{6}_{3}\mathrm{Li}$ from the current total world production of Lithium during one year approximately amounts to the total world energy consumption per year of the late 2000s. Furthermore, the oceans contain a small proportion of Lithium, which could eventually be used to raise the potential energy to tens of thousands of years of the current total world energy consumption. And finally, the much more abundant $^{7}\mathrm{Li}$ can also be used provided that it is mixed with Beryllium, acting as a neutron multiplier. This is the reason why fusion is commonly deemed an (almost) inexhaustible source of energy.

### D-T cross section and Lawson criterion

The cross section depends on the energy of the colliding particles, that is, their velocity: $\sigma = \sigma(v)$. To infer the reaction rate, and then the power, which one can expect from D-T reactions at a given temperature, one has to sum the product $\sigma(v)v$ over all possible velocities. Assuming isotropic velocity distributions for both D and T and stoechiometric proportions, there is a mean number $f(v)\mathrm{d}v$ of interacting centres with velocity between $v$ and $v + \mathrm{d}v$. Thus the reaction rate is:

$$\frac{\mathrm{d}N}{\mathrm{d}t} = n_D n_T \int_0^\infty \sigma(v) v f(v) \mathrm{d}v = n_D n_T \langle \sigma v \rangle, \tag{1.6}$$

where the quantity $\langle \sigma v \rangle$ is a function of the ion temperature which characterizes the distribution $f$. The distribution $f$ can be written as a function of the Deuterium and Tritium velocity distribution functions:

$$f(v) = 4\pi v^2 \int f_D(\boldsymbol{v} + \boldsymbol{u}) f_T(\boldsymbol{u}) \mathrm{d}^3\boldsymbol{u}, \quad v \equiv |\boldsymbol{v}|. \tag{1.7}$$

Fig. 1.2 represents the quantity $\langle \sigma v \rangle$ for the D-T reaction. The temperature which maximizes the reaction rate is of the order of a few tens of keV. However magnetohydrodynamic phenomena constrain the temperature at which the plasma can be heated for a given magnetic field, so that the plasma is heated up to a temperature of typically 10 keV (less in current day tokamaks). At this temperature, the reaction rate is 10 times less the peak reaction rate. Also, the logarithmic derivative of $\langle \sigma v \rangle$ with temperature is close to 2 in this regime of temperatures close to 10 keV, so that the fusion power is proportional to the square of the density $n$ and approximately to the square of the temperature $T$. Thus it is a convenient approximation to write $P_\alpha \propto p^2$, where $P_\alpha$ is the fusion power and

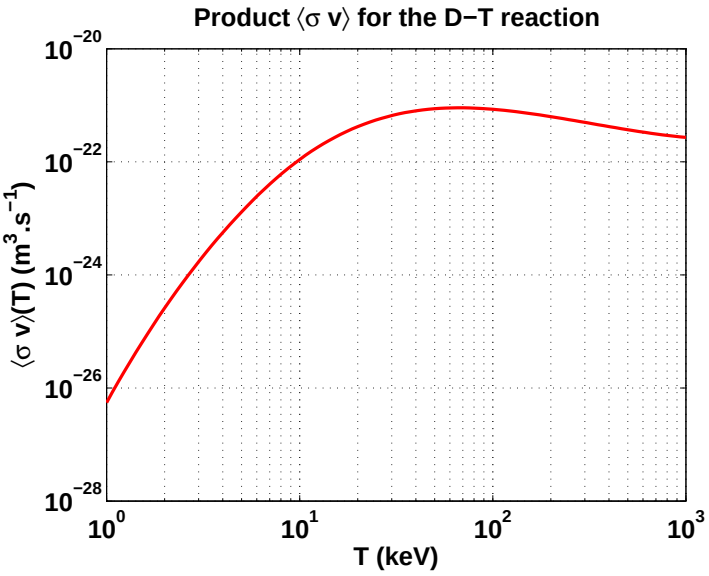


Figure 1.2: Product $\langle \sigma v \rangle$ for the D-T reaction [Huba 2007].

$p = nk_BT$ the thermal pressure[3]. Before going any further, we need to know what kind of device will be used to heat the plasma to temperatures of several keV. The issue is that in order for the plasma to be in thermal equilibrium, the losses must be compensated by the injected power, which is the sum of an auxiliary power and the fusion power carried by the $\alpha$ particles: $P_{\text{heat}} = P_\alpha + P_{\text{aux}}$. It is convenient to define the quality factor $Q$ by the ratio of the fusion power $P_{\text{fus}}$ to the auxiliary power $P_{\text{aux}}$: $Q = P_{\text{fus}}/P_{\text{aux}}$. We want $Q$ to be as high as possible. Achieving $Q = 10$ during a few hundreds of seconds is one of ITER's main goals. The plasma is transparent to neutron so their energy is not available, only the power $P_\alpha = P_{\text{fus}}/5$ carried by the $\alpha$ particles can heat the plasma. We also define the energy confinement time $\tau_E$, which characterizes the characteristic decay time of the energy of the plasma. It is the energy content $W_{\text{th}}$ divided by the losses $P_{\text{loss}}$: $P_{\text{loss}} = W_{\text{th}}/\tau_E$[4]. The thermal energy content is split in half between the electrons and ions. For stoechiometric conditions, we have $n_D = n_T = n_e/2$, so that $W_{\text{th}} = 3n_ekT$, where $V$ is the plasma volume. Hence the injected power compensates the losses when

$$P_\alpha + P_{\text{aux}} = P_\alpha \left(1 + \frac{5}{Q}\right) = \frac{3n_eVT}{\tau_E},$$

with $P_\alpha = \Delta E_f \langle \sigma v \rangle n_e^2 V/20$. Assuming that all the power is provided by the $\alpha$ particles ($Q = \infty$), we must have

$$n_e\tau_E = \frac{60T}{\langle \sigma v \rangle \Delta E_f}, \tag{1.8}$$

which is called the Lawson criterion. At the temperatures where fusion can be envisaged,

[3] In the following we will drop the Boltzmann constant $k_B$ and simply assume that $T$ is in units of energy.

[4] In steady state. Otherwise the proper definition is $\tau_E = W_{th}/(P_{\text{loss}} - \mathrm{d}_t W_{th})$

$\langle \sigma v \rangle \propto T^2$ approximately. Hence the product $nT\tau_e$, called "triple product", is approximately independent of temperature at the condition $P_\alpha = 3n_eVT/\tau_E$, and this constant is approximately $3 \times 10^{21}$ keV.s.m$^{-3}$. The condition for achieving fusion is often expressed in terms of this triple product:

$$n_e T \tau_E \gtrsim 3 \times 10^{21} \text{keV.s.m}^{-3} = 4.8 \times 10^5 \text{Pa.s.} \tag{1.9}$$

This means that there are two ways of triggering fusion reactions in a plasma.

- High density and short confinement time. This is the strategy adopted in so called inertial confinement fusion. A beam of highly collimated powerful lasers impacts a millimeter size cryogenized D-T target, delivering it an energy of the order of 1 MJ in nanoseconds. If done with sufficient symmetry, this can lead to implosion of the target, which is driven to high pressures for a very short time, overcoming Lawson criterion and triggering fusion reactions.

- Low density and long confinement time. In this approach, steady state plasma conditions are a goal. Stars use the large gravitational field generated by their mass to retain the plasma confined over very long times. The core of the sun is at a temperature of $15 \times 10^6$ K, and a mass density of 150 times that of water on earth[5]. Obviously this gravitational type of confinement is not feasible on earth, and other ways have to be found to confine the fusion mixture. In laboratory fusion plasmas, magnetic fields are used to balance the thermal pressure. This approach is called magnetic confinement fusion. Most commonly, experiments are carried out in the topologically closed configuration of a torus, even if historically, the first attempts were done on linear mirror machines. A torus is shown on Fig. 1.3, together with the directions of the poloidal and toroidal angles.

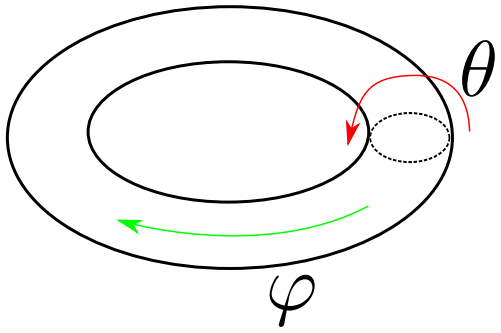


Figure 1.3: A torus with the directions of the poloidal and toroidal angles.

[5] This represents the third possibility: long confinement time and high density. Notice that the first step of the reaction in the sun, involving two protons has an extremely low cross section because the primary product, $^2_2$He or "diproton", must decay to a D nucleus through weak interaction (which is weak, hence rare, as indicated in its name). Without this, the sun would have burnt its hydrogen much too fast, and we would not be here to discuss it.

### Magnetic confinement

Making large magnetic fields is technically difficult. In order to avoid the important Ohm losses in standard (copper) conductors, superconducting coils are used. One of the most advanced technologies involving Niobium-Titanium alloy will be used on ITER. These superconductors have a critical field[6] of 15 T, that is, the field on the coil boundary cannot exceed 15 T. This implies a field at the center of the torus chamber of the order of 5 T, as we will see. The magnetic energy density, that is, its pressure, is $B^2/2\mu_0$. This sets the order of magnitude of the maximum thermal pressure which can be handled. In practice, the pressure which can be handled is much lower than the magnetic pressure. It is customary to define the ratio between the thermal and magnetic pressures $\beta$:

$$\beta = \frac{2\mu_0 p}{B^2} \tag{1.10}$$

In typical devices, this ratio is limited to $\beta \sim 10^{-2}$ because of magnetohydrodynamic limitations. Taking these values ($\beta = 10^{-2}$, $B = 5$ T) for the pressure $nT$ in the triple product criterion sets the confinement time to about 1 s. In turn, for a temperature of the order of 10 keV (where the fusion cross section is significant), the density must be of the order of $10^{20}$ m$^{-3}$. Finally, in order to have decent total fusion power, the volume is fixed by setting an upper limit to the losses $3nVT/\tau_E$. Setting this limit to 100 MW, one sees that several hundreds of cubic meters of plasma are required, and this yields several hundreds MW of fusion power. These values are slightly different from the actual ITER requirements, but they have the right order of magnitude. The actual ITER parameters for inductive discharges are shown on Table 1.1.

| | |
|---|---|
| Major radius $R_0$ | 6.2 m |
| Minor radius (horizontal) $a$ | 2 m |
| Minor radius (vertical) | 3.4 m |
| Magnetic field $B_0$ | 5.3 T |
| Plasma volume $V$ | 830 m$^3$ |
| Confinement time $\tau_E$ | 3.7 s |
| Volume averaged density $\langle n_e \rangle$ | $1.01 \times 10^{20}$ |
| $\beta$ | 0.026 |
| Temperature $T$ | 17 keV |
| Fusion Power $fus$ | 500 MW |

Table 1.1: A few ITER parameters for inductive discharges [Mukhovatov 2003].

Let us now give a closer look in the way the plasma is confined. The effect of a magnetic field is to make charged particles with charge $q$ and mass $m$ gyrate around the field lines at the cyclotron pulsation $\omega_c = qB/m$ and with a radius $\rho_L = mv_\perp/qB$, called the Larmor radius. $v_\perp$ is the velocity transverse to the magnetic field, of the order of the thermal velocity $v_t = \sqrt{T/m}$ . Particles are also freely streaming along the field line

[6] Above the critical field, superconductivity is lost.

at the parallel velocity $v_\parallel \sim v_t$. Thus a first naive guess is to install toroidal current coils around the torus to drive a toroidal magnetic field $\mathbf{B} = B_T\hat{\boldsymbol{\varphi}}$. Note that because of Ampère's theorem, the quantity

$$\oint_{R=C^{te}} \mathbf{B}\cdot \mathrm{d}\boldsymbol{l} = 2\pi R B_T, \tag{1.11}$$

where $R$ is the major radius of the torus, is constant when $R$ varies, since the surface encircled by the contour of the integral is crossed by the fixed current in the coils. Thus $B_T \propto 1/R$. The two halves of the poloidal section are hence called the *Low Field Side* (LFS) and *High Field Side* (HFS). It is easy to show that a configuration with only a toroidal field is unstable. Indeed the particles are subject to other forces, on top of the magnetic force: electric and inertial forces. Coupled to the magnetic field, they yield vertical drift velocities, directed upward for the electrons and downward for the ions, if the toroidal magnetic field points in the direction of the green arrow of Fig. 1.3. This generates a charge separation and a vertical electric field. There is also a drift associated with this electric field, but now it is the same for electrons and ions, and directed outward. Hence the plasma expands radially, causing a fast loss of the confinement. It can be shown that the confinement is lost in a time $\tau$ which has the following scaling

$$\tau \sim \frac{R_0}{v_t}\sqrt{\frac{a/R_0}{\beta}}, \tag{1.12}$$

where $v_t = \sqrt{T/m}$ is the particles' thermal speed, $R_0$ is the major radius of the torus and $a$ its minor radius. This time is a fraction of $\mu$s for a standard size device, clearly $\tau \ll \tau_E$. To counter this issue, the field lines must be twisted by the addition of a poloidal field. Thus the particles spend comparable times on both sides of the tokamak, inner and outer, which stabilizes the aforementioned instability[7]. There are different ways of setting up this secondary field $B_p$:

- In stellarators the toroidal coils are tilted in such a way that they generate by themselves the two necessary components of the magnetic field.
- In tokamaks a toroidal current of a few MA is driven in the core of the plasma, which generates the poloidal field component. This thesis deals only with the tokamak case.

The structure of the resulting magnetic field has many consequences. An important one is the splitting of the particles in two populations: the *trapped* particles and the *passing* particles. Since the plasma is strongly magnetized, the Larmor radius is small $\rho_L \ll R$, so the magnetic momentum $\mu = mv_\perp^2/2B$, where $B$ is the modulus of the magnetic field $\mathbf{B}$, is adiabatically conserved. Because of this, the particles undergo a force $-\mu\nabla_\parallel B$ n the parallel direction ($\nabla_\parallel \equiv \mathbf{b}\cdot\nabla$ with $\mathbf{b} = \mathbf{B}/B$). Hence if the particle's parallel velocity is not large enough, it is trapped between two mirror points. This is a

[7] However more benign instabilities related to the centrifugal "hoop" force remain present and must be studied and dealt with.

classical result: a magnetic field varying along its field lines constitutes a magnetic well. The other particles are passing. As a function of the radial coordinate $r$ and the torus major radius $R_0$, the fraction of trapped particles is $f_t = \sqrt{2r/R_0}$. This separation into two populations has consequences, which study constitutes the neoclassical physics:

- There is a radial inward pinch, called Ware pinch [Ware 1970], due to the conservation of the toroidal momentum of the trapped particles. More generally, there is a convective and diffusive transport linked with the particular trajectories of the trapped particles. This is thoroughly studied in the framework of neoclassical transport. In tokamaks, the neoclassical diffusive transport is in general dominated by the turbulent transport in the perpendicular direction.

- There is a current, called *bootstrap current*, proportional to the pressure gradient, associated with the trapped particles population. This bootstrap current should play an important role on the future tokamak ITER and constitute a significant fraction of the total current used to generate the poloidal field.

### The tokamak

We can now detail the basic principles of a tokamak. Fig. 1.4 presents a model of the ITER tokamak as it is planned. The identified elements can be described as follows:

1. The toroidal field coils. They are superconducting to prevent power losses and heating of the coils due to Joule effect.

2. The poloidal field coils. During a discharge, the current in these coils is varied. This induces a toroidal electric field which drives the current of several MA according to the resistive Ohm's law $E_\varphi = \eta j_\varphi$, where $\eta$ is the resistivity. We shall come back to Ohm's law in detail in the following chapters. Thus a tokamak functions as a transformer. The total current in the coil is varied from $+I$ to $-I$ during the discharge. Because of this, a tokamak is intrinsically a pulsed machine, unless the current is externally driven. Such external current drivers already exist and will be made available in the ITER tokamak in a second phase of operation.

3. The main plasma chamber.

4. The vertical stability control coils. These coils generate a vertical magnetic field, used to control the position and shape of the plasma.

5. Antennas of the heating systems. A part of the power required to heat the plasma to 10 keV is the ohmic power $P_{\text{Ohm}} = \eta|\mathbf{J}|^2$. However for an ITER size tokamak, this is unsufficient and additional power is required, totalizing about 50 MW. Once the plasma is hot enough and fusion reactions are triggered, the main heating power comes from the reaction products, the 3.5 MeV $\alpha$ particles.

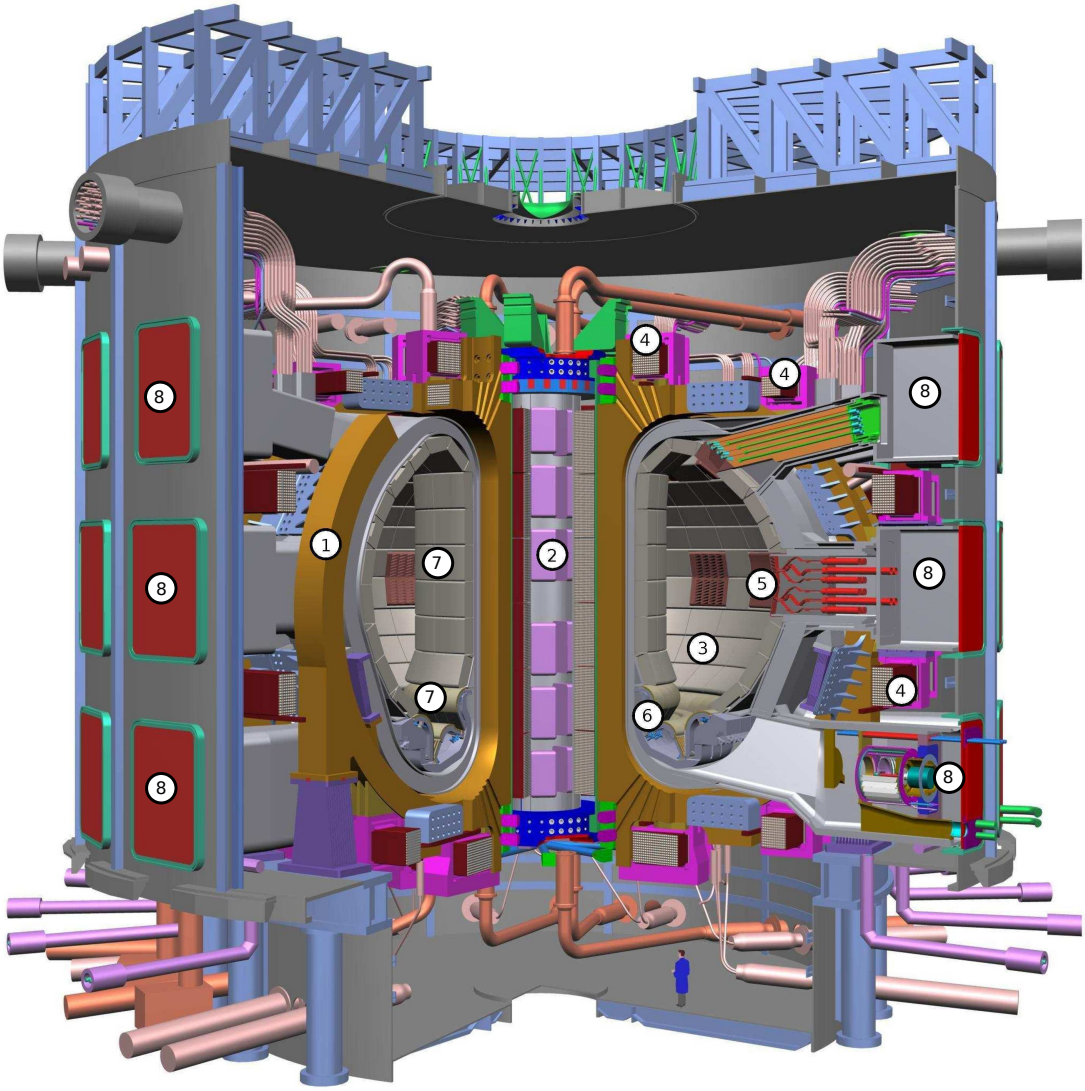


Figure 1.4: The ITER tokamak.

6. The *divertor*. This device is made of targets in the bottom part of the tokamak, and is intended to collect the very high energy fluxes escaping the plasma, as well as the ashes. Fluxes are as high as 10 $MW.m^{-2}$ in steady-state, and very resilient materials must be used. The solution which is most commonly accepted is to use Tungsten (W).

7. Plasma facing components. These components must be designed to undergo little damage from the steady state neutron and heat fluxes. The heat fluxes being mainly taken to the divertor, they can be made with lighter elements, cheaper and less contaminant with high-Z impurities. As we will see, contamination of the plasma by high-Z impurities is an issue.

8. Port plugs. These port plugs are used to implement the heating and fueling systems, as well as the numerous diagnostics.

The plasma is separated in different regions, corresponding to different magnetic topologies. Fig. 1.5 represents a view of the poloidal plane of ITER, where different regions are highlighted. In the core the helical magnetic field lines wind around the torus and define nested flux surfaces up to a flux surface called the magnetic separatrix or Last Closed Flux Surface (LCFS). After the LCFS, field lines are open and directed on the *strike points* of the divertor plates. The region located between the LCFS and the edge is called the *Scrape-Off Layer* (SOL).

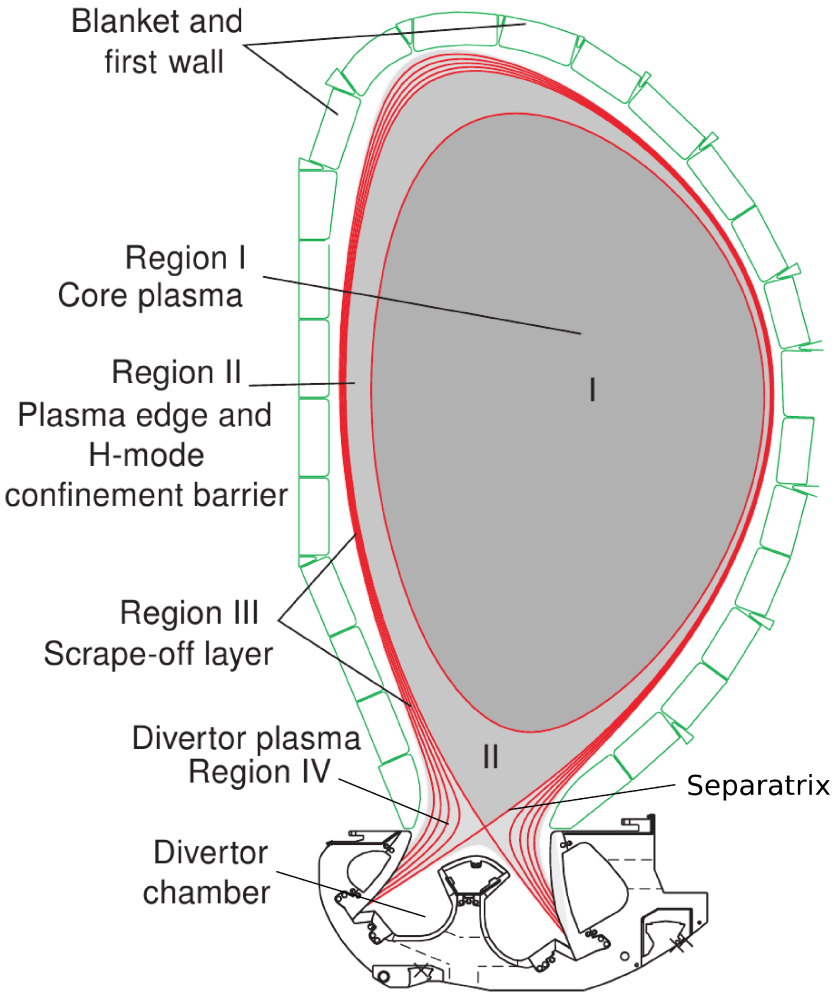


Figure 1.5: Magnetic topology in the poloidal plane. Figure taken from [ITER 1999a].

### H mode and L mode

It was discovered in 1982 [Wagner 1982] that diverted tokamaks[8] can develop a configuration of enhanced confinement called H mode (High confinement mode), as opposed to

[8]Some tokamaks, like Tore Supra, do not have a divertor. The plasma is only supported by *limiters*. In this case the first magnetic field line touching the limiter defines the LCFS.

standard conditions, L mode (Low confinement mode), when the heating power exceeds a certain threshold. In H mode, pressure and density profiles display a steep gradient in the edge region, close to the SOL, called the *pedestal*. The physics of H mode is closely linked to turbulence suppression, but is far from being elucidated yet. Fig. 1.6 shows the pressure profile in H mode compared to L mode. In the region of the pedestal, transport is significantly decreased. The most widespread interpretation is that small scale turbulence feeds back on the mean profiles, namely the radial electric field and the associated electric drift velocity, and develops so-called *zonal flows*, sheared poloidal flows which actually reduce turbulence by tearing apart the associated small scale convection cells. No model however is able to predict the value of the power threshold necessary to trigger the H mode. The problem with H mode is that it comes with *Edge Localized Modes* (ELMs), a magnetohydrodynamic instability which effects will be detailed below.

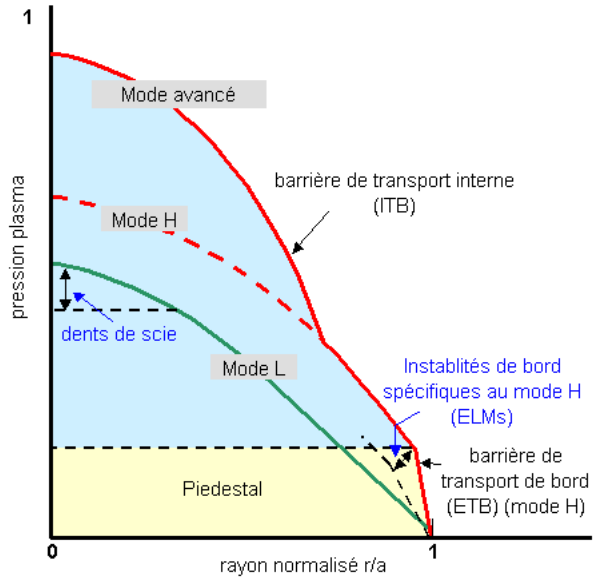


Figure 1.6: Typical pressure profiles in L mode and H mode.

### Safety of a tokamak

One now understands why a tokamak is intrisically safe and clean. The reactants present in large quantities on site are the inert Deuterium and Lithium, while the products are neutrons and the inert He nuclei. The reactions are so difficult to initiate that if the confinement is lost, the temperature immediately drops and reactions stop. The concept of critical mass is absent because this is not a chain reaction, contrary to the fission of heavy elements. There is not any long term radioactive waste generated. The radioactivity produced on site comes from the neutron bombardment of the wall. The neutrons are intended to collide on Lithium or to be slowed down while transferring their energy to water, but some neutrons first collide on the wall and cause displacements in the metallic lattice, as well as nuclear reactions which make the wall radioactive. Given the elements produced by these reactions, the radioactivity of the waste decreases

rapidly after the machine shut down, compared to fission reactors. In 100 hundred years, radioactivity per unit mass is between one order of magnitude higher and one order of magnitude lower than coal ash radioactivity, depending on the alloys chosen for the machine. Despite its *in situ* production, a small quantity of Tritium is always present on site, in the reactor chamber or stored, waiting to be fueled in. This quantity amounts, in the case of ITER, to a few grams, and in case of major accident, it will escape in the atmosphere and its concentration will rapidly drop to acceptable levels. Tritium is dangerous by ingestion. The lethal dose is of the order of 1 mg, so if Tritium is uniformly spread, its concentration is below the lethal level in a radius of a few meters. Thus a large scale contamination is not to be feared, even if the effects of small quantities of Tritium on the organism must be evaluated for a more precise assessment of risks.

It is now clear why fusion gathers scientists of all around the world, striving to produce usable energy from this very large energy source. It is time to address the issues faced by the tokamak community. These issues will all have to find a solution if a fusion device is to be commercialized eventually.

### 1.1.3 The issues

Most researchers in the community are now confident that it is possible to confine a D-T plasma at more than 10 keV for a few hundreds of seconds and trigger nuclear reactions, totalizing in a thermal fusion power of several hundreds of MW. This is one of ITER's objectives, and it will probably be attained. A much more difficult matter is the achievement of a steady-state operation. Steady-state, in a first sense, means not being limited by the amount of flux available in the poloidal field coils. In this sense, a plasma discharge lasting a few hours or a few days with reliable external and bootstrap currents would be a big success. In a second sense, a steady-state tokamak must operate not only for hours, but for days, weeks, months and years[9]. This last goal is much more difficult to reach. We will now detail the most difficult issues, whether they apply to reaching steady-state in the first sense or in the second sense.

#### Magnetohydrodynamics and disruptions

A tokamak plasma is extremely hot on the inside, 2-10 keV, while it is rather cold close to the edge, a few eV. The pressure and current density are very peaked, that is, they come with large gradients. Velocity distributions are also generally far from Maxwellian: $\alpha$ particles are born with a very peaked velocity distribution centered around 3.5 MeV, while external heating systems also modify the velocity distribution. In other words, on the thermodynamical point of view, a tokamak plasma is a genuine free energy reservoir, far from thermodynamical equilibrium, which makes it keen to develop a lot of instabilities. Some of the instabilities linked with inhomogeneities in the position space can be quite well described in a fluid framework. The fluid framework of magnetized plasmas is called magnetohydrodynamics (MHD). The MHD instabilities can trigger the apparition

[9]Note that even DEMO may still be a pulsed machine with discharges a few hours long, however PFCs being in general quite sensitive to thermal cycles, this is not an ideal situation.

of magnetic islands which increase the transport of particles and heat from the core to the edge and thus decrease the confinement time, while the goal is to maximize it.

The sawtooth phenomenon is triggered by an MHD instability called the internal kink mode. This instability periodically flushes the plasma core, up to mid-radius approximately, which is equivalent to transiently increasing the transport on a large part of the plasma. The peak pressure and density are reduced significantly, and this transiently reduces the associated fusion power. However the flushing effect from sawteeth can also have a positive effect when it comes to evacuating impurities and ashes from the core. This problematic will be developed in this thesis.

In addition to degrade confinement, some instabilities can have more serious consequences, like ELMs. When an ELM is triggered in H mode, the heat perturbation generated enters the SOL and propagates rapidly along the field lines and hits the divertor targets, releasing their energy. The peak heat load due to an ELM can be as high as 20 MW.m$^{-2}$ (transient), to be added to the steady ∼10 MW.m$^{-2}$ heat flux on the divertor plates [Pitts 2011]. These heat loads can damage or melt the divertor components and must be avoided. Several ways exist to mitigate the ELMs or their effects. For instance, instead of preventing ELMs from happening, one can trigger frequent ELMs with a smaller energy per ELM. ELMs can be triggered by injecting high velocity pellets into the plasma, or controlled by applying magnetic perturbations from small coils located in the vacuum vessel. These techniques will have to be mastered for future large scale tokamaks.

Disruption is an other phenomenon which must be imperatively avoided in large tokamaks. When a disruption occurs, the confinement is lost abruptly, there is a thermal quench, which is often caused by a primary MHD instability. The thermal quench increases the resistivity[10], causing a current quench in the plasma. An other serious issue is the generation of *runaway* electrons during a disruption. If the electric field is above a certain threshold, called the Dreicer field $E_{\text{Dreicer}} = (n_e e^3 \log\Lambda)/(4\pi\varepsilon_0^2 T_e)$, where $e$ is the electron charge, $T_e$ the electron temperature, and $\log\Lambda$ the Coulomb logarithm, the electrons decouple from the main plasma and are accelerated to relativistic velocities. The Dreicer field is of the order of a few V.m$^{-1}$, to be compared to the toroidal inductive electric field (used to generate the toroidal current) of a few 0.01 V.m$^{-1}$. Because of the resistivity sharp increase at the thermal quench, the ohmic electric field is transiently significantly increased as well and overwhelms the Dreicer field, which results in the production of a large current of runaway electrons. In ITER, runaway electrons generated at major disruptions are predicted to attain the energy of 12 MeV[11] and to carry 10 MA of current. These electrons end up in the walls, causing damage to it. Disruptions are one of the most serious issues for ITER and future tokamaks.

[10] The resistivity is proportional to the collision frequency, which is proportional to $T^{-3/2}$. This is counter-intuitive, because one naively expects a got plasma with fast particles to be more collisional. However when particles move fast, their interaction time is decreased in a Coulomb collision, so that the collision cross-section is decreased.

[11] The energy at rest of an electron, $\mathcal{E}_e = m_e c^2$, is 0.511 MeV.

### Turbulence and impurities

Turbulence is such an important matter because it is directly linked to the transport of heat and particles in the plasma, and to the physics of H mode. Understanding, predicting and controlling the turbulent transport coefficients is very important. Nowadays, such an understanding remains fragmented. However, as was the case for designing planes in the past, ITER has been designed using scaling laws. The scaling law of the confinement time $\tau_E$ used for designing ITER is shown on Fig. 1.7. The scaling law was determined to fit several machines in H-mode. Extrapolation to ITER parameters predicts a confinement time of a few seconds.

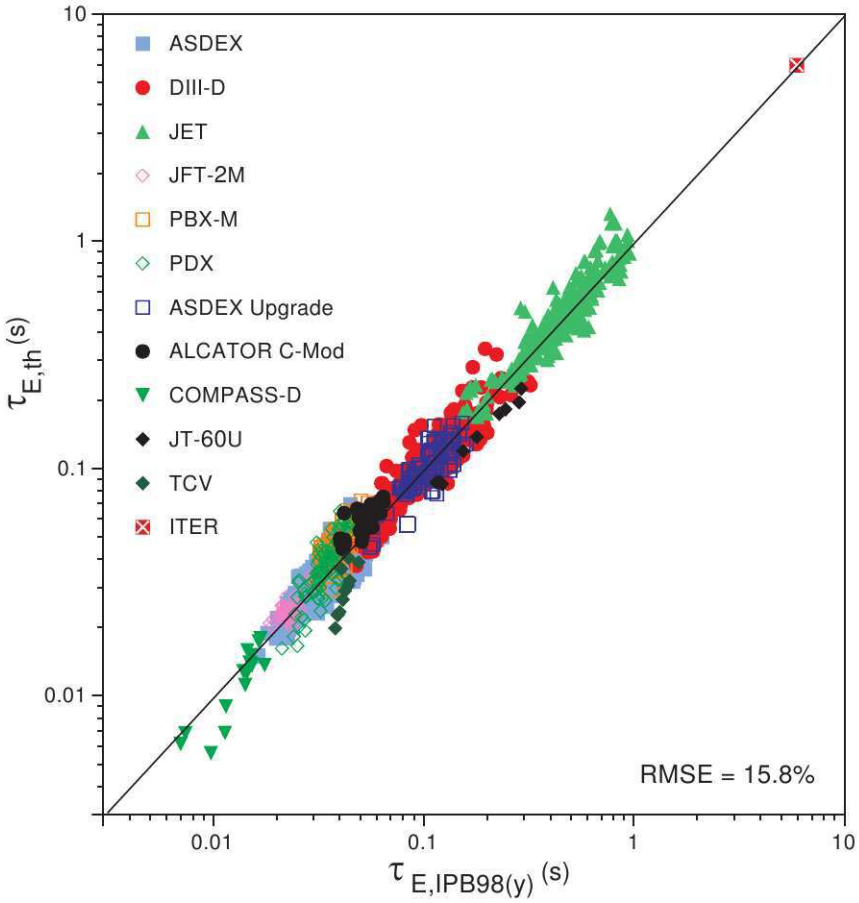


Figure 1.7: Confinement time scaling law used for designing ITER [ITER 1999b]. Notice that this scaling is only relevant to H-mode, and also, that ITER has been scaled down a little bit since 1999.

Turbulence is also related to the density transport which may be an even more serious problem. Indeed, particles ${}^{A}_{Z}X$ are transported differently radially, across flux surfaces, depending on their mass number $A$ and their charge $Z$, so it is important to know the steady-state profiles of the different impurities. Indeed an important source of power losses has been disregarded above: the radiation emitted by accelerated charged particles. There are two main sources of such losses in the plasma:

- The cyclotron losses associated to the cyclotron motion around the field lines. They are proportional to $1/m_s^3$, where $m_s$ is the mass of the considered species. Thus only the electrons contribute to these losses. However, the plasma is optically thick at the electron cyclotron frequency, so that these losses are dynamically reabsorbed by the plasma. Hence they can be neglected compared to the second source of losses.

- The second source of losses is the bremsstrahlung radiation emitted during the Coulomb collisions.

Bremsstrahlung losses read:

$$P_b = \frac{n_e n_i Z^2 e^6}{96\pi\varepsilon_0^3 m_e^2 c^3 \lambda_c}, \tag{1.13}$$

where $\lambda_c$ is the distance of minimal approach between electrons and ions. Its expression differs from *Eq.* (1.1) because of quantum effects. At 10 keV, $\lambda_c$ is of the order of $\hbar/m_e v_{te}$. The important thing is the $Z^2$ factor at the numerator. It means that the tolerable impurity concentration of heavy impurities is much lower than that of light impurities. The main part of the wall is made from Beryllium (Be) for this reason. Be only lightly contaminates the plasma in terms of bremsstrahlung losses. On top of this, heavy impurities can have enough electrons so that they are not fully stripped even in the deepest core. When this is the case, there are line radiations and radiative recombination losses on top of the bremsstrahlung losses. The divertor targets are in Tungsten ($^{183.8}_{74}$W) to withstand the heat fluxes in the SOL and heat loads from ELMs. The problem with W is that in addition to the fact that its charge number is large (large bremsstrahlung losses), it is never fully stripped in the plasma (typically, $Z = 30-50$ between 1 keV and 10 keV). The combined bremsstrahlung, line emission and radiative recombination losses are very important. As a result, a maximum relative concentration of $1.9\times10^{-4}$ can be tolerated in the core of ITER plasmas to be able to reach the ignition condition [Pütterich 2010].

Hence the control of impurity transport is crucial in tokamak plasmas, especially when W is used as the dominant material in the divertor. In steady state regime, if transport is local, the density profile of an element is determined by two coefficients:

- The radial pinch velocity $V_{\text{pinch}}$

- The diffusion coefficient $D_\perp$

Indeed the radial flux of an impurity $Z$ with density $n_Z$ can be written $\Gamma_r = n_Z V_{\text{pinch}} - D_\perp \partial_r n_Z$. In steady state, and in the absence of a source at $r = 0$, the flux must vanish, so that the density $n_Z$ verifies

$$\frac{\partial_r n_Z}{n_Z} = \frac{V_{\text{pinch}}}{D_\perp}. \tag{1.14}$$

The diffusion coefficient is usually dominated by turbulence and is typically of the order of 1 $\text{m}^2.\text{s}^{-1}$. The pinch velocity is of the order of 0.1 $\text{m.s}^{-1}$. It can be negative or positive, depending on the type of turbulence happening in the plasma. When it is positive, the profile is peaked, while it is hollow in the other case. Here one of the biggest difficulties of

tokamak design appears: the necessity to confine the plasma well with peaked pressure and electron density profiles, and to have on the contrary a very poor confinement of the impurities. This is a very difficult issue on the JET tokamak with the W divertor installed in 2012, the so-called ITER Like Wall (ILW). W indeed tends to accumulate in the core, thus leading to a radiative collapse of the discharge: the radiative losses become so large that the temperature decreases until the plasma chokes. This issue will have to be solved for future tokamaks, in particular ITER. This thesis is in large part concerned with this issue because, as indicated above, sawteeth can periodically flush the core from impurities. The impurity transport induced by the sawtooth instability will be developed in chapter 7.

### PFCs and divertor conception

The design of PFCs and especially the divertor is a very delicate and subtle task because of the aforementioned issues. The best tradeoff between resistance, cost, and low plasma contamination will have to be found. As we have seen, currently W is considered the most promising solution because it seems to be the only solid material able to resist the 10 $MW.m^{-2}$ arriving on the divertor plate, and the additional transient heat loads due to ELMs in H-mode. However, other innovative solutions are envisaged in the future, like flowing liquid lithium PFCs (not planned to be used on ITER, though). Instead of arriving on a solid surface, the SOL plasma would hit molten lithium targets. The advantage of a liquid target is that it cannot deform or be damaged. There are active or passive ways to let the lithium flow in the PFC in order to help heat extraction. Lithium has two other advantages, which is that it is a low $Z$ material, thus it does not lead to worrying radiation losses, and also it is a low recycling material, (which means there is low reinjection of cold gas in the plasma). Low wall recycling has been generally observed to clearly improve the plasma performance. This low recycling of lithium walls is due to its good chemical reactivity with hydrogen, which is then retained in the PFC. Unfortunately, this has the crucial counterpart that it leads to high tritium retention in the wall, which should be avoided by any means.

On top of this, the plasma facing components, as well as the tokamak structure, undergo a heavy 14 MeV neutron bombardment. This induces displacements in the structures, leading to premature ageing. The long term consequences are still not fully understood as this neutron energy is one order of magnitude higher than what is obtained in fission reactors, and 14 MeV neutrons are difficult to produce. To help answer this material issue, the International Fusion Materials Irradiation Facility (IFMIF) is under design in Rokkasho, Japan. The facility would produce the 14 MeV fusion neutrons out of deuteron beams colliding on a lithium target. Thus tokamak PFCs will be tested under realistic neutron bombardment.

### Conclusion

The purpose of this section was not to be exhaustive, by any means. Many other issues need to be tackled, like the performances and reliability of the superconducting toroidal

field coils and of the heating systems, the resilience of diagnostics to the neutron flux, the Lithium blanket which will produce the Tritium, remote handling in a radioactive environment, porosity of materials after long neutron exposition, fuel retention, etc. We did not emphasize the material aspect of the issues which will have to be tackled, but we tried to make clear the fact that the physics issues *in fine* amount to material issues. Disruptions are dangerous because they are damaging, so are ELMs, and even turbulent transport is a material issue since impurity transport limits what can be used for PFCs. If these issues find a way out in the coming years and with ITER, then an optimistic future can be foreseen for tokamaks.

We now introduce the sawtooth phenomenon, which is the focus of this thesis.

## 1.2 Introduction to the sawtooth phenomenon

Sawteeth, also called internal disruptions, are fast relaxation oscillations of the core temperature and density profiles. They were first discovered in 1974 by Von Goeler *et al.* [von Goeler 1974] on raw Soft X-Ray (SXR) measurements, see Fig. 1.8 which reproduces the original figure. On the core signal, a slow ramp phase is followed by a rapid crash, which amplitude on the temperature can reach a few keV. Edge signals on the contrary exhibit periodic sharp increase, corresponding to the core energy being redistributed rapidly from the core region to the edge. On current machines, the sawtooth period ranges typically between 20 ms and 500 ms, while the crash time is very short, typically 100 $\mu$s [Edwards 1986]. The sawtooth period on ITER will be longer, ranging between a few seconds and 100 seconds [Porcelli 1996]. Shortly after their discovery, sawteeth drew a lot of attention from the fusion community because of their disruptive nature, and significant theoretical efforts were undertaken to understand the triggering mechanism and the very short crash time. A few aspects have been rapidly discovered [Bussac 1975, Kadomtsev 1975],

- Sawteeth are triggered by the internal kink instability, with poloidal and toroidal mode numbers $\mathsf{m} = \mathsf{n} = 1$.
- Magnetic field lines are reconnected at the resonant surface of the instability, where the winding number of the field lines, $q$, also called safety factor, is equal to one.
- Sawteeth flatten the temperature and density profiles over a disk of radius larger than the $q = 1$ radius.

The details of the internal kink stability have been thoroughly studied, and the linear structure of this instability is well known in a number of relevant situations, both in ideal (dissipation free) and non-ideal regimes, with toroidal geometry included, etc. See for example [Bussac 1975, Ara 1978, Deblank 1991] and linear MHD textbooks for the linear theory. Several attempts have been made to investigate the non-linear regime of the crash, which determines the characteristic time of the crash phase. Resistivity $\eta$ was first identified as the key ingredient for dissipating field lines at the reconnection

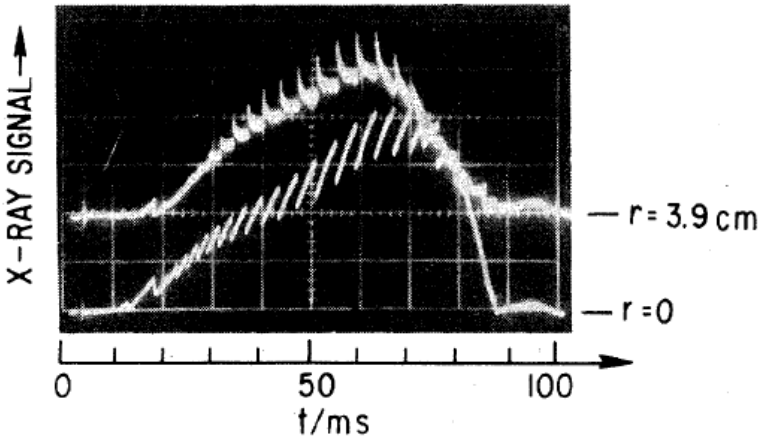


Figure 1.8: Original figure appearing in reference [von Goeler 1974]. The periodic relaxation oscillations are visible on the SXR signal.

layer, but the crash time $\tau_{\text{rec}}$ obtained with this assumption, $\tau_{\text{rec}} \propto \eta^{1/2}$ (see chapter 2), was found typically one order of magnitude slower than in the experiment. Several non-linear attempts were made, and some progress has been achieved, in the theoretical [Rosenbluth 1973, Waelbroeck 1989, Wang 1993, Zakharov 1993, Rogers 1995] and simulation [Aydemir 1992, Biskamp 1994, Lütjens 2009, Halpern 2011b] domains, but the fast crash phase still resists a convincing theoretical description. As we will see in chapter 5, the phenomenology is actually extremely diverse and rich, which makes it difficult to give a simple theoretical description.

Today, the concern about sawteeth is manifold. First the fusion power $P_\alpha \propto p^2$ drops significantly after the sawtooth crash. This drop is transient and the time-averaged drop in fusion power depends strongly on the sawtooth period. More precisely it depends on the ratio between the characteristic pressure build-up time, of the order of 1 s in ITER, and the sawtooth period. If the sawtooth period is of the order of 1 s, then the average drop in the fusion power can be more than 10%, while it is only a few % in the case where the sawtooth period is 100 s.

Second, and more importantly, sawteeth have been found to sometimes trigger secondary instabilities, like *neoclassical tearing modes* (NTMs) [Buttery 2004]. A tearing mode is an MHD instability which acts as to reconnect field lines on rational surfaces of the safety factor $q$. They are denoted by their poloidal and toroidal mode numbers $\mathsf{m}$ and $\mathsf{n}$, written as a couple $(\mathsf{m}, \mathsf{n})$. NTMs are (2,1) or (3,2) tearing modes. The NTM is called neoclassical because its growth rate is positive only when the island is sufficiently large to overcome the stabilizing effect of the bootstrap current[12]. On the one hand, the basic dynamics and onset of the tearing mode is well understood. It is ruled by completely non-linear physics: when a seed island is present, it causes the pressure to flatten, which reduces the bootstrap current and its stabilizing influence. On the other hand, the mechanisms of NTM triggering by the sawtooth crash are still poorly understood.

[12] This is the reason why they are called "neoclassical", since the bootstrap current is a neoclassical effect, as explained in section 1.1.2. The bootstrap current is proportional to the pressure gradient.

However the dominant parameter has been identified to be the sawtooth period rather than its amplitude [Chapman 2010a].

A tearing typically saturates at a finite island width $W_0$. The presence of a large island[13] enhances the radial transport and thus degrades the confinement. In some cases, the confinement is so bad after destabilization of the NTM that it further triggers a major disruption. A way to avoid this is to use localized current drive to invert the process and eliminate the tearing island. Also, a lot of progress have been made recently to tailor the sawtooth period in large tokamaks [Chapman 2011, Graves 2012], with the purpose of avoiding long sawtooth periods, more keen to trigger an NTM. This thesis will lightly tackle this problematic in section 2.2.7.

Finally, there may be a more positive aspect of sawteeth. As already mentioned, the plasma impurity content is a very serious issue for tokamaks, especially impurity accumulation in the core. In theory, sawteeth should help reduce the impurity content by regularly washing the core from the impurities and He ashes. If this process is efficient and is able to prevent build up of the impurity profiles in the core, then the advantage can balance the disadvantage of transiently reducing the fusion power. This is the main focus of the present thesis.

## 1.3 Outline of the thesis

The fundamental theoretical tools necessary to tackle the sawtooth phenomenon are presented in chapter 2. The different sets of MHD equations used to study the phenomenon numerically are derived, as well as the linear stability and triggering of the sawtooth, using the ideal MHD energy principle for the internal kink mode. The principle of magnetic field reconnection is also presented.

The numerical tools are presented in chapter 3: the equilibrium code CHEASE and the nonlinear MHD code XTOR-2F, which are the basic numerical tools underlying this work. The different regimes of sawtooth oscillations available as a function of the physical parameters are discussed. Also, an advection/diffusion bidimensional code developed for proof-of-principle purposes is presented.

Chapter 4 is concerned with the nonlinear evolution of the magnetic island, which determines the time scale of the sawtooth crash. Kadomtsev's model, the most commonly invoked model for the sawtooth crash dynamics, is detailed. The rest of the chapter is dedicated to comparing XTOR-2F's results in the framework of resistive MHD and bifluid MHD with analytical models. The contribution to the basic understanding of the sawtooth phenomenon is emphasized.

After presenting the main diagnostics used to collect the experimental data, chapter 5 details a few significant experimental features of the sawtooth, based mainly on the Tore Supra and JET tokamaks. It is understood why the sawtooth is an extremly rich and diverse phenomenon which cannot be grabbed in one sentence, and why it still resists a fully convincing description. Some of the data presented can be regarded as simple curiosities but they have been included to convince the reader of the complexity

[13] It is said to be large if $W_0$ is more than a few percents of the minor radius

of the phenomenon and its relations with many other tokamak phenomena. The last two subsections document the experimental data which motivated the present thesis, namely, the observed transport of impurities by the sawtooth crash and the observation of very specific electron density structures after the sawtooth crash on both Tore Supra and JET.

The last two chapters represent the core of the thesis. In chapter 6, the electron density measurements are modeled with the XTOR-2F code. A good qualitative agreement is found between the measurements and the simulations, and a satisfying physical understanding of the structures is obtained. Namely, the physical mechanism of density redistribution is shown to be different from that of the temperature, which behaves accordingly to Kadomtsev's model. The importance of carrying the same study for impurities is underlined.

In chapter 7, the impurity model implemented in XTOR-2F is justified and simulations of the transport induced by a sawtooth crash are carried out for different types of precrash impurity density profiles (peaked or hollow). The results are compared to Kadomtsev's model, which is shown to be in quite good quantitative agreement with the simulations. This result is a rather surprising one, as chapter 6 shows that the density (be it the electron density or the impurity density) is dominated by an essentially different mechanism during the sawtooth crash. A possible reason for this agreement is given, and the interest for sawtooth modeling is emphasized, since Kadomtsev's model is very fast to implement.

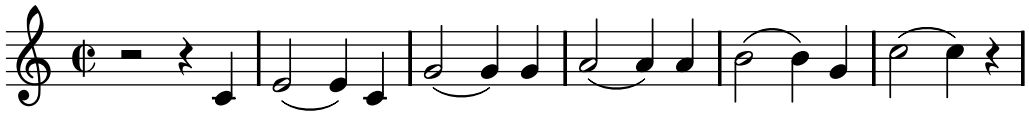

*Te Deum (H. 146)*
**Marc-Antoine Charpentier**

Chapter 2

# The sawtooth instability: fundamentals

## Contents



Unfortunately, there is no such thing as a standard first principle model for the sawtooth instability. As will be discussed in Chapter 5, it appears that sawtooth phenomenology is extremely rich and diverse and cannot be grasped in a simple sentence. However, some features included in most models have been repeatedly reported as essential and their pedagogical interest justifies a more in-depth description. Namely,

the sawtooth cycles have always been associated with the presence of a $q = 1$ surface in the plasma. This motivated research on the internal kink mode, which essential features we will derive in section 2.2, after a first contact with MHD theory in section 2.1. Also, the sawtooth mechanism involves magnetic reconnection, usually very fast, leading to profile relaxation. The first author to propose a precise reconnection model for the sawtooth was Kadomtsev [Kadomtsev 1987], inspired by the work of Sweet and Parker [Sweet 1958, Parker 1963]. It is well known today that Kadomtsev's resistive reconnection model is not able to account for the very fast time scale of the sawtooth crash. However, it provides a good basis of knowledge for anybody interested in sawtooth. The basics of magnetic reconnection in tokamaks will be presented in section 2.3. Kadotsev's model and its implications will be presented only in chapter 4.

## 2.1 Magnetohydrodynamics

### 2.1.1 Magnetic configuration in a tokamak

We start with the description of the tokamak magnetic field and safety factor. The magnetic field is set up in order to balance the pressure force due to the pressure gradient between the dense hot core and the cold edge. Thus the basic equilibrium relation is

$$\mathbf{J} \times \mathbf{B} = \nabla p, \tag{2.1}$$

where $\mathbf{J}$ is the electric current running through the plasma, and $\mathbf{J} \times \mathbf{B}$ the magnetic force. This relation has the important consequence that the pressure is constant on magnetic field lines: $\mathbf{B} \times \nabla p = 0$ and $\mathbf{J} \times \nabla p = 0$.

At equilibrium, the magnetic field of a tokamak is usually structured in nested toric surfaces[1] (see Fig. 2.1). In the standard case, a magnetic field line densely fills this surface, while it winds around and around the torus. There are cases where a field line closes back on itself after one or more toroidal turns, and such surfaces are called rational surfaces. Note than if one field line closes back on itself, all field lines of the surface have the same property, otherwise (if they would densely fill the surface), the field lines would eventually cross, which is forbidden for any well-behaved vector field. To fix notations, Fig. 2.2 shows the definitions of the geometrical angles and coordinates for a toroidal configuration. The triplet $(\nabla r, \nabla\theta, \nabla\varphi)$ is direct. It is convenient to define the toroidal and poloidal fluxes:

$$\Psi_T = \iint_{\mathcal{S}_1} \mathbf{B} \cdot \mathrm{d}\mathbf{S} = \oint_{\mathcal{C}_1} \mathbf{A} \cdot \mathrm{d}\mathbf{l} \tag{2.2}$$

$$\Psi_p = \iint_{\mathcal{S}_2} \mathbf{B} \cdot \mathrm{d}\mathbf{S} = \oint_{\mathcal{C}_2} \mathbf{A} \cdot \mathrm{d}\mathbf{l}, \tag{2.3}$$

and the integration contours $\mathcal{C}_1$ and $\mathcal{C}_2$ and surfaces $\mathcal{S}_1$ and $\mathcal{S}_2$ are shown on Fig. 2.3. Thus

[1] The conditions for this to be possible are actually quite restrictive (see for example [White 2006]), but this holds for the equilibrium state of a tokamak core. However during unstable evolution of the plasma, we will see that magnetic surfaces are often destroyed with the formation of magnetic islands or even stochastic regions, where a field line densely fills a finite volume of the tokamak.

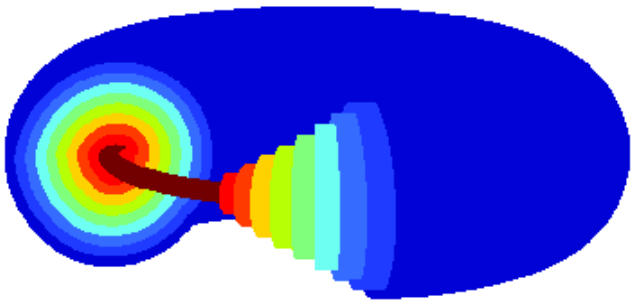

Figure 2.1: Nested tori representing the magnetic surfaces.

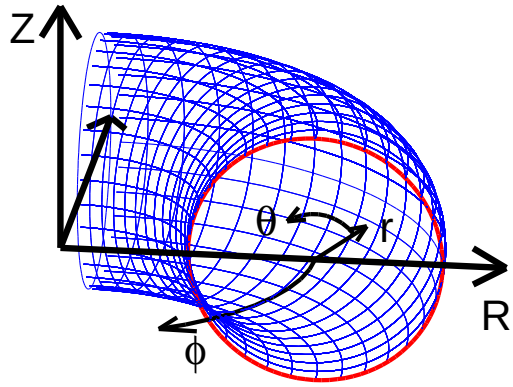


Figure 2.2: Geometrical definitions for a tokamak configuration.

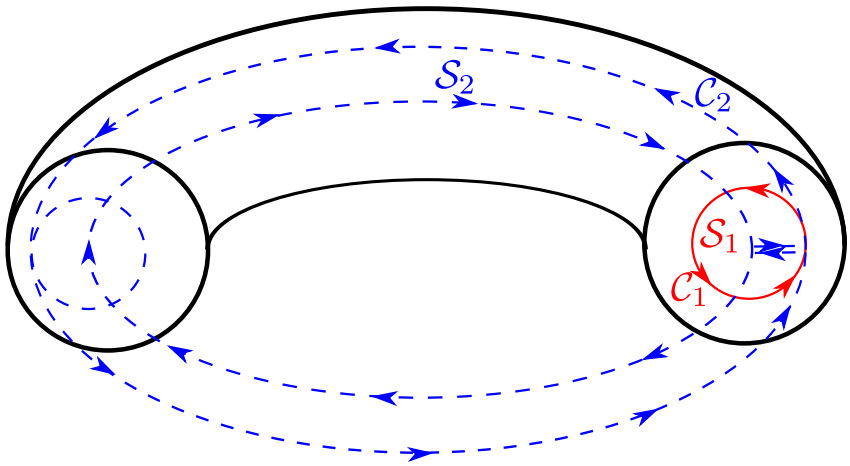


Figure 2.3: Integration contours for computation of the toroidal ($\mathcal{C}_1$) and poloidal ($\mathcal{C}_2$) fluxes.

it is possible to label the flux surfaces with their toroidal or poloidal flux. Traditionally, the poloidal flux is denoted $\psi$ and defined by $\psi \equiv \Psi_p/2\pi$, which makes the expression of

the magnetic field more convenient. The toroidal flux is also redefined: $\Psi_T/2\pi$ is used and still called $\Psi_T$. Usually the poloidal flux (or rather its square root) is chosen as a radial coordinate. With our conventions, it increases from the magnetic axis toward the edge. Thus the magnetic configuration can be described using the basis $(\nabla\varphi, \nabla\psi, \nabla\varphi \times \nabla\psi)$, and the magnetic field can be written

$$\mathbf{B} = C_1\nabla\varphi + C_2\nabla\psi + C_3\nabla\varphi \times \nabla\psi. \tag{2.4}$$

Because of the definition of the flux surfaces as constant $\psi$ surfaces, we have $\mathbf{B}\cdot\nabla\psi = 0$, whence $C_2 = 0$. Since a tokamak is axisymmetric (neglecting the ripple induced by the finite spacing between coils), the equilibrium quantities depend only on $\psi$ and on the poloidal angle $\theta$. The field is dominated by the toroidal contribution generated by the toroidal field coils. Applying Ampère's theorem on a contour at $R = C^{te}$, we see that

$$\oint \mathbf{B}\cdot\mathrm{d}\mathbf{l} = \oint R^2\mathbf{B}\cdot\nabla\varphi\mathrm{d}\varphi = 2\pi C_1 = \mu_0 I_{tot}, \tag{2.5}$$

where $I_{tot}$ is the total current in the external coils. Thus the contribution of the external coils to $C_1$ is constant. We can easily show that the contribution of the plasma currents to $C_1$ depends only on $\psi$. Take on a flux surface any toroidal contour at $R = C^{te}$, and using that $\mathbf{J}\cdot\nabla p = 0$, $\mathbf{B}\cdot\nabla p = 0$ and $p = p(\psi)$ (we anticipate a little bit over the following, see the discussion of *Eq.* (2.40)). Thus there is no current through the flux surface and obviously the result of Ampère's theorem is independent of the initial choice of the contour. Hence the contribution of the plasma to $C_1$ is also a flux function, and since $\mathbf{J}_\perp = (\mathbf{B}\times\nabla p)/B^2$, the correction is of order $\beta$. In the following we denote $C_1$ by $I(\psi)$. By computing the poloidal flux with the expression for $\mathbf{B}$, we also see that $C_3 = 1$, and we write the magnetic field

$$\mathbf{B} = I(\psi)\nabla\varphi - \nabla\psi\times\nabla\varphi, \tag{2.6}$$

The toroidal field is $\mathbf{B}_T = I\nabla\varphi$ and the poloidal field is $\mathbf{B}_P = -\nabla\psi\times\nabla\varphi$.

We now define the safety factor $q$ of the magnetic configuration as the pitch of the magnetic field lines. It is equal to the number of turns made in the toroidal direction for each turn in the poloidal direction. Since when moving a distance $\mathrm{d}\boldsymbol{r}$, a scalar quantity $f$ varies by $\mathrm{d}f = \mathrm{d}\boldsymbol{r}\cdot\nabla f$, we can formally write the definition of $q$:

$$q \equiv \frac{1}{2\pi}\int \frac{\mathbf{B}\cdot\nabla\varphi}{\mathbf{B}\cdot\nabla\theta}\mathrm{d}\theta. \tag{2.7}$$

Since $\mathrm{d}^3\boldsymbol{x} = \mathcal{J}\mathrm{d}\psi\mathrm{d}\theta\mathrm{d}\varphi$ with $\mathcal{J} = [(\nabla\psi\times\nabla\theta)\cdot\nabla\varphi]^{-1}$, we can develop *Eq.* (2.7) to write that

$$q = \frac{\mathrm{d}}{\mathrm{d}\psi}\left(\frac{1}{4\pi^2}\int^{\psi}\oint \frac{I}{R^2}\mathrm{d}^3\boldsymbol{x}\right), \tag{2.8}$$

and since the integral between the brackets is nothing but the toroidal flux[2] *Eq.* (2.2), we have

$$q(\psi) = \frac{\mathrm{d}\Psi_T}{\mathrm{d}\psi}. \tag{2.9}$$

[2]Not forgetting the $2\pi$ factor and using axisymmetry which implies that the toroidal integral results in $1/2\pi\oint\mathrm{d}^3\boldsymbol{x} = \oint_{\varphi=C^{te}} R\mathrm{d}^2\boldsymbol{x}$.

This makes the definition of the safety factor independent of the choice of coordinates.

### 2.1.2 The Grad-Shafranov Equation

Since $p$ and $I$ depend only on $\psi$, the force balance equation can be rewritten as an equation for $\psi$, which reads:

$$\nabla \cdot \frac{1}{R^2}\nabla\psi = \frac{j_\varphi}{R} = -p'(\psi) - \frac{II'(\psi)}{R^2}. \tag{2.10}$$

This is Grad-Shafranov's equation. Solving this equation amounts to finding the $\psi$ function for given $p'(\psi)$ and $I(\psi)$ profiles. Since $I = RB_T$ is linked to the toroidal field, it is mainly related to the externally applied coil currents, however it also includes the diamagnetic response of the plasma (generated by the poloidal currents) and thus it cannot be simply given as a function of externally applied conditions. We have a similar problem for the pressure: the total pressure is not involved, but only its gradient with respect to the solution $\psi$. It is not easy to circumvent this issue. For instance, one cannot give the pressure profile as a function of the geometrical coordinate $r$ since the solution will not preserve this constraint. In particular, the magnetic axis has no reason to be located at the geometrical center of the torus, and indeed it is not. In practice, one must provide the functions $p'$ and $II'$ and solve for $\psi$. These functions can be defined arbitrarily or fitted on experimental measurements. The numerical solution provides the equilibrium magnetic configuration (given by $\psi(r)$) and radial profile of the pressure (through $p'(\psi(r))$, with the function $p'$ given as input).

The solution of Grad-Shafranov's equation is necessary as an input to MHD codes. In this thesis, the CHEASE code [Lutjens 1996] was used. The code is described in section 3.1.

We now come to the study of plasma dynamics, starting from kinetic concepts.

### 2.1.3 Kinetic description of a plasma

To study the sawtooth phenomenon, we will adopt a fluid framework known as magnetohydrodynamics (MHD). The fluid equations are derived from the kinetic description of the plasma. We will briefly sketch the origin of the kinetic formalism, then describe how the fluid equations are derived. A population of $N$ particles of the species $s$, with mass $m_s$ and charge $e_s$, located at $\boldsymbol{x}_i(t)$ and with velocity $\boldsymbol{u}_i(t)$, is described by its distribution function in the real and velocity space $F_s(\boldsymbol{x}, \boldsymbol{u}, t)$. The exact (classical) distribution function is a sum of Dirac functions over all the $N$ particles:

$$F_s(\boldsymbol{x}, \boldsymbol{u}, t) = \sum_{i=1}^{N} \delta(\boldsymbol{x} - \boldsymbol{x}_i(t))\delta(\boldsymbol{u} - \boldsymbol{u}_i(t)). \tag{2.11}$$

The fundamental equation

$$\frac{\mathrm{d}F_s}{\mathrm{d}t} = 0 \tag{2.12}$$

expresses conservation of particles and momentum in the phase space. In *Eq.* (2.12), $\frac{\mathrm{d}}{\mathrm{d}t} \equiv \frac{\partial}{\partial t} + \boldsymbol{u}\cdot\nabla + \boldsymbol{a}\cdot\nabla_{\boldsymbol{u}}$, where $\boldsymbol{u}$ is the velocity, $\boldsymbol{a}$ the acceleration and $\nabla_{\boldsymbol{u}}$ is a notation for $\frac{\partial}{\partial \boldsymbol{u}}$. In the case where only electromagnetic forces are considered, the equation can thus be rewritten

$$\frac{\partial F_s}{\partial t} + \boldsymbol{u}\cdot\nabla F_s + \frac{e_s}{m_s}(\mathbf{E}_{ex} + \boldsymbol{u}\times\mathbf{B}_{ex})\cdot\nabla_{\boldsymbol{u}} F_s = 0, \tag{2.13}$$

where $\mathbf{E}_{ex}$ and $\mathbf{B}_{ex}$ are the exact electric and magnetic fields. This equation is called Klimontovitch equation. It must be noted that here, the fields $\mathbf{E}_{ex}$ and $\mathbf{B}_{ex}$ have the same behavior as the exact distribution $F_s$, that is, they are singular in the vicinity of the particles. Thus this equation is of no practical use, it is much more convenient to work with an averaged distribution $f_s = \langle F_s\rangle$ and fields $\mathbf{E} = \langle\mathbf{E}_{ex}\rangle$, $\mathbf{B} = \langle\mathbf{B}_{ex}\rangle$, where the average $\langle\cdot\rangle$ is a spatial average on mesoscopic scales[3], or equivalently if the ergodic theorem is applicable, an ensemble average over many realizations. Using this average, a new equation can be written, called the kinetic equation:

$$\frac{\partial f_s}{\partial t} + \boldsymbol{u}\cdot\nabla f_s + \frac{e_s}{m_s}(\mathbf{E} + \boldsymbol{u}\times\mathbf{B})\cdot\nabla_{\boldsymbol{u}} f_s = \mathcal{C}_s(f_s), \tag{2.14}$$

where $\mathcal{C}_s(f_s)$ denotes the collision operator:

$$\mathcal{C}_s(f_s) = -\frac{m_s}{e_s}\langle(\delta\mathbf{E} + \boldsymbol{u}\times\delta\mathbf{B})\cdot\nabla_{\boldsymbol{u}}\delta f_s\rangle, \tag{2.15}$$

and $\delta A \equiv A - \langle A\rangle$. There exist analytical approximations for the collision operator, which have many interesting properties, but we will not detail this issue. The collision operator describes all the processes linked with the spiky behavior of the fields in the plasma – friction between species, resistivity, viscosity, etc. It is a small term in *Eq.* (2.14) because are rare in hot plasmas. We will neglect it for the time being and focus on ideal MHD. We will reintroduce collisional effects later on. The kinetic equation where the collision operator is neglected is called Vlasov equation.

$$\frac{\partial f_s}{\partial t} + \boldsymbol{u}\cdot\nabla f_s + \frac{e_s}{m_s}(\mathbf{E} + \boldsymbol{u}\times\mathbf{B})\cdot\nabla_{\boldsymbol{u}} f_s = 0. \tag{2.16}$$

### 2.1.4 Derivation of fluid equations

The ideal (non-collisional) fluid equations are obtained by taking moments of Vlasov equation, *i.e.*, multiplying by powers of $\boldsymbol{u}$, and integrating over the whole velocity space. The density $n_s$, velocity $\boldsymbol{v}_s$ and pressure tensor $\bar{\bar{\boldsymbol{p}}}_s$ are defined as follows:

$$n_s = \int f_s \,\mathrm{d}^3\boldsymbol{u} \tag{2.17}$$

$$n_s\boldsymbol{v}_s = \int \boldsymbol{u} f_s \,\mathrm{d}^3\boldsymbol{u} \tag{2.18}$$

$$\bar{\bar{\boldsymbol{p}}}_s = m_s\int \boldsymbol{u}'\boldsymbol{u}' f_s \,\mathrm{d}^3\boldsymbol{u}, \quad \boldsymbol{u}' = \boldsymbol{u} - \boldsymbol{v}_s. \tag{2.19}$$

[3] For instance it can be an average on spatial scales larger than the average distance between particles, but small compared to the Debye length on which electric potentials are screened by the plasma.

We also denote by $\rho_s = m_s n_s$ the mass density. The pressure tensor is decomposed into the scalar pressure $p_s$ and the stress tensor $\bar{\bar{\boldsymbol{\pi}}}_s$: $\bar{\bar{\boldsymbol{p}}}_s = p_s \mathbb{1} + \bar{\bar{\boldsymbol{\pi}}}_s$, where $\mathbb{1}$ denotes the identity tensor. The stress tensor contains the anisotropic and off-diagonal terms of the pressure tensor. Integration of Vlasov equation on the velocity space yields the continuity equation:

$$\frac{\partial n_s}{\partial t} + \nabla \cdot (n_s \boldsymbol{v}_s) = 0. \tag{2.20}$$

Multiplying Vlasov equation by $\boldsymbol{u}$ and integrating yields the momentum equation:

$$\frac{\partial}{\partial t}(\rho_s \boldsymbol{v}_s) + \nabla \cdot (\rho_s \boldsymbol{v}_s \boldsymbol{v}_s + \bar{\bar{\boldsymbol{p}}}_s) = n_s e_s (\mathbf{E} + \boldsymbol{v}_s \times \mathbf{B}). \tag{2.21}$$

Using *Eq.* (2.20) and the identity $\nabla \cdot \boldsymbol{a}\boldsymbol{b} \equiv \boldsymbol{b}\nabla \cdot \boldsymbol{a} + \boldsymbol{a} \cdot \nabla \boldsymbol{b}$, the momentum equation can be rewritten

$$\rho_s \left( \frac{\partial \boldsymbol{v}_s}{\partial t} + \boldsymbol{v}_s \cdot \nabla \boldsymbol{v}_s \right) = n_s e_s (\mathbf{E} + \boldsymbol{v}_s \times \mathbf{B}) - \nabla p_s - \nabla \cdot \bar{\bar{\boldsymbol{\pi}}}_s. \tag{2.22}$$

In theory, the process must be continued for an infinite number of powers of $\boldsymbol{u}$. Such an infinite set of equations is fully equivalent to the kinetic problem. Reducing the number of equations is an audacious step, and the price to pay for this reduction is high. Indeed note that each equation involves the quantity given by the next order of the calculation. The continuity equation involves the velocity, while the velocity (or momentum) equation involves the pressure, which evolution is given by Vlasov equation multiplied by $\boldsymbol{u}^2$ and integrated over the velocity space. Similarly, a new third order unknown appears in the pressure equation derived from the kinetic formulation. This issue is called the *closure* issue. If the process is stopped after a number of iterations, the last unknown must be expressed as a function of the other to *close* the equations. There exist many attempts to derive theoretical closures as exact as possible. For instance, a closure can be derived to mimic the behavior of kinetic calculations [Chang 1992], or by asymptotic expansion in a small parameters, and this is called asymptotic closure. When higher order moments are simply assumed to vanish, this is called a truncation closure. The closures that we will consider here are an ideal truncation closure (no dissipation) and an asymptotic closure relevant to collisional and highly magnetized plasmas, developed by Braginskii [Braginskii 1965].

At the following order, one obtains the pressure equation:

$$\frac{\partial p_s}{\partial t} + \boldsymbol{v}_s \cdot \nabla p_s + \Gamma p_s \nabla \cdot \boldsymbol{v}_s + (\Gamma - 1)\left[\nabla \cdot \mathbf{q}_s + \bar{\bar{\boldsymbol{\pi}}}_s : \nabla \boldsymbol{v}_s\right] = 0, \tag{2.23}$$

with the notation $\bar{\bar{\mathbf{A}}} : \nabla \mathbf{B} \equiv A_{ij} \partial_j B_i$. $\Gamma = 5/3$ is the ratio of specific heats, as $C_v = 3/2 n_s$ and $C_p = C_v + n_s$, and $\mathbf{q}_s$ is defined by

$$\mathbf{q}_s = \int \frac{m_s u_s'^2}{2} \boldsymbol{u}_s' f_s \mathrm{d}^3 \boldsymbol{u}, \quad \boldsymbol{u}_s' = \boldsymbol{u} - \boldsymbol{v}_s. \tag{2.24}$$

One sees from this expression that $\mathbf{q}_s$ is the microscopic heat flux: the particles with kinetic energy $\frac{1}{2} m_s u_s'^2$ have a flux $\boldsymbol{u}_s' f_s$ in phase space. Now the closure problem appears,

since $\mathbf{q}_s$ is not known as a function of the other quantities. For the moment, we will simply assume $\nabla \cdot \mathbf{q}_s = 0$, which is consistent with a Maxwellian distribution assumption, thus adopting a truncation closure. We will see an asymptotic closure in section 2.1.6.

Let us write an equation for the energy density of the system:

$$\mathcal{E} = \frac{B^2}{2\mu_0} + \varepsilon_0 \frac{E^2}{2} + \sum_s \left( \frac{3}{2} p_s + \rho_s \frac{v_s^2}{2} \right). \tag{2.25}$$

We use

$$\frac{\partial}{\partial t}\left( \frac{B^2}{2\mu_0} + \varepsilon_0 \frac{E^2}{2} \right) = -\nabla \cdot \left( \frac{\mathbf{E} \times \mathbf{B}}{\mu_0} \right) - \mathbf{E} \cdot \mathbf{J} \tag{2.26}$$

$$\frac{\partial}{\partial t}\left( \rho_s \frac{v_s^2}{2} \right) = -\frac{v_s^2}{2} \nabla \cdot \rho_s \boldsymbol{v}_s - \rho_s \boldsymbol{v}_s \cdot \nabla \frac{v_s^2}{2} + n_s e_s \mathbf{E} \cdot \boldsymbol{v}_s - \boldsymbol{v}_s \cdot \nabla p_s - \boldsymbol{v}_s \cdot \nabla \cdot \bar{\bar{\boldsymbol{\pi}}}_s, \tag{2.27}$$

where $\mathbf{J} = \sum_s n_s e_s \boldsymbol{v}_s$. The first equation comes from Ampère's and Faraday's laws combined together. In deriving it, the identity $\nabla \cdot (\mathbf{E} \times \mathbf{B}) = \mathbf{B} \cdot \nabla \times \mathbf{E} - \mathbf{E} \cdot \nabla \times \mathbf{B}$ has been used. The second equation comes from *Eq.* (2.22) and *Eq.* (2.20). Note that the power given from the electromagnetic field to the particles, $\mathbf{E} \cdot \mathbf{J}$, is counted negatively in *Eq.* (2.26) and positively in *Eq.* (2.27), so they cancel out. Hence using *Eq.* (2.23) for the pressure term, we obtain the following energy balance equation:

$$\frac{\partial \mathcal{E}}{\partial t} + \nabla \cdot \left[ \frac{\mathbf{E} \times \mathbf{B}}{\mu_0} + \sum_s \left( \rho_s \frac{v_s^2}{2} \boldsymbol{v}_s + \frac{3}{2} p_s \boldsymbol{v}_s + \bar{\bar{\boldsymbol{p}}} \cdot \boldsymbol{v}_s + \mathbf{q}_s \right) \right] = 0. \tag{2.28}$$

Thus without surprise energy is conserved and its flux is given by the following contributions:

- The Poynting flux
$$\frac{\mathbf{E} \times \mathbf{B}}{\mu_0},$$
- The flux of kinetic energy
$$\frac{\rho_s v_s^2}{2} \boldsymbol{v}_s,$$
- The flux of internal energy
$$\frac{3}{2} p_s \boldsymbol{v}_s,$$
- The work done by pressure forces
$$\bar{\bar{\boldsymbol{p}}}_s \cdot \boldsymbol{v}_s = p_s \boldsymbol{v}_s + \bar{\bar{\boldsymbol{\pi}}} \cdot \boldsymbol{v}_s,$$
- The heat flux linked with the individual erratic particle motion
$$\mathbf{q}_s.$$

Note that the total pressure tensor is involved in the work done by the pressure forces, while only the scalar pressure carries internal energy.

Now *Eqs.* (2.20), (2.22) and (2.23) constitute a closed system of equations provided the fields $\mathbf{E}$ and $\mathbf{B}$ are given. We now assume both ions and electrons verify *Eqs.* (2.20), (2.22) and (2.23). $\mathbf{E}$ and $\mathbf{B}$ verify Maxwell's equations:

$$\nabla \cdot \mathbf{B} = 0, \tag{2.29}$$

$$\nabla \cdot \mathbf{E} = \frac{\rho}{\varepsilon_0}, \tag{2.30}$$

$$\partial_t \mathbf{B} = -\nabla \times \mathbf{E}, \tag{2.31}$$

$$\partial_t \mathbf{E} = c^2 \nabla \times \mathbf{B} - \frac{\mathbf{J}}{\varepsilon_0}. \tag{2.32}$$

Because of the very small electron inertia, $\rho_e \ll \rho_i$, the left hand side of the electron momentum equation tends very rapidly to zero, in a characteristic time

$$\tau_{e,mom} \sim \frac{\rho_e v_e}{|\nabla p_e|} \sim \frac{a}{v_{te}}.$$

This time is a fraction of $\mu$s for standard tokamak conditions, this scale is below any other fluid time scale[4], and to a fair approximation, we can neglect electron inertia[5], so that the electric field verifies

$$\mathbf{E} + \boldsymbol{v}_e \times \mathbf{B} = -\frac{\nabla p_e}{n_e e}. \tag{2.33}$$

This equation is the Ohm's law, it gives the electric field as a function of $\boldsymbol{v}_e$, $\mathbf{B}$ and $p_e$, which have their own evolution equations, so that *Eq.* (2.32) is not useful anymore as an evolution equation for $\mathbf{E}$. Rather we shall show that the time variation of the electric field is negligible, so that *Eq.* (2.32) reduces to a constitutive relation between $\mathbf{B}$ and $\mathbf{J}$:

$$\nabla \times \mathbf{B} = \mu_0 \mathbf{J}. \tag{2.34}$$

Indeed

$$\left| \frac{\varepsilon_0 \partial_t \mathbf{E}}{\nabla \times \mathbf{B}/\mu_0} \right| \sim \frac{v_E a/\tau_{evol}}{c^2} \ll 1,$$

where $v_E = |\boldsymbol{v}_E| = |\mathbf{E} \times \mathbf{B}/B^2|$, and $\tau_{evol}$ is the characteristic time of evolution of the profiles. Indeed $\boldsymbol{v}_E$ is the cross field electric drift briefly mentioned in the introduction. Even for the fastest physically possible evolution, $a/(\tau_{evol} c) \lesssim 1$, the ratio $v_E/c$ is much smaller than one, since necessarily $v_E$ is smaller than the thermal velocity, which is much smaller than $c$.

[4] For instance shear-Alfvén waves propagate with a maximum velocity $V_A \sim 10^7 \mathrm{m.s}^{-1}$.

[5] The importance of electron inertia in reconnection events, has been debated [Drake 1991, Biskamp 1994] but there is no consensus yet.

### 2.1.5 Single fluid ideal MHD

#### The MHD ordering

Before deriving the equations, we need to say a few words about the MHD ordering allowing for such a derivation. The following considerations are mainly taken from Ref. [Hazeltine 2003], chapters 4.1 and 6.4.

The most fundamental small parameter characterizing a magnetized plasma is the ratio between the Larmor radius $\rho_L$ and the macroscopic scale $L$ of the confining configuration, $\rho^\star = \rho_L/L$. Only when the Larmor radius is small, $\rho^\star \ll 1$, is one in the presence of a magnetized plasma. To be more precise, since electron Larmor radii are smaller by a factor of $\sqrt{m_i/m_e} \simeq 60$ than ion Larmor radii, the ion Larmor radius must be small. In the fundamental kinetic equation, *Eq.* (2.14), the different terms can be given an ordering, in terms of a certain power of $\rho^\star$ multiplied by $f\omega_c$, where $\omega_c = eB/m$ is the cyclotron frequency, the most fundamental time scale at the microscopic level. For instance, obviously the term corresponding to Larmor gyration is the largest term, $(e/m)\boldsymbol{u}\times\mathbf{B}\cdot\nabla_{\boldsymbol{u}} f \sim \omega_c f$. Almost all other terms can be given an ordering, which is at least of order $\rho^\star\omega_c f$. The term linked with the perpendicular electric field in the kinetic equation, $(e/m)\mathbf{E}_\perp \cdot \nabla_{\boldsymbol{u}} f$, cannot be given such an ordering *a priori*. Using $\boldsymbol{v}_E = \mathbf{E}\times\mathbf{B}/B^2$, this is a term of order $(v_E/v_t)\omega_c f$. Thus the unknown is the importance of perpendicular electric fields in the plasma, or, equivalently, of $v_E/v_t$. For a given $\rho^\star$ ordering, an expansion of the kinetic equation is carried out, and obviously different orderings will give different approximations of the kinetic equation. For instance the ordering $v_E/v_t \sim \rho^\star$ leads to the gyro-kinetic equation, and a special case of it, the drift-kinetic equation, when $k_\perp\rho_L \to 0$, $k_\perp$ being the typical perpendicular wave number. MHD theory assumes large perpendicular electric field, thus the following ordering is used

$$\frac{v_E}{v_t} \sim \mathcal{O}(1). \tag{2.35}$$

This has important consequences for the derivation of the equations. Most importantly, it implies that in MHD the perpendicular velocity is the electric drift

$$\boldsymbol{v}_\perp = \frac{\mathbf{E}\times\mathbf{B}}{B^2}. \tag{2.36}$$

Indeed, according to *Eq.* (2.22),

$$\boldsymbol{v}_\perp = \frac{\mathbf{E}\times\mathbf{B}}{B^2} + \boldsymbol{v}_s^\star + \frac{\mathbf{B}\times\rho_s\left(\partial_t\boldsymbol{v}_s + \boldsymbol{v}_s\cdot\nabla\boldsymbol{v}_s\right)}{n_s e_s B^2}, \tag{2.37}$$

where

$$\boldsymbol{v}_s^\star = \frac{\mathbf{B}\times\nabla p_s}{n_s e_s B^2} \tag{2.38}$$

is the diamagnetic velocity, and it is straightforward to see that $|\boldsymbol{v}_s^\star/v_t| \sim \delta_M$. The following term, traditionally called polarization velocity, is even smaller. Thus in this theory, it is quite easy to merge the different species equations together since they have the same velocity. Thus we assume in the following that $\boldsymbol{v}_{e\perp} = \boldsymbol{v}_{i\perp} = \mathbf{E}\times\mathbf{B}/B^2$. This assumption will be relaxed when finite $\delta_M$, or as they are often referred to, finite Larmor radius (FLR) effects, are reintroduced.

### Derivation of the MHD equations

We now derive the equations verified by the plasma considered as a single fluid with mass density

$$\rho = \rho_e + \rho_i,$$

momentum

$$\rho \boldsymbol{v} = \rho_e \boldsymbol{v}_e + \rho_i \boldsymbol{v}_i,$$

and pressure

$$p = p_i + p_e.$$

To obtain the evolution equation for $\rho$, the two electron and ion continuity equations are simply added to exactly obtain

$$\frac{\partial \rho}{\partial t} + \nabla \cdot (\rho \boldsymbol{v}) = 0. \tag{2.39}$$

Injecting Ohm's law, *Eq.* (2.33), in the ion momentum equation, and noting that $\rho \simeq \rho_i$ and $\rho \boldsymbol{v} \simeq \rho_i \boldsymbol{v}_i$, the ion momentum equation can be recast into

$$\rho \left( \frac{\partial \boldsymbol{v}}{\partial t} + \boldsymbol{v} \cdot \nabla \boldsymbol{v} \right) = \mathbf{J} \times \mathbf{B} - \nabla p, \tag{2.40}$$

with $\mathbf{J} = n_e e(\boldsymbol{v}_i - \boldsymbol{v}_e)$. This equation means that the equilibrium equation is (neglecting inertia) $\mathbf{J} \times \mathbf{B} = \nabla p$ as we have seen in section 2.1.1. The equation $\mathbf{J} \times \mathbf{B} = \nabla p$ implies $\mathbf{J}_\perp = \mathbf{B} \times \nabla p / B^2$. This result, where the diamagnetic drifts seem to reenter through the back-door, is not inconsistent with our MHD ordering, which assumes diamagnetic drifts are negligible. Indeed the electric field, which is the large term in our ordering, disappears after the summation of the two equations, so that only the remaining terms are present. Notice that in our MHD ordering, $\mathbf{J}$ cannot be computed from the difference between $\boldsymbol{v}_i$ and $\boldsymbol{v}_e$, since this difference makes sense only at the next order. Hence the correct relation for $\mathbf{J}$ is the constitutive relation, the Ampère's law $\mu_0 \mathbf{J} = \nabla \times \mathbf{B}$.

The two pressure equations are summed up, giving, with our assumptions and neglecting all parallel current terms,

$$\frac{\partial p}{\partial t} + \boldsymbol{v} \cdot \nabla p + \Gamma p \nabla \cdot \boldsymbol{v} = 0. \tag{2.41}$$

With the continuity equation *Eq.* (2.39), it is equivalent to the adiabatic equation of state

$$\frac{\mathrm{d}}{\mathrm{d}t} \left( \frac{p}{\rho^\Gamma} \right) = 0. \tag{2.42}$$

Finally, a last step is needed to close the equations and arrive at the standard ideal MHD system. In our ordering, it is straightforward, since we neglect the pressure gradient and any dissipative mechanism (ideal model), that Ohm's law, *Eq.* (2.33), reads

$$\mathbf{E} + \boldsymbol{v} \times \mathbf{B} = 0. \tag{2.43}$$

This Ohm's law is also called the "frozen-in-law". Indeed when it is verified, the plasma is frozen to the plasma, that is, two points initially on a given magnetic field line will remain on this field line at any time in the future, regardless of the plasma motion. This is demonstrated in appendix B. This prevents any form of field line breaking, or magnetic reconnection. We study magnetic reconnection in section 2.3 Therefore, the final ideal MHD system of equations can be written:

$$\frac{\partial \rho}{\partial t} + \nabla \cdot \rho \boldsymbol{v} = 0, \tag{2.44}$$

$$\rho \left( \frac{\partial \boldsymbol{v}}{\partial t} + \boldsymbol{v} \cdot \nabla \boldsymbol{v} \right) = \mathbf{J} \times \mathbf{B} - \nabla p, \tag{2.45}$$

$$\frac{\partial p}{\partial t} + \boldsymbol{v} \cdot \nabla p + \Gamma p \nabla \cdot \boldsymbol{v} = 0, \tag{2.46}$$

$$\frac{\partial \mathbf{B}}{\partial t} = \nabla \times (\boldsymbol{v} \times \mathbf{B}) . \tag{2.47}$$

The ideal MHD equations are the most simple set of fluid equations used to model a plasma[6]. In spite of the quite harsh assumptions and simplifications used to derive it, it allows a first approach to most confined plasma issues. It is valid if dissipation is a weak effect, if finite orbit effects are negligible and if purely kinetic effects can be neglected. These kinetic effects are characterized by Landau resonances, which happen whenever the mode's frequency resonates with the characteristic frequencies of particle motion. When the resonance condition is met, there can be energy transfer between particles and MHD waves. There are three such characteristic frequencies, corresponding to the three invariant of motion: the cyclotron frequency for trapped and passing particles, the bounce frequency and the toroidal drift frequency for trapped particles, and the poloidal and toroidal transit frequencies (of the order of $v_t/qR$) and $v_t/R$ respectively) for the passing particles. We must have $\omega \gg \mathbf{k} \cdot \boldsymbol{v}$ or $\omega \ll \mathbf{k} \cdot \boldsymbol{v}$, where $\omega$ is the MHD mode frequency, $\mathbf{k}$ its wave vector and $\boldsymbol{v}$ the particles' velocity, dominantly in the direction of $\mathbf{b} \equiv \mathbf{B}/|\mathbf{B}|$. Since MHD modes are generated at resonance surfaces where $\mathbf{k} \cdot \mathbf{b} = k_\parallel = 0$, $k_\parallel$ is in general quite small and the condition to avoid Landau resonances is usually written $\omega \gg k_\parallel v$. We must also have $\omega \gg \omega_D$, where $\omega_D$ is the toroidal drift frequency of trapped particles.

We herafter give the basic plasma waves contained in the ideal MHD equations. Linearizing the MHD system in the case of homogeneous equilibrium, one finds three waves (the demonstration is in every MHD textbook, see for instance [Biskamp 2000]):

1. The shear-Alfvén wave with dispersion relation

$$\omega_A^2 = k_\parallel^2 V_A^2, \tag{2.48}$$

with

$$k_\parallel = \mathbf{k} \cdot \mathbf{b}, \quad \text{and} \quad V_A = \frac{B}{\sqrt{\mu_0 \rho}} \tag{2.49}$$

[6] Actually, reduced MHD, a reduced version where only scalars describing the poloidal plane are used, based on the anisotropy introduced by the large toroidal guide field, is even simpler.

is the Alfvén velocity, typically $V_A \sim 10^7\,\mathrm{m.s}^{-1}$ in tokamaks. The corresponding time scale is the Alfvén time $\tau_A = R_0/V_A \sim 10^{-7}$ s. It is the fastest time scale in MHD problems. The shear-Alfvén wave describes motions transverse to the field line, and the restoring force is linked with the energy necessary to bend a field line. The mode is transverse and incompressible, that is, $\mathbf{k}\cdot\tilde{\boldsymbol{v}} = 0$, where $\tilde{\boldsymbol{v}}$ is the velocity perturbation. The perturbed magnetic field is aligned with $\tilde{\boldsymbol{v}}$: $\tilde{\mathbf{B}} = \pm\sqrt{\mu_0\rho_0}\tilde{\boldsymbol{v}}$.

2. The fast magnetosonic wave with dispersion relation

$$\omega_F^2 = \frac{1}{2}\mathbf{k}^2(V_A^2 + c_s^2)\left(1 + \sqrt{1 - 4\frac{k_\parallel^2 V_A^2 c_s^2}{\mathbf{k}^2(V_A^2 + c_s^2)^2}}\right), \tag{2.50}$$

with $c_s = \sqrt{\gamma p/\rho} = v_t\sqrt{\gamma}$ the sound speed.

3. The slow magnetosonic wave with dispersion relation

$$\omega_S^2 = \frac{1}{2}\mathbf{k}^2(V_A^2 + c_s^2)\left(1 - \sqrt{1 - 4\frac{k_\parallel^2 V_A^2 c_s^2}{\mathbf{k}^2(V_A^2 + c_s^2)^2}}\right) \tag{2.51}$$

The ratio between Alfvén velocity and sound speed is such that $c_s^2 = \beta V_A^2 \ll V_A^2$ in tokamaks, since $\beta \ll 1$. Hence the two magnetosonic waves have frequencies

$$\omega_F^2 \simeq \mathbf{k}^2 V_A^2 \tag{2.52}$$
$$\omega_S^2 \simeq k_\parallel^2 c_s^2. \tag{2.53}$$

The slow magnetosonic wave is a sound wave modified by the presence of the magnetic field, while the fast magnetosonic wave is the compressional modification of a pure magnetic Alfvén wave.

### 2.1.6 Braginskii equations

The ideal MHD closure is a truncation closure (higher order quantities are merely neglected) relying on the hypothesis of high collisionality, whereby distributions are considered Maxwellian, and large transverse electric fields. There are more precise ways to derive a fluid closure, called asymptotic closures, which use the smallness of some expansion parameter(s). Braginskii derived such an asymptotic closure in 1965 for the limiting case of collisional, magnetized plasmas [Braginskii 1965]. The magnetized plasma assumption is that the Larmor radius be small compared to the macroscopic dimension of the plasma. Alternatively, the cyclotron frequency must be large compared to characteristic times of evolution of the plasma. When we restrict ourselves to low frequency MHD, this condition is easily met. The collisional plasma limit applies when the mean free-path is small compared to the macroscopic dimension. It is actually not satisfied at all in the parallel direction in tokamak plasmas, which are known for being very weakly collisional.

We will write Braginskii's equations for each species and use them to write two models:

1. A resistive and diffusive model, which we will call $\eta\chi$MHD.

2. A bifluid model, which we will call bifluid MHD.

Braginskii's equations for the species $s$ (ion or electron) read:

$$\frac{\partial n}{\partial t} + \nabla \cdot n\boldsymbol{v}_s = 0 \tag{2.54}$$

$$m_s n \left( \frac{\partial \boldsymbol{v}_s}{\partial t} + \boldsymbol{v}_s \cdot \nabla \boldsymbol{v}_s \right) = -\nabla p_s - \nabla \cdot \bar{\bar{\boldsymbol{\pi}}}_s + n e_s (\mathbf{E} + \boldsymbol{v}_s \times \mathbf{B}) + \mathbf{R}_{\mathbf{s'},\mathbf{s}} \tag{2.55}$$

$$\frac{\partial p_s}{\partial t} + \boldsymbol{v}_s \cdot \nabla p_s + \Gamma p_s \nabla \cdot \boldsymbol{v}_s + (\Gamma - 1)\bar{\bar{\boldsymbol{\pi}}}_s : \nabla \boldsymbol{v}_s + (\Gamma - 1)\nabla \cdot \mathbf{q}_s = (\Gamma - 1) W_s, \tag{2.56}$$

where $\bar{\bar{\mathbf{A}}} : \nabla \mathbf{B} \equiv A_{ij} \partial_i B_j$, and we used quasi-neutrality, $n_i = n_e = n$. Note the similarity with equations (2.20), (2.22) and (2.23). $\mathbf{R}_{s',s}$ is the force exerted by the species $s'$ on the species $s$, and we have $\mathbf{R}_{i,e} = -\mathbf{R}_{e,i}$. Its expression is

$$\mathbf{R}_{i,e} = ne \left( \eta_\parallel \mathbf{J}_\parallel + \eta_\perp \mathbf{J}_\perp \right) - 0.71 n \nabla_\parallel T_e - \frac{3 n \nu_e}{2|\omega_{c,e}|} \mathbf{b} \times \nabla_\perp T_e, \tag{2.57}$$

with $\nabla_\parallel \equiv \mathbf{b} \cdot \nabla$, and the parallel and perpendicular resistivities:

$$\eta_\perp = \frac{\eta_\parallel}{0.51} = \frac{m_e \nu_e}{n e^2}, \tag{2.58}$$

and $\nu_e$ is the electron collision frequency. The collision frequency is proportional to $T_e^{-3/2}$, and the parallel resistivity takes the form of the so-called Spitzer resistivity:

$$\eta_\parallel = 0.51 \frac{m_e^{1/2} e^2 \ln \Lambda}{6\sqrt{2} \pi^{3/2} \varepsilon_0^2} T_e^{3/2}, \tag{2.59}$$

where $\ln \Lambda$ is the Coulomb logarithm.

When writing Ohm's law as the electron momentum equation, this inter-species friction modifies the electric field in making its parallel component non-vanishing. This has important consequences for magnetic reconnection. The second term in $\mathbf{R}_{i,e}$ is called the thermal force and the last one originates from collisions between neighbouring gyroorbits in the presence of a temperature gradient.

The ion and electron heat fluxes are

$$\mathbf{q}_i = -\kappa_\parallel^i \nabla_\parallel T_i - \kappa_\perp^i \nabla_\perp T_i + \kappa_\times^i \mathbf{b} \times \nabla_\perp T_i \tag{2.60}$$

$$\mathbf{q}_e = -\kappa_\parallel^e \nabla_\parallel T_e - \kappa_\perp^e \nabla_\perp T_e - \kappa_\times^e \mathbf{b} \times \nabla_\perp T_e - 0.71 \frac{T_e \mathbf{J}_\parallel}{e} - \frac{3 T_e \nu_e}{2e|\omega_{c,e}|} \mathbf{b} \times \nabla_\perp T_i. \tag{2.61}$$

We do not give the expressions for $\kappa_\parallel$ and $\kappa_\perp$ as they are irrelevant to the core plasma of the tokamak, even though parallel and perpendicular transport of this form are crucial. At

this level, it is sufficient to say that Braginskii's theory predicts a very strong anisotropy between parallel and perpendicular heat fluxes. Namely,

$$\frac{\kappa_{\parallel}^{s}}{\kappa_{\perp}^{s}} = \mathcal{O}\left(\left(\frac{\omega_{c,s}}{\nu_s}\right)^2\right) \gg 1, \tag{2.62}$$

since $\omega_{c,s} \gg \nu_s$, so the parallel transport is very much faster than perpendicular transport. This prediction of the theory is very well verified, with about 8 orders of magnitude of difference.

The $\kappa_\times$ are linked only with the strong magnetization assumption and are relevant to the tokamak case:

$$\kappa_{\times}^{i} = \frac{5nT_i}{2m_i|\omega_{c,i}|} \tag{2.63}$$

$$\kappa_{\times}^{e} = \frac{5nT_e}{2m_e|\omega_{c,e}|}. \tag{2.64}$$

At the microscopic level, this heat flux comes from the non compensation of the fluxes associated with the gyromotion of particles in the presence of a temperature gradient. This is very much related to the diamagnetic velocities,*Eq.* (2.38). This heat flux does not depend on the collision frequency and is relevant to tokamaks.

The expression of $W_i$ and $W_e$ are:

$$W_i = \frac{3m_e}{m_i} n(T_e - T_i)\nu_e \tag{2.65}$$

$$W_e = -W_i + \frac{\mathbf{J}\cdot\mathbf{R}_{i,e}}{ne}. \tag{2.66}$$

This means there is an energy exchange between electrons and ions when the temperatures are not equal (friction between faster and slower parts in the distribution function resulting in net exchange), and production of thermal energy because of the work of the dissipative force $\mathbf{R}_{i,e}$, in particular, we find the ohmic power $\eta_{|}\mathbf{J}_{\parallel}^2 + \eta_{\perp}\mathbf{J}_{\perp}^2$.

We do not go into the predictions for the stress tensor $\bar{\bar{\boldsymbol{\pi}}}$, which are quite complicated, and give the viscous contributions. Again, there are collisional contributions, and other related to the strong magnetized plasma assumption. We will only use an important result about the stress tensor when we derive the bifluid equations. We now come to the $\eta\chi$MHD model.

### 2.1.7 The $\eta\chi$MHD model

We derive the model in an heuristic manner. Braginskii's theory is very instructive in that it highlights and gives an expression for several important processes in magnetized collisional plasmas, namely:

- Resistivity: since resistivity is directly proportional to the electron collision frequency, which is in turn proportional to $T_e^{-3/2}$, we see that hot plasmas are less resistive and keen to dissipate energy via the Joule (or ohmic) effect. This is also the

reason why additional heating methods must be employed: ohmic heating can bring the plasma temperature only to a few keV, then its efficiency decreases too much. However the small remaining resistivity plays an important role in the dynamics of the sawtooth instability.

- The strong transport anisotropy introduced by the strong guide field $\mathbf{B}$. The ratio $\kappa_\parallel/\kappa_\perp$ scales with $|\mathbf{B}|^2$.
- The presence of FLR effects (collisional or not) in the heat fluxes, heat sources and inter-particle friction.

The $\eta\chi$MHD model just adds dissipation to the ideal MHD model, in the form of resistivity, viscosity and the anisotropic pressure transport. On top of that, there is also a particle diffusion coefficient in the continuity equation, and restoring sources:

$$\frac{\partial \rho}{\partial t} + \nabla \cdot (\rho \boldsymbol{v}) = \nabla \cdot (D \nabla \rho) + S, \tag{2.67}$$

$$\rho \left( \frac{\partial \boldsymbol{v}}{\partial t} + \boldsymbol{v} \cdot \nabla \boldsymbol{v} \right) = \mathbf{J} \times \mathbf{B} - \nabla p + \nabla \nu \nabla \boldsymbol{v}, \tag{2.68}$$

$$\frac{\partial p}{\partial t} + \boldsymbol{v} \cdot \nabla p + \Gamma p \nabla \cdot \boldsymbol{v} = \nabla \cdot \left[ \rho \chi_\perp \nabla \left( \frac{p}{\rho} \right) \right] + \nabla \cdot \left[ \rho \chi_\parallel \nabla_\parallel \left( \frac{p}{\rho} \right) \right] + H, \tag{2.69}$$

$$\frac{\partial \mathbf{B}}{\partial t} = \nabla \times (\boldsymbol{v} \times \mathbf{B}) - \nabla \times \eta \mathbf{J}, \tag{2.70}$$

with $S = -\nabla \cdot D \nabla \rho_0$, $H = -\nabla \cdot \rho \chi_\perp \nabla \frac{p_0}{\rho}$, $\rho_0$ and $p_0$ the equilibrium density and pressure. Note that the diffusion in the pressure equation is on the temperature $p/\rho$. The notation $\nabla \nu \nabla \boldsymbol{v}$ stands for $\nabla (\nu \nabla \cdot \boldsymbol{v}) - \nabla \times (\nu \nabla \times \boldsymbol{v})$.

Notice we have neglected any anistropy in the resistivity, since this anisotropy is quite small. Resistive Ohm's law in this model reads:

$$\mathbf{E} + \boldsymbol{v} \times \mathbf{B} = \eta \mathbf{J}. \tag{2.71}$$

Assuming constant resistivity, and denoting[7] $\bar{\eta} \equiv \eta/\mu_0$, which has the dimension of a diffusion coefficient, the induction equation can be seen as a diffusion equation for the magnetic field

$$\frac{\partial \mathbf{B}}{\partial t} = \nabla \times (\boldsymbol{v} \times \mathbf{B}) + \bar{\eta} \nabla^2 \mathbf{B}. \tag{2.72}$$

The $\nabla \times (\boldsymbol{v} \times \mathbf{B})$ term is similar to an advection term. We will see in section 2.2.3 that the first effect of the resistivity is to increase the growth rate and make the internal kink mode unstable even when it is ideally stable. Resistivity is also the most simple effect allowing for field-line reconnection. Indeed the ideal Ohm's law is also called frozen-in-law, meaning that the plasma is frozen to the magnetic field. Let us develop this point to introduce the concept of magnetic reconnection.

[7] We use this notation to avoid writing $\mu_0$ several times.

### 2.1.8 Bifluid modification of the MHD equations

Relaxing the MHD ordering, with now small perpendicular electric fields, $v_E/v_t \simeq \delta_M$, the diamagnetic drifts are reintroduced, and also, in theory, the polarization drifts, which are the lowest order of the last term in *Eq.* (2.37). It also reintroduces the stress tensor $\bar{\bar{\boldsymbol{\pi}}}$, which has been completely neglected so far. Dealing with $\bar{\bar{\boldsymbol{\pi}}}$ rapidly gets very intricate so we will only give the result. We will also neglect the polarization velocity. In theory, it should be kept as it introduces corrections of order $k_\perp^2\rho_s^2$ to the dispersion relation of MHD waves, with $\rho_s = 1/eB\sqrt{m_i T_e}$ the ion sound Larmor radius. This effect has probably a significant influence in the thin inertial layer where reconnection takes place during the sawtooth crash (see chapter 4), because $\rho_s$ can be larger than the current sheet radial width. However, it is not implemented in XTOR-2F, mainly for numerical reasons, so it will be skipped in the following. We now derive bifluid equations which will be very close to XTOR-2F equations, except for the transport terms on density and pressure. In our new ordering, the ion and electron velocities are

$$\boldsymbol{v}_i = \boldsymbol{v}_E + \boldsymbol{v}_i^\star + \boldsymbol{v}_{\parallel i}, \tag{2.73}$$

$$\boldsymbol{v}_e = \boldsymbol{v}_E + \boldsymbol{v}_e^\star + \boldsymbol{v}_{\parallel i} - \frac{j_\parallel}{n_e e}\mathbf{b}, \tag{2.74}$$

$$\tag{2.75}$$

In the following, we write $\boldsymbol{v} = \boldsymbol{v}_E + \boldsymbol{v}_{\parallel i}$, which will be our dynamic velocity variable. The diamagnetic part $\boldsymbol{v}_i^\star$ evolves according to the pressure (dominantly) and magnetic (marginally) evolutions. We retain Ohm's law as *Eq.* (2.33) with the addition of the resistive term $\eta\mathbf{J}$. It is straightforward to find Ohm's law as a function of $\boldsymbol{v}$:

$$\mathbf{E} + \boldsymbol{v}\times\mathbf{B} = -\frac{\nabla_\parallel p_e}{n_e e}\mathbf{b} + \eta\mathbf{J}, \tag{2.76}$$

in accordance with the discussion at the end of the preceding subsection. We will see that during the sawtooth crash, the parallel gradient of the pressure can become larger than the resistive term and significantly accelerate the reconnection process.

We take the occasion to make a point about the denomination of the electron parallel pressure gradient term. In the following of this thesis, we will refer to it as the Hall term. The problem is that there is some confusion in the literature about what exactly the Hall term is. It is not obvious in the way we have written Ohm's law, but there is a $\mathbf{J}\times\mathbf{B}$ term hidden in the generalized version of Ohm's law. Namely, the generalized Ohm's law is often written (see for instance [Priest 2000]):

$$\mathbf{E} + \boldsymbol{v}_i\times\mathbf{B} = \eta\mathbf{J} + \frac{m_e}{n_e e^2}\left[\frac{\partial\mathbf{J}}{\partial t} + \nabla\cdot(\boldsymbol{v}\mathbf{J} + \mathbf{J}\boldsymbol{v})\right] + \frac{\mathbf{J}\times\mathbf{B}}{n_e e} - \frac{\nabla p_e}{n_e e}, \tag{2.77}$$

considering a scalar electron pressure instead of the full pressure tensor. In this equation, $\mathbf{J}\times\mathbf{B}$ is often called the Hall term and the pressure gradient, the thermal force. But sometimes what is denoted "Hall term" is the sum $\mathbf{J}\times\mathbf{B} - \nabla p_e$, in particular in Ref. [Priest 2000]. When Ohm's law is written in the manner of *Eq.* (2.33), even the $-\nabla p_e$

term itself can be called the Hall term, for instance in Ref. [Wang 1993]. *Eq.* (2.77) can be reorganized to yield *Eq.* (2.76), after neglecting the electron inertia term, (the term proportional to $m_e$). Indeed, replacing $\boldsymbol{v}_{i\perp}$ by $\boldsymbol{v}_E + \boldsymbol{v}_i^\star$, and using $\boldsymbol{v}_i^\star \times \mathbf{B} = 1/(n_e e)\nabla_\perp p_i$, $\mathbf{J}\times\mathbf{B} = \nabla_\perp p = \nabla_\perp p_i + \nabla_\perp p_e$, one obtains

$$\mathbf{E} + \boldsymbol{v}_E \times \mathbf{B} + \frac{\nabla_\perp p_i}{n_e e} = \frac{\nabla_\perp p_i}{n_e e} + \frac{\nabla_\perp p_e}{n_e e} - \frac{\nabla p_e}{n_e e}, \tag{2.78}$$

which is obviously equivalent to *Eq.* (2.76). The problem with this approach is that it assumes that the equilibrium relation $\mathbf{J}\times\mathbf{B} = \nabla_\perp p$ is dynamically verified. The deviation from this relation in the dynamic evolution of the plasma may also introduce new physically interesting terms. Nevertheless, in the following we will call Hall term the term proportional to $-\nabla_\parallel p_e$, since it is the non-ideal effect in XTOR-2F's Ohm's law related to the $\mathbf{J}\times\mathbf{B}$ term.

Next the continuity equation, *Eq.* (2.54), is developed with the new velocity expression, neglecting the electron momentum in the divergence. This gives

$$\frac{\partial \rho}{\partial t} + \nabla\cdot(\rho\boldsymbol{v}) + \frac{m_i}{e}\nabla p_i \cdot \nabla\times\frac{\mathbf{B}}{B^2} = 0. \tag{2.79}$$

In the following we use the notation $\boldsymbol{\Xi} \equiv \nabla\times(\mathbf{B}/B^2)$. The neglect of the electron part in the pressure equation is however evidently not possible. To derive the evolution equation of $p = p_e + p_i$ in the bifluid framework, we start from Braginskii's species pressure equation, *Eq.* (2.56), neglecting the stress tensor, $W_s$ and retaining in $\mathbf{q}_s$ only the cross heat flux $\pm\kappa_\times^s \mathbf{b}\times\nabla_\perp T_s$, we obtain the following evolution equation for $p_e$ and $p_i$:

$$\frac{\partial p_e}{\partial t} + \boldsymbol{v}\cdot\nabla p_e + \Gamma p_e \nabla\cdot\boldsymbol{v} + \Gamma\frac{T_e}{e}\nabla p_i\cdot\boldsymbol{\Xi} - \Gamma\frac{p_e}{e}\nabla T_e\cdot\boldsymbol{\Xi} + \Gamma\frac{j_\parallel}{e}\nabla_\parallel T_e = 0 \tag{2.80}$$

$$\frac{\partial p_i}{\partial t} + \boldsymbol{v}\cdot\nabla p_i + \Gamma p_i \nabla\cdot\boldsymbol{v} + \Gamma\frac{T_i}{e}\nabla p_i\cdot\boldsymbol{\Xi} + \Gamma\frac{p_i}{e}\nabla T_i\cdot\boldsymbol{\Xi} = 0. \tag{2.81}$$

Notice the asymmetry between the ion and electron equations, the latter involving the ion pressure because we have explicitly written $\nabla\cdot\mathbf{J}_\parallel = -\nabla\cdot\mathbf{J}_\perp = -\nabla p\cdot\boldsymbol{\Xi}$. We have also used $\boldsymbol{v}_s^\star\cdot\nabla p_s = 0$. Neglecting the parallel current term, the sum of the two equations yields for the total pressure:

$$\frac{\partial p}{\partial t} + \boldsymbol{v}\cdot\nabla p + \Gamma p\nabla\cdot\boldsymbol{v} + \frac{\Gamma}{e}\left(T\nabla p_i + p_i\nabla T_i - p_e\nabla T_e\right)\cdot\boldsymbol{\Xi} = 0. \tag{2.82}$$

We finally need the momentum equation. This is where the stress tensor kicks in. It is possible to show that the total derivative of the diamagnetic velocity,

$$\frac{\partial \boldsymbol{v}_i^\star}{\partial t} + \boldsymbol{v}\cdot\nabla\boldsymbol{v}_i^\star + \boldsymbol{v}_i^\star\cdot\nabla\boldsymbol{v}_i^\star, \tag{2.83}$$

is cancelled by a part of the stress tensor. There are also terms in the tensor to cancel the inertia term $\boldsymbol{v}_i^\star\cdot\nabla\boldsymbol{v}_\parallel$. This is usually referred to as the diamagnetic cancellation [Hazeltine 2003, Ramos 2005]. The r.h.s. of the momentum equation is not modified and we finally obtain

$$\frac{\partial \boldsymbol{v}}{\partial t} + \boldsymbol{v}\cdot\nabla\boldsymbol{v} + \boldsymbol{v}_i^\star\cdot\nabla\boldsymbol{v}_\perp = \mathbf{J}\times\mathbf{B} - \nabla p. \tag{2.84}$$

The magnetic field evolves according to $\partial_t \mathbf{B} = \nabla \times \mathbf{E}$, with $\mathbf{E}$ given by *Eq.* (2.76). Reintroducing the same transport coefficients as in the $\eta\chi$MHD model[8], we finally obtain the following model:

$$\frac{\partial \rho}{\partial t} + \nabla \cdot \rho \boldsymbol{v} + \frac{m_i}{e} \nabla p_i \cdot \boldsymbol{\Xi} = \nabla \cdot D \nabla \rho + S, \tag{2.85}$$

$$\rho \left( \frac{\partial \boldsymbol{v}}{\partial t} + \boldsymbol{v} \cdot \nabla \boldsymbol{v} + \boldsymbol{v}_i^\star \cdot \nabla \boldsymbol{v}_\perp \right) = \mathbf{J} \times \mathbf{B} - \nabla p + \nabla \nu \nabla \left( \boldsymbol{v} + \boldsymbol{v}_i^\star \right), \tag{2.86}$$

$$\frac{\partial p}{\partial t} + \boldsymbol{v} \cdot \nabla p + \Gamma p \nabla \cdot \boldsymbol{v} + \frac{\Gamma}{e} \left( T \nabla p_i + p_i \nabla T_i - p_e \nabla T_e \right) \cdot \boldsymbol{\Xi} = \ldots$$
$$\nabla \cdot \rho \chi_\perp \nabla \frac{p}{\rho} + \nabla \cdot \rho \chi_\parallel \nabla_\parallel \frac{p}{\rho} + H, \tag{2.87}$$

$$\frac{\partial \mathbf{B}}{\partial t} = \nabla \times \boldsymbol{v} \times \mathbf{B} + \nabla \times \left( \frac{\nabla_\parallel p_e}{ne} \mathbf{b} \right) - \nabla \times \eta \mathbf{J}, \tag{2.88}$$

These two models, $\eta\chi$MHD and bifluid MHD, are solved by the XTOR-2F code which will be presented in chapter 3 and used in chapters 6, 7 and 4. We will now give a few elements about the magnetic configuration in a tokamak.

We now use the ideal, then resistive and bifluid equations to derive some results about the stability of the (1/1) internal kink mode linked with the sawtooth crash.

## 2.2 The internal kink mode

### 2.2.1 The ideal MHD energy principle

It is impossible to understand the sawtooth dynamics without an idea of the internal kink instability. We will give here a few elements about the kink mode, without giving the proper derivation in the general case. In a few limiting cases, the dispersion relation and structure of the kink mode can be exactly derived. However these situations are often irrelevant in terms of plasma parameters, or of low practical use. The problem is that even though the instability is due to the resonance condition $k_\parallel = 0$ on a given surface in the plasma, where $\mathbf{k}$ is the mode wave number, the energy and structure actually depends on the detailed structure everywhere in the plasma[9]. In essence, an instability is a displacement of the plasma, coupled to an electromagnetic perturbation through the MHD equations. The displacement is parameterized using the Lagrangian displacement $\boldsymbol{\xi}(\boldsymbol{x}_0, t)$, defined by:

$$\boldsymbol{X}(\boldsymbol{x}_0, t) = \boldsymbol{x}_0 + \boldsymbol{\xi}(\boldsymbol{x}_0, t), \tag{2.89}$$

where $\boldsymbol{X}(\boldsymbol{x}_0, t)$ denotes the position vector at time $t$ of a plasma element located in $\boldsymbol{x}_0$ at time $t = 0$. *A priori*, the function $\boldsymbol{\xi}$ can be any function of space and time, and the game consists in finding the most unstable function allowed by *Eqs.* (2.44)-(2.47), in

[8] Just note that the viscosity now applies to the total velocity $\boldsymbol{v} + \boldsymbol{v}_i^\star$.

[9] More precisely for radii $r$ inside the resonant surface, $r < r_s$.

other words, the one which maximizes the growth rate, hence the use of a variational principle. Given the initial freedom in the choice of $\boldsymbol{\xi}$, and the globality of the problem, where the plasma as a whole must be considered, it is clearly seen why the instability growth rate and structure cannot be easily derived.

Assuming the plasma is at rest at $t = 0$, we have $\mathrm{d}\boldsymbol{x}_0/\mathrm{d}t = 0$ and the velocity of the plasma is simply the partial derivative of the Lagrangian displacement:

$$\boldsymbol{v} = \frac{\mathrm{d}\boldsymbol{\xi}}{\mathrm{d}t} = \frac{\partial \boldsymbol{\xi}}{\partial t}, \tag{2.90}$$

Integrating the ideal MHD equations with respect to time, the linearized pressure, magnetic and current perturbations can be expressed as a function of $\boldsymbol{\xi}$:

$$\delta p = -\boldsymbol{\xi} \cdot \nabla p - \Gamma p \nabla \cdot \boldsymbol{\xi} \tag{2.91}$$

$$\delta \mathbf{B} = \nabla \times (\boldsymbol{\xi} \times \mathbf{B}) \tag{2.92}$$

$$\delta \mathbf{J} = \frac{1}{\mu_0} \nabla \times \delta \mathbf{B}. \tag{2.93}$$

The momentum equation describing the evolution of $\boldsymbol{\xi}$ reads:

$$\rho \frac{\partial^2 \boldsymbol{\xi}}{\partial t^2} = \delta \mathbf{J} \times \mathbf{B} + \mathbf{J} \times \delta \mathbf{B} - \nabla \delta p \equiv \mathbf{F}(\boldsymbol{\xi}). \tag{2.94}$$

We look for normal modes with pulsation $\omega$: $\boldsymbol{\xi}(\boldsymbol{x}, t) = \boldsymbol{\xi}(\boldsymbol{x}) e^{i\omega t}$. Then *Eq.* (2.94) is integrated over the whole volume after multiplying by $\boldsymbol{\xi}^\star$, the complex conjugate of $\boldsymbol{\xi}$. We define the energy

$$E(\boldsymbol{\xi}^\star, \boldsymbol{\xi}) = -\frac{1}{2} \int \mathrm{d}^3\boldsymbol{x}\, \rho\omega^2 |\boldsymbol{\xi}|^2 - \frac{1}{2} \int \mathrm{d}^3\boldsymbol{x}\, \boldsymbol{\xi}^\star \cdot \mathbf{F}(\boldsymbol{\xi}) \equiv K(\boldsymbol{\xi}^\star, \boldsymbol{\xi}) + \delta W(\boldsymbol{\xi}^\star, \boldsymbol{\xi}), \tag{2.95}$$

following the usual notation, and we have $E(\boldsymbol{\xi}^\star, \boldsymbol{\xi}) = 0$. The first term represents the kinetic energy due to the mode, the second term its potential energy. The operator $\mathbf{F}$ has the interesting property that it is self-adjoint, so that $\delta W(\boldsymbol{\eta}^\star, \boldsymbol{\xi}) = \delta W(\boldsymbol{\xi}, \boldsymbol{\eta}^\star)$. The normal mode solution $\boldsymbol{\xi}$ is obtained by extremalization of the energy, in other words *Eq.* (2.94) is the Euler equation for the variational formulation $E(\boldsymbol{\xi}^\star, \boldsymbol{\xi})$. Indeed,

$$\frac{\delta E}{\delta \boldsymbol{\xi}^\star} = -\rho\omega^2 \boldsymbol{\xi} - \mathbf{F}(\boldsymbol{\xi}), \tag{2.96}$$

so that $\delta E/\delta \boldsymbol{\xi}^\star = 0$ is equivalent to *Eq.* (2.94). Thus the technique to obtain the mode structure is to extremalize $E$ with respect to $\boldsymbol{\xi}$, and then determining the (complex) frequency $\omega$ by:

$$\omega^2 = -\frac{\int \mathrm{d}^3\boldsymbol{x}\, \boldsymbol{\xi}^\star \cdot \mathbf{F}(\boldsymbol{\xi})}{\int \mathrm{d}^3\boldsymbol{x}\, |\boldsymbol{\xi}|^2}. \tag{2.97}$$

Note that since $\mathbf{F}$ is self-adjoint, $\omega^2 \in \mathbb{R}$, so the modes are purely growing or damped, or purely oscillating, in the framework of ideal MHD.

This technique can be used to exactly determine the unstable mode driven by a given equilibrium. It is done extensively in Refs. [Bussac 1975, Connor 1985, Deblank 1991],

in toroidal geometry, and applied to $q$ profiles significantly flat in a given region inside the $q = 1$ surface. However the steps are rather painful and sometimes the physics is difficult to highlight. We will adopt a different formulation, using what is known as the energy principle.

The energy principle states that an equilibrium is unstable if and only if there exists a function $\boldsymbol{\xi}$ for which the change in the potential energy is negative, $\delta W(\boldsymbol{\xi}^\star, \boldsymbol{\xi}) < 0$. Since $E(\boldsymbol{\xi}^\star, \boldsymbol{\xi}) = 0$, it is obvious that an unstable mode, which does possess a kinetic energy (K $>$0), has $\delta W < 0$. The reciprocal is also true, see [Bernstein 1958]. Practically, we will take the poloidal and toroidal wave numbers of the mode, $\mathsf{m}$ and $\mathsf{n}$, for granted, here $(\mathsf{m}, \mathsf{n}) = (1, 1)$, and minimize the potential energy to find the most unstable mode. This way, we can arrive to a certain mode structure, even though it may not represent the exact normal mode. However in practice, the mode obtained following this procedure is not very different from the exact one. In particular, the exact mode, in toroidal geometry, cannot be purely a $(1, 1)$ mode, because of the toroidal coupling arising due to the magnetic field toroidal curvature. We will see in the simulations that indeed, the $(1, 1)$ internal kink comes with sidebands.

First we will exhibit a convenient form for $\delta W$. Replacing the expression of $\mathbf{F}$ in $\delta W$ and integrating by parts the term $\boldsymbol{\xi}^\star \cdot \delta\mathbf{J} \times \mathbf{B}$ and $-\boldsymbol{\xi}^\star \cdot \nabla\Gamma p \nabla \cdot \boldsymbol{\xi}$, and also using the self-adjointness of the operators, one obtains

$$\delta W = \frac{1}{2} \int \mathrm{d}^3\boldsymbol{x} \left[ |\delta\mathbf{B}|^2 + \Gamma p |\nabla \cdot \boldsymbol{\xi}|^2 - \boldsymbol{\xi}^\star \cdot \nabla(\boldsymbol{\xi} \cdot \nabla p) - \boldsymbol{\xi}^\star \cdot \mathbf{J} \times \delta\mathbf{B} \right]. \tag{2.98}$$

To perform the integration by parts, we assumed the perturbed quantities all vanish on the plasma surface $\boldsymbol{\xi}(r = a) = 0$, restricting our study to internal modes[10]. The expression for $\delta W$, *Eq.* (2.98), can be simplified into

$$\delta W = \frac{1}{2} \int \mathrm{d}^3\boldsymbol{x} \Big[ |\delta\mathbf{B}_\perp|^2 + \frac{B^2}{\mu_0} |\nabla \cdot \boldsymbol{\xi}_\perp + 2\boldsymbol{\xi}_\perp \cdot \boldsymbol{\kappa}|^2 + \Gamma p \, |\nabla \cdot \boldsymbol{\xi}|^2 - (\boldsymbol{\xi}_\perp \cdot \nabla p)(2\boldsymbol{\xi}_\perp^\star \cdot \boldsymbol{\kappa}) - J_\parallel (\boldsymbol{\xi}_\perp \times \mathbf{B}) \cdot \delta\mathbf{B}_\perp \Big]. \tag{2.99}$$

See appendix C for the steps of the calculation. In this expression, the first term is the energy associated to the bending of field-lines. The second term is the energy necessary to compress the magnetic field in the transverse direction, and the third one is the energy necessary to compress the plasma. All these terms are positive, and hence are stabilizing. The last two terms have indefinite sign and can be either stabilizing or destabilizing. They are respectively proportional to the pressure gradient and to the parallel current, and are called the pressure term and the current term (or interchange and kink terms).

The minimization is now performed in the cylindrical limit. Toroidal effects are absent in this limit, the tokamak is simply a cylinder of length $L = 2\pi R_0$ in the $z$ direction, with perdiodic boundary conditions. The $z$ variable is replaced with the equivalent of the toroidal angle, $\varphi = z/R_0$. The equilibrium magnetic field is written:

$$\mathbf{B} = B_\theta(r)\hat{\boldsymbol{\theta}} + B_\varphi(r)\hat{\boldsymbol{\varphi}}, \tag{2.100}$$

[10] Usually, the surface terms, as well as a term corresponding to the magnetic energy in the vacuum, are considered. They are used to study external modes.

where $\hat{\boldsymbol{\theta}}$ and $\hat{\boldsymbol{\varphi}}$ are the unit vectors in the poloidal and toroidal directions (we reserve bold hatted notations for unit vectors). For this configuration, the safety factor $q = \mathrm{d}\psi_T/\mathrm{d}\psi = rB_\varphi/(R_0 B_\theta)$. Indeed $\mathrm{d}\psi_T = rB_\varphi \mathrm{d}r$ and $\mathrm{d}\psi = R_0 B_\theta \mathrm{d}r$. The $(1,1)$ mode is written

$$\boldsymbol{\xi}(\boldsymbol{r}) = \boldsymbol{\xi}(r) e^{i\mathbf{k}\cdot\boldsymbol{r}} = \boldsymbol{\xi}(r) e^{i(\theta-\varphi)}, \tag{2.101}$$

with $\mathbf{k} = \hat{\boldsymbol{\theta}}/r - \hat{\boldsymbol{\varphi}}/R_0$, and $\boldsymbol{\xi}(r)$ is conveniently written $\boldsymbol{\xi}(r) = \xi_r(r)\hat{\boldsymbol{r}} + \xi_\eta(r)\hat{\boldsymbol{\eta}} + \xi_\parallel(r)\mathbf{b}$. Here $\hat{\boldsymbol{\eta}}$ is the vector orthogonal to $\mathbf{b}$ and $\hat{\boldsymbol{r}}$:

$$\hat{\boldsymbol{\eta}} = \frac{B_\varphi \hat{\boldsymbol{\theta}} - B_\theta \hat{\boldsymbol{\varphi}}}{B}. \tag{2.102}$$

There are three degrees of freedom in $\boldsymbol{\xi}$, so $\delta W$ will be minimized twice in order to get an expression involving only one degree of freedom, $\xi_r$.

First note that $\xi_\parallel$ is involved only in the $\Gamma p|\nabla\cdot\boldsymbol{\xi}|^2$ term, all other terms involve only the perpendicular component $\boldsymbol{\xi}_\perp$. Thus $\delta W$ is minimized with respect to $\xi_\parallel$ by $\nabla\cdot\boldsymbol{\xi} = 0$, that is, most unstable modes are incompressible. This gives $\xi_\parallel$ as a function of $\boldsymbol{\xi}_\perp$:

$$0 = ik_\parallel \xi_\parallel + \nabla\cdot\boldsymbol{\xi}_\perp, \tag{2.103}$$

noting that in the cylindrical limit, $\nabla\cdot\mathbf{b} = -1/B\nabla_\parallel B = 0$, and with $k_\parallel = \mathbf{k}\cdot\mathbf{b} = (B_\theta/r - B_\varphi/R_0)/B$. We define $F \equiv \mathbf{k}\cdot\mathbf{B} = k_\parallel B$. Thus

$$\xi_\parallel = i\frac{B}{F}\nabla\cdot\boldsymbol{\xi}_\perp. \tag{2.104}$$

Note that this expression becomes singular on magnetic surfaces where $F$ vanishes. These magnetic surfaces are $q = 1$ surface, indeed

$$F = \frac{B_\theta}{r}(1 - q(r)) = \frac{B_\varphi}{R_0}\left(\frac{1}{q(r)} - 1\right). \tag{2.105}$$

However it can be shown that this singularity does not contribute to $\delta W$, so that the expression obtained by replacing *Eq.* (2.104) in *Eq.* (2.99) remains valid in the presence of $q = 1$ surfaces.

A similar procedure can be carried out for the component $\xi_\eta$, which must be isolated in a single positive expression. The expression of $\xi_\eta$ as a function of $\xi_r$ is determined and replaced in *Eq.* (2.99). The steps are elaborate but straightforward. The expression of $\xi_\eta$ is

$$\xi_\eta = \frac{i}{r(1/r^2 + 1/R_0^2)B}\left(G(r\xi_r)' - 2\frac{B_\theta}{R_0}\xi_r\right), \quad G = \frac{B_\varphi}{r} + \frac{B_\theta}{R_0}. \tag{2.106}$$

Finally, the following form is obtained for $\delta W$:

$$\delta W = \frac{2\pi^2 R_0}{\mu_0}\int_0^a \mathrm{d}r\left(f(r)|\xi_r'|^2 + g(r)|\xi_r|^2\right), \tag{2.107}$$

with the following expressions for $f$ and $g$:

$$f = \frac{r^3 F^2}{1+\varepsilon^2} \tag{2.108}$$

$$g = \frac{\varepsilon^2}{1+\varepsilon^2}\left(2\mu_0 p' + rF^2 + \frac{2}{r}B_\varphi^2\frac{\varepsilon^2}{1+\varepsilon^2}(1 - \frac{1}{q^2})\right), \tag{2.109}$$

with $\varepsilon = r/R_0 \ll 1$ since we are in the cylindrical (or high aspect ratio) approximation.

Note that since the ratio between the thermal and magnetic pressures, $\beta$, is small, typically $\beta \sim (a/R_0)^2$, all three terms in the expression of $g$ are *a priori* of the same order of magnitude. We have $f = f_0 + f_2 + \mathcal{O}(\varepsilon^4)$ and $g = g_2 + \mathcal{O}(\varepsilon^4)$. The solution $\xi_r$ is also expanded in powers of $\varepsilon$: $\xi_r = \xi_{r0} + \xi_{r2} + \mathcal{O}(\varepsilon^4)$. The general Euler equation giving $\xi_r$ is easily obtained:

$$\frac{\mathrm{d}}{\mathrm{d}r}\left(f\frac{\mathrm{d}\xi_r}{\mathrm{d}r}\right) - g\xi_r = 0. \tag{2.110}$$

At lowest order, this equation reads

$$\frac{\mathrm{d}}{\mathrm{d}r}\left(r^3F^2\frac{\mathrm{d}\xi_{r0}}{\mathrm{d}r}\right) = 0 \quad \Longrightarrow \quad r^3(1-q(r))\xi'_{r0} = C^{te} = 0. \tag{2.111}$$

Therefore at lowest order, $\xi'_r = 0$, except around resonant surfaces where $q = 1$. For monotonic $q$ profiles with $q_0 = q(0) < 1$, there is only one such surface at radius $r_s$ and thus we have:

$$\xi_{r0}(r) = \begin{cases} \xi_\infty & r < r_s \\ 0 & r > r_s, \end{cases} \tag{2.112}$$

The solution $\xi_{r0} = 0$ for $r > r_s$ corresponds to the external vanishing boundary condition. The other solution $\xi_\infty$ is free, and will grow exponentially with time if the mode is unstable. It is not necessary to go further in the Taylor expansion because the minimized energy can already be obtained at lowest order. Replacing *Eq.* (2.112) in *Eq.* (2.107) yields

$$\delta W_{min} = \frac{2\pi^2 R_0}{\mu_0}\xi_\infty^2 \int_0^{r_s} g_2 \mathrm{d}r. \tag{2.113}$$

The expression of $g_2$, as a function of $q$ and with $\beta = 2\mu_0 p/B_\varphi^2$, reads

$$g_2 = -2\varepsilon^2\mu_0 p\left[\frac{\varepsilon^2}{\beta}\frac{3q+1}{rq^2}[1-q] - \frac{p'}{p}\right]. \tag{2.114}$$

This convenient form clearly highlights the driving terms for the instability. The first term corresponds to the current-driven instability and the second one to the pressure-driven instability. It is seen that in a cylinder, with standard peaked pressure profiles, $p'/p < 0$, and monotonic $q$ profile, the existence of a $q = 1$ surface is a sufficient condition for instability of the $(1,1)$ kink mode[11]. It is also a necessary condition, because otherwise $r_s$ must be set to zero and the integral in *Eq.* (2.113) vanishes. This result changes in toroidal geometry, as will be seen in section 2.2.5. Even though this energy does not give the growth rate of the normal mode associated with a given equilibrium, it is expected that the larger the minimum energy $\delta W_{min}$, the larger the growth rate, since it represents the change in potential energy for a given displacement. So the key factor in driving the kink unstable is the current peaking, quantified by $1-q$, and the pressure peaking $-p'/p$, acts as to increase the drive. For parabolic profiles, performing the integral over the current part of $g_2$ shows that typically $\delta W_{min} \propto 1 - q_0$, at least for $1 - q_0 \ll 1$.

[11] Note that writing $\int_0^{r_s} g_2\,\mathrm{d}r$ supposes the existence of a $q = 1$ surface.

This means that as a general rule, the lower the core safety factor, the more unstable the configuration.

These features of the kink (necessity of a $q = 1$ surface, driving by both current and pressure peaking) are essential, however remember that the results of this section are exact only in cylindrical geometry and for ideal MHD. Next we will derive the approximate mode structure and growth rate of the ideal kink mode.

### 2.2.2 The ideal mode structure and growth rate

The only way to derive the mode structure properly is to extremalize the sum $E = K + \delta W$. Here we will check that the kinetic energy of the mode is negligible everywhere except inside a thin layer around the $q = 1$ surface where $\xi_r$ varies rapidly and inertia is expected to play a role. Hence extremalization of $\delta W$ only is sufficient outside the resonance layer. The small thickness of the layer allows solving the problem exactly inside the layer, then matching asymptotically the inner solution to the outer solution, which is obtained without taking inertia into account.

First, the following order of the Euler equation for $\delta W$ is derived:

$$\frac{\mathrm{d}}{\mathrm{d}r}\left(f_0\frac{\mathrm{d}\xi_{r2}}{\mathrm{d}r} + f_2\frac{\mathrm{d}\xi_{r0}}{\mathrm{d}r}\right) - g_2\xi_{r0} = 0. \tag{2.115}$$

Since $\mathrm{d}\xi_{r0}/\mathrm{d}r$ vanishes, the solution is obtained in the two regions $r < r_s$ and $r > r_s$:

$$\frac{\mathrm{d}\xi_{r2}}{\mathrm{d}r} = \begin{cases} \dfrac{\xi_\infty}{r^3F^2}\displaystyle\int_0^r g_2\mathrm{d}r & r < r_s \\ \dfrac{\alpha}{r^3F^2} & r > r_s, \end{cases} \tag{2.116}$$

where $\alpha$ is a yet undetermined constant.

According to *Eq.* (2.116), the derivative of $\xi_r$ diverges close to the resonant surface. We expect inertia to be important only in this region. The kinetic energy is

$$K(\boldsymbol{\xi}^\star, \boldsymbol{\xi}^\star) = -2\pi^2 R_0 \int \mathrm{d}r\, r\rho\omega^2 \left(|\xi_r|^2 + |\xi_\eta|^2 + |\xi_\parallel|^2\right). \tag{2.117}$$

The parallel contribution is negligible. Indeed

$$\nabla\cdot\boldsymbol{\xi}_\perp = \frac{(r\xi_r)'}{r} + i\frac{\xi_\eta}{B}G. \tag{2.118}$$

Replacing the expression for $\xi_\eta$, *Eq.* (2.106), we find that at lowest order,

$$\xi_\parallel = \frac{2iB_\theta}{FR}\left(\xi_r - (r\xi_r)'\right), \tag{2.119}$$

so that if $\xi_r' = 0$, the lowest order of $\xi_\parallel$ vanishes. In the opposite case (in the layer), it is already of order $B_\theta/FR \sim \varepsilon/(1-q)$, so its contribution to the energy $|\xi_\parallel|^2$ is $\mathcal{O}(\varepsilon^2)$. Thus we will always neglect it compared to $\xi_r$ and $\xi_\eta$.

In the layer, the dominant contribution to the energy is the $\xi_r'$ term in $\xi_\eta$, so that $K$ writes (in terms of the growth rate $\gamma = i\omega$):

$$K = 2\pi^2 R_0 \rho \gamma^2 \int \mathrm{d}r\, r^3 |\xi_r'|^2. \tag{2.120}$$

Inside the layer, the Euler equation to solve is

$$\frac{\mathrm{d}}{\mathrm{d}r}\left(r^3\left(\gamma^2\mu_0\rho + F^2\right)\frac{\mathrm{d}\xi_r}{\mathrm{d}r}\right) = 0. \tag{2.121}$$

In the thin layer, the variable $r$ is replaced with $x \equiv r - r_s$, the density is assumed constant, $\rho = \rho_0$, and $F$, which vanishes for $r = r_s$, is Taylor expanded: $F \simeq F'x$. The Euler equation now reads

$$r_s^3 \frac{\mathrm{d}}{\mathrm{d}x}\left(\left(\gamma^2\mu_0\rho_0 + |F'|^2x^2\right)\frac{\mathrm{d}\xi_r}{\mathrm{d}x}\right) = 0, \tag{2.122}$$

Hence

$$\frac{\mathrm{d}\xi_r}{\mathrm{d}X} = \frac{K_1}{1+X^2}, \quad X^2 = \frac{|F'|^2}{\gamma^2\mu_0\rho_0}x^2, \tag{2.123}$$

assuming $\gamma^2 > 0$, and with $K_1$ a constant. Finally

$$\xi_r = K_2 + K_1 \arctan X. \tag{2.124}$$

The two constants are determined by the condition that the layer solution $\xi_r$ must have the values given by *Eq.* (2.112) when $X$ tends to $\pm\infty$. This gives

$$\xi_r = \xi_\infty\left(\frac{1}{2} - \frac{1}{\pi}\arctan\left(\frac{|F'|x}{\gamma\sqrt{\mu_0\rho_0}}\right)\right). \tag{2.125}$$

Finally the growth rate can be determined, using the condition that the derivatives at both ends of the inner layer in $X \to \pm\infty$ have to match the outer solution *Eq.* (2.116). This procedure is called asymptotic matching. Reexpressed in $r$ and $x$, *Eq.* (2.123) for $x \to \pm\infty$ reads

$$\frac{\mathrm{d}\xi_r}{\mathrm{d}r} = -\frac{\xi_\infty\gamma\sqrt{\mu_0\rho_0}}{|F'|x^2}. \tag{2.126}$$

Comparing to *Eq.* (2.116) with $F \simeq F'x$, we finally obtain the growth rate

$$\gamma = -\frac{\pi}{r_s^3|F'|\sqrt{\mu_0\rho_0}}\int_0^{r_s} g_2 \mathrm{d}r. \tag{2.127}$$

The constant $\alpha$ is also found:

$$\alpha = \xi_\infty \int_0^{r_s} g_2 \mathrm{d}r. \tag{2.128}$$

The resulting displacement is displayed on Fig. 2.4, for parabolic pressure and safety factor profiles, $q_0 = 0.7$, $\beta = 1\%$, $r_s = a/2$, $R_0/a = 3.5$.

Now let us check *a posteriori* that the expressions obtained for $\xi_r$, $\xi_\eta$, $\xi_\parallel$ and $\gamma$ indeed make $K(\boldsymbol{\xi}^\star, \boldsymbol{\xi})$ small when $\xi_r$ vanishes. We already noted that parallel inertia is negligible.

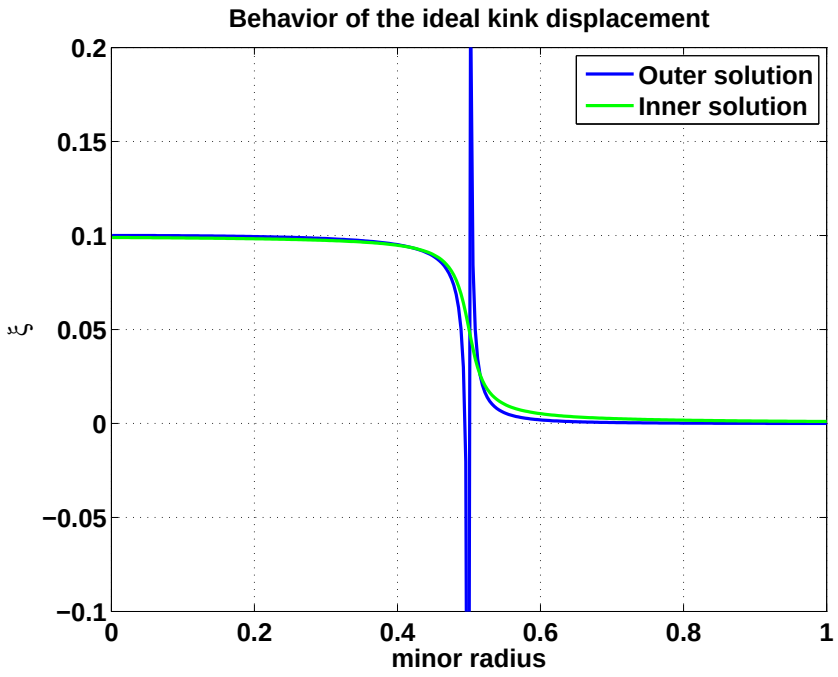


Figure 2.4: Behavior of the inner and outer solutions for a standard analytic equilibrium

Thus, since $\xi_\eta$ and $\xi_r$ are of the same order, a typical term in the kinetic energy is of the order $2\pi^2 R_0 r \rho_0 \gamma^2 |\xi_r|^2$, while a typical term in $\delta W$ is $2\pi^2 R_0 g_2/\mu_0 |\xi_r|^2$. Hence

$$\frac{K}{\delta W} \sim \frac{\mu_0 \rho_0 r_s \gamma^2}{g_2} \sim \frac{\pi^2 g_2}{r_s^3 |F'|^2} \tag{2.129}$$

Introducing the magnetic shear at the resonance layer,

$$\hat{s} = \frac{r_s q'}{q}, \tag{2.130}$$

we have $|F'| = \hat{s} B_\varphi/(R_0 r_s q)$. Taking the current term as an order of magnitude for $g_2$, and noticing that $\hat{s} \simeq (1 - q_0) \equiv \Delta q$, we get

$$\frac{K}{\delta W} \sim \frac{\pi^2}{\Delta q} \frac{r_s^2}{R_0^2} \lesssim 1. \tag{2.131}$$

The condition $K \ll \delta W$ is only marginally satisfied even outside the resonance layer for small values of $\Delta q$. The matching procedure fails when $q$ is too close to 1, which is equivalent to having a too wide inertial layer. Indeed, the inertial layer thickness $\delta$ can be infered from the argument in the arctan function,

$$\frac{\delta}{r_s} \sim \frac{\gamma \sqrt{\mu_0 \rho_0}}{r_s |F'|} \sim \frac{\pi g_2}{r_s^3 |F'|^2} \sim \frac{K}{\delta W}. \tag{2.132}$$

Note, however, that the stability condition

$$\int_0^{r_s} g_2 \, \mathrm{d}r > 0 \tag{2.133}$$

exactly holds.

### 2.2.3 Resistive modification of the growth rate

The importance of resistivity in the plasma is determined by the magnetic Reynolds number

$$R_m = \frac{aV}{\bar{\eta}}, \tag{2.134}$$

where $V$ is the typical fluid velocity. Defining the resistive time $\tau_R$ and the Lundquist number $S$:

$$\tau_R = \frac{a^2}{\bar{\eta}} S = \frac{\tau_R}{\tau_A}, \tag{2.135}$$

the magnetic Reynolds number can be written

$$R_m = S \frac{V}{V_A}. \tag{2.136}$$

Typical values of the Lundquist number in tokamaks are $S \sim 10^8 - 10^9$, whereas typically $V/V_A \sim 10^{-3} - 10^{-4}$. Hence $R_m$ is large and the resistivity is small. The resistivity can become an important effect only in parts of the fluid where the typical length scale is much reduced. This is just what happens during the evolution of the internal kink mode. Indeed we have just seen that the effect of the internal kink mode is to induce a rigid helical shift of the core, which is pushed toward the $q = 1$ surface. Flux surfaces lying outside the $q = 1$ surface do not move, hence the inner flux surfaces are squeezed at the resonant surface, resulting in a finite jump of magnetic field over a small distance. This means there is a current sheet of Sweet-Parker type, where we expect the resistivity to have a significant effect.

To derive the modification of the growth rate by resistivity, the method, again, is to asymptotically match a singular layer solution to an outer ideal solution. The outer solution is still given by *Eq.* (2.116). Let us derive the resistive equations which must be used in the layer. The magnetic perturbation produces a $\mathbf{J} \times \mathbf{B}$ force which accelerates the plasma, and the resulting velocity enters the Ohm's law, which in turn relates the velocity to the magnetic perturbation, which closes the loop. The analysis is carried out first in a cylinder, with length $R$ and vertical coordinate $\varphi = z/2\pi R$ (and periodic boundary conditions in $\varphi = 2\pi$). The unit vector basis is $\left(\hat{\boldsymbol{r}}, \hat{\boldsymbol{\theta}}, \hat{\mathbf{z}}\right)$. We use again the growth rate $\gamma$ and write the perturbations to be proportional to $\exp(\gamma t + i(\theta - \varphi))$. Perturbed quantities are denoted by the subscript 1.

The magnetic field is written

$$\begin{aligned} \mathbf{B} &= \mathbf{B}_{eq} - \nabla\psi_1 \times \hat{\mathbf{z}} \\ &= B_0 \left( \hat{\mathbf{z}} + \frac{r}{Rq} \hat{\boldsymbol{\theta}} \right) - \nabla\psi_1 \times \hat{\mathbf{z}}, \end{aligned} \tag{2.137}$$

where $\psi_1$ is the poloidal flux perturbation. Note that $\psi_1 \hat{\mathbf{z}}$ is minus the perturbed magnetic potential[12]: $\psi_1 = -A_{z,1}$. In our high aspect ratio approximation, we write $\boldsymbol{v}_1 = \hat{\mathbf{z}} \times \nabla\Phi_1$

[12] In particular, compared to the flux derived in section 2.1.1, the flux here is divided by $R_0$. This is only for convenience purpose.

with $\Phi_1 = \Phi_1/B_0$. The problem is determined by the two scalar quantities $\Phi_1$ and $\psi_1$, so two scalar equations will be sufficient. The first is the projection of the perturbed Ohm's law in the $\hat{\mathbf{z}}$ direction. With $\boldsymbol{v} \times \mathbf{B} = \nabla_\perp \phi_1$, we can write

$$-\partial_t \mathbf{A} - \mathbf{b}\nabla_\parallel \phi = \eta \mathbf{J}. \tag{2.138}$$

Projected on $\hat{\mathbf{z}}$, and taking only the perturbed part, this gives, with $\mu_0 j_{z1} = \nabla_\perp^2 \psi_1$:

$$\partial_t \psi_1 - \nabla_\parallel \phi_1 = \bar{\eta} \nabla_\perp^2 \psi_1. \tag{2.139}$$

Now for any scalar $f$, the parallel gradient has expression

$$\nabla_\parallel f = \frac{\partial_\varphi f}{R} - \frac{(\hat{\mathbf{z}} \times \nabla f)}{B_0} \cdot \nabla \psi. \tag{2.140}$$

Let us define the helical flux $\Psi^\star$ such that

$$\Psi^\star = \int_0^{\psi_0} (1-q) \mathrm{d}\psi + \psi_1 = \Psi_0^\star + \psi_1, \tag{2.141}$$

where $\psi_0$ is the equilibrium poloidal flux. The helical flux is the magnetic flux through a helical ribbon defined by the magnetic axis and the helical curve with pitch 1 on the flux surface labelled by $\psi_0$. Thus $\mathrm{d}\Psi_0^\star/\mathrm{d}r = 0$ when $q = 1$. The helical flux is well adapted to the study of $(1,1)$ perturbations[13]. Indeed, note that the helical flux perturbation is also $\psi_1$, and that $\nabla\psi = \nabla\Psi^\star + q\nabla\psi_0$, so that the parallel gradient now writes

$$\begin{aligned}
\nabla_\parallel f &= \frac{\partial_\varphi f}{R} - q\frac{\nabla\psi_0 \times \hat{\mathbf{z}}}{B_0} \cdot \nabla f - \frac{\hat{\mathbf{z}} \times \nabla f}{B_0} \cdot \nabla \Psi^\star && (2.142)\\
&= \frac{\partial_\varphi f}{R} + \frac{q B_{\theta 0}}{r B_0} \partial_\theta f - \frac{\hat{\mathbf{z}} \times \nabla f}{B_0} \cdot \nabla \Psi^\star && (2.143)\\
&= -\frac{\hat{\mathbf{z}} \times \nabla f}{B_0} \cdot \nabla \Psi^\star && (2.144)\\
&= \frac{\hat{\mathbf{z}}}{B_0} \cdot (\nabla \Psi^\star \times \nabla f), && (2.145)
\end{aligned}$$

since $f = f_0(r) + f_1$ and $f_1 \propto \exp(\gamma t + i(\theta - \varphi))$.

Notice that as a function of the helical flux, the magnetic field is now

$$\mathbf{B} = B_0 \left( \hat{\mathbf{z}} + \frac{r}{R} \hat{\boldsymbol{\theta}} \right) - \nabla \Psi^\star \times \hat{\mathbf{z}}. \tag{2.146}$$

Using the link between $\phi_1$ and $\boldsymbol{v}_1$, this transforms the Ohm's law in the very convenient form

$$\partial_t \Psi^\star + \boldsymbol{v}_1 \cdot \nabla \Psi^\star = \bar{\eta} \nabla_\perp^2 \psi_1, \tag{2.147}$$

or, after linearization,

$$\partial_t \psi_1 + \boldsymbol{v}_1 \cdot \nabla \Psi_0^\star = \bar{\eta} \nabla_\perp^2 \psi_1. \tag{2.148}$$

[13] Evidently the definition of the helical flux can be adapted to any mode numbers. The pitch of the helix just needs to be transformed into $\mathsf{m}/\mathsf{n}$.

Now developing this equation close to the $q = 1$ surface, where $|\nabla\Psi_0^\star| = \mathrm{d}\Psi_0^\star/\mathrm{d}r = (q-1)B_{\theta 0} = r_s B_0(q-1)/Rq$, and with $\boldsymbol{v}_1 \cdot \hat{\boldsymbol{r}} = \gamma\xi_r$, one obtains the first scalar equation:

$$\gamma\psi_1 + \gamma\frac{r_s B_0}{Rq}(q-1)\xi_r = \bar{\eta}\nabla_\perp^2\psi_1. \tag{2.149}$$

Secondly, we use the $\hat{\mathbf{z}}$ component of the curl of the ideal momentum equation, *Eq.* (2.40). Assuming constant density and neglecting the non-linear term, we obtain, since $\nabla\cdot\mathbf{J}$ and $\nabla\cdot\mathbf{B}$ both vanish:

$$\rho_0\partial_t\nabla_\perp^2\phi_1 = \hat{\mathbf{z}}\cdot(\mathbf{B}\cdot\nabla\mathbf{J} - \mathbf{J}\cdot\nabla\mathbf{B}) \tag{2.150}$$

Since the derivatives of $\hat{\boldsymbol{r}}$ and $\hat{\boldsymbol{\theta}}$ have no component in the $\hat{\mathbf{z}}$ direction, the r.h.s. is equal to $\mathbf{B}\cdot\nabla j_z - \mathbf{J}\cdot\nabla B_z = \mathbf{B}\cdot\nabla j_z$. The equilibrium part vanishes, and the perturbed part is linearized into $\mathbf{B}_1\cdot\nabla j_{z,eq} + \mathbf{B}_{eq}\cdot\nabla j_{z1}$. Since $j_{z,eq}$ depends only on $r$, we have

$$\mathbf{B}_1\cdot\nabla j_{z,eq} = -i\frac{\psi_1}{r}\frac{\mathrm{d}j_{z,eq}}{\mathrm{d}r}. \tag{2.151}$$

The other term is

$$\mathbf{B}_{eq}\cdot\nabla j_{z1} = -i\frac{B_0}{Rq}(q-1)\nabla_\perp^2\psi_1. \tag{2.152}$$

Since we are in the layer where the derivatives are large, the first term is of order $(\delta/a)^2$ compared to the second one, and hence it is neglected. Usually, the radial displacement $\xi_r$ is used instead of the stream function $\phi_1$. Since $v_{r1} = \gamma\xi_r$, we have $\phi_1 = i\gamma r B_0\xi_r$. Replacing $\phi_1$ with $\xi_r$, keeping only the highest order derivatives, our second equation reads

$$\gamma^2\rho_0 r\frac{\mathrm{d}^2\xi_r}{\mathrm{d}r^2} = -\frac{B_0}{Rq}(q-1)\frac{\mathrm{d}^2\psi_1}{\mathrm{d}r^2}. \tag{2.153}$$

The last step to obtain the equations valid in the resistive layer is to Taylor expand the $(q-1)$ terms and to normalize the equations. Writing this time $x = (r-r_s)/r_s$, $(q-1)/q \simeq \hat{s}x$, normalizing the growth rate to $\tau_I \equiv R_0/\hat{s}V_A = \tau_A/\hat{s}$ and the flux[14] to $-B_0\hat{s}r_s/R_0$, we obtain

$$\begin{cases} \psi = -x\xi_r + \dfrac{\hat{\eta}}{\lambda}\dfrac{\mathrm{d}^2\psi}{\mathrm{d}x^2} \\[2ex] \lambda^2\dfrac{\mathrm{d}^2\xi_r}{\mathrm{d}x^2} = x\dfrac{\mathrm{d}^2\psi}{\mathrm{d}x^2}, \end{cases} \tag{2.154}$$

where $\psi = -\psi_1 R_0/(B_0 s r_s)$, $\lambda = \gamma\tau_I$ and $\hat{\eta} \equiv \bar{\eta}\tau_I/r_s^2$ characterizes the resistivity. Note that setting $\bar{\eta} = 0$, one recovers *Eq.* (2.122), here $\frac{\mathrm{d}}{\mathrm{d}r}\left(\lambda^2 + x^2\frac{\mathrm{d}}{\mathrm{d}r}\xi_r\right) = 0$.

These equations have been solved and the asymptotic matching carried out in [Ara 1978]. The details can be found in this reference. This yields a resistive growth

[14] Our convention opposite to Ref. [Ara 1978] for the flux in *Eq.* (2.137) leads to a minus sign in the normalization to recover the same equations. Also note that this is not a normalization properly speaking, since here $\psi$ has the same dimension as $\xi_r$, that is, a distance.

rate given by the following implicit equation,

$$\hat{\lambda} = \hat{\lambda}_I \frac{\hat{\lambda}^{9/4}\Gamma\left((\hat{\lambda}^{3/2}-1)/4\right)}{8\Gamma\left((\hat{\lambda}^{3/2}+5)/4\right)}, \tag{2.155}$$

where $\hat{\lambda} = \lambda/\hat{\eta}^{1/3}$, and $\hat{\lambda}_I = \lambda_I/\hat{\eta}^{1/3}$, $\lambda_I = \gamma_I\tau_I$ being the normalized ideal growth rate derived in the preceding subsection.

The Gamma function is defined by

$$\Gamma(x) \equiv \int_0^\infty e^{-t}t^{x-1}\mathrm{d}t. \tag{2.156}$$

and $\Gamma(n+1) = n!$ if $n$ is an integer. *Eq.* (2.155) can be solved numerically, for instance with a Newton method. The solution for $\hat{\lambda}$ is displayed on Fig. 2.5

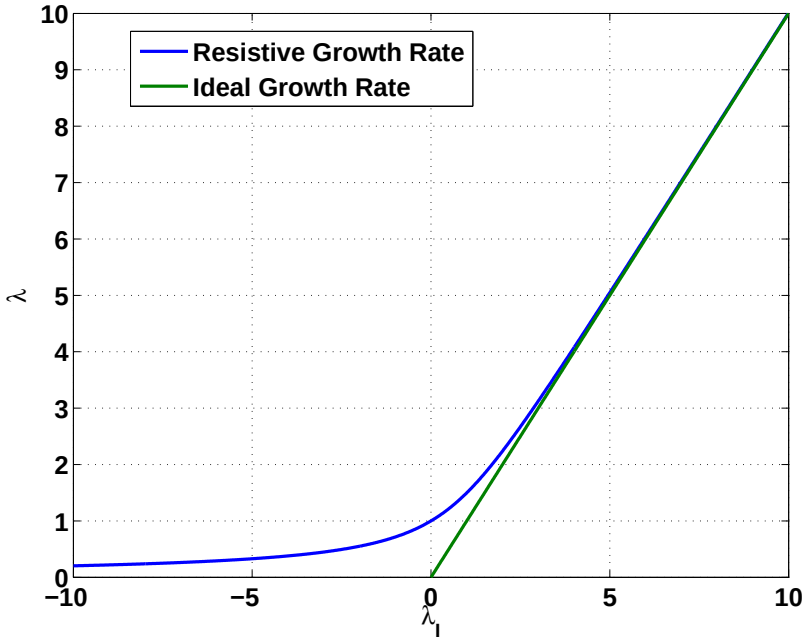


Figure 2.5: Normalized resistive growth rate given by *Eq.* (2.155) as a function of the ideal growth rate.

It is seen that the kink is resistively unstable, $\hat{\lambda} > 0$, even when it is ideally stable, $\hat{\lambda}_I < 0$. At marginal stability, $\lambda_I = 0$, the growth rate, normalized to the fundamental Alfvén time $\tau_A = R_0/V_A$, is

$$\gamma\tau_A = S^{-1/3}\hat{s}^{2/3}\left(\frac{a}{r_s}\right)^{2/3}, \tag{2.157}$$

where $S$ is the Lundquist number, $\hat{s}$ the shear at $q = 1$ and $\varepsilon$ the global inverse aspect ratio. This equation gives the typical order of magnitude of a resistive growth rate,

$\gamma\tau_A \sim 10^{-4} - 10^{-3}$ for typical values of the parameters in Tore Supra. The left part of the curve, $|\hat{\lambda}_I| \gg 1$ and $|\hat{\lambda}_I| < 0$, is usually called the tearing branch, $|\hat{\lambda}_I| < 1$ corresponds to the resistive kink, and $\hat{\lambda}_I \gg 1$ to the limit of ideal kink mode.

### 2.2.4 Bifluid effects on the internal kink mode

The influence of bifluid effects on the internal kink mode have also been studied in [Ara 1978]. The obtained dispersion relation is very similar except that the ion diamagnetic frequency is introduced in the velocity equation and the electron diamagnetic frequency is introduced in the Ohm's law. The derivation is done in appendix D. The result is

$$\begin{cases} \psi = -x\xi_r + \dfrac{\hat{\eta}}{\lambda - i\lambda_e}\dfrac{\mathrm{d}^2\psi}{\mathrm{d}x^2} \\ \\ \lambda\left(\lambda - i\lambda_i\right)\dfrac{\mathrm{d}^2\xi_r}{\mathrm{d}x^2} = x\dfrac{\mathrm{d}^2\psi}{\mathrm{d}x^2}, \end{cases} \tag{2.158}$$

with the same normalizations as before, and $\lambda_i = -\omega_e^\star\tau_I$, $\lambda_e = -\omega_i^\star\tau_I$, with $\omega_e^\star$ and $\omega_i^\star$ the diamagnetic frequencies defined by:

$$\omega_e^\star = -\frac{p'_{e0}(r_s)}{n_e e B_0 r_s} > 0, \quad \omega_i^\star = \frac{p'_{i0}(r_s)}{n_e e B_0 r_s} < 0. \tag{2.159}$$

This system exhibits the same form as *Eq.* (2.154), with the transformation $\lambda^2 \to \lambda\left(\lambda - i\lambda_i\right)$ and $\hat{\eta}/\lambda \to \hat{\eta}/(\lambda - i\lambda_e)$. The essential meaning of the difference between this system of equations and the single fluid case is that in the layer, there is a coupling between the magnetic flux evolution and the velocity of the fluid through the magnetic force $\mathbf{J}\times\mathbf{B}$. In a single fluid approach, the magnetic flux is advected by the global plasma velocity $\boldsymbol{v}$. But the bifluid approach reveals that because of small electron inertia, Ohm's law is nothing but the electron momentum equation, thus the magnetic flux is advected by the electron velocity, which is expressed by *Eq.* (D.2). However momentum is still carried by the heavy ions. Therefore, in the first equation, $\gamma$ is replaced with $\gamma + i\omega_e^\star$ and in the second one, the $\partial_t$ still gives a $\gamma$ contribution, while the link between $\xi_r$ and $\boldsymbol{v}_{i1}$ gives a $\gamma + i\omega_i^\star$ contribution.

The resolution of the asymptotic matching is also carried out in [Ara 1978], the computation is similar to the resistive case, and the solution adopts the same form. The (complex) growth rate is now given by

$$\left(\hat{\lambda}(\hat{\lambda} - i\hat{\lambda}_i)\right)^{1/2} = \hat{\lambda}_I \frac{\Lambda^{9/4}\Gamma\left((\Lambda^{3/2} - 1)/4\right)}{8\Gamma\left((\Lambda^{3/2} + 5)/4\right)}, \tag{2.160}$$

with

$$\Lambda = \left(\hat{\lambda}(\hat{\lambda} - i\hat{\lambda}_i)(\hat{\lambda} - i\hat{\lambda}_e)\right)^{1/3}, \tag{2.161}$$

and $\hat{\lambda} = \lambda/\hat{\eta}^{1/3}$, $\hat{\lambda}_i = \lambda_i/\hat{\eta}^{1/3}$, $\hat{\lambda}_e = \lambda_e/\hat{\eta}^{1/3}$.

The solutions can be studied numerically. Here we give a few limiting cases.

- In the case of marginal stability, $\hat{\lambda}_I = 0$, the non trivial solution is obtained when the numerator is infinite, that is, the argument of the $\Gamma$ function is zero, *i.e.* $\Lambda = 1$:

$$\hat{\lambda}\left(\hat{\lambda} - i\hat{\lambda}_i\right)\left(\hat{\lambda} - i\hat{\lambda}_e\right) = 1. \tag{2.162}$$

  Assuming $T_e = T_i$ for simplicity, and defining $\hat{\lambda}^\star = \hat{\lambda}_i = -\hat{\lambda}_e > 0$, we see that if $\hat{\lambda}^\star \gg 1$, the solution to the preceding equation is $\hat{\lambda} \sim 1/\hat{\lambda}^{\star 2}$. This means the bifluid effects are strongly stabilizing in this case.

- In the limit of very small resistivity, relevant to tokamaks, we will have $|\hat{\lambda}|$, $|\hat{\lambda}_e|$ and $|\hat{\lambda}_i|$ all larger than unity, and the Gamma function can be developed using its properties for large arguments:

$$\frac{\Gamma(z)}{\Gamma(z+a)} \underset{|z|\to\infty}{\sim} z^{-a}. \tag{2.163}$$

  In this case, the dispersion relation reduces to

$$\lambda\left(\lambda - i\lambda_i\right) = \lambda_I^2, \tag{2.164}$$

  the solution of which is

$$\lambda \simeq \lambda_I\left[1 - \frac{\lambda_i^2}{4\lambda_I^2}\right]^{1/2} + i\frac{\lambda_i}{2}. \tag{2.165}$$

  Looking at our ansatz $f_1 \propto e^{\gamma t + i(\theta-\varphi)}$, we see that this means that the imaginary part of the argument is $i\left(-\omega_i^\star/2t + \theta - \varphi\right)$ (since $\lambda_i \propto -\omega_i^\star$). This implies that looking at fixed $\varphi$, the phase is constant if

$$\theta = \frac{\omega_i^\star}{2}t + \theta_0, \tag{2.166}$$

  that is, the mode rotates in the ion direction at half the diamagnetic frequency.

  Also, the real part of $\lambda$, which gives the growth rate, shows that in theory the mode is completely stabilized if $\lambda_i = 2\lambda_I$: Diamagnetic effects are stabilizing and we will indeed observe this stabilization in the simulations (see chapter 4).

In both cases above, large $\hat{\lambda}$ is assumed. However, even at the high Lundquist number relevant to tokamaks, this condition is only marginally satisfied. Indeed, using normalized variables, we have:

$$\hat{\lambda}_i = \frac{1}{2}\frac{\beta\hat{d}_i}{\hat{L}_{pi}}\left(\frac{r_s}{a}\right)^{2/3} S^{1/3}\hat{s}^{-2/3}, \tag{2.167}$$

where $\beta = 2\mu_0 p_0/B_0^2$ is the toroidal beta, $\hat{d}_i = d_i/a$ is the normalized ion skin depth ($d_i = c/\omega_{pi} = \sqrt{m_i/n_e e^2\mu_0}$), $\hat{L}_{pi} = p_{i0}/(R_0 p_i'(r_s))$ is the normalized ion pressure gradient scale length, $\varepsilon = r_s/R_0$, $S$ is the Lundquist number and $\hat{s}$ the shear at $q = 1$. Taking typical Tore Supra ohmic values, $\beta \sim 2\times10^{-3}$, $\hat{d}_i \sim 0.08$, $r_s = 0.3$ m, $a = 0.7$ m, $R_0 = 2.5$ m, $S \sim 2\times10^8$ and $\hat{s} \sim 0.1$, we obtain a quantity of order $\lesssim 1$.

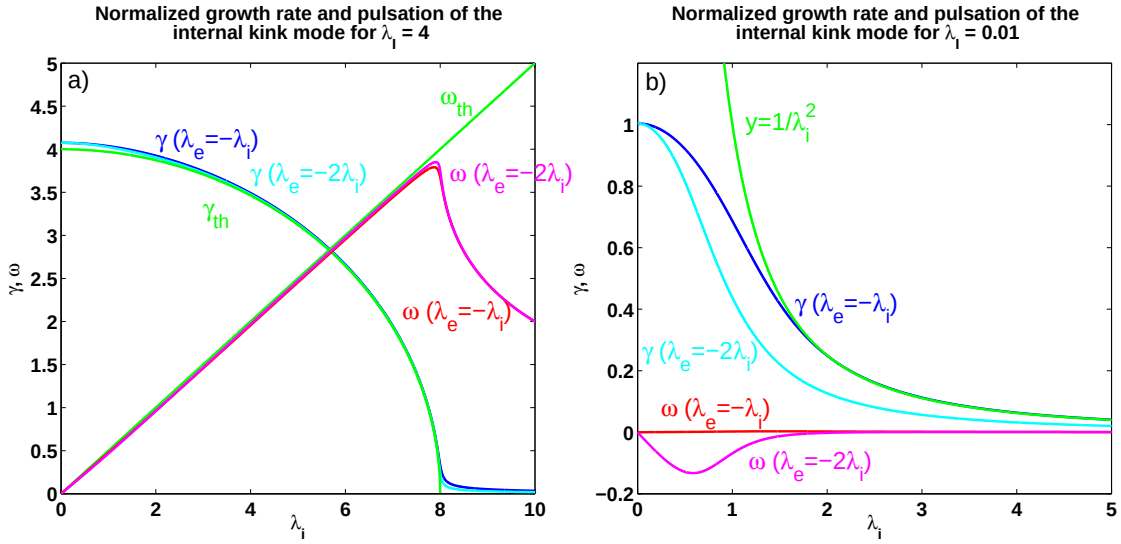


Figure 2.6: Kink mode growth rate and pulsation as a function of $\lambda_i$ and $\lambda_e$, for two values of $\lambda_I$ (strong ideal instability and marginal ideal stability). In green, the two asymptotic cases are plotted.

Some numerical solutions of *Eq.* (2.160) are plotted on Fig. 2.6. They are obtained using Newton's method (see section 3.2.1) applied to the complex plane. The plotted quantities are the normalized, hatted quantities, that is, normalized to $\hat{\eta}^{1/3}$. On panel a), the growth rate and pulsation of the bifluid resistive kink mode are represented as a function of $\lambda_i$ for $\lambda_I = 4$. The blue and red curves represent the case $\lambda_e = -\lambda_i$ (think of it as $T_e = T_i$), whereas the magenta and cyan curves represent the case $\lambda_e = -2\lambda_i$ ($T_e = 2T_i$). The green curves are a plot of *Eq.* (2.165). The curves on panel b) are the same for $\lambda_I = 0.01$, that is, marginal ideal stability[15].

It is seen on panel a) that for strong ideal instability, the pulsation is virtually equal to $\omega_i^\star/2$ in the first phase where stabilization is not full yet. For $\lambda_i > 2\lambda_I$, the growth rate saturates at a small finite value, and the pulsation becomes significantly different from $\omega_i^\star/2$. For strong ideal instability, the electron diamagnetic frequency have a very little effect on both the pulsation and the growth rate.

On panel b), for marginal ideal stability, we see a larger difference when varying the electron diamagnetic frequency. Namely, the stabilization is faster (though still never full) for stronger diamagnetic frequency ($\lambda_e = -2\lambda_i$). The predicted scaling, $\lambda = \lambda^{\star -2}$, correctly fits the blue curve for large $\lambda_i$. The frequency almost vanishes in the case $\lambda_e = -\lambda_i$, whereas it becomes negative (in the direction of $\omega_e^\star$) for $\lambda_e = -\lambda_i$.

There are other important stabilizing effects for the internal kink mode, which are now reviewed.

[15] Strictly speaking, marginal stability is for $\lambda_I = 0$, but the solutions cannot be plotted for $\lambda_I = 0$.

### 2.2.5 Stabilization by the toroidal curvature

The results of section 2.2.3 and section 2.2.4 must be completed by important results in toroidal geometry, derived in 1975 [Bussac 1975] (that is, before the results of [Ara 1978]). It was found that the ideal kink mode is stabilized by the toroidal curvature, so that a certain criterion on the poloidal beta at the $q = 1$ surface, $\beta_{p1}$, must be satisfied for the instability to occur. We have indeed

$$\delta W \propto -(\beta_{p1}^2 - \beta_{pc}^2), \tag{2.168}$$

where

$$\beta_{pc} = 0.3\left(1 - \frac{5r_s}{3a}\right), \tag{2.169}$$

and the poloidal beta at the $q = 1$ surface is defined by

$$\beta_{p1} = \frac{8\pi}{B_\theta(r_s)^2}\left(\langle p\rangle_1 - p(r_s)\right). \tag{2.170}$$

In this expression, $\langle p\rangle_1$ is the volume average of the pressure within the $q = 1$ surface. Since the mode is unstable when $\delta W < 0$, $\beta_{p1} > \beta_{pc}$ is required for the kink to be unstable. Then resistive and bifluid effects modify the value of the critical beta, $\beta_{pc}$, so that smaller $\beta_{p1}$ can be unstable, but that explains why tokamak plasmas with $q < 1$ can be observed to be stable. Also, notice that the cylindrical result (where there is no critical poloidal beta, or in other words $\beta_{pc} = 0$) is not recovered in the limit $a/R_0 \to 0$.

### 2.2.6 Stabilization by trapped fast particles and sawtooth triggering

To address the final question of sawtooth triggering, the question of the effect of a population of fast particles remains to be tackled. Fast or suprathermal particles are particles which have their velocity much larger than the thermal velocity. They always exist in the tail of a Maxwellian distribution but here we are interested in the case where the distribution function of such particles is well above the Maxwellian distribution level. These populations can have several origins:

- The 3.5 MeV $\alpha$ particles generated by the fusion reactions
- The fast particles generated by the Neutral Beam Injector (1 MeV in ITER)
- The fast particles generated by other additional heating methods, such as Ion Cyclotron Resonant Heating (ICRH).

The fast particles add a separate contribution $\delta W_f$ to the MHD potential energy, which is usually stabilizing in standard conditions [Porcelli 1991, Coppi 1990]. They have been originally studied in Refs. [Chen 1984, White 1989, Coppi 1989] There is also a contribution of the collisionless thermal trapped particles, called Kruskal-Oberman term [Kruskal 1958], and the total potential energy is written

$$\delta W = \delta W_{MHD} + \delta W_{KO} + \delta W_f, \tag{2.171}$$

and $\delta W_{MHD}$ is the purely MHD contribution, including the effects of toroidal curvature and possibly other geometrical effects.

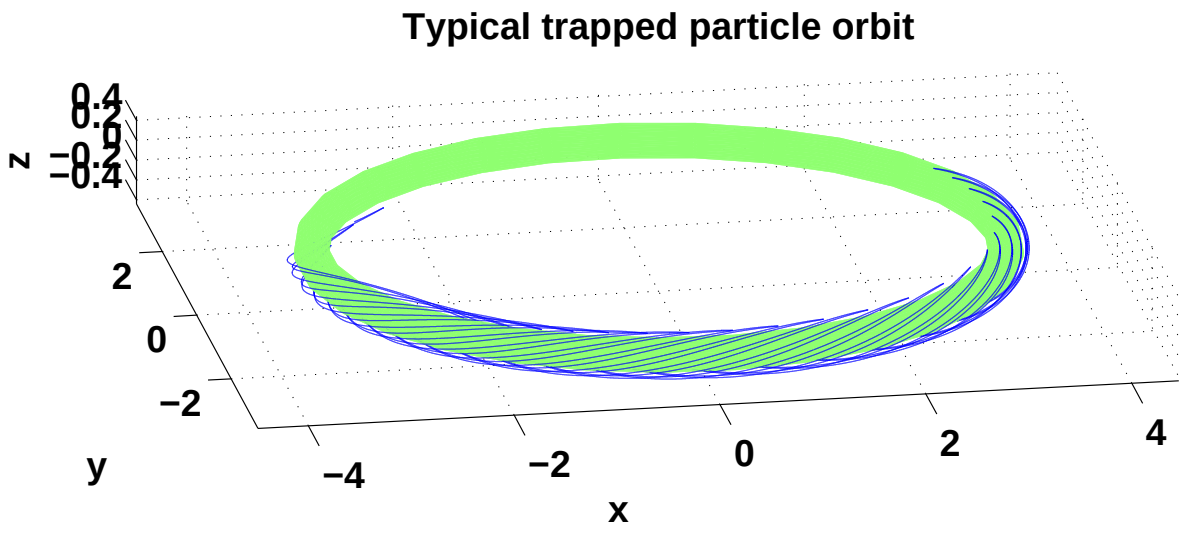


Figure 2.7: Typical orbit of a trapped particle in a tokamak. A slow toroidal precession (from the right to the left) is observed on top of the bounce motion. The fast cyclotron motion is averaged out.

We can give a heuristic explanation of the effect of fast particles on the MHD stability. In addition to their bounce motion describing the banana orbits described in the introduction, trapped particles undergo a drift motion in the toroidal direction, at the drift pulsation $\omega_D$ (see Fig. 2.7). This frequency is of the order of $\rho v_t/(aR_0)$, where $\rho$ is the Larmor radius of the particle. Because of the small factor $\rho/a$, it is sufficiently small that it can compete with the characteristic frequencies of MHD instabilities[16]. There are two mechanisms of interaction of trapped particles with these instabilities:

- A resonant or kinetic part (also called non-adiabatic) coming from the fact that particles and waves can exchange energy at the resonance, that is, if the mode pulsation $\omega$ is sufficiently close to the drift pulsation $\omega_D$.
- A non-resonant or fluid part (also called adiabatic) linked with the adiabatic conservation of the third motion invariant associated to the toroidal drift motion, $\mathcal{P}_\varphi = mB_\varphi v_\parallel/B - Ze\psi$ ($m$ is the ion's mass, $Z$ its charge number and $\psi$ the poloidal flux), for particles with $\omega_D \gg \omega$.

The second one can be interpreted as follows [Porcelli 1991]. The third invariant of motion $\mathcal{P}_\varphi$ is closely related to the poloidal flux through the current loop corresponding to the particle's bounce-averaged toroidal motion. Since this flux is adiabatically conserved,

[16] It is actually of the same order of magnitude as the diamagnetic frequency, $\omega^\star \sim (T/eB)(T'/r_sT) = (\sqrt{Tm}/eB)(\sqrt{T/m}/rL_T) = (\rho/a)(v_t/L_T)$, and $L_T$, the temperature gradient length, is of the order of the minor radius.

when **B** varies adiabatically due to the mode's perturbation, the radius of the current loop will slowly adjust (either contract or expand). The resulting mean displacement of the particle can be interpreted as a work done against the trapped particle's pressure, hence the mode gains or loses energy in the process. In general, the effect of trapped particles $\delta W_{KO}$ and the contribution of the fast trapped particles to $\delta W_f$, is stabilizing, which means the terms are positive.

In the following, we normalize $\delta W$ so that $\gamma\tau_A = -\delta\hat{W}$. Going back to the growth rate's expression, *Eq.* (2.127), we see that we must take:

$$\delta\hat{W} = \frac{\mu_0 R_0}{2\pi\hat{s}B_0^2 r_s^2\xi^2}\delta W. \tag{2.172}$$

Heuristic criteria for sawtooth triggering are given in Ref. [Porcelli 1996]. They are briefly explained here. The reader may refer to this reference for more details and a prediction of the sawtooth period in ITER. Regarding the fast trapped particles, they are sufficient to stabilize when they complete many toroidal orbits during a characteristic time of the instability, that is, if $\omega_D \gg -\delta\hat{W}_{core}$, where $\delta\hat{W}_{core} \equiv \delta\hat{W}_{MHD} + \delta\hat{W}_{KO}$ is the thermal contribution. Conversely, when $-\delta\hat{W}_{core}$ is too large, the fast particles are not sufficient to stabilize the mode. Hence the crash is triggered when

$$-\delta\hat{W}_{core} > c_1\omega_D\tau_A, \tag{2.173}$$

where $c_1$ is a dimensionless parameter depending on the profiles and on the fast particles' concentration. For ITER standard conditions and looking at $\alpha$ particles, $c_1$ is of order 1.

Secondly, consider that when the total $\delta\hat{W}$ is large and negative, the physics inside the resonant layer is not sufficient to stabilize the mode. The dominant effects playing a role in the layer are the diamagnetic effects, with relevant parameter $\omega_i^\star\tau_A$ and the finite Larmor radius effects, where the relevant parameter is the normalized Larmor radius, $\hat{\rho} = \rho/a$. Thus the kink is unstable when[17]

$$-\delta\hat{W} > \max(\omega_i^\star\tau_A, \hat{\rho}). \tag{2.174}$$

Finally, when on the contrary $|\delta W|$ is small, $-\hat{\rho} < -\delta\hat{W} < \max(\omega_i^\star\tau_A, \hat{\rho})$, the mode will be unstable unless the diamagnetic effects are large enough to stabilize the mode (*cf.* section 2.2.4). This happens typically when $\omega_i^\star$ is equal to a few times the mode's growth rate obtained at $\omega_i^\star = 0$. Thus a last criterion for instability is

$$-\hat{\rho} < -\delta\hat{W} < \max(\omega_i^\star\tau_A, \hat{\rho}) \quad \text{and} \quad \omega_i^\star < c_3\gamma, \tag{2.175}$$

with $c_3 \sim 2-4$. Here $\gamma$ is not the ideal growth rate we have derived but the growth rate obtained in the so-called ion-kinetic regime [Pegoraro 1989], where ion temperature is high and hence finite Larmor radius effects important. The criterion (2.175) can be transformed in a criterion on the magnetic shear at $q = 1$, $\hat{s}$. The kink is unstable if

$$\hat{s} > \hat{s}_{crit} = \alpha\left(S^{1/3}\hat{\rho}\right)^{1/2}\left(\frac{\beta_1 R^2}{r_s^2}\right)^{7/12}\frac{r_s}{L_n}\left(\frac{r_s}{L_p}\right)^{1/6}, \tag{2.176}$$

[17] The reader will find a factor $1/2$ in Ref. [Porcelli 1996] in front of the diamagnetic term, but we do not want to discuss order of unity factors here.

where $\alpha$ is a parameter of order 1, $S$ is the Lundquist number, $\beta_1$ the toroidal beta at $q = 1$, $L_n = (\partial_r n/n)^{-1}$ and $L_p = (\partial_r p/p)^{-1}$ are respectively the density and pressure gradient lengths. In the Porcelli paper, these rules, *Eqs.* (2.173–2.175) are used to predict the sawtooth period in ITER. A "natural" sawtooth period of 1 to 10 s is obtained, while it is predicted that in presence of fast particles, the period could be between 10s and 1000 s.

### 2.2.7 Sawtooth control with ICRH

We anticipate a little bit over section 5.2 where the phenomenology of sawteeth is presented to give an example of application of the influence of fast particles on MHD stability. It will be seen in section 5.2.5 that long sawteeth, often called monster sawteeth, are extremely keen to trigger confinement degrading NTMs. On ITER, NTMs and their mode locking are really a source of concern, because this may lead to disruptions [Wesson 1989], and major disruptions are virtually intolerable in ITER. Thus it seems better to destabilize sawteeth to obtain frequent and less deleterious crashes.The concepts of the preceding subsection can be used to control the sawtooth period. One of the most obvious is to act on the current, as one of the criteria of sawtooth instability says that increasing the magnetic shear makes the internal kink more unstable, *Eq.* (2.176). However these means can be quite expensive in terms of power consumption, and this would amount to reduce the power efficiency of a reactor. Fortunately, there is an other mechanism which is less power consuming. Note that when addressing the influence of energetic particles on the internal kink mode stability, we overlooked the contribution of passing particles. A lot of efforts have been undertaken to model precisely the influence of these particles on the internal kink mode. As for the trapped particles, the analytical theory is rather involved (see in particular Refs. [Graves 2004, Graves 2009, Graves 2010]) and out of the scope of this manuscript. However we can attempt to give a hint as to why energetic passing particles matter. A quite convincing overview of the physics at stake can be found in section 2 of Ref. [Chapman 2011].

Regarding the contribution of passing particles, it has been found that barely passing particles (particles which are close to the trapped/passing boundary in phase space), the orbits of which have large radial extension (the radial extension also increases with the energy of the particle), are able to destabilize the sawtooth if there is an asymmetry of the distribution in the parallel velocity $v_\parallel$, such that there are more particles in the co-passing direction (the direction of the current), than in the opposite counter-passing direction. To get a grasp as to why such an effect is possible, consider that the distribution function in velocity space can be written as a function of three invariants which are exact invariants for the equilibrium Hamiltonian, the energy $\mathcal{E}$, the magnetic momentum $\mu$ and the third invariant $\mathcal{P}_\varphi = mB_\varphi v_\parallel/B - Ze\psi$. When the Hamiltonian is perturbed, so are these quantities.Consider the perturbation of the particle's energy $\delta\mathcal{E}$. It can be written:

$$\delta\mathcal{E}(t) = Ze\int_{-\infty}^{t} \boldsymbol{v}\cdot\delta\mathbf{E}\mathrm{d}t', \tag{2.177}$$

where $\delta\mathbf{E}$ is the perturbed electric field due to the mode. Now since the structure of

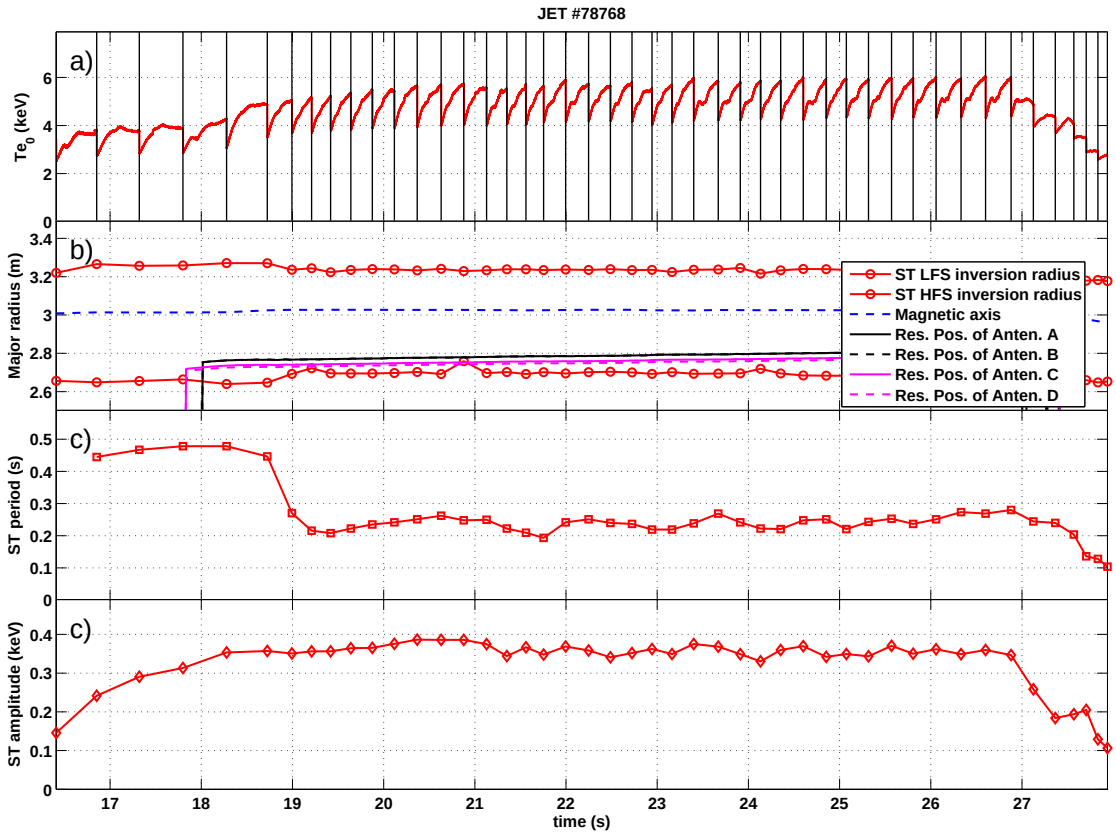


Figure 2.8: Demonstration of sawtooth control on JET pulse #78768. Core temperature (a), location of inversion radii of the sawtooth, magnetic axis, and ICRH resonance position (b), sawtooth period (c) and amplitude of the sawtooth crash (d).

the electric field derives from that of the MHD displacement $\boldsymbol{\xi}$, it is large in the inside of the $q = 1$ surface, and small outside, and we see that a passing particle which has an orbit width larger than the width of the mode's inertial region on $q = 1$ will have a non-vanishing contribution in the energy, *Eq.* (2.177), hence positive or negative work will be done on the passing particles, which can stabilize or destabilize the mode. We also see that co-passing and counter-passing particles will have opposite contributions (if their trajectory is really symmetric with respect to the $q = 1$ surface), hence the need for an asymmetry in the co/counter-passing directions.

It is possible to generate such distributions using ICRH minority heating[18], that is, heating an ion species present in the plasma in small concentration, typically $^1$H or $^3$He with a concentration of the order of 1%.

On ITER, it is thought that about 10 MW of ICRH minority heating, combined with other more conventional ways of destabilizing the sawtooth, will be sufficient to decrease the sawtooth period below the threshold of NTM triggering [Chapman 2013].

[18] Heating the main ions with ion cyclotron waves is impossible because the component of the wave which rotates in the same direction as the ions vanishes at the resonance for the main ions.

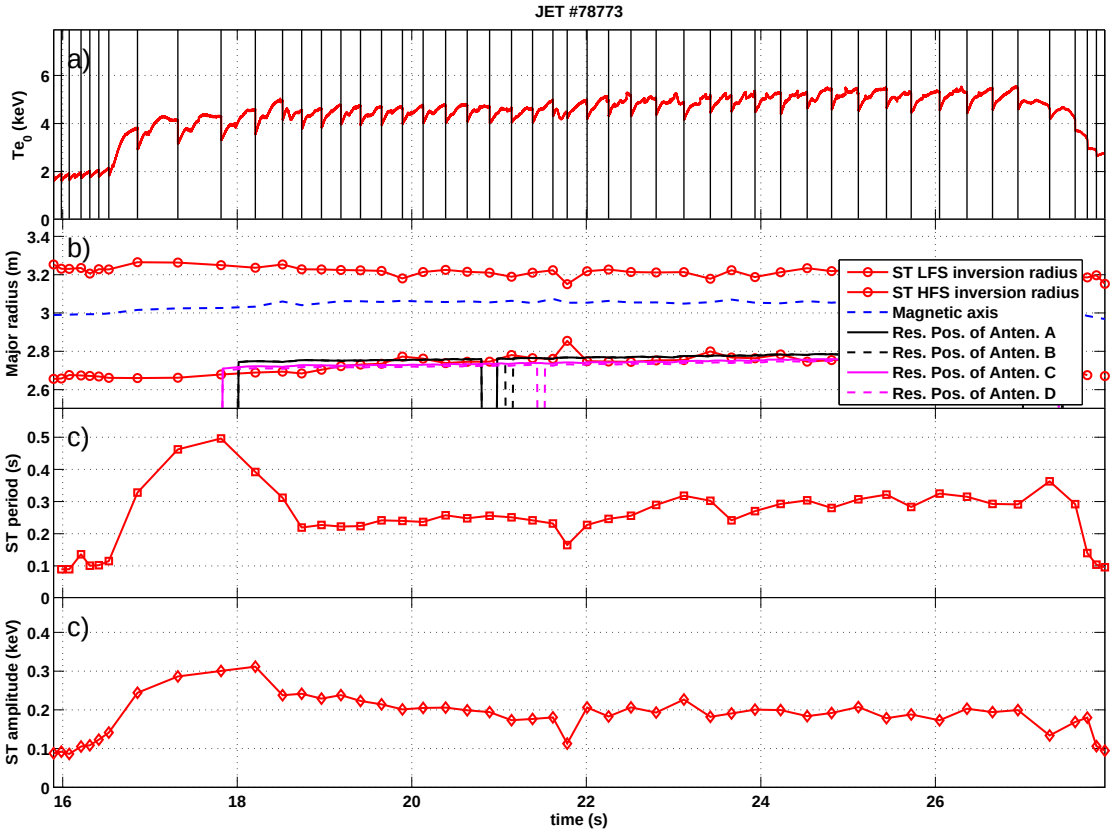


Figure 2.9: Demonstration of sawtooth control on JET pulse #78773 in H-mode. Core temperature (a), location of inversion radii of the sawtooth, magnetic axis, and ICRH resonance position (b), sawtooth period (c) and amplitude of the sawtooth crash (d).

Notice that this threshold is an empirical one [Chapman 2010a] and should be taken with caution when extrapolating to ITER. First demonstration of principle on JET used minority heating of $^3$He with the resonance position on the HFS [Graves 2012]. The ICRH wave was launched in the counter-current direction, which in theory should shorten the sawtooth. A good control was demonstrated, as seen on Fig. 2.8. In the absence of a precise measurement of the safety factor profile, the $q = 1$ surface is determined from the inversion radius of the sawtooth on the ECE profiles. After NBI is switched on (before the first time displayed on the figure), the sawtooth period is increased and reaches a steady value of about 500 ms. At around $t = 18$ s, ICRH is switched on, and it can be seen (panel(b)) to be located very close to the $q = 1$ surface, just inside. The effect on the sawtooth period can be immediately seen. It drops and stabilizes to 200 ms, which is only twice as much as the ohmic value. JET pulse #78768 is an L-mode discharge, and the control should be also demonstrated in H-mode. In JET pulse #78773, the NBI is increased from 4.8 to 6.4 MW, which triggers a transition to H-mode. The result can be seen on Fig. 2.9, which displays exactly the same features as Fig. 2.8. When the current is generated in the opposite direction, on the contrary, longer sawteeth are obtained, and

eventually NTM triggering can be observed.

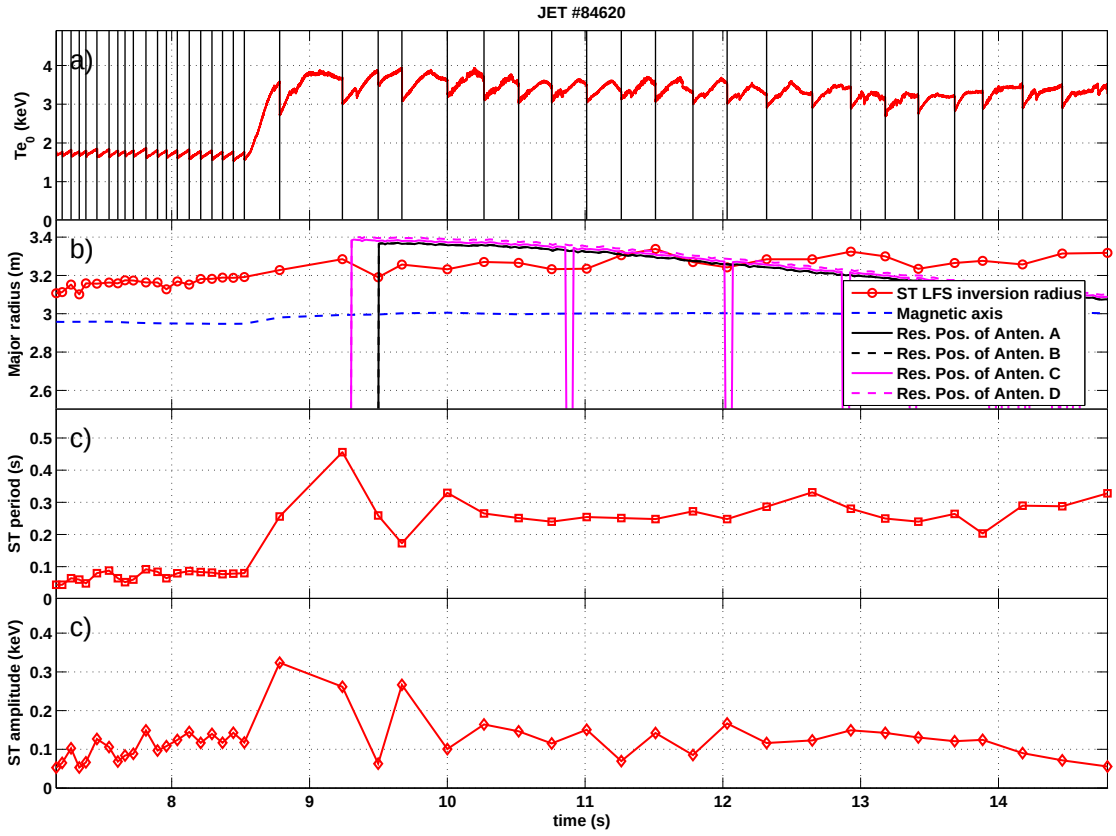


Figure 2.10: sawtooth control on JET pulse #84620 in H-mode. Core temperature (a), location of inversion radii of the sawtooth, magnetic axis, and ICRH resonance position (b), sawtooth period (c) and amplitude of the sawtooth crash (d).

However, these first experiments were not fully relevant to ITER because on ITER, the HFS will not be reachable by ICRH waves for minority heating. Only the LFS $q = 1$ surface will be reachable, and thus control must be demonstrated with ICRH on the LFS. Such experiments are currently ongoing on JET. It is too soon to draw a definitive conclusion, but the first results are encouraging, as shown on Fig. 2.10. We see that now the resonance position is on the LFS, and again, the reduction of the sawtooth period after the ICRH wave is launched can be observed. The preliminary results seem to indicate that the resonance position does not need be as close to the $q = 1$ surface as predicted by theory. Indeed, on panel (b), we see that the control of the sawtooth period is maintained even when the resonance position is separated from the $q = 1$ surface by $\pm 20$ cm.

Before concluding on the internal kink mode, we close this chapter with a few basic principles on magnetic reconnection, which will be useful in the following.

## 2.3 Magnetic reconnection

### 2.3.1 Formal reconnection criterion

We have already said that when the electric field is given by ideal Ohm's law $\mathbf{E}+\boldsymbol{v}\times\mathbf{B}=0$, two fluid elements initially on a given field line stay on that field line for ever. This has a very important consequence: there can be no breaking of field lines. If initially the magnetic field has a given topology separating the plasma in different regions which are not interconnected, then this separation must endure during the dynamical evolution of the plasma. When this topological condition is not met, field lines can break and reconnect. There are many examples of magnetic reconnection in astrophysical and laboratory plasmas. It is thought to be the source of heat in the solar corona, much hotter than the solar surface, and is probably linked to the physics of solar flares and the related coronal mass ejection. There is magnetic reconnection at the interface between the solar wind and the magnetosphere of the Earth. In fusion laboratory plasmas, sawteeth seem to always involve magnetic reconnection, though not always complete. In general, as soon as a magnetic island can be observed, like in the case of tearing modes for instance, there must have been magnetic reconnection, since the topology of the magnetic field is changed.

In the present case of interest, the sawtooth instability, we have seen that the lowest order plasma motion in the $q<1$ region is a rigid helical shift. In the same time, the $q>1$ region does not move, so that inner magnetic flux surfaces are pressed toward the $q=1$ surface, creating a current sheet there[19]. In this current sheet, the ideal Ohm's law, *Eq.* (2.43), will not be valid anymore, and non-ideal effects will cause magnetic reconnection.

A formal criterion for reconnection can actually be derived. Formally, let us denote by $\mathcal{P}$ the proposition:

*There cannot be any field line breaking in the magnetic field evolution.*

The negation of $\mathcal{P}$, $\neg\mathcal{P}$, can be written

*There is, at some point in space and time, field line breaking (reconnection) during the magnetic field evolution.*

It can be quite easily demonstrated (see [Hornig 1996]) that

$$\mathcal{P} \Longleftrightarrow \exists(\sigma,\boldsymbol{u}),\ \partial_t\mathbf{B}+\boldsymbol{u}\cdot\nabla\mathbf{B}-\mathbf{B}\cdot\nabla\boldsymbol{u}=\sigma\mathbf{B}. \tag{2.178}$$

This is demonstrated using generating functions for the field $\mathbf{B}$ and the flow $\boldsymbol{u}$ advecting the field line.

The condition $\nabla\cdot\mathbf{B}=0$ leads to the condition on the couple $(\sigma,\boldsymbol{u})$:

$$\mathbf{B}\cdot\nabla\left(\sigma-\nabla\cdot\boldsymbol{u}\right)=0. \tag{2.179}$$

[19] Notice that the current between two flux surfaces labeled by the fluxes $\psi_1$ and $\psi_2$ and separated by a distance $l$ is proportional to $(\psi_2-\psi_1)/l^2$. If one surface is rigidly shifted so that the distance between them is decreased, the current will also increase.

Let us denote by $\mathcal{K}$ the space of such fields. Using this notation and the curl of the cross product, we have

$$\mathcal{P} \iff \exists(\sigma, \boldsymbol{u}) \in \mathcal{K},\ \partial_t \mathbf{B} + \boldsymbol{u} \cdot \nabla \mathbf{B} - \mathbf{B} \cdot \nabla \boldsymbol{u} = \sigma \mathbf{B} \tag{2.180}$$

$$\iff \exists(\sigma, \boldsymbol{u}) \in \mathcal{K},\ \partial_t \mathbf{B} = \nabla \times (\boldsymbol{u} \times \mathbf{B}) + \mathbf{B}\,(\sigma - \nabla \cdot \boldsymbol{u}) \tag{2.181}$$

$$\iff \exists(\sigma, \boldsymbol{u}) \in \mathcal{K},\ \mathbf{E} + \boldsymbol{u} \times \mathbf{B} = \mathbf{S}, \text{ where } \nabla \times \mathbf{S} = -\mathbf{B}\,(\sigma - \nabla \cdot \boldsymbol{u})\,, \tag{2.182}$$

where we see the link with Ohm's law appear. So a criterion for reconnection is

$$\neg\mathcal{P} \iff \forall(\sigma, \boldsymbol{u}) \in \mathcal{K}, \mathbf{E} + \boldsymbol{u} \times \mathbf{B} \neq \mathbf{S}, \text{ where } \nabla \times \mathbf{S} = -\mathbf{B}\,(\sigma - \nabla \cdot \boldsymbol{u}) \tag{2.183}$$

### 2.3.2 Application to special cases of Ohm's law

Now we can demonstrate that if Ohm's law is of the form

$$\mathbf{E} + \boldsymbol{v} \times \mathbf{B} = \nabla_\parallel F, \tag{2.184}$$

with $F$ any scalar quantity, there is no reconnection possible. Indeed let $\boldsymbol{v}' \equiv (\mathbf{B} \times \nabla_\perp F)/B^2$, $\boldsymbol{u} \equiv \boldsymbol{v} + \boldsymbol{v}'$, $\sigma \equiv \nabla \cdot (\boldsymbol{v} + \boldsymbol{v}')$, then Ohm's law is

$$\mathbf{E} + \boldsymbol{u} \times \mathbf{B} = \nabla F, \tag{2.185}$$

Obviously $(\sigma, \boldsymbol{u}) \in \mathcal{K}$, and $\mathbf{S} \equiv \nabla F$ verifies the condition $\nabla \times \mathbf{S} = -\mathbf{B}\,(\sigma - \nabla \cdot \boldsymbol{u})$.

In section 2.1.8 we have seen that when bifluid effects are added to the MHD model, an additional term $-\nabla_\parallel p_e / n_e e$ appears in Ohm's law. As we will see, it is able to modify the dynamics of reconnection. We would like to know if this term leads to reconnection by itself or is only responsible for a change of topology. Neglecting resistivity, the Ohm's law is:

$$\mathbf{E} + \boldsymbol{v} \times \mathbf{B} = -\frac{\nabla_\parallel p_e}{n_e e}. \tag{2.186}$$

If there is no polytropic relation between $p_e$ and $n_e$, then the r.h.s cannot be *a priori* put in the form of a parallel gradient, and there can be reconnection. However the criterion needs to be checked properly. It appears that it is much easier to demonstrate that an Ohm's law does freeze magnetic field lines than the opposite. Indeed the latter case, (showing that there is reconnection) requires to check all the fields $(\sigma, \boldsymbol{u}) \in \mathcal{K}$. This is probably a difficult problem and we will not attempt to solve it.

### 2.3.3 Biskamp's criterion

We would like to point out a possible mistake, or at least misleading statement, in Ref. [Biskamp 2000]. It is said[20] (equation (2.35)) that "a formal criterion for reconnection is

$$\mathbf{B} \times \nabla \times \mathbf{R}_\parallel \neq 0. \tag{2.187}$$

[20] Only changing the notations.

Here $\mathbf{R}_\parallel = R_\parallel \mathbf{b}$ is the parallel component of the nonideal part in Ohm's law, since the perpendicular component can always be incorporated in the general velocity $\boldsymbol{u}$ by writing $\mathbf{R}_\perp = \boldsymbol{u}' \times \mathbf{B}$, $\boldsymbol{u} = \boldsymbol{v} - \boldsymbol{u}'$."

This is misleading because this is only a necessary condition to have reconnection. Indeed, let Ohm's law be written in the most general way as

$$\mathbf{E} + \boldsymbol{v} \times \mathbf{B} = \mathbf{R}. \tag{2.188}$$

It is true that we can write $\mathbf{R}_\perp = \boldsymbol{u}' \times \mathbf{B}$ with $\boldsymbol{u} = \boldsymbol{v} - \boldsymbol{u}'$ and obtain

$$\mathbf{E} + \boldsymbol{u} \times \mathbf{B} = \mathbf{R}_\parallel. \tag{2.189}$$

Now supposing that $\mathbf{B} \times \nabla \times \mathbf{R}_\parallel = 0$, there exists $(\sigma, \mathbf{w}) \in \mathcal{K}$ such that $\mathbf{E} + \mathbf{w} \times \mathbf{B} = \mathbf{S}$ with $\mathbf{S}$ the solution to $\nabla \times \mathbf{S} = -\mathbf{B}\,(\sigma - \nabla \cdot \mathbf{w})$. Indeed, since $\mathbf{B} \times \nabla \times \mathbf{R}_\parallel = 0$, there exists $\lambda$ such that $\nabla \times \mathbf{R}_\parallel = \lambda \mathbf{B}$, and $\mathbf{w} = \boldsymbol{u}$, $\sigma = \nabla \cdot \mathbf{w} - \lambda$, $\mathbf{S} = \mathbf{R}_\parallel$ is a solution. Therefore we can safely write

$$\mathbf{B} \times \nabla \times \mathbf{R}_\parallel = 0 \implies \mathcal{P}, \tag{2.190}$$

and hence

$$\neg\mathcal{P} \implies \mathbf{B} \times \nabla \times \mathbf{R}_\parallel \neq 0. \tag{2.191}$$

However the reciprocal is not true, as can be seen with the counterexample of *Eq.* (2.184), since there exists a scalar function[21] $F$ such that $\mathbf{B} \times \nabla \times \nabla_\parallel F \neq 0$, and for which there is no reconnection ($\mathcal{P}$ is true).

To conclude, we can say that only non-potential parallel electric fields (parallel fields which cannot be put in the form of $\nabla_\parallel F$) can lead to reconnection, but *a priori* not all such fields do so. This condition seems quite restrictive and makes the omnipresence of reconnection in both astrophysical and laboratory plasmas interesting.

### 2.3.4 Sweet-Parker scaling of reconnection

The most well-known and easiest paradigm of reconnection is the Sweet-Parker mechanism [Sweet 1958, Parker 1963]. It is instructive to derive its main features. Reconnection is supposed to occur only in small regions of space where field gradients become important, giving rise to localized current sheets. Such sheets arise quite naturally in MHD. We will see for instance that the kink instability is characterized by a radial displacement which at lowest order is constant in a region of space and vanishing in an other one. Thus a region is projected against the other, carrying the magnetic flux with it and increasing significantly its gradients. The sheet tends to be elongated in one direction, thus it is characterized by a length $2L$ and a thickness $2\delta \ll 2L$. Since the current sheet arises from the flux advection by the flow, it is natural to take the inflow velocity $\boldsymbol{v}_i$ perpendicular to the longitudinal direction (along $L$) and the magnetic field $\mathbf{B}_i$ parallel to it. We aim at determining the thickness $\delta$ as a function of the macroscopic length $L$. This involves computing the outflow velocity $\boldsymbol{v}_o$ and magnetic field $\mathbf{B}_o$. Fig. 2.11 shows

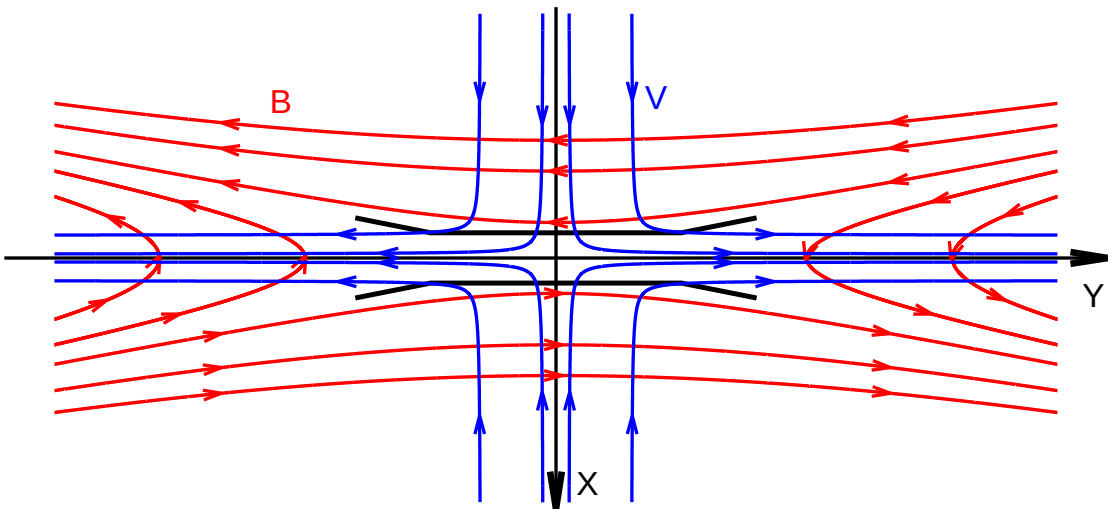


Figure 2.11: Structure of a Sweet-Parker current sheet. Streamlines (blue) and magnetic field lines (red). Away from the current sheet in the center, ideal MHD is valid and the flow carries the field lines with itself.

the basic structure of the flow and magnetic field. The inflow velocity $\boldsymbol{v}_i$ is in the $\hat{\boldsymbol{x}}$ direction, the outflow $\boldsymbol{v}_o$ in the $\boldsymbol{e}_y$ direction. The inflow field $\mathbf{B}_i$ is dominantly in the $-\boldsymbol{e}_y$ direction and the outflow field $\mathbf{B}_o$ in the $\hat{\boldsymbol{x}}$ direction (on the $x = 0$ line). Opposing magnetic field lines are reconnected and taken away by the flow in the sheet. The current in the sheet is in the plane perpendicular to the figure, along $\hat{\mathbf{z}}$. The center of the sheet is a null point of the reconnecting magnetic field, it vanishes. It is also a stagnation point for the flow. Here we are considering a steady reconnection process, that is, independent of time. For such a thing to be possible, the electric field $\mathbf{E}$ must be uniform on the domain[22], owing to $\partial_t \mathbf{B} = -\nabla \times \mathbf{E}$. In the Sweet-Parker model, Ohm's law is purely resistive, $\mathbf{E} + \boldsymbol{v} \times \mathbf{B} = \eta \mathbf{J}$. Hence away from the sheet where the current is small, Ohm's law yields the scaling $E = v_i B_i$, while at the center of the sheet where the field vanishes, it gives $E = \eta j$, and using Ampère's law, the current is roughly $B_i/\mu_0 \delta$. This gives $\delta$ as a function of the inflow velocity,

$$\delta = \bar{\eta}/v_i. \tag{2.192}$$

Secondly, using mass conservation across the sheet directly yields

$$L v_i = \delta v_o. \tag{2.193}$$

Finally, the momentum conservation equation must be used. It is written

$$\rho\,(\boldsymbol{v} \cdot \nabla \boldsymbol{v}) = \mathbf{J} \times \mathbf{B} - \nabla p. \tag{2.194}$$

In the $\hat{\boldsymbol{x}}$ direction, magnetic tension and inertia can be neglected because of the small curvature of the field lines and we expect the outflow to be enhanced by the consumption

[21] Check for instance that $F = B^2/2$ yields, using $\mathbf{J} \times \mathbf{B} = \nabla_\perp p$ and $\nabla_\perp \left(p + B^2/2\mu_0\right) = B^2 \boldsymbol{\kappa}$, and the smallness of $\beta$: $\mathbf{B} \times \nabla \times \nabla_\parallel B^2/2 = B^2 \nabla_\perp \nabla_\parallel B - \mu_0 \nabla_\perp p \nabla_\parallel B \simeq B^2 \nabla_\perp \nabla_\parallel B \neq 0$.

[22] At least its curl must vanish.

of magnetic energy in the sheet. Thus $\mathbf{J} \times \mathbf{B} = -\nabla B^2/2\mu_0$ and integration from the outer region to the center of the sheet where the magnetic field vanishes, and denoting $p_i$ the inflow pressure and $p_N$ the pressure at the neutral point, we have

$$p_N = p_i + \frac{B_i^2}{2\mu_0}. \tag{2.195}$$

Integrating along the sheet in the $\boldsymbol{e}_y$ direction, now the magnetic force is given by $(\mathbf{J} \times \mathbf{B})_y = jB_x$, with $j = B_i/\mu_0\delta$. The momentum equation can be written

$$\rho v_y \partial_y v_y = jB_x - \partial_y p. \tag{2.196}$$

This equation can be evaluated at a point half-way along the sheet ($y = L/2$), where $v_y \sim v_o/2$, $\partial_y v_y \sim v_o/L$, $B_x \sim B_o/2$, $-\partial_y p \sim -(p_o - p_N)/L = B_i^2/(2\mu_0 L)$, which gives

$$\begin{aligned} \rho \frac{v_o}{2}\frac{v_o}{L} &= \frac{B_i B_o}{2\mu_0\delta} + \frac{B_i^2}{2\mu_0 L} \\ &= \frac{B_i^2}{2\mu_0 L}\left(1 + \frac{B_o L}{B_i \delta}\right). \end{aligned} \tag{2.197}$$

Using $B_o/\delta + B_i/L \sim \nabla \cdot \mathbf{B} = 0$ yields the outflow velocity, which we write in terms of the initial Alfvén velocity $v_{Ai} = B_i/\sqrt{\mu_0\rho}$:

$$v_o = \sqrt{2} v_{Ai}. \tag{2.198}$$

Here the $\sqrt{2}$ factor comes from the combined effect of pressure and magnetic forces. Some authors give the pressure force as the basic mechanism for acceleration along the sheet (see [Biskamp 2000] for example), whereas both effects have comparable amplitudes.

In the process, the magnetic field amplitude is reduced by a factor $\delta/L$, while the velocity is enhanced by $L/\delta$. Using *Eqs.* (2.192) and (2.193), we find the scaling of the sheet width $\delta$ as a function of the macroscopic quantities and the resistivity (omitted the factor $\sqrt{2}$ for convenience):

$$\delta \sim \sqrt{\frac{\bar{\eta} L}{v_{Ai}}}. \tag{2.199}$$

Defining the magnetic Reynolds number $R_{mi} \equiv L v_{Ai}/\bar{\eta}$, we have

$$\frac{\delta}{L} \sim R_{mi}^{-1/2}. \tag{2.200}$$

We see that in this Sweet-Parker model, the outflow velocity is given by the reconnecting field amplitude, and the inflow velocity, which sets the flux reconnection rate, is fixed by the outflow velocity and the resistivity. The square root scaling with $R_{mi}$ implies that in this model reconnection is quite slow, since $R_{mi}$ is quite large in tokamaks, typically $10^3 - 10^4$ (taking the poloidal field in the Alfvén velocity).

We will see in section 4.1.3 the time scale of complete reconnection of the $q < 1$ region of the tokamak implied by the Sweet-Parker model, and in section 5.2.3 the comparison to the experiments will show that it is much too slow to explain the observed sawtooth crash time. This is one of the long standing problems faced by magnetic reconnection theory in plasmas.

## 2.4 Summary: Basic features of the sawtooth cycle

In this chapter we have explored the basic concepts necessary to understand the sawtooth phenomenon, starting with a presentation of MHD theory in section 2.1. The sawtooth crash is always observed after the triggering of an internal $\mathsf{m} = 1$, $\mathsf{n} = 1$ kink mode, which we have studied in section 2.2. The effect of the plasma motion inside the resonant $q = 1$ surface is to rigidly push the core towards this surface, creating a current sheet where non-ideal effects cause magnetic reconnection. We have studied the basis of magnetic reconnection in section 2.3. Thus we can state that:

- The kink mode can be destabilized only when there is a $q = 1$ surface in the plasma.
- The kink mode is characterized, at lowest order, by a rigid shift of the inner core (the $q < 1$) region.
- It is destabilized by resistivity, that is, it can be unstable even when there is ideal stability.
- It is stabilized by bifluid effects.
- It is also stabilized by toroidicity.
- It can be stabilized or destabilized by kinetic effects, that is, by the resonances with particle motion in the tokamak (thermal or fast particles).
- Its natural nonlinear evolution involves magnetic reconnection.

We will see in the following chapters how the reconnection phase leads to the redistribution of particles and heat, and to the reorganization of the magnetic field. The plasma then diffusively relaxes to the unstable configuration, leading to a new crash, which closes the sawtooth cycle.

In the next chapter, we first present the numerical tools used throughout this thesis.

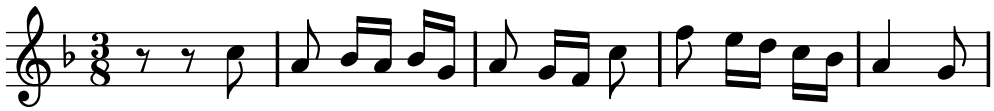

*Erfreue Dich, Seele (BWV 21)*
**Johann-Sebastian Bach**

CHAPTER 3

# Numerical methods

## Contents



This PhD work has been mainly concerned with numerical simulations. The most important tool for these simulations is the XTOR-2F MHD code [Lütjens 2010]. Its basic features and capabilities are presented in section 3.2. The MHD code needs an equilibrium and thus takes as input the output from an equilibrium code, CHEASE [Lutjens 1996], briefly presented in section 3.1. Poincaré plots are introduced in section 3.2.2. I also wrote a simple 2D advection-diffusion code with fixed potential flow to study the influence of the kink flow on the density profile. It is presented in section 3.3. All the postprocessing was done with MATLAB®.

## 3.1 The CHEASE code

### 3.1.1 The Grad-Shafranov equation

The CHEASE (Cubic Hermite Element Axisymmetric Static Equilibrium) code solves the Grad-Shafranov equation, *Eq.* (2.10) (*cf.* section 2.1.2) The functions $p'$ and $II'$ (where $'$ denotes derivation with respect to the solution $\psi$) must be given as input. In practive, we use the fact that the the flux surface averaged toroidal current density $\langle j_\varphi \rangle$ and parallel current density $\langle j_\parallel \rangle$ are linear combinations of $p'$, $II'$ and $I'/I$, so that specifying $p'$ and $\langle j_\parallel \rangle$ or $p'$ and $\langle j_\varphi \rangle$ does the job and is more intuitive.

An other way of specifying the profiles is by using the results of an experimental equilibrium reconstruction code, such as EFIT [Lao 1985] in the case of the JET tokamak for example. Thus conditions as close as possible to the experimental ones can be reproduced, at least for the current, pressure and the related safety factor.

### 3.1.2 Resolution of the Grad-Shafranov equation

*Eq.* (2.10) is solved in a weak variational formulation using cubic Hermite finite elements and Picard iterations on the resulting non-linear problem. Specifically, Grad-Shafranov is transformed in the following equation:

$$\int_\Omega \frac{1}{R}\nabla\omega\cdot\nabla\psi \mathrm{d}S = -\int_\Omega \omega j_\varphi \mathrm{d}S, \tag{3.1}$$

where $\omega$ is a function of the same functional space as $\psi$ and $\Omega$ is the simulation domain. *Eq.* (3.1) is obtained by multiplication by $\omega$ and integration by part of the divergence term. This problem is non-linear, the right-hand side representing the input functions $p'$ and $TT'$ depending on the solution $\psi$. *Eq.* (3.1) can be rewritten formally as

$$\boldsymbol{A}\cdot\boldsymbol{x} = \boldsymbol{B}(\boldsymbol{x}) \tag{3.2}$$

where $\boldsymbol{x}$ represents all the unknowns ($\psi$, its first derivatives and mixed second derivative necessary to the cubic element interpolation, at every point of the mesh) and $\boldsymbol{B}$ depends non-linearly on $\boldsymbol{x}$. The Picard iteration method consists in starting with an initial guess $\boldsymbol{x}_0$ and solving successfully the equation $\boldsymbol{A}\cdot\boldsymbol{x}_k = \boldsymbol{B}(\boldsymbol{x}_{k-1})$, $\boldsymbol{x}_k$ being the $k^{th}$ iteration of the solution. The process is stopped when $\|\boldsymbol{x}_k - \boldsymbol{x}_{k-1}\| < \varepsilon$ for a given maximum error $\varepsilon$ and some norm $\|\cdot\|$.

### 3.1.3 Scaling of the equilibrium

For given specified profiles $p'$ and $TT'$ and solution $\psi$, there exist two classes of equilibria. Firstly, the safety factor is related to $T(\psi)$ by the relation

$$q(\psi) = \frac{T(\psi)}{2\pi}\oint_{\psi=C^{te}} \frac{\mathrm{d}l_p}{R\,|\nabla\psi|}, \tag{3.3}$$

where $\mathrm{d}l_p$ is the length element along the flux surface in the poloidal direction. Since only $II' = 1/2(I^2)'$ is involved in Grad-Shafranov equation, we see that we can modify the safety factor of the equilibrium without changing the solution $\psi$ neither the pressure, just by adding a constant to $I^2$:

$$I^2_{new} = I^2_{old} + K_1. \tag{3.4}$$

Secondly, Grad-Shafranov's equation is invariant by the rescaling

$$\psi_{new} = K_2\psi_{new} \tag{3.5}$$

$$I_{new} = K_2 I_{new} \tag{3.6}$$

$$p_{new} = K_2^2 p_{new}. \tag{3.7}$$

Notice that since $\beta$, the plasma beta, is proportional to $p/I^2$, this rescaling modifies the absolute values of pressure and current, but not $\beta$. In practice, these transformations are very convenient because they allow the user to specify a given value of $q$ at a given radial point, for instance $q = 1$ at mid radius, or, alternatively, the total plasma current.

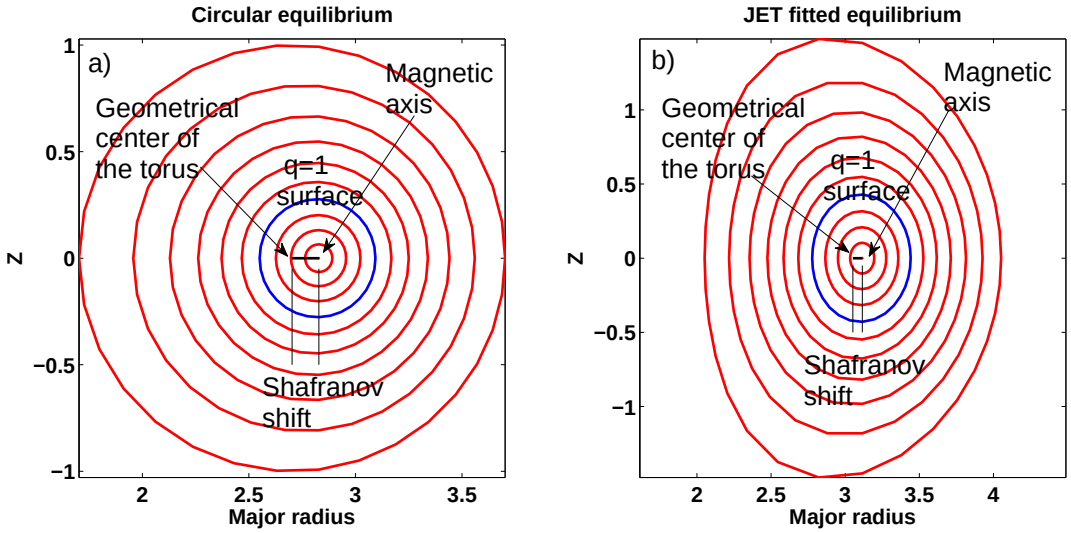


Figure 3.1: Magnetic surfaces and Shafranov shift for the circular equilibrium used in this thesis (a) and for a JET fitted equilibrium using EFIT data (b). The blue circle represents the position of the $q = 1$ surface.

### 3.1.4 Shafranov shift

Because of the toroidal geometry of the configuration, the nested torus constituting the magnetic surfaces are shifted toward larger $R$. This is due to the fact that surface elements (for a given poloidal and toroidal angle element) are larger on the LFS than on the HFS, with a discrepancy of order $\varepsilon$. Hence the pressure force, directed toward increasing $r$, is higher on the HFS than on the LFS, which results in a force directed toward increasing $R$. This effect is called the Shafranov shift $\Delta$. The Shafranov shift is roughly proportional to the pressure. Fig. 3.1 shows the flux structure for two different equilibria. The first one is a circular boundary equilibrium obtained with parameters relevant to Tore Supra plasmas. The second one has been produced using EFIT data. The Shafranov shift and the position of the $q = 1$ surface have been plotted in both cases. Notice that JET plasmas have in principle an X-point and thus are up-down asymmetric. It is possible to work with such geometries in XTOR-2F but resolution is faster when EFIT data are symmetrized and regularized, with no X-point in the final result. This is acceptable if one is interested only on core instabilities, as is the case in this thesis.

## 3.2 The XTOR-2F code

The aim of the XTOR-2F code is to solve a set of non-linear full resistive MHD equations in three dimensions, starting from the equilibrium provided by the CHEASE code. It is called XTOR-2F as a reference to the 2Fluid model it is able to solve. It can also solve the standard $\eta\chi$MHD model. We first present the resolution method and then show the three main types of evolution of kink unstable equilibria in XTOR-2F.

### 3.2.1 The Newton-Krylov solver

Be it the $\eta\chi$MHD or bifluid model, the system of equations solved by the code can be formally written

$$\dot{\boldsymbol{x}} = F(\boldsymbol{x}), \tag{3.8}$$

where $x$ denotes the unknown fields, the dot denotes partial time derivative and $F$ is

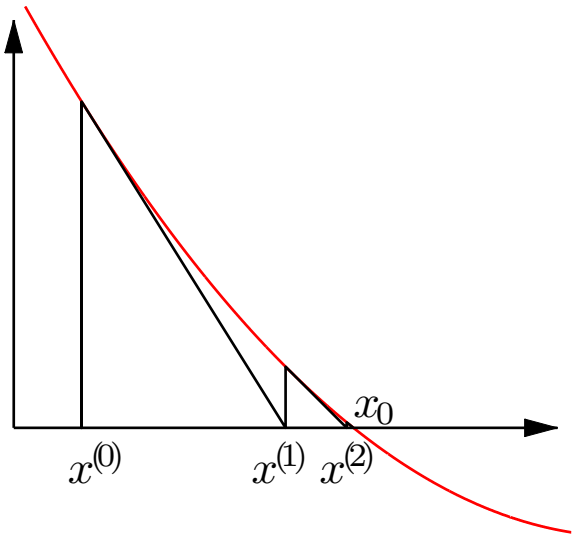


Figure 3.2: Principle of Newton's iterative method of resolution of a non-linear equation.

a non-linear operator. The mesh is discretized with `lmax` points in the radial direction (plus two points at each edge of the radial mesh to provide the boundary conditions), `mmax` in the poloidal direction and `nmax` in the toroidal direction. There are 8 variables: 3 for $\boldsymbol{v}$, 3 for $\mathbf{B}$, 1 for $\rho$ and one for $p$, so that the number of unknowns, or the size of $\boldsymbol{x}$, is $8 \times$ `lmax` $\times$ `mmax` $\times$ `nmax`. The strategy in XTOR-2F is to solve *Eq.* (3.8) using a fully implicit scheme. This means that the unkwown enters the non-linear operator, and a fully non-linear equation must be solved at each step. The Newton's method is used to solve this non-linear problem. It is an iterative method which principle is very simple. If one looks for the zero $x_0$ of a non-linear function $f$, $f(x_0) = 0$, then provided one knows an approximate solution $x^{(0)}$,

$$x^{(1)} \equiv x^{(0)} - \frac{f(x^{(0)})}{f'(x^{(0)})}$$

should be a better approximation. The principle is presented on Fig. 3.2. If the initial solution $x^{(0)}$ is close enough to $x_0$, then the convergence is in theory very fast, at least quadratic if the multiplicity of the root is one, so that the number of correct digits doubles at each step.

For multidimensional systems, the principle is the same but at each Newton step, a large linear system

$$\boldsymbol{A} \cdot \boldsymbol{x} = \boldsymbol{B} \tag{3.9}$$

must be solved. This system is solved also by an iteration method using Krylov subspaces [Knoll 2004]. The combination of the Newton and Krylov methods is implemented in the NITSOL library [Pernice 1998] used in XTOR-2F. Different Krylov algorithms are available in NITSOL, and the fastest in the case of XTOR-2F is called Generalized Minimal RESidual (GMRES). Thus there are two levels of iterations at each time step: one corresponding to the Newton iterations, and one corresponding to the Krylov iterations.

### Numerical scheme

The implicit scheme adopted to solve *Eq.* (3.8) is the following:

$$\boldsymbol{x}_{n+1} - \boldsymbol{x}_n = \Delta t F \left( \frac{\boldsymbol{x}_{n+1} + \boldsymbol{x}_n}{2} + c(\boldsymbol{x}_{n+1} - 2\boldsymbol{x}_n + \boldsymbol{x}_{n-1}) \right), \tag{3.10}$$

with $c > 0$ (typically 1), $\Delta t$ the time step and $\boldsymbol{x}_n$ the solution at the $n^{th}$ time iteration. The positive constant $c$ makes the scheme both more implicit and stable. The scheme is linearly unconditionally stable when $c > 0$. Introducing $\boldsymbol{\Delta}_n = \boldsymbol{x}_{n+1} - \boldsymbol{x}_n$ and $\bar{\boldsymbol{x}} = (1-c)\boldsymbol{x}_n + c\boldsymbol{x}_{n-1}$, the problem amounts to finding the zeros of the operator $G$:

$$G(\boldsymbol{\Delta}_n, \bar{\boldsymbol{x}}) \equiv \boldsymbol{\Delta}_n - \Delta t F \left[ \left( \frac{1}{2} + c \right) \boldsymbol{\Delta}_n + \bar{\boldsymbol{x}} \right]. \tag{3.11}$$

Thus at each Newton step (at the $k^{th}$ iteration, say), the following linear system must be solved:

$$G'(\boldsymbol{\Delta}_n, \bar{\boldsymbol{x}}) \boldsymbol{\Delta}_n^{k+1} = G(\boldsymbol{\Delta}_n^k, \bar{\boldsymbol{x}}), \tag{3.12}$$

where $G'$ is the derivative of $G$ with respect to $\boldsymbol{\Delta}_n$: $G'_{i,j} = \partial G_i / \partial \boldsymbol{\Delta}_{n,j}$. However before solving this linear system, it must be preconditioned. Preconditioning is a crucial element of the resolution. It consists in first applying to the vectors a matrix $M^{-1}$ which is close to the inverse of $G'$. In the case of XTOR-2F, it is a physical preconditioner based on the linearized MHD problem. More details can be found in Ref. [Lütjens 2010]. So finally, the Krylov method is applied to

$$M^{-1} G'(\boldsymbol{\Delta}_n, \bar{\boldsymbol{x}}) \boldsymbol{\Delta}_n^{k+1} = M^{-1} G(\boldsymbol{\Delta}_n^k, \bar{\boldsymbol{x}}) \tag{3.13}$$

to solve for $\boldsymbol{\Delta}_n^{k+1}$.

### Discretization and mesh

The code uses finite differences in the radial direction and Fourier decompositon in the two periodic directions, poloidal and toroidal. The radial coordinate is a flux coordinate deduced from CHEASE. Namely, it is the square root of the poloidal flux, $s \equiv \sqrt{(\psi - \psi_0)/(\psi_a - \psi_0)}$, where $\psi_0$ and $\psi_a$ are the values of the poloidal flux at the centre and at the edge. Since the flux increases quadratically with the radius, this quantity can be seen as an approximation of the radius.

To carefully treat the derivatives on the radial mesh, two meshes actually exist in the code, called integer and staggered (half-integer) meshes. The first one goes from $s = -\Delta s$ to $s = 1$, and the second one from $s = -\Delta s/2$ to $1 + \Delta s/2$, where $\Delta s$ is the interval between two mesh points (constant). Thus one has to be careful, when manipulating scalar and vector quantities, to the mesh on which they are defined. For instance, scalar quantities like the pressure of density are defined on the staggered mesh, and $\mathbf{B}$ has its radial component on the integer mesh, and its poloidal and toroidal components on the staggered mesh. This allows to limit the number of operations required when computing the divergence and curl of the fields. Indeed, for a general system of coordinates $(\psi, \theta, \varphi)$, with Jacobian $\mathcal{J} = [\nabla\psi \cdot (\nabla\theta \times \nabla\varphi)]^{-1}$, the divergence of a vector fied $\mathbf{A}$ can be written:

$$\nabla \cdot \mathbf{A} = \frac{1}{\mathcal{J}} \partial_i \left( \mathcal{J} A^i \right), \tag{3.14}$$

with summation over repeated indices, and where $A^i$ is the $i^{th}$ contravariant component of $\mathbf{A}$ (see appendix A). One sees that taking the divergence of a quantity defined like $\mathbf{B}$ produces a scalar defined on the staggered mesh, since the finite differences send a quantity defined on a given mesh to the other mesh. The velocity is of the same type as $\mathbf{B}$, this allows to treat properly all the terms proportional to the divergence of the velocity, in the pressure and density equations. Also, notice that taking the gradient of a scalar transforms it into a vector of the same type as $\boldsymbol{v}$ and $\mathbf{B}$.

Let us also look at the curl. With the formula

$$(\nabla \times \mathbf{A})^i = \frac{1}{\mathcal{J}} \varepsilon^{ijk} \partial_j A_k, \tag{3.15}$$

where $\varepsilon^{i,j,k}$ is the Levi-Civita symbol, one sees that a vector of the type of $\mathbf{B}$ is transformed in a vector with the radial component on the staggered mesh and the two others on the integer mesh. A similar thing happens for the cross product. This is very useful for the term $\nabla \times (\boldsymbol{v} \times \mathbf{B})$ in the induction equation, where one can check that starting from two $\mathbf{B}$ type vectors ($\boldsymbol{v}$ and $\mathbf{B}$), one ends up smoothly with a $\mathbf{B}$ type vector as well.

Occasionally, when the physical model is complexified, quantities are introduced which cannot be well integrated in this framework. This is the case with the bifluid terms in the pressure and density equations for instance, where one takes the scalar product of the gradient of a scalar quantity with the curl of a quantity of the same type as $\mathbf{B}$. Also multiplying a vector quantity by a scalar is not straightforward. In such cases, the appropriate quantities are simply interpolated on the complementary mesh. Still, on average, the use of two meshes makes the treatment of derivation much cleaner and convenient.

### Aliasing constraints and resolved modes

Because of the Fourier discretization in the poloidal and toroidal directions, certain "aliasing" constraints must be respected. In order to explain the problem, let us concentrate only on one direction, say the toroidal one. The toroidal coordinate $\varphi$ is cut into $\mathtt{nmax}$ values. In other words, $\varphi$ is sampled at the "frequency[1]" $\mathtt{nmax}$. According to the Nyquist-Shannon sampling theorem, the sampling frequency $\mathtt{nmax}$ must be at least twice the frequency of the highest mode in the simulation. Denoting the latter $\mathtt{N}$, we see that we must have $\mathtt{N} \leq \mathtt{nmax}/2$. Indeed, the samples of two signals with frequencies $\mathtt{n}$ and $\mathtt{n} + k{\times}\mathtt{nmax}$, where $k \in \mathbb{Z}$, are identical[2]. Thus when sampling a signal at a frequency smaller than twice the signal frequency, one introduces new frequencies, not present in the original signal (hence the word "aliasing"). This holds for the resolution of linear systems and implies that the available Fourier domain is $\mathtt{n} \in [\![-\mathtt{nmax}/2, \mathtt{nmax}/2]\!]$. However for non-linear systems, aliasing constraints are even more restrictive.

Indeed consider the product of two terms, for instance $\mathbf{J}$ and $\mathbf{B}$ in the $\mathbf{J}\times\mathbf{B}$. Both will have non vanishing components at the frequency $\mathtt{N}$. So when performing the product, the coupling between these two components will yield the frequencies $\mathtt{N} - \mathtt{N} = 0$ and $\mathtt{N} + \mathtt{N} = 2\mathtt{N}$. Now if there exists $k \in \mathbb{Z}$ such that $2\mathtt{N} - k \times \mathtt{nmax}$ lies in the range of modeled frequencies, when sampling the product of terms, the high frequency $2\mathtt{N}$ will be reproduced unphysically at $2\mathtt{N} - k \times \mathtt{nmax}$. Taking the smallest possible $k$, $k = 1$, we must have $2\mathtt{N} - \mathtt{nmax} < -\mathtt{N}$, that is, $2\mathtt{N} - \mathtt{nmax}$ must be sent out of the range of the resolved mode. Similarly, the symmetric (and equivalent condition) must hold for the other end of the spectrum: $-2\mathtt{N} + \mathtt{nmax} > \mathtt{N}$. The situation is summed up on Fig. 3.3. Notice that there are actually couplings between more than 2 modes in XTOR-2F for some terms, so in principle the dealiasing constraint should be even more restrictive than the one described here. However, this difficulty is avoided in the code because after each multiplication between two fields, projectors are applied on the product. These operators project the result on the resolved modes. Hence in a multiplication involving three fields, a first step is the multiplication of the first two fields, then the result is projected on the resolved modes, and thanks to this operation there is no aliasing problem during the multiplication between the first product and the third field.

In XTOR-2F, the input is not the maximum resolved toroidal mode but the size of tables for toroidal discretization, $\mathtt{nsmax}$. We see that it is equal to $2\mathtt{N} + 1$ (since $\mathtt{n} \in [\![-\mathtt{N}, \mathtt{N}]\!]$). Thus in XTOR-2F, we must have $\mathtt{nsmax} \leq 2/3\mathtt{nmax} + 1$, and the highest toroidal mode is $\mathtt{nsmax}/2\text{-}1$.

In the poloidal direction, the resolved modes are in the band $[\![\mathtt{n}-\mathtt{minf}, \mathtt{n}+\mathtt{msup}]\!]$. With the same aliasing constraints, we see that we must have[3] $\mathtt{nsmax}/2\text{-}1+\mathtt{msup} < \mathtt{mmax}/3$. The mode $\mathtt{n} = 0$ is resolved separately, it must verify[4] $\mathtt{mn0} < \mathtt{mmax}/3$.

[1] We should rather call this a wave-number, but thinking of it as frequencies makes it more intuitive.

[2] To see this consider two samples $s_1$ and $s_2$ of two sinusoidal signals, one at the frequency $n$, the other at the frequency $n + k{\times}\mathtt{nmax}$. Then the $p^{th}$ sample ($p \in \mathbb{Z}$) of $s_1$ is $s_1(p) = \sin(np\Delta\varphi)$, with $\Delta\varphi = 2\pi/\mathtt{nmax}$. The $p^{th}$ sample of $s_2$ is $s_2(p) = \sin[(n + k \times \mathtt{nmax})p\Delta\varphi] = \sin(np\Delta\varphi + 2\pi kp) = s_1(p)$.

[3] The actual aliasing constraints implemented in XTOR-2F are in fact slightly more restrictive and read: $\mathtt{nsmax} \leq 2/3\mathtt{nmax}$ and $\mathtt{nsmax}/2\text{-}1+\mathtt{msup} \leq 2/3(\mathtt{mmax}/2\text{-}1)$.

[4] Again, in XTOR-2F, the condition is slightly more restrictive, $\mathtt{mn0} \leq 2/3(\mathtt{mmax}/2\text{-}1)$.

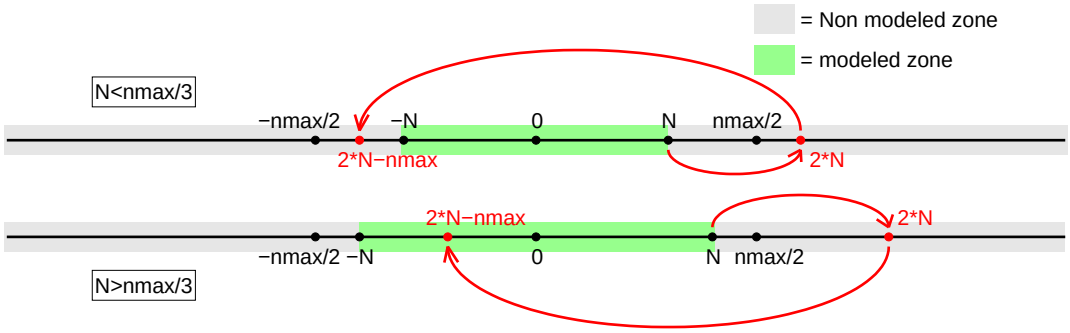


Figure 3.3: Schematic showing the condition for avoiding aliasing problems. In the first case (top) the condition `N`<`nmax`/3 is respected, so that the replica lies outside of the resolved domain. However, when `N`>`nmax`/3, the high frequency signal is replicated inside the modeled domain, and thus aliasing problems occur.

Once the resolved domain is set, we see that in order for the field spectra to stay in the resolved domain, the fields must be frequently projected on the resolved modes. Thus all inadequate frequencies are eliminated.

### Normalization

The equations are normalized in the following way:

- The basic length scale is the minor radius of the plasma $a$.
- The basic time scale is the Alfvén time $\tau_A = R_0/V_A$, where $R_0$ is the plasma major radius and $V_A$ the usual Alfvén velocity defined.
- The basic velocity is the Alfvén velocity multiplied by the inverse aspect ratio: $(a/R_0)V_A = (a/R_0)B_0/\sqrt{\mu_0\rho_0}$, where $B_0$ is the magnitude of $\mathbf{B}$ on axis and $\rho_0$ the plasma mass density on axis.
- The basic magnetic field is $B_u = B_0(a/R_0)$.
- The basic pressure is $\rho_0(a/R_0)^2V_A^2$.

### Normalized bifluid equations

In the case of $\eta\chi$MHD, the dimensionless parameters are the dissipation coefficients: the resistivity, viscosity, particle and heat perpendicular diffusivities, and parallel heat diffusivity. Consistently with our normalizations, they are expressed in units of $a^2/\tau_A$. The Lundquist number is defined by $S = \tau_R/\tau_A = \mu_0 a^2/(\eta\tau_A) \propto \eta^{-1}$ ($\tau_R$ is the resistive time), typically $S \sim 10^8 - 10^9$ in large tokamaks. In XTOR-2F, it is difficult to operate at $S > 10^7$ due to excessive simulation times when the resistive time is large. In the bifluid

MHD case, an additional parameter appears in front of all diamagetic terms, denoted by $\alpha$:

$$\alpha \equiv \frac{R_0}{a\omega_{ci}\tau_A} = \frac{m_i}{ea\sqrt{\mu_0\rho_0}}. \tag{3.16}$$

Note that $\alpha$ can easily be related to the ion skin depth, which is often used to normalize diamagnetic terms in other plasma communities, in particular space plasmas problems. The ion skin depth is

$$d_i \equiv \frac{c}{\omega_{pi}} \tag{3.17}$$

where $\omega_{pi}$ is the ion plasma frequency

$$\omega_{pi} = \sqrt{\frac{n_i e^2}{\varepsilon_0 m_i}}. \tag{3.18}$$

Thus we easily see that

$$\alpha = \frac{d_i}{a} = \hat{d}_i. \tag{3.19}$$

The normalized bifluid MHD equations are thus

$$\frac{\partial \rho}{\partial t} + \nabla \cdot \rho \boldsymbol{v} + \alpha \nabla p_i \cdot \nabla \times \frac{\mathbf{B}}{B^2} = \nabla \cdot D_\perp \nabla \rho + S, \tag{3.20}$$

$$\rho \left( \frac{\partial \boldsymbol{v}}{\partial t} + \boldsymbol{v} \cdot \nabla \boldsymbol{v} + \alpha \boldsymbol{v}_i^\star \cdot \nabla \boldsymbol{v}_\perp \right) = \mathbf{J} \times \mathbf{B} - \nabla p + \nabla \nu \nabla \left( \boldsymbol{v} + \boldsymbol{v}_i^\star \right), \tag{3.21}$$

$$\frac{\partial p}{\partial t} + \boldsymbol{v} \cdot \nabla p + \Gamma p \nabla \cdot \boldsymbol{v} + \alpha \Gamma \left( T \nabla p_i + p_i \nabla T_i - p_e \nabla T_e \right) \cdot \nabla \times \frac{\mathbf{B}}{B^2} = \ldots$$
$$\nabla \cdot \rho \chi_\perp \nabla \frac{p}{\rho} + \nabla \cdot \rho \chi_\parallel \nabla_\parallel \frac{p}{\rho} + H, \tag{3.22}$$

$$\frac{\partial \mathbf{B}}{\partial t} = \nabla \times \boldsymbol{v} \times \mathbf{B} + \alpha \nabla \times \left( \frac{\nabla_\parallel p_e}{\rho} \mathbf{b} \right) - \nabla \times \eta \mathbf{J}, \tag{3.23}$$

and with this normalization the diamagnetic velocity $\boldsymbol{v}_i^\star$ is

$$\boldsymbol{v}_i^\star \equiv \frac{\mathbf{B} \times \nabla p_i}{\rho B^2}. \tag{3.24}$$

We have kept the same notation for the normalized dissipative coefficients. In the following, unless otherwise noted, the values given for these coefficients refer to the normalized values. The parameter $\alpha$ can be arbitrarily tuned. Typical experimental values for this parameter in Tore Supra are $0.05 - 0.1$. In the simulations the value $\alpha = 0.1$ is used unless otherwise specified. Note that since the dynamics of the sawtooth instability in XTOR-2F is mainly fixed by the two time scales related to the resitivity and the diamagnetic effects, the ratio between the resistive time and the diamagnetic time scale, or equivalently, the product $S\alpha$, should be set to the experimental value. Since $S$ is too small by roughly one order of magnitude, $\alpha$ should be rescaled up by an order of magnitude, which is currently not possible because the diamagnetic terms do not behave well numerically when they are too large. The maximum values for the parameter $\alpha$ to run

XTOR-2F are of the order of $0.1 - 0.2$, depending on the equilibrium and on the value of the resistivity. These values are close to the experimental ones, so the problem lies more in the resistivity. It is possible to make internal kink simulations with $10^7 \leq S < 10^8$ but $S = 10^8$ requires an excessive amount of simulation time.

#### Boundary conditions

For any numerical code solving a set of partial differential equations (PDE), much care is required in defining the boundary conditions (BC). Indeed the solution of a PDE on a compact domain of space is determined both by the initial conditions and the BC, which must be dictated by the physics.

In XTOR-2F, a perfectly conducting wall is assumed at the boundary. This means that there cannot be any normal magnetic field at this surface, which is equivalent to saying that the last mesh surface is always a magnetic flux surface. The BC on the velocity are free-slip BC, *i.e.*:

$$v^r = 0, \qquad \partial_r v^\theta = 0, \qquad \partial_r v^\varphi = 0. \tag{3.25}$$

These conditions on $\mathbf{B}$ and $\boldsymbol{v}$ are sufficient to determine the BC for all the ideal MHD part of the equations, including $p$ and $\rho$. However when dissipation, resistivity and bifluid terms are added, additional conditions must be explicitly written for $\mathbf{J}$, $p$ and $\rho$.

### 3.2.2 Poincaré plots

Plotting the magnetic field components can be instructive, in particular the radial magnetic field, normal to the equilibrium flux surfaces, is closely related to the MHD displacement. However it is difficult, if not impossible, to infer from these plots the structure of the magnetic field, when it is no longer organized in nested tori. To see the island structure and/or the zones where the magnetic field lines are stochastic, a more sophisticated tool is needed. This is provided by the Poincaré plots. Such plots are obtained by picking a given position in the poloidal plane and following the field line along the torus by integration. The field line comes back in the initial poloidal plane, where a point is drawn. Several hundreds of turns are typically used in order to give an idea of the flux surface. The integration scheme usually involves Runge-Kutta integration.

Fig. 3.4 shows three Poincaré plots showing different behaviors. They are obtained using 59×13 seed points (59 radial positions and 13 angles) and 500 toroidal turns. In panel a), this is the equilirium configuration with well nested flux surfaces. Note the position of the $q = 1$ surface is visible as the radius where only the 13 poloidal seed-points are visible. Indeed at $q = 1$, the field line closes on itself after a toroidal turn. Panel b) displays an $\mathsf{m} = 1$ magnetic island with no stochasticity. This is taken during the reconnection phase of a sawtooth crash. Panel c) shows the magnetic structure at the end of the sawtooth crash in a case with higher poloidal and toroidal resolution than in a) and b). There is a wide stochastic zone in the region of the initial $q = 1$ surface. This stochastic zone is due to the couplings between island chains with mode numbers $(\mathsf{n}+1, \mathsf{n})$, with $\mathsf{n}$ quite large. Sometimes one is tempted to speak of stochasticity by just

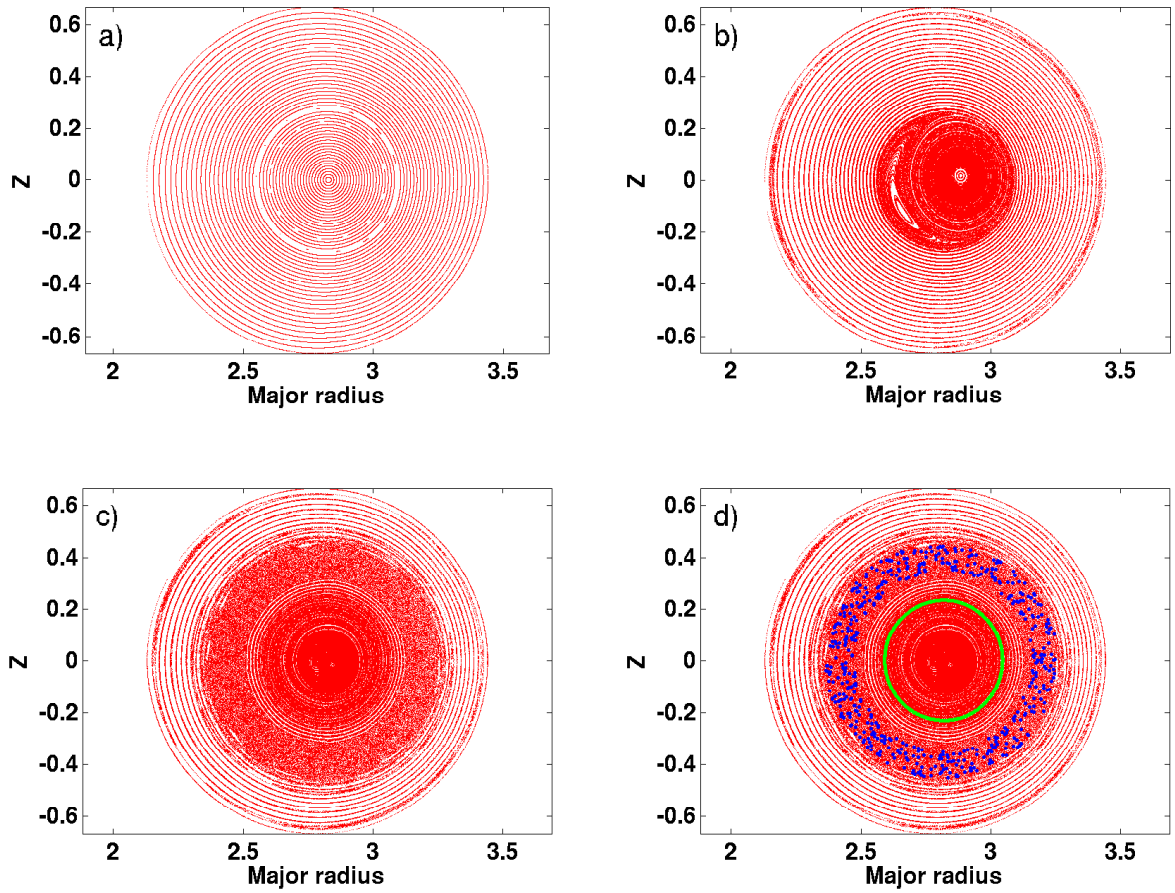


Figure 3.4: Nested equilibrium magnetic surfaces (a), m = 1 island during the sawtooth crash (b), stochasticity for a highly resolved case (c), and same image as (c) with 2 field lines plotted (d), one in the stochastic region (blue) and one in the non stochastic region (green). Notice that it is impossible to tell from image (c) where the stochastic zone starts and ends. Only the innermost 60% of the plasma are shown on these images.

looking at a Poincaré plot. However this can be misleading, since sometimes imprecision of the integration scheme or of the solution $\mathbf{B}$ gives an impression of stochasticity on the figure. Thus the only way to reliably infer stochasticity is by plotting the points corresponding to a fixed field lines and observing a wide radial extension. This is done in panel d), the same image as c) with two field lines shown in blue (stochastic) and green (non stochastic).

### 3.2.3 Simulation of sawteeth: influence of $\beta_p$, $\chi_\perp$, $\eta$ and $\alpha$

Since the beginning of the development of XTOR (the name of the code before the bifluid effects were added), a lot of efforts have been undertaken to identify the different regimes of evolution of kink unstable equilibria. Two basic behaviours can be obtained upon non-linear evolution of the internal kink mode.

- A 3D helical equilibrium
- A regime of sustained kink cycles, which can be further refined in
  - A simple kink cycling regime with no or low separation of time scales between the ramp time and reconnection time
  - A so-called "sawtooth cycling" regime with a clear separation of scales.

For the 3D helical equilibrium, the magnetic surfaces are displaced into a small amplitude 1/1 mode with a self-sustained current sheet on $q = 1$. The energy necessary for this constantly reconnecting state is provided by the heat source in the pressure equation, thriving to regenerate the initial pressure gradient. The flow is organized in two convection cells which constantly drive the pressure appearing in the center toward the $q = 1$ surface. The safety factor is very close to 1 inside the core, so it has a very low shear. Fig. 3.5 shows the evolution of the pressure for this regime. It is seen that the helical state results from the non-linear evolution of a primary 1/1 internal kink instability (the crash of the kink is indicated between vertical dashed lines on panel (a)). Panel (b) shows the parallel current structure with the current sheet at the resonance surface. It is seen how the current density is flattened in the core by the sustained plasma motion which drives always more flux toward the current sheet. Notice an other flattening of the current at the edge. It is due to saturated large amplitude tearing modes. Panel (c) shows a Poincaré plot of the magnetic field during the helical state. The current sheet is at the left, at $R \simeq 2.6$. A complex structure of islands can be seen in the core. Only the innermost 60% of the plasma are visible, so the tearing cannot be seen.

In the case of the kink cycling, the instability responsible for the helical state is not strong enough to prevent the pressure from rising in the center. Thus the safety factor also has enough time to decrease from 1 toward its equilibrium value, and at some point a pressure threshold is reached, triggering the 1/1 instability. At the end of each reconnection phase, there is not enough free energy for the instability responsible for the helical state, and the cycle starts again. However the time scales are not well separated. Fig. 3.6 shows the evolution of the kinetic energies and pressure. It is seen that the pressure cycles are not characterized by any clear separation of time scales between the ramp phase of the pressure and the reconnection time.

In the case of sawtooth cycling, the dynamics is generally similar to the kink cycling, except that now a clear separation of scales is visible. The evolution of kinetic energies and pressure is shown on Fig. 3.7. This regime can be obtained only with the bifluid model in XTOR-2F, where diamagnetic effects are added.

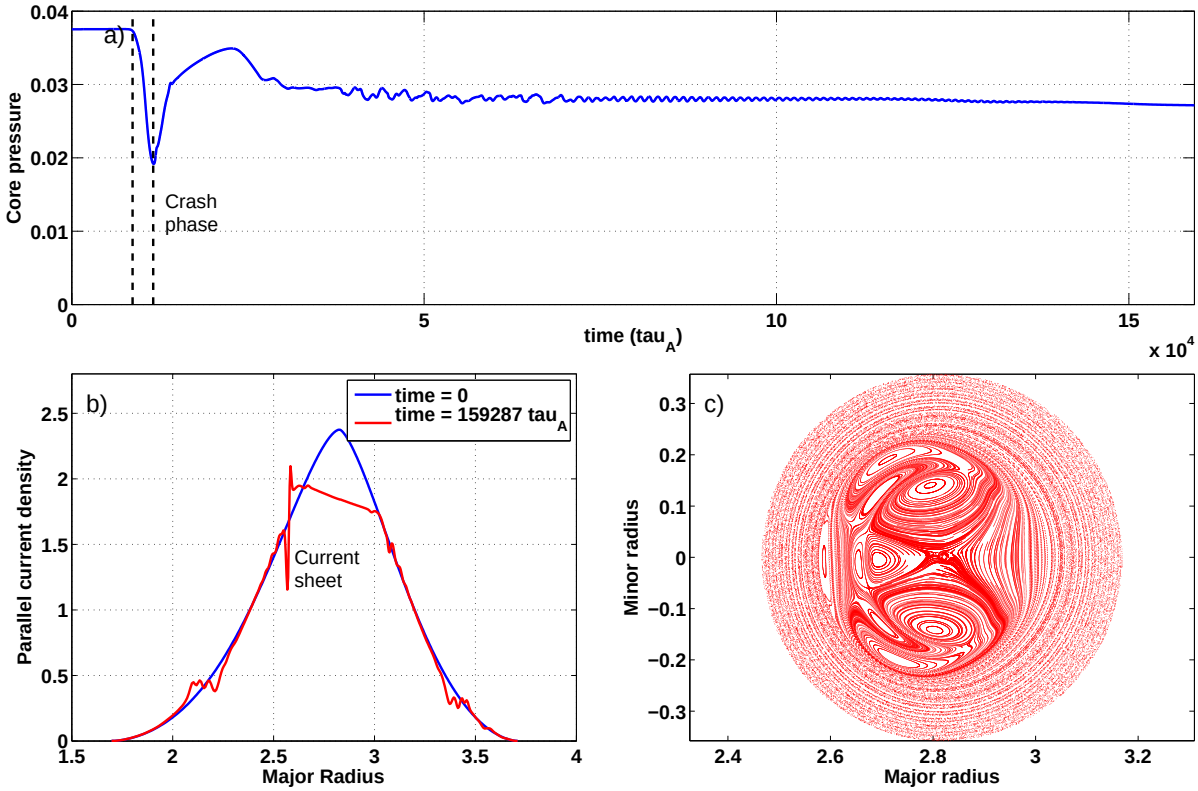


Figure 3.5: Pressure evolution (a), current density at the beginning and the end of the simulation (b) and Poincaré plot (innermost 60%) at the end of the simulation for the helical state regime (c).

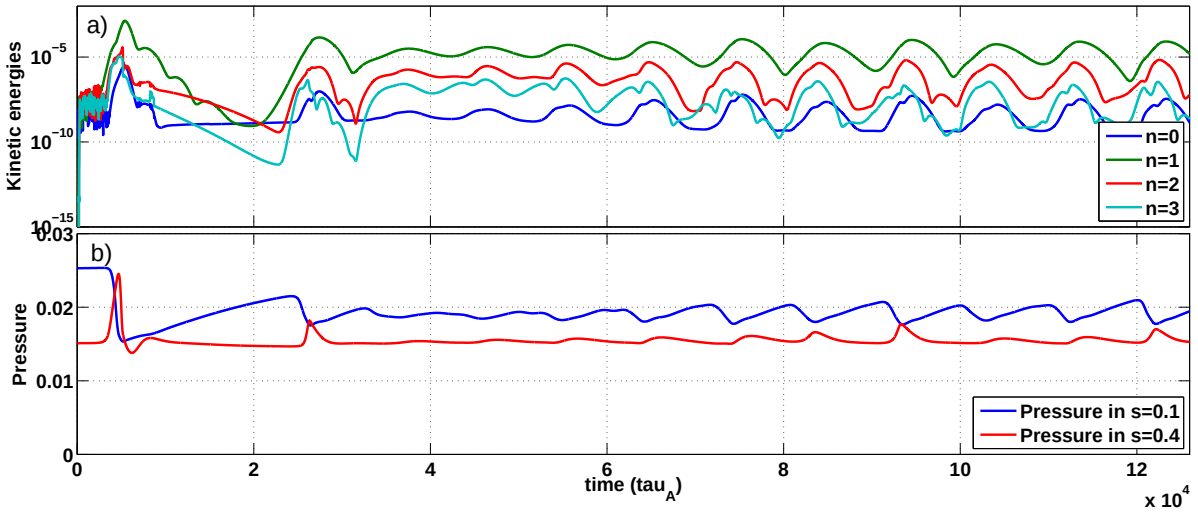


Figure 3.6: Kinetic energy (a) and pressure (b) evolution for the kink cycling regime.

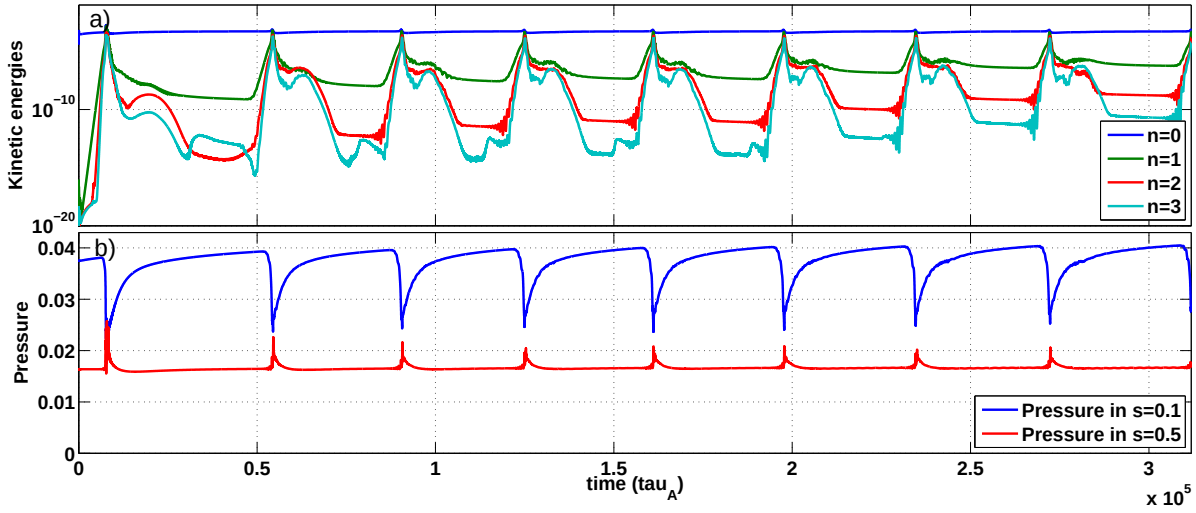


Figure 3.7: Kinetic energy (a) and pressure (b) evolution for the sawtooth cycling regime.

The conditions for obtaining these different regimes are explained in details in the two references [Halpern 2011a] and [Halpern 2011b]. There is an emphasis on the transition between 3D helical equilibrium and kink cycling in the first one, with the influence of $\beta_p$ and $\chi_\perp$, mostly, while the second insists on the transition between kink cycling and sawtooth regime, with an emphasis on the role of $\eta$ (or $S$), and $\alpha = d_i/a$. Recall that the $\alpha$ parameter quantifies the magnitude of diamagnetic effects.

Fig. 3.8 shows the different regimes obtained when varying $\beta_p$ and $\chi_\perp$ in a case with low magnetic shear and $\eta\chi$MHD(no diamagnetic effects). It can be seen that for low $\beta_p$ and low $\chi_\perp$, the helical state is obtained, while kink cycling is obtained at moderate $\chi_\perp$ and higher $\beta_p$. As said above, this is interpreted as a competition between the strength of the post-crash low shear instability responsible for the helical state and the heat source reconstructing the pressure. However one sees that sustained kink cycles are recovered for very high $\chi_\perp$ (orange triangles on the figure). Fig. 3.9 shows the influence of varying $\eta$ or the Lundquist number $S$, and the amplitude of diamagnetic effects, while keeping $\beta_p$ and $\chi_\perp$ fixed, for a case which is in the helical state regime in the framework of $\eta\chi$MHD. Recall that increasing $S$ amounts to decreasing the resistivity $\eta$, and that typical experimental values of $S$ are in the range $10^8 - 10^9$. It is seen on the figure that kink cycling, and then sawtooth cycling, are obtained when $S$ or $\alpha$ is increased. On top of the separation of scales, a strong acceleration of the crash is observed due to the diamagnetic effects, as can be seen on Fig. 3.7. The time scales are found to be almost relevant to tokamaks. However, since a realistic value of the resisitivity cannot be achieved due to the numerical limitations, it is impossible to know if other physical effects are required in order to account for the fast crash observed in the experiments. However, effects like electron inertia or polarization drifts, which are neglected in XTOR-2F, are known to have a significant acceleration effect on reconnection.

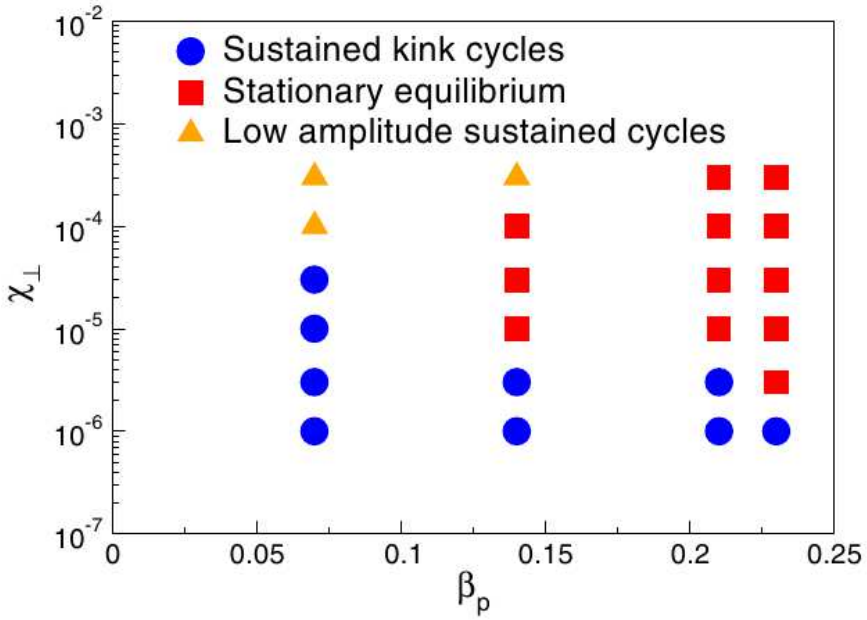


Figure 3.8: Kink cycling regime versus helical state regime dependence on $\beta_p$ and $\chi_\perp$ for a low shear equilibrium. Figure taken from [Halpern 2011a]

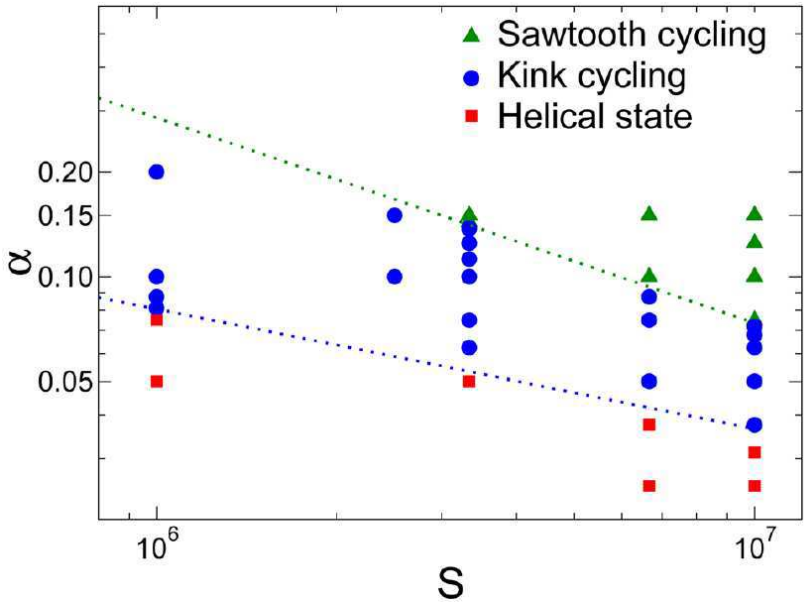


Figure 3.9: Different regimes of cycling when varying $S$ and $\alpha$. Figure taken from [Halpern 2011b]

The study of chapters 6 and 7 will all be in the sawtooth cycling regime, using the values $S = 10^7$, $\chi_\perp = 3 \times 10^{-6}$, $\beta_p = 0.2$, and $\alpha = 0.1$.

## 3.3 A 2D advection-diffusion code

I have developed an other numerical tool to study internal kink related physics. In section 6.1 we will study some structures appearing in the core at some point in the sawtooth cycle and we will see that the formation of these structures could very well be due to the influence of the kink flow in the post-crash phase, when a postcursor is present. Thus it seemed useful to dispose of a code able to simulate advection by an imposed flow, rather than to rely on the complex XTOR-2F resolution, which may not be able to reproduce the relevant flow pattern. Indeed, the kink modes produced by XTOR-2F tend to grow nonlinearly and lead to a crash rather than to a nonlinear saturation, as often observed in the experiment. Thus the code solves advection and diffusion of a scalar under the action of a potential (divergence-less) flow in 2D cylindrical geometry. A radial pinch velocity $V_{\text{pinch}}$ (not divergence-less) can also be added, as well as a restoring source. In other words, given a potential $\phi$, the code solves the following equation:

$$\partial_t n + (\boldsymbol{e}_z \times \nabla\phi) \cdot \nabla n = \nabla \cdot D\nabla(n - n_0) - \nabla \cdot (nV_{\text{pinch}}) \,, \tag{3.26}$$

for a given diffusion coefficient profile $D(r)$ and pinch velocity profile $V_{\text{pinch}}(r)$. The restoring source is provided by the $-\nabla \cdot D\nabla n_0$ on the r.h.s. To simulate the advection by a potential flow the Arakawa scheme [Arakawa 1966] is very well adapted. The code uses an implicit finite differences Arakawa scheme. It is second order in space and even though Dirichlet (fixed value) boundary conditions are applied on a circle, a Cartesian mesh is used. The only implementation difficulty was to write properly the boundary conditions on the points neighbouring the boundary circle. The code is written in MATLAB®. At each time step, a sparse linear system is solved by LU decomposition.

A 1D version, limited to the diffusion and pinch velocities, was also written with an implicit finite differences scheme.

## 3.4 Summary

In this section, we have presented the numerical tools used for this work, namely:

- The CHEASE code which provides the equilibrium to the MHD code.
- The XTOR-2F code to solve the MHD problem
- The Poincaré plots as a postprocessing
- The 2D and 1D advection/diffusion codes.

The following chapters extensively use all these tools to study sawtooth related issues, focusing in particular on reconnection dynamics in chapter 4 and on the electron and impurity densities in chapters 6 and 7.

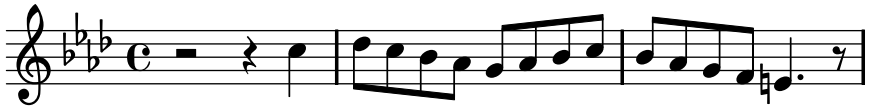

*If music be the food of love*
**Henry Purcell**

Chapter 4

# Non-linear evolution of the magnetic island

## Contents



## 4.1 The Kadomtsev model

In this section we will describe the mechanism of the profile relaxation induced by the non-linear evolution of the sawtooth crash. It will be seen that simple arguments can provide a very simple model to predict the post-crash profiles, and even give an analytical expression for one class of initial $q$ profiles. We will follow the approach from [Furno 2001, Porcelli 1999]. We will see that the model does not necessarily imply a full flattening of the temperature and density profiles. The post-crash $q$ profile is also not perfectly flat but increases very slowly.

### 4.1.1 The model's hypotheses

To derive the results of this section, we will need only 3 conservation laws:

1. Helical flux conservation, that is $\partial_t \Psi^\star + \boldsymbol{v} \cdot \nabla \Psi^\star = 0$. This equation is valid in the plasma except in a narrow layer around the reconnection layer where non-ideal effects are important. This conservation law is the reason why the reconnecting field lines have identical $\Psi^\star$.

2. Toroidal flux conservation. At lowest order in the aspect ratio, this law is equivalent to the conservation of the volume encircled by the reconnecting surfaces. Indeed the dominant almost homogeneous toroidal field is not affected by the reconnection process, so that toroidal flux is equivalent to plasma volume.

3. Thermal energy conservation. The initial and final helical fluxes are denoted $\Psi_i^\star$ and $\Psi_f^\star$. This energy conservation law means that the energy content encircled between the surfaces with fluxes $\Psi_i^\star$ and $\Psi_i^\star + \mathrm{d}\Psi_i^\star$ is equal to the final energy content between the surfaces with final flux $\Psi_f^\star + \mathrm{d}\Psi_f^\star$. It is implicitly assumed that temperature homogenization along the reconnected field line takes place on a very fast time scale, while the crash is assumed fast enough to prevent perpendicular transport. This conservation law means that we neglect heat generation through viscous dissipation of the reconnection jets.

It is clear that these three conservation laws, together with the geometry of the problem completely determine the final state of the plasma. Indeed, the final radius of a surface with final flux $\Psi_f^\star$ is determined by the toroidal flux conservation law, which fixes the final $q$ profile, while the final pressure profile is determined by the energy conservation law. In spite of its simplicity, this model is very instructive. We will now apply it to an example of analytic initial $q$ profile to show the methodology.

### 4.1.2 Magnetic flux reconnection and profile relaxation

#### Magnetic flux relaxation

We take an initial $q_i$ profile of the form

$$q_i = \frac{q_0}{1 - \Delta q (\frac{r}{r_s})^2}, \tag{4.1}$$

with $\Delta q = 1 - q_0$, $q_i(r_s) = 1$. The interest of this profile is that it allows an analytic resolution of the problem. Arbitrary profiles could be easily treated numerically. The associated $q_i$ and $j_\varphi \simeq (r/q)' B_0/(R_0 \mu_0)$ profiles are represented on Fig. 4.1 for $q_0 = 0.9$ and $r_s = \sqrt{3 - 3q_0}$ such that $j_\varphi(a) = 0$. Note that such a distribution is unrealistic since the $q$ profile at the edge is much lower than typical tokamak values.

Recall the expression *Eq.* (2.141) of the equilibrium helical flux,

$$\Psi_i^\star(\psi_0) = \int_0^{\psi_0} (1 - q_i) \mathrm{d}\psi, \tag{4.2}$$

where $\psi$ is the poloidal flux, $\mathrm{d}\psi = q^{-1}\mathrm{d}\Psi_T = q^{-1} R_0^{-1} B_0 r \mathrm{d}r + \mathcal{O}(\varepsilon)$[1]. We normalize the helical flux to $B_0 R_0 \Delta q r_s^2/(2q_0)$: $\bar{\Psi}^\star = \Psi^\star 2q_0 R_0/(B_0 \Delta q r_s^2)$. Thus as a function of the

[1] We adopt the same normalization for the flux as in *Eq.* (2.137).

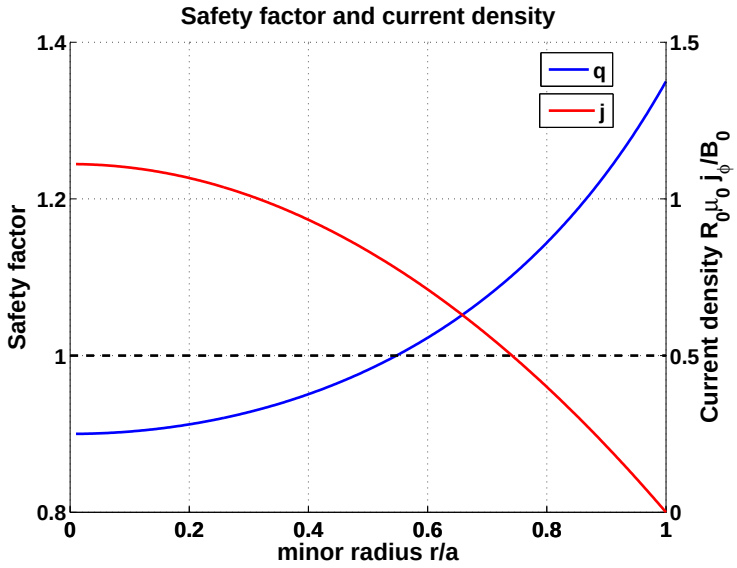


Figure 4.1: Initial safety factor $q_i$ and current $j_\varphi$ profiles corresponding to *Eq.* (4.1).

radius $r$, the initial helical flux is written

$$\bar{\Psi}_i^\star(r) = \frac{q_0}{\Delta q r_s^2}\int_0^r 2rdr(q_i^{-1}-1) = \frac{r^2}{r_s^2}\left(1-\frac{r^2}{2r_s^2}\right). \tag{4.3}$$

It is represented on Fig. 4.2.

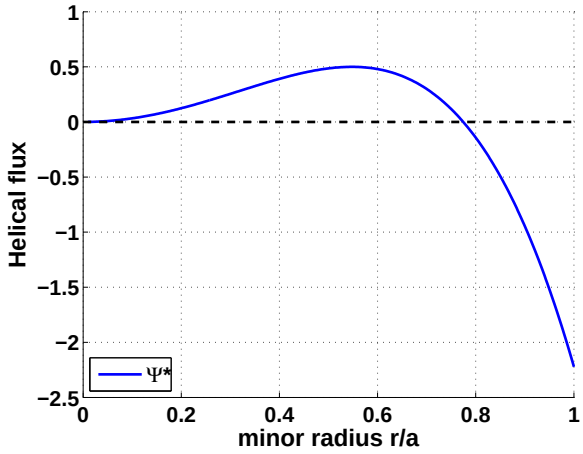


Figure 4.2: Initial helical flux.

The geometry of the problem is presented on Fig. 4.3. The mixing radius $r_{\rm mix}$ is defined as the radius of the surface reconnecting with the magnetic axis, that is: $\bar{\Psi}_i^\star(r_{\rm mix}) = \bar{\Psi}_i^\star(0)$. Here $r_{\rm mix} = \sqrt{2}r_s$. Two surfaces initially at radii $r_1 = (1-\sqrt{1-2\bar{\Psi}_i^\star})r_s$ and $r_2 = (1+\sqrt{1-2\bar{\Psi}_i^\star})r_s$, with identical helical flux reconnect. Because of the structure of the MHD displacement studied in section 2.2, the surfaces with $r < r_s$ move toward the surfaces with $r > r_s$, which do not move. After the reconnection, the separatrix

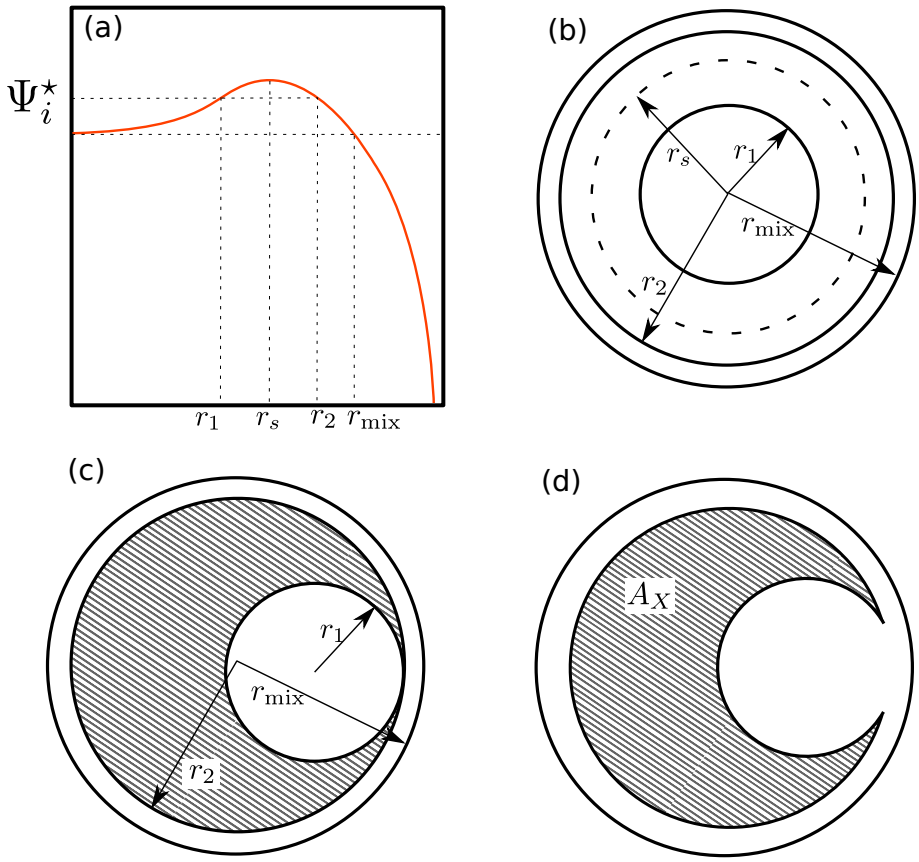


Figure 4.3: Helical flux (a), initial flux surfaces (b), displacement of a core surface towards the separatrix (c), reconnection takes place (d).

unfolds until it becomes a new circle with radius $r_f(\bar{\Psi}_i^\star)$, leaving the enclosed surface $A_X \equiv \pi(r_2^2 - r_1^2)$ invariant, that is $r_2^2 - r_1^2 = r_f^2$, which determines the unknown $\bar{\Psi}_f^\star(r)$. The final relaxed flux is

$$\bar{\Psi}_f^\star(r) = \frac{1}{2}\left(1 - \frac{r^4}{4r_s^4}\right). \tag{4.4}$$

The relaxed safety factor is also easily obtained by inverting *Eq.* (4.2):

$$q_f(r) = \left(1 + \frac{\Delta q r_s^2}{2q_0 r}\frac{\mathrm{d}\bar{\Psi}_f^\star}{\mathrm{d}r}\right)^{-1} = \left(1 - \frac{\Delta q}{4q_0}\frac{r^2}{r_s^2}\right)^{-1}. \tag{4.5}$$

### Temperature and density relaxation

We take initial temperature profiles of the form $T_i = T_0(1 - r^2/a^2)^{\alpha_T}$, $\alpha_T$ determining the peakedness of the profile. We assume first that the density is homogeneous. We will add a density profile later, together with a particle conservation law. Hence energy conservation is equivalent to temperature conservation. The relaxed temperature $T_f$ is

determined from the relation

$$T_f(r) = T_i(r_1)\left|\frac{r_1}{r}\frac{\mathrm{d}r_1}{\mathrm{d}r}\right| + T_i(r_2)\left|\frac{r_2}{r}\frac{\mathrm{d}r_2}{\mathrm{d}r}\right| \quad (4.6)$$

$$= \frac{T_i(r_1)+T_i(r_2)}{2}. \quad (4.7)$$

Thus only for $\alpha_T = 1$ is the relaxed temperature profile perfectly flat and equal to $T(r_s)$. For instance, for a more peaked $\alpha_T = 2$, we find:

$$T_f(r) = T_i(r_s)\left(1 + \frac{r^4}{4(a^2 - r_s^2)^2}\right). \quad (4.8)$$

Interestingly, this profile displays a hotter ring around $r = r_{\mathrm{mix}}$. The amplitude of this hot ring increases with the peaking of the initial profile. Whatever $\alpha_T$, there is a temperature discontinuity at $r = r_{\mathrm{mix}}$, which is rapidly regularized by the perpendicular diffusion.

It is seen that the usual assumption that magnetic reconnection flattens all the profiles is not supported by theoretical considerations. Post-crash profiles happen to be typically flatter than pre-crash profiles, but there is no reason a priori for a full flattening of the profiles.

If now the density is not homogeneous and we add a particle conservation law, *Eq.* (4.7) splits into two equations. Volume elements do not change, so that we have:

$$p_f(r) = \frac{p_i(r_1)+p_i(r_2)}{2} \quad (4.9)$$

$$n_f(r) = \frac{n_i(r_1)+n_i(r_2)}{2}. \quad (4.10)$$

The initial and relaxed profiles of safety factor, helical flux, temperature and density in the case $T_i = T_0(1-r^2/a^2)$ and $n_i = n_0(1-r^2/a^2)$ are represented on Fig. 4.4. Note that $p_i = p_0(1-r^2/a^2)^2$. It is remarkable that despite identical initial profiles, temperature and density behave differently after the crash, because of energy conservation law applying to the pressure rather than the temperature. In particular, it is interesting to note that the temperature inversion radius $r_{\mathrm{inv}}$, defined by the relation $T_i(r_{\mathrm{inv}}) = T_f(r_{\mathrm{inv}})$, is not strictly equal to $r_s$, even if very close. In our example, the hot ring close to $r_{\mathrm{mix}}$ has quite a large amplitude, $\delta T/T_0 \sim 10\%$, but the very large temperature discontinuity at $r_{\mathrm{mix}}$ will partly diminish its amplitude through rapid diffusion.

In spite of its extreme simplicity, this analytic toy model displays the key features of full reconnection Kadomtsev model in the case of monotonic safety profiles:

- $q_f(0) = 1$
- A diminished slope for $q_f$ compared to $q_i$ in the region $r < r_{\mathrm{mix}}$.
- $T_f(0) = T_i(r_s)$.
- $n_f(0) = n_i(r_s)$.
- Profiles significantly flattened

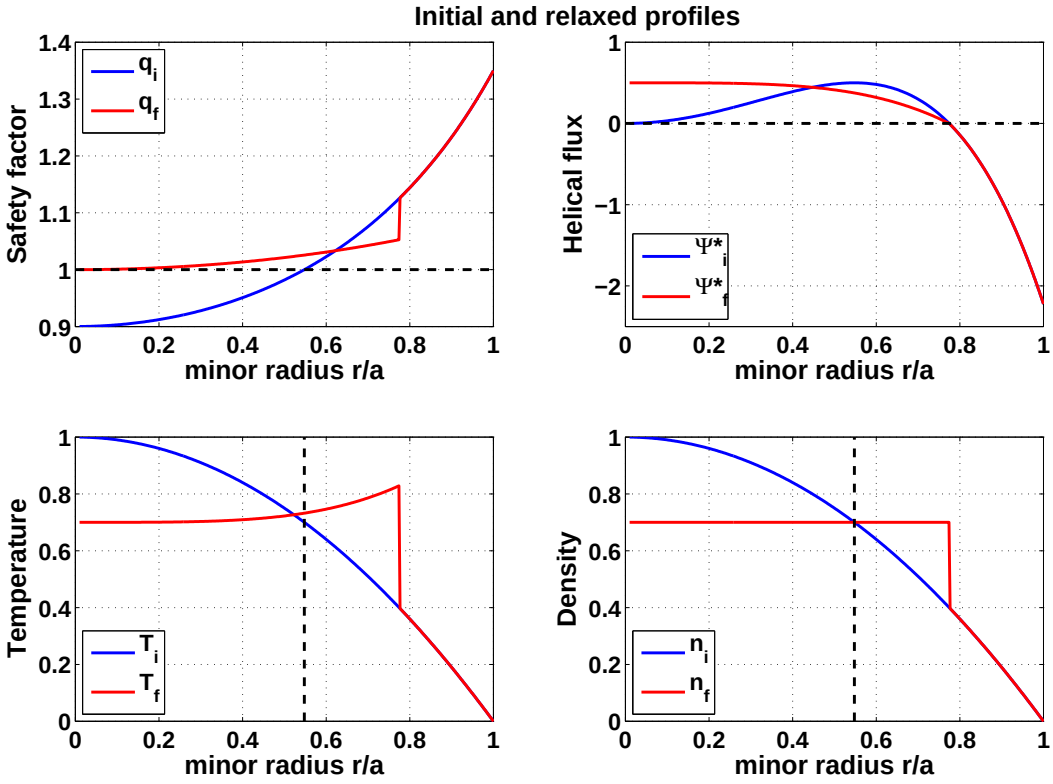


Figure 4.4: Initial and relaxed profiles of safety factor (a), helical flux (b), temperature (c), and density (d) for analytic profiles. The vertical dotted line on (c) and (d) represents the resonant surface location $r = r_s$.

- Inversion radius close to $r_s$.

The first 4 points can be derived rigorously, and the last two at least heuristically. Here we normalize the flux only to $B_0/R_0$ so that $\bar{\Psi}^\star$ has the dimensions of $r^2$. In this normalization, we have

$$q = \frac{1}{1 + (1/r)\frac{\mathrm{d}\Psi^\star}{\mathrm{d}r}}, \tag{4.11}$$

so that $q_i(r_s) = 1$ is equivalent to $\mathrm{d}\bar{\Psi}_i^\star/\mathrm{d}r = 0$. Thus $\bar{\Psi}_i^\star = \bar{\Psi}_{i0}^\star + \bar{\Psi}_0^{\star\prime\prime}(r - r_s)^2/2 + \mathcal{O}\left((r - r_s)^3\right)$. Let us evaluate $\mathrm{d}\bar{\Psi}_f^\star/\mathrm{d}r|_{r=0}$. For a small final radius $\delta r_f \ll r_s$, $\bar{\Psi}_f^\star(\delta r_f) = \bar{\Psi}_i^\star(r_s + \delta r)$ where $(\delta r_f)^2 = 2r_s\delta r$ from helical and toroidal flux conservation. Hence

$$\begin{aligned} \left.\frac{\mathrm{d}\bar{\Psi}_f^\star}{\mathrm{d}r}\right|_{r=0} &= \lim_{\delta r_f \to 0} \frac{\bar{\Psi}_f^\star(\delta r_f) - \bar{\Psi}_f^\star(0)}{\delta r_f} \\ &= \lim_{\delta r_f \to 0} \frac{\bar{\Psi}_0^{\star\prime\prime}}{8r_s^2}\delta r_f^3 \\ &= 0. \end{aligned} \tag{4.12}$$

This implies $q_f(0) = 1$. Secondly, the first and second derivatives of $q_f$ are written

$$\begin{aligned} q_f'(0) &= 0 \qquad (4.13)\\ q_f''(0) &= 2\left(-\frac{1}{r^3}\frac{\mathrm{d}\bar{\Psi}_f^\star}{\mathrm{d}r}\bigg|_0 + \frac{1}{r^2}\frac{\mathrm{d}^2\bar{\Psi}_f^\star}{\mathrm{d}r^2}\bigg|_0 - \frac{1}{2r}\frac{\mathrm{d}^3\bar{\Psi}_f^\star}{\mathrm{d}r^3}\bigg|_0\right)\\ &= -2\frac{\bar{\Psi}_0^{\star\prime\prime}}{r_s^2}\left(\frac{1}{8} - \frac{3}{8} + \frac{3}{8}\right)\\ &= -\frac{\bar{\Psi}_0^{\star\prime\prime}}{4r_s^2}. \qquad (4.14)\end{aligned}$$

Thus we find that in the Kadomtsev model, the $q$ profile after reconnection close to the axis is

$$q_f = 1 - \frac{\bar{\Psi}_0^{\star\prime\prime}}{8}\frac{r^2}{r_s^2} + \mathcal{O}\left(r^3\right). \qquad (4.15)$$

If the parabolic contribution is dominant in the initial safety factor, then $q_i'(r) \sim q_i'' r$ so $q_i'' \sim q'(r_s)/r_s = -\bar{\Psi}_0^{\star\prime\prime}/r_s^2$, and

$$\frac{q_f'}{q_i'} \sim \frac{1}{4}. \qquad (4.16)$$

To understand the four points regarding temperature and density profiles, note that the flattening of the temperature and density profiles is a consequence of the mixing of the temperatures implied by *Eq.* (4.6). For close to parabolic $q$ profiles, $|\frac{r_1}{r}\frac{\mathrm{d}r_1}{\mathrm{d}r}| \sim |\frac{r_2}{r}\frac{\mathrm{d}r_2}{\mathrm{d}r}| \sim 1/2$ and $|T_i(r_1) - T_i(r_s)| \simeq |T_i(r_2) - T_i(r_s)|$ so that $T_f(r) \simeq T_i(r_s)$. However, $T_f(0) = T_i(r_s)$ and $n_f(0) = n_i(r_s)$ are exact results, because close to the resonant surface the preceding relations between volume elements are equalities.

### Numerical implementation

When the safety factor is different from *Eq.* (4.1) (but still monotonic), the post-crash profiles must be computed numerically. In practice, the helical flux is computed, its maximum value $\Psi_{max}^\star$ is determined, and the interval $[0, \Psi_{max}^\star]$ is sampled with $n_\Psi$ values. For each value $\Psi^\star$ of the helical flux, the radii of the reconnecting surfaces on the left and the right of the separatrix, $r_l(\Psi^\star)$ and $r_r(\Psi^\star)$, are determined, and the toroidal flux increments between the new radii and the ones obtained at the preceding step are computed on the left and on the right: $\delta\Psi_{T,l}(\Psi^\star)$ and $\delta\Psi_{T,r}(\Psi^\star)$. The final radius $r_f(\Psi^\star)$ of the surface with helical flux $\Psi^\star$ is determined from the condition of toroidal flux conservation:

$$\Psi_{T,f}(\Psi^\star) = \sum_{\Psi=0}^{\Psi^\star}\left(\delta\Psi_{T,l}(\Psi) + \delta\Psi_{T,r}(\Psi)\right), \qquad (4.17)$$

and the correspondance between radius and toroidal flux is used.

The final density or pressure, generically denoted $n_f$, is determined as a function of the initial profile $n_i$, according to the conservation rule, and using the fact that toroidal flux conservation is almost the same as volume conservation. Thus we find:

$$n_f(r_f(\Psi^\star)) = \frac{n_i(r_l(\Psi^\star))\delta\Psi_{T,l}(\Psi^\star) + n_i(r_r(\Psi^\star))\delta\Psi_{T,r}(\Psi^\star)}{\delta\Psi_{T,l}(\Psi^\star) + \delta\Psi_{T,r}(\Psi^\star)}. \qquad (4.18)$$

We have derived the main geometrical features of Kadomtsev model, but we have not investigated the dynamics of the reconnection yet. This is the topic of the next subsection.

### 4.1.3 Resistive evolution of the island

As explained in section 2.2, the kink instability is associated with a current sheet where the current density becomes large. This means that resistivity can become important in Ohm's law. Here we will see that when reconnection is dominated by resistivity, the reconnection time scales as

$$\tau_{\rm rec} = \sqrt{\tau_{R,s}\tau_I}, \tag{4.19}$$

with $\tau_{R,s} = r_s^2/\bar{\eta}$ the relevant resistive time and $\tau_I = \sqrt{\mu_0\rho}/\Psi_0^{\star\prime\prime} = \tau_A/\hat{s}$ the relevant Alfvén time ($\hat{s}$ is the shear), as in section 2.2.3. To derive this result, we will need, again, very few elements.

1. The general topology of the reconnection: we assume that there is a Sweet-Parker (*cf.* section 2.3.4) current sheet of thickness $\delta$ and half angular width $\pi/2$ as a first approximation[2].

2. Ohm's law, which we will write

$$\partial_t\Psi_1^\star + \boldsymbol{v}\cdot\nabla\Psi_1^\star = \bar{\eta}\nabla_\perp^2\Psi_1^\star. \tag{4.20}$$

   In this context where non-ideal effects are dominated by resistivity, the meaning of Ohm's law is clear, it contains all the physics necessary to understand the phenomenon. In the frame moving with the current sheet, the flux is convected by the velocity $v \simeq \pm u_0$ from each side. This process tends to compress the flux at the resonant surface, while the resistivity tends to dissipate the flux, resulting in a finite sheet thickness $\delta$. Dimensional analysis immediately yields

$$\delta \simeq \frac{\bar{\eta}}{u_0}. \tag{4.21}$$

3. Finally note that $W = 2\xi$, so that $\dot{W} = 2\dot{\xi} = 4u_0$. Indeed, *Eq.* (4.20) in the ideal region linearized around $\boldsymbol{v} = 0$ yields $\Psi_1^\star = -x\xi_r\Psi_0^{\star\prime\prime}$, and the total helical flux is $\Psi^\star = \Psi_0^{\star\prime\prime}/2\,(x^2 - 2x\xi_r)$, with $x = r - r_s$, $\xi_r = \xi\cos\theta$ for $x < 0$, $\xi_r = 0$ for $x > 0$. Therefore the separatrix, where $\Psi_1^\star = 0$, is delimited by the lines $x = 0$ and $x = 2\xi\cos\theta$ for $\theta \in [\pi/2, 3\pi/2]$, and $W = 2\xi$. Then recall the preceding section, where it was seen that the reconnection layer at $r = r_2$ moves from $r_s$ to $r_{\rm mix}$, because the plasma is stationary for $r > r_2$ while the flux needs to be reconnected on both sides. Thus the relative velocity $u_0$ between the plasma and the sheet is $u_0 = \dot{\xi}/2$.

[2] This approximation will be relaxed in section 4.2.1, where it is shown that it is actually close to 60°.

According to Sweet-Parker reconnection model, the current sheet width is defined by the point where the outcoming velocity is the Alfvén velocity computed with the helical field at the entrance of the sheet

$$v_A^\star \equiv \left.\frac{B_\theta(1-q)}{\sqrt{\mu_0\rho}}\right|_{x=\xi/2} = \frac{1}{\sqrt{\mu_0\rho}}\frac{\mathrm{d}\Psi_0^\star}{\mathrm{d}r} = \frac{1}{\sqrt{\mu_0\rho}}\frac{\Psi_0^{\star\prime\prime}\xi}{2}. \tag{4.22}$$

We write mass conservation across the sheet.

$$\int_0^{\frac{\pi}{2}} r_s u_0 \cos\theta \mathrm{d}\theta = \delta v_A^\star, \tag{4.23}$$

that is

$$u_0 = \frac{\delta}{r_s} v_A^\star. \tag{4.24}$$

Using the scaling $\delta \sim \bar{\eta}/u_0$ and replacing the expression for $v_A^\star$, we find that

$$\frac{\mathrm{d}}{\mathrm{d}t}\left(\frac{W}{r_s}\right) = 2\sqrt{\frac{\bar{\eta}\Psi_0^{\star\prime\prime}}{r_s^2\sqrt{\mu_0\rho}}}\left(\frac{W}{r_s}\right)^{1/2}, \tag{4.25}$$

so that the island growth is given by

$$\frac{W}{r_s} = \left(\frac{t}{\tau_{\mathrm{rec}}}\right)^2. \tag{4.26}$$

Finally the island is growing quadratically in a timescale $\tau_{\mathrm{rec}}$, where $\tau_{\mathrm{rec}}$ is defined by *Eq.* (4.19).

This model needs some caveats. First, the evolution equation for $W$ is valid only for small island widths, so that taking $W = r_s$ in *Eq.* (4.26) to obtain the reconnection time $\tau_{\mathrm{rec}}$ does not really make sense. Also, the sheet width $\delta$ cannot be constant across the sheet if the latter extends from $\theta = \pi/2$ to $\theta = -\pi/2$. Indeed the scaling $\delta \sim \bar{\eta}/u_0$ comes from equilibrating the l.h.s. and the r.h.s. of Ohm's law. This actually reads:

$$u_0 \cos\theta = \frac{\bar{\eta}}{\delta(\theta)}, \tag{4.27}$$

since the motion inside $q = 1$ is a mere displacement in the $x$ direction. We allow the sheet thickness to depend on $\theta$. Note that since $\Psi^\star \propto W^2$, the ratio between the advective terms and the time derivative term is of order $W/\delta$ in Ohm's law, so the preceding equation becomes valid only after $W$ becomes much larger than the sheet width $\delta$. *Eq.* (4.27) shows that our assumption that the sheet extends from $\theta = -\pi/2$ to $\theta = \pi/2$ cannot be correct since this implies a divergence in $\delta$. More precise models will be studied in chapter 4. In spite of this, gives the correct scaling. We can express it with more usual quantities, since the quantity $\Psi_0^{\star\prime\prime}$ is not very meaningful. It can be pretty easily shown that $\Psi_0^{\star\prime\prime} \simeq \hat{s}B_0/R_0$, where as usual $\hat{s}$ is the shear at the $q = 1$ surface, $\hat{s} \equiv r_s q'(r_s)/q$. Taking the $T^{-3/2}$ dependence of resistivity, we obtain the following scaling for the Kadomtsev reconnection time:

$$\tau_{\mathrm{rec}}(s) = 3\times10^{-3}\times r_s(\mathrm{m})\times R_0(\mathrm{m})^{1/2}\times n_0(10^{19}\mathrm{m}^{-3})^{1/4}\times s^{-1/2}\times B_0(\mathrm{T})^{-1/2}\times T_{e0}(\mathrm{keV})^{3/4}, \tag{4.28}$$

where we immediately see that 1 ms is the typical order of magnitude for hot tokamak plasmas. To obtain this value, we used Spitzer's parallel resistivity, *Eq.* (2.59), and everything except temperature is expressed in S.I. units. We will compare this scaling with the experimentally deduced crash times in section 5.2.3.

### 4.1.4 Discussion

We have presented the Kadomtsev model which constitues the most notorious paradigm for the sawtooth instability. It is easy to handle and reproduces at least the observed collapse of the temperature and the link with the internal kink mode. However, as will be seen in section 5.2, many experimental features are not reproduced, most importantly the time scale of the crash is too long compared to the experiment, and the safety factor is not seen to rise to 1 after the sawtooth crash in most cases.

Now we have a better idea of the sawtooth instability and its effect on the plasma density and temperature. It is seen why it is an important phenomenon in tokamaks. On the one hand, the frequent reorganization of the core means that the fusion power in a reactor[3] is transiently reduced significantly when the profiles are peaked, but on the other hand the accumulation of impurities (medium or high $Z$ impurities coming from the wall, and He ash) must be avoided, and we see that sawteeth may be a way to remedy this, as suggested in Refs. [Nave 2003, Belo 2004, Nakano 2009]. Nowadays, there is a consensus toward trying to obtain frequent sawteeth by destabilizing the internal kink mode rather than stabilizing it (see section 2.2.7). The impurity issue will be investigated in chapter 7 with XTOR-2F, and there will also be a comparison with Kadomtsev model.

In the following subsection, we briefly outline an alternative notorious model of the sawtooth crash, developed by Wesson in 1986 [Wesson 1986].

### 4.1.5 Wesson's model

In Wesson's model, the basic hypothesis is that of a very flat safety factor profile in the core. Thus there is no magnetic shear and the interchange of flux tubes becomes easily possible. The (1/1) eigenfunction in the case where $1 - q \sim 10^{-2}$ is quite different from the step function studied in section 2.2. Indeed the asymptotic matching of Fig. 2.4 completely fails when $q$ is too close to 1. The model assumes that the safety factor approaches unity from above and has an off-axis minimum. The instability is of ideal type and triggered very rapidly. A cold bubble from the more external region is driven inside while the hot core is distorted in a crescent-shaped structure.

The main problem with this model is the assumption of a very flat safety factor. As we will see in section 5.2.6, this is inconsistent with the core safety factor measurements of many machines.

[3] $P_{fus} \propto p^2$ roughly in a range of parameters relevant to a reactor.

## 4.2 Refined Kadomtsev-like evolution

### 4.2.1 Waelbroeck's model

Kadomtsev's model can be refined significantly using the fact that the reconnection time is much longer than the Alfvén time, which means the nonlinear evolution of the island can be regarded as a series of quasi-static equilibria. This was done by Waelbroeck in 1989 [Waelbroeck 1989] and precised by Zakharov four years later [Zakharov 1993]. Their work allows to give a method to compute the poloidal extension of the current sheet and the precise relation between the island with and the MHD displacement. Taking the curl of the static ideal equation of motion, *Eq.* (2.45), and neglecting the inertia term, one obtains

$$\mathbf{B} \cdot \nabla \mathbf{J} = \mathbf{J} \cdot \nabla \mathbf{B}. \tag{4.29}$$

Starting from this equation, it is possible to show that the actual relations between the island with $W$, the core MHD displacement $\xi_0$ and the position of the separatrix $x_s$, are

$$x_s = 0.4\xi_0, \quad W = 1.84\xi_0. \tag{4.30}$$

Also, the model predicts that the current sheet is a ribbon of angular width $\theta_0 \simeq 60°$. These results are found by solving a set of two implicit equations. We did not carry out the numerical resolution but the derivation of Waelbroeck's equations is done in appendix F.

The magnetic structure during the nonlinear evolution can be seen on Fig. 4.5. One sees the ribbon spreading $-60° < \theta < 60°$ at the separatrix. The flux surfaces are slightly deformed in front of the sheet Notice that the results for $x_s$ and $W$ are pretty close to the

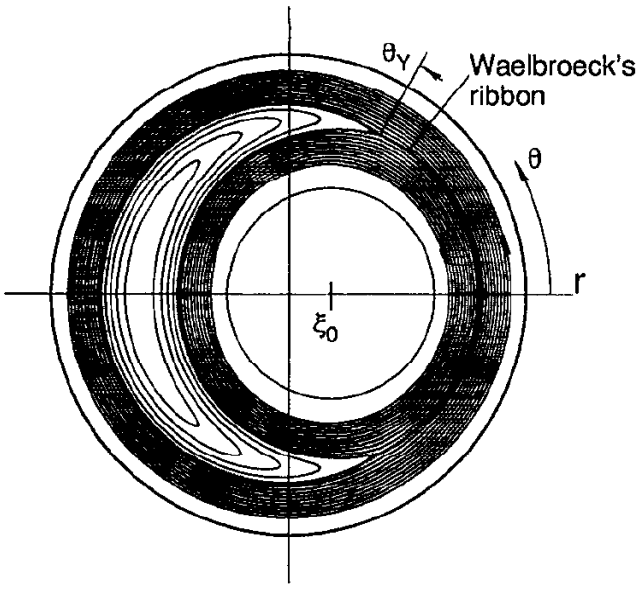


Figure 4.5: Nonlinear magnetic structure according to Waelbroeck's model. Figure taken from [Zakharov 1993].

ones deduced from simpler geometrical considerations in section 4.1.3, namely $x_s = \xi_0/2$

and $W = 2\xi_0$. Thus this analysis still holds and the same behaviour is obtained but the precise numerical result is modified. Also, notice that now the divergence discussed before due to the choice $\theta_0 = \pi$ disappears. In particular, *Eq.* (4.24) becomes

$$u_0 = \frac{\delta(\theta_0)}{r_s \sin\theta_0} v_A^\star, \tag{4.31}$$

where $\delta(\theta_0)$ is the sheet width at the end point of the sheet. And we have already seen that Ohm's law actually implies (*Eq.* (4.27)):

$$u_0 = \frac{\bar{\eta}}{\delta(\theta_0)\cos\theta_0}. \tag{4.32}$$

Here $u_0 = \dot{\xi}_0 - \dot{x_s} = (1-0.4)\dot{W}/1.84$. Thus putting eveything together, we see that the reconnection time, *Eq.* (4.19), must be multiplied by

$$2(1-0.4)\sqrt{\frac{2}{1.84}\cos\theta_0 \sin\theta_0} \simeq 0.82, \tag{4.33}$$

which is very close to 1. Hence Kadomtsev's result is almost not modified but the theoretical geometrical structure of the magnetic field is precised.

We now proceed to a comparison of these results with XTOR-2F simulations of the resistive kink.

### 4.2.2 Comparison with XTOR-2F

The equilibrium used for this study is the same as the one used for Fig. 3.5. Also, the same Lundquist number $S = 10^7$ is used. Fig. 4.6 shows two Poincaré plots for this typical resistive kink simulation. Panel b) shows apparently a good agreement with the qualitative feature of Waelbroeck's model that there is a ribbon between the tips of the island, corresponding to the current sheet. However this feature is not found in the early stage of the reconnection process, panel a), which is surprising considering that Waelbroeck's analysis normally applies to thin island (recall that we repeatedly made this assumption in the preceding analysis). Fig. 4.7 shows the same Poincaré plots in the $(r, \theta)$ space. The extension of the ribbon can be easily measured on panel b). It is approximately 70°, which is almost twice smaller than Waebroeck's prediction, $2\theta_0 = 120°$. Notice that the angular extension of the current sheet is closer to Waelbroeck's value, around 130° throughout the reconnection (see Fig. 4.8).

It is also interesting to compare the relations between $\xi_0$, the displacement of the magnetic axis, $x_s$, the position of the separatrix, and the island width $W$. These three quantities are evaluated by hand on the poincare plots. A large number of Poincaré plots is used (more than 200) and the fluctuations related to the imprecise evaluation by hand are smoothed by averaging over a few points. The results are shown on Fig. 4.9. On panels a) and b), the blue curve is $\xi_0$. The red curve is $W$ on panel a) and $x_s$ on panel b). The evolution of the different quantities are seen to be best correlated in the early nonlinear phase. Selecting the time range in which the agreement is good, the values of the ratios $x_s/\xi_0$ and $W/\xi_0$ are evaluated. We find

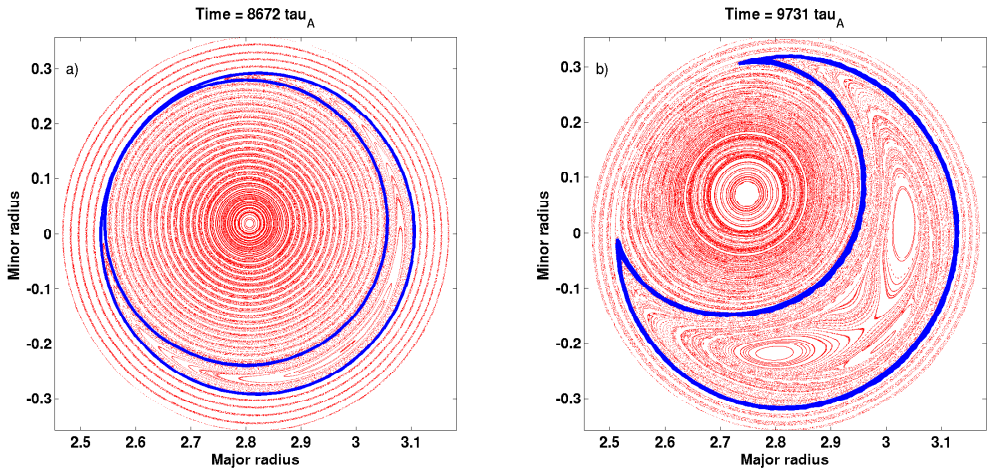


Figure 4.6: Poincaré plots at the beginning of the nonlinear phase (a) and in the far nonlinear stage (b). Field lines closest to the separatrices are displayed in blue. As usual, only the innermost part of the plasma where the reconnection is happening is displayed.

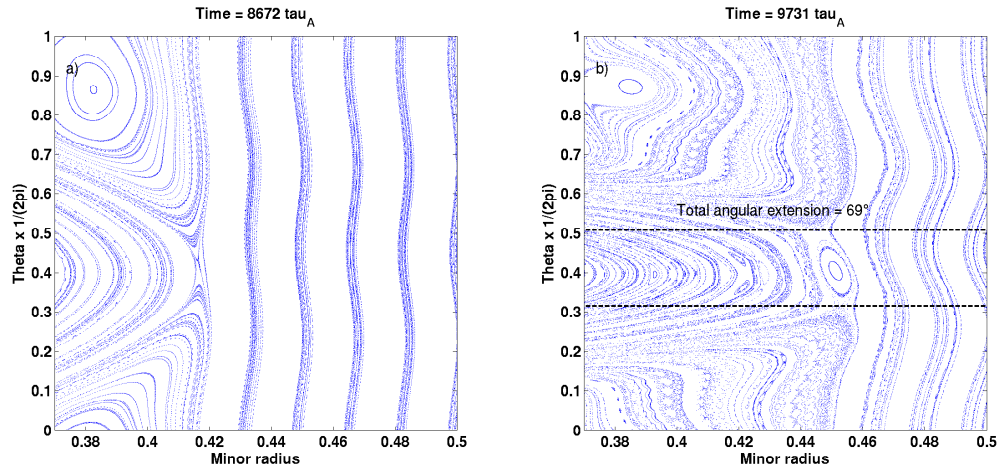


Figure 4.7: Same figure as Fig. 4.6 plotted in the $(r, \theta)$ space. On panel (b), the angular extension of the sheet can be seen to be about 70°, almost twice smaller than Waelbroeck's prediction, which is $2 \times 60° = 120°$. Notice that the small island seen on panel b) at $r = 0.45, \theta/2\pi = 0.4$ is too small to be seen on Fig. 4.6 b).

$$x_s = (0.41 \pm 0.02)\xi_0, \quad W = (1.78 \pm 0.13)\xi_0, \tag{4.34}$$

in good agreement with Waelbroeck's model. On the figure, the curves corresponding to the fits are are plotted, where the good agreement can be seen for early times. The agreement is not good toward the end of the reconnection process, especially for $x_s$. This is not surprising since for large values of $x$, the flux departs further and further away from

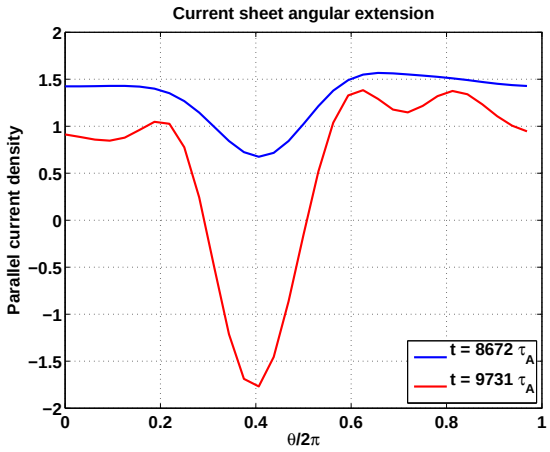


Figure 4.8: Current sheet angular extension in the early and late stages of reconnection. The angular extension is not seen to change, only the amplitude of the current sheet is modified.

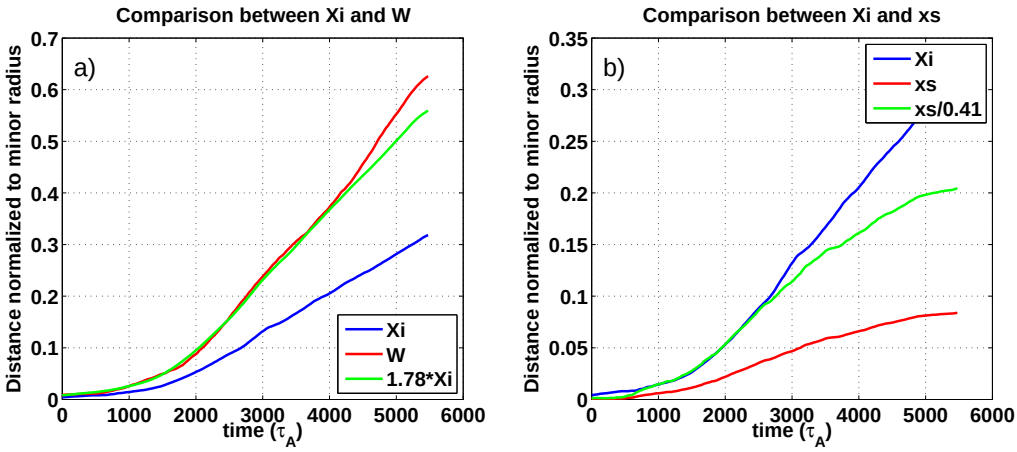


Figure 4.9: Comparison of the relations between $\xi_0$, $x_s$ and $W$ with Waelbroeck's model. $\xi_0$ and $W$ (a), $\xi_0$ and $x_s$ (b).

a quadratic expression. Fig. 4.10 shows the time derivative of the displacement $\xi_0$. It is seen that the initial phase is linear (compatible with a quadratic island growth), during roughly the first 1000 Alfvén times, then the slope increases by a factor of almost 3, and then there is a saturation after around 2500 Alfvén times (corresponding to even slower linear growth) until the end of the reconnection phase. Since the initial phase has the same scaling as Kadomtsev's/Waelbroeck's model, it is interesting to compare the fitted quadratic coefficient with XTOR-2F's value. Translated into XTOR-2F's normalization, Waelbroeck's reconnection time is

$$\tau_{rec,XTOR} = 0.82 \frac{r_s}{a} \left( \frac{\eta_0}{\eta(r_s)} \frac{S}{\hat{s}} \right)^{1/2}, \tag{4.35}$$

where $\eta_0$ is the resistivity in the centre, $\eta(r_s)$ the resistivity at the resonant surface, $S$

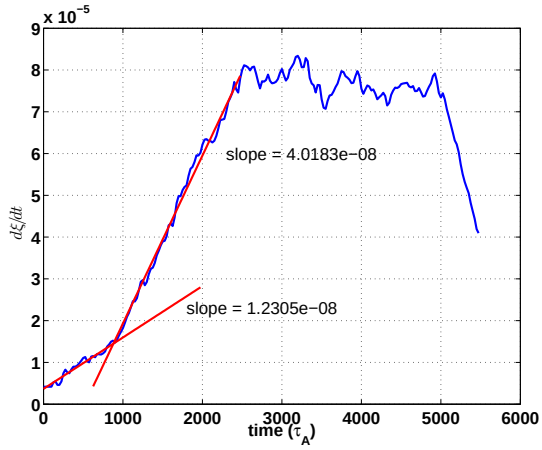


Figure 4.10: Evolution of $\mathrm{d}\xi_0/\mathrm{d}t$ during the reconnection

the Lundquist number and $\hat{s}$ the shear at the $q = 1$ surface. This implies for $\mathrm{d}_t\xi_0$ a slope $(2/(1.8 \times 0.82^2))(a/r_s)(\eta(r_s)/\eta_0)S^{-1}\hat{s} \simeq 1.3 \times 10^{-7}$, with $S = 10^{-7}$, $\hat{s} = 0.2$, $\eta(r_s) = 1.6\eta_0$ and $r_s = 0.4a$. With these values, we also obtain $\tau_{rec,XTOR} \sim 2000\tau_A$. Comparing to the figure, we see that the value for the slope of $\mathrm{d}_t\xi_0$ is one order of magnitude too high for the early nonlinear phase, but has the good order of magnitude (still 2-3 times too large) for the second phase (from $1000\tau_A$ to $2500\tau_A$). Note that the change of slope at $t \simeq 1000\tau_A$ could correspond to the aforementioned transition where $W$ becomes much larger than $\delta$ and where Kadomtsev's scalings become a good estimate.

## 4.3 The bifluid case: asymmetric island with 1 X-point

As we will see, the structure of the sheet is significantly modified when the bifluid term corresponding to Hall terms is added in XTOR-2F's Ohm's law. Recall that in this case Ohm's law is

$$\mathbf{E} + \boldsymbol{v} \times \mathbf{B} = -\frac{\nabla_{\parallel} p_e}{n_e e} + \eta \mathbf{J}. \tag{4.36}$$

The discovery that the nonlinear evolution of the internal kink mode can be accelerated in a bifluid framework compared to single fluid dates back to the beginning of the 1990s, with the work of Zakharov & Rogers [Zakharov 1992, Zakharov 1993], Aydemir [Aydemir 1992], and Wang & Bhattacharjee [Wang 1993]. The linear stabilization due to the bifluid effects was already well known [Ara 1978], and quite ironically, it was also found by Rogers in 1995 [Rogers 1995] that these effects may also stabilize the kink nonlinearly, leading to a small amplitude saturated state, rather than to a destabilization. Before discussing this apparent contradiction, let us first derive the reconnection scaling obtained when the bifluid term is taken to be dominant over the resistive term. We will then compare to the XTOR-2F case. This analysis is taken from Ref. [Wang 1993].

### 4.3.1 Wang's model

We have already derived the relevant scalar expression for Ohm's law when the parallel electron pressure gradient is involved, *Eq.* (D.2). It is recalled below, with the resistive term removed:

$$\partial_t \Psi^\star + (\boldsymbol{v}_1 + \boldsymbol{v}_e^\star) \cdot \nabla \Psi^\star = 0. \tag{4.37}$$

In the current sheet, the inflow $v_r$ is imposed by the diamagnetic term:

$$v_r = -v_{er}^\star = -\frac{\partial_\theta p}{n e r_s B_0}. \tag{4.38}$$

We use the latter equation to relate the velocity at the entrance of the sheet to the velocity at the other end of the sheet. Integrating from 0 to $\theta_0$, one obtains:

$$\begin{aligned} u_0 \sin\theta_0 &= \int_0^{\theta_0} v_r \mathrm{d}\theta \\ &= \int_0^{\theta_0} -\frac{\partial_\theta p}{n e r_s B_0} \\ &\simeq \int_0^{\theta_0} \frac{\partial_\theta \left(\rho v_\theta^2\right)}{n e r_s B_0} \\ &\simeq \frac{1}{\omega_{ci} r_s} {v_A^\star}^2. \end{aligned} \tag{4.39}$$

To go from the second to the third line, we used the results of section 2.3.4, where it was shown that the pressure term and the magnetic force term play comparable roles in the acceleration along the sheet. Finally for the last line we use, again, the fact that the outflow velocity is the reduced Alfvén velocity.

This implies the following scaling for the island growth (taking for simplicity $u_0 = \dot{W}/4$ and $V_A^\star = \hat{s} W/4\tau_A$):

$$\frac{\mathrm{d}W}{\mathrm{d}t} = \frac{1}{4} \frac{r_s}{R_0} \frac{\alpha \hat{s}^2}{\sin\theta_0} \frac{a}{\tau_A} \left(\frac{W}{r_s}\right)^2, \tag{4.40}$$

where $\alpha = d_i/a$ is the normalized ion skin depth and $\theta_0$ is the angular extension of the inertial layer (which does not need be the same as in Waelbroeck's model[4]). This can be a faster growth than the resistive growth of Kadomtsev's model. Indeed, assuming that $\theta_0$ is the same in both cases, the ratio between the growth rates $\mathrm{d}W/\mathrm{d}t$ of *Eq.* (4.40) (index 2) and *Eq.* (4.25) (index 1) is[5]

$$\frac{\mathrm{d}_t W_2}{\mathrm{d}_t W_1} = \frac{1}{8} \frac{r_s}{R_0} \frac{\alpha \hat{s}^{3/2} S^{1/2}}{\sqrt{\tan\theta_0}} \left(\frac{W}{r_s}\right)^{3/2}. \tag{4.41}$$

[4]Notice that Waelbroeck's model results from purely geometrical assumptions and not from the physics in Ohm's law. Thus we could expect his results to be still valid. However the bifluid term in Ohm's law introduces poloidal asymmetries which make the geometry more complicated, and also the faster growth predicted by *Eq.* (4.40) probably leads to the breakdown of the equilibrium assumption used for *Eq.* (F.2), Waelbroeck's basic equation.

[5]Introducing $(\sin\theta_0 \cos\theta_0)^{-1/2}$ in *Eq.* (4.25) to account for the angular width of the sheet.

With experimental values of the parameters, $\alpha \sim 0.1$, $S = 2 \times 10^8$, $\hat{s} = 0.2$ and assuming $\tan\theta_0 \sim 1$, this ratio is of the order of 2 toward the end of reconnection $W \to r_s$. The growth can be further enhanced when $\theta_0$ becomes small. Also, solving *Eq.* (4.40), we see that the growth is explosive:

$$\frac{W}{W_0} = \frac{t_c}{t_c - t}, \tag{4.42}$$

where

$$\frac{t_c}{\tau_A} = \frac{\sin\theta_0}{\alpha \left(\frac{W_0}{r_s}\right) \hat{s}^2}, \tag{4.43}$$

and $W_0$ is the island width at $t = 0$. There is explosive growth of the island width when $t \to t_c$, but since $t_c$ depends so critically on $W_0$, this time is not very meaningful and of low practical use. Also, this explosive growth holds only when $W \gg r_s$, which obviously does not make any sense. When comparing to XTOR-2F, it is more useful to compare directly $\mathrm{d}_t W$ with $W^2$ following *Eq.* (4.40). However we do not expect a significant increase of the island growth rate in XTOR-2F case, because the Lundquist number is $S = 10^7$ only, in which case *Eq.* (4.41) actually predicts a growth slower than in the resistive case.

### 4.3.2 Comparison with XTOR-2F

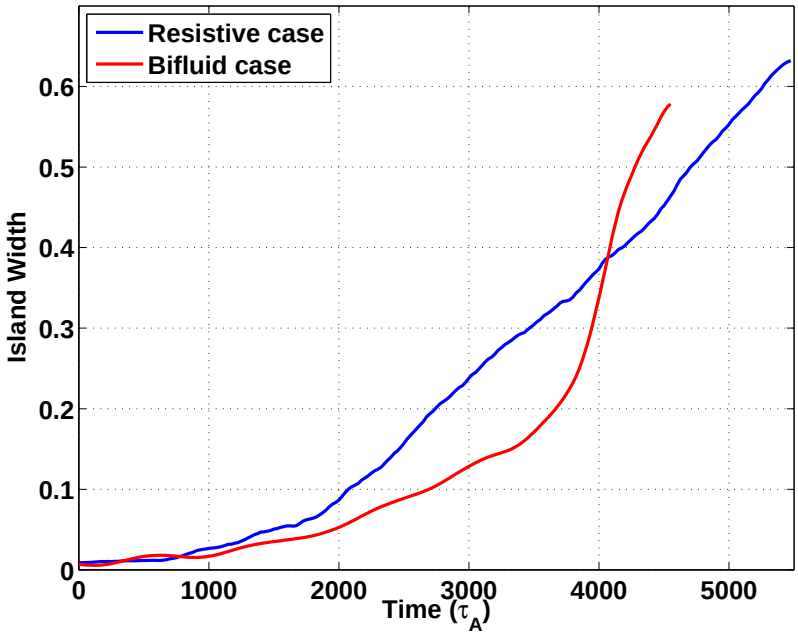


Figure 4.11: Comparison between island width evolution for the resistive (blue) and bifluid (red) cases. A significant stabilization followed by a fast destabilization can be observed in the bifluid case.

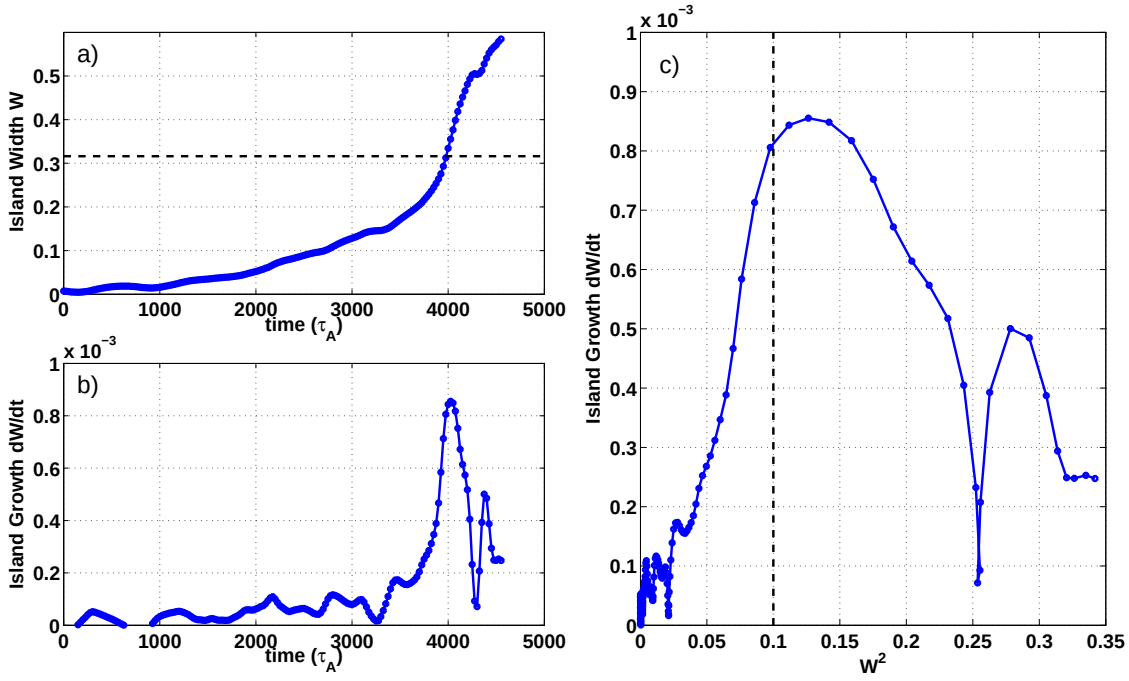


Figure 4.12: Island width (a), island width time derivative $\mathrm{d}W/\mathrm{d}t$ versus time (b) and width time derivative $\mathrm{d}W/\mathrm{d}t$ versus $W^2$ (c). Distances are normalized to $a$ and time to $\tau_A$, as usual.

The simulation used in this subsection to compare XTOR-2F's island growth with the bifluid (or Hall) term in Ohm's law is exactly the same as in section 4.2.2. The only difference is that we have set $\alpha$ to 0.1 instead of 0. As a result, there are additional terms in the continuity, pressure, momentum and induction equations. The terms are proportional to the ion diamagnetic frequency $\omega_i^\star$ for the three first ones, and to the electron diamagnetic frequency $\omega_e^\star$ for the last one. We have checked by switching off alternatively the ion and electron terms that the most important to obtain the features presented in this subsection is the latter term. The evolution over several sawtooth crashes was presented in section 3.2.3, see Fig. 3.7.

The results of the simulation are displayed on Figs. 4.11, 4.12 and 4.13. On Fig. 4.11, the island width growth over time is plotted for the bifluid case, compared to the resistive case. We note that the growth is at first much slower than in the resistive case, by typically a factor of 2. Then, at $t = 3500\ \tau_A$, island growth suddenly accelerates and becomes almost one order of magnitude higher than in the resistive case. It takes almost 4000 Alfvén times for the island width to reach $W/a = 0.2$, and the last phase which leads to $W/a = 0.6$ lasts less than 1000 $\tau_A$. Translated in seconds, using an Alfvén time of $2 \times 10^{-7}$ s (note that $\alpha = 0.1$ has the good order of magnitude), the first phase lasts almost 1 ms and the second one only a few hundreds of microseconds.

Fig. 4.12 shows the comparison of the island growth with that expected from

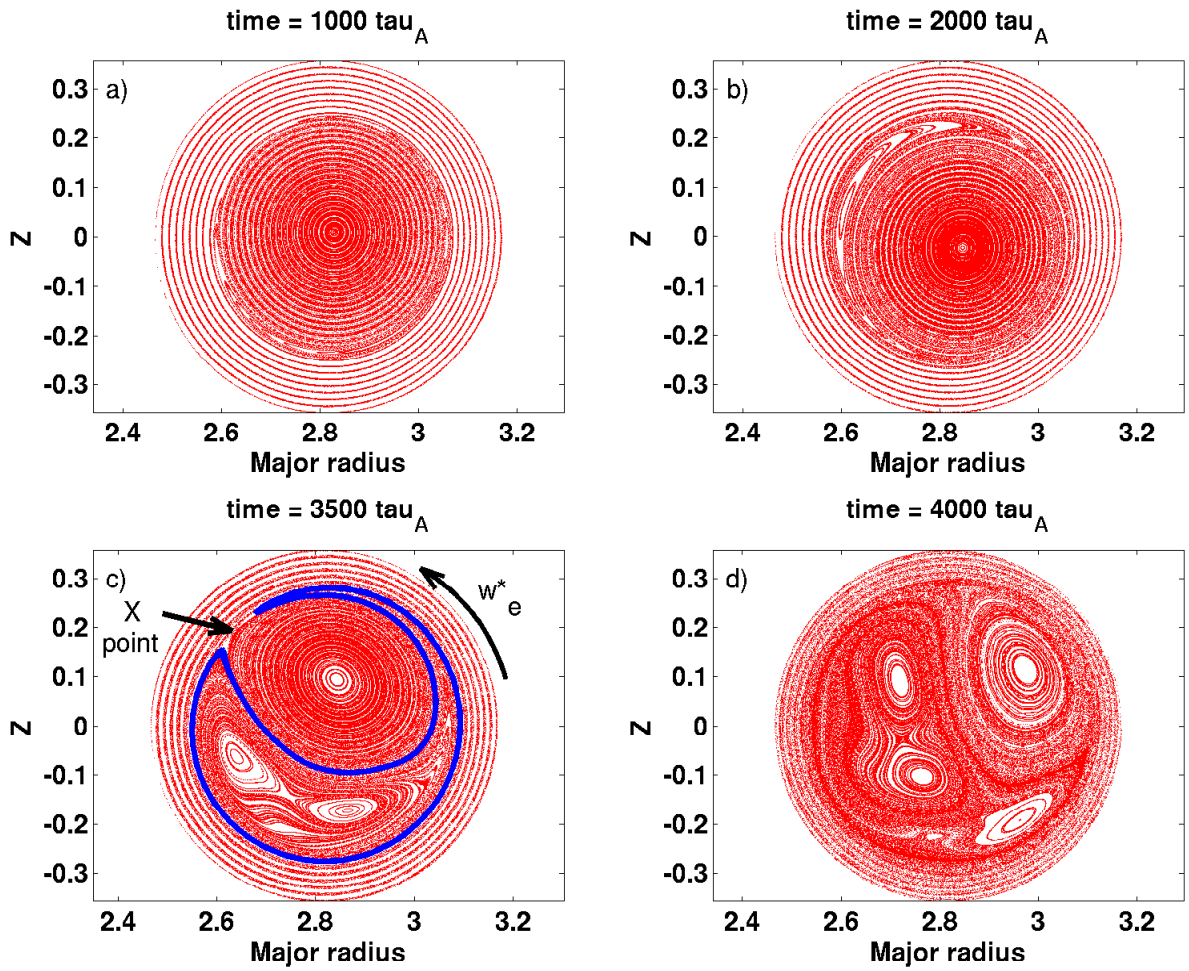


Figure 4.13: Poincaré plots of the magnetic field during Island growth, at $t = 1000$, 2000, 3000 and 4000 $\tau_A$ (a), (b), (c), (d). As usual, the origin of times coincides with the beginning of the reconnection phases, which lasts approximately 5000 $\tau_A$. On panel (c), a field line closest to the separatrix, the inferred position of the X-point, and the electron diamagnetic direction are shown.

*Eq.* (4.40). It is seen that until $(W/a)^2 = 0.1$ (vertical dashed line on panel (c) and corresponding horizontal dashed line on panel(a)), $\mathrm{d}_t W$ is reasonably linear[6] with respect to $W^2$. The slope is of the order of $10^{-2}$, which is more than one order of magnitude larger than predicted by *Eq.* (4.40). Indeed when written in XTOR-2F units, this equation predicts a slope $(1/4)(a/r_s)(a/R_0)\alpha\hat{s}^2/\sin\theta_0 \sim 7\times10^{-4}$ with $a = 2r_s$, $\alpha = 0.1$, $\hat{s} = 0.2$, and $\sin\theta_0$ of order 1.

We now come to the angular extension of the sheet, $\theta_0$. Wang's model predicts that it should be small, typically $\sin\theta_0 \simeq \theta_0 \simeq (\hat{s}\alpha)^{1/2} \sim 0.1$. We see that it is supposed to

[6]Plotting $\log(\mathrm{d}_t W)$ versus $\log(W)$, the overall slope is compatible with a value of 2, however in the faster phase, it is closer to 3.

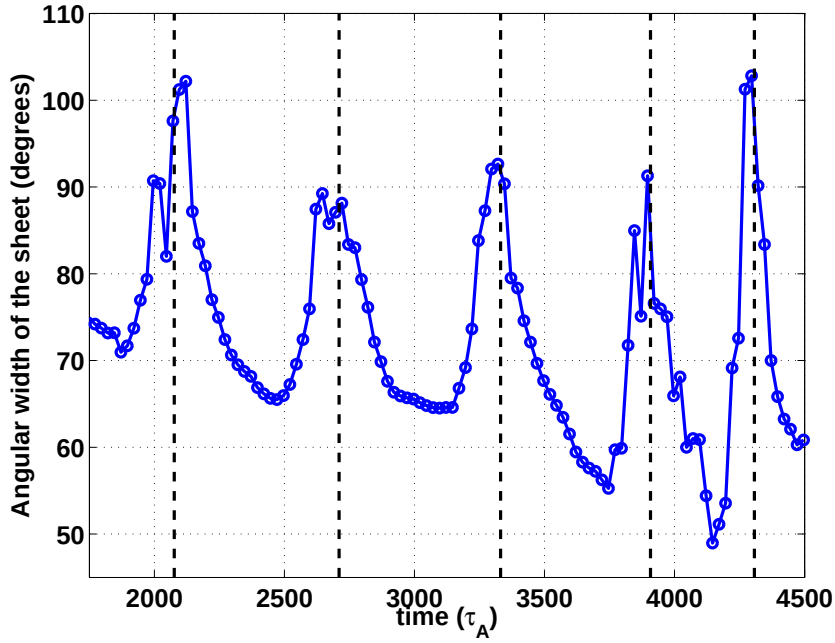


Figure 4.14: Evolution of the current sheet angular extension in the bifluid simulation. The vertical dashed lines indicate the times when the sheet center is at the position $\theta = 0$ (Low Field Side).

enhance the island growth by an other order of magnitude. This is due to the fact that reducing the size of the inlet with fixed outflow velocity (the reduced Alfvén velocity) results in increasing the inflow. This change should be seen on the magnetic flux as the formation of an X-point, instead of the usual ribbon with two Y-points at the end. Also, the current sheet should significantly shrink. Fig. 4.13 shows indeed a change of topology. After $t = 3000\ \tau_A$ (b), the island and expelled core are seen to adopt an asymmetric structure. The island extends in the poloidal direction: on top of the expelled core on panel (b), a thin band coming from the island seems to penetrate the sheet. Note that this penetration is in the direction of the electron diamagnetic drift, which is consistent with the fact that the magnetic flux is advected at the total electron velocity. The thin band seems to detach the expelled core from the inertial layer, thereby in principle reducing the amplitude of the current sheet at this location (which amounts in reducing its angular extension).

This change of regime compared to the previous resistive case could be due to the combination of the scaling of *Eq.* (4.40) and the change of topology we have just discussed. However, contrary to what the Poincaré plots suggest, the actual extension of the current sheet is not much reduced, as seen on Fig. 4.14. The figure is quite difficult to read because of the important modulation at the rotation frequency of the mode. Namely, the current sheet is widest when the current sheet is on the low field side and thinnest when it is on the high field side. On top of this modulation, we see a secular decrease of the angular width of about 20°. However, this change is quite small and does not lead to the width

predicted by the model, despite the fact that an X-point configuration can be seen on the Poincaré plots. This is because the detachment of the expelled core from the layer is actually quantitatively quite small, thus the current obtained as the reconnecting field jump across the two branches of the separatrix divided by the distance between these separatrices remains significant.

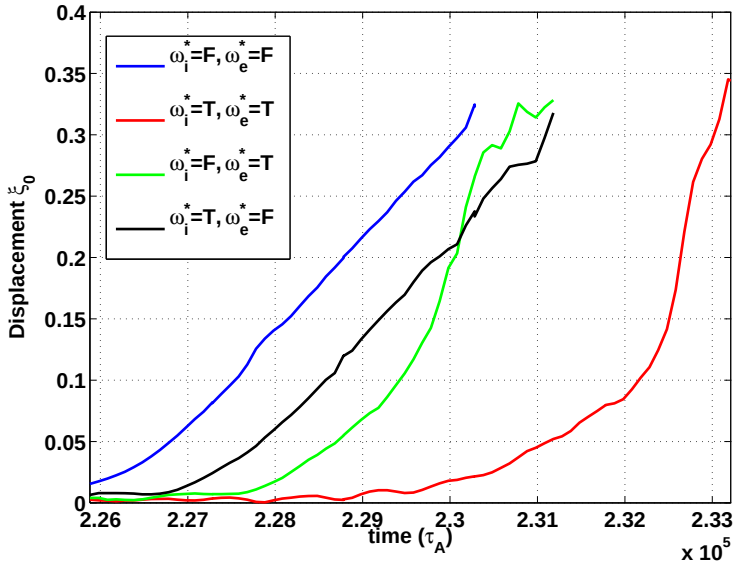


Figure 4.15: Comparison between the displacement $\xi_0$ in four simulations where ion and electron bifluid effects are separately switched on/off. In the legend, the symbol T/F refers to the option being set to True/False in the code.

Let us also emphasize that the phenomena we describe here are for sure due to the bifluid term in Ohm's law. In XTOR-2F, it is possible to switch on/off the ion and electron bifluid terms separately. The only electron term is in Ohm's law, the others are all ion terms. Fig. 4.15 shows the comparison between the displacement $\xi_0$ in four simulations. The blue curve is obtained with all bifluid terms switched off, the red one has all bifluid terms switched on, the black one has only the ion diamagnetic terms and finally the green one only the electron term in Ohm's law. The four simulations have been launched at the same time, starting from a simulation with both diamagnetic terms switched on, shortly before a sawtooth crash. We can draw a few conclusions from this figure. First, the significant acceleration in the far nonlinear phase of reconnection is indeed observed only when the electron diamagnetic effect is switched on. The ion diamagnetic effect does not affect the reconnection rate at all (the black and blue curves have the same slopes). The green curve has a slightly smaller slope than the red one in the fast phase, but basically the evolution is virtually identical in this late phase. There are, however, more differences between all the simulations in the early phase (for $\xi_0 < 0.1$). Indeed, it is clearly seen that diamagnetic terms have a stabilizing effect on the kink mode, as predicted by theory (*cf.* section 2.2.4). Compared to the purely resistive case (blue), the mode is always triggered later when at least one diamagnetic effect is switched on. It

seems, however, to be only a linear stabilization when only one effect is switched on. In this case, it seems to only delay the triggering of the mode but without really affecting the nonlinear phase, as the slopes of the blue, black and green curves are very similar in the early nonlinear phase. However when both effects are present (red), not only is the triggering of the mode delayed for a longer time, but the slope in the early nonlinear phase is also much reduced compared to the three other cases.

To summarize, Wang's calculations predict that when the dynamics in the sheet is dominated not by resistivity but by the parallel pressure gradient, the island growth scales with $W^2$ rather $W^{1/2}$. This should accelerate the reconnection with respect to the resistive case when $W$ is large, if the resistivity is really small (see*Eq.* (4.41)) and if the angular width of the sheet becomes small, transitioning to an X-point configuration instead of Waelbroeck's ribbon. In our XTOR-2F simulations, the resistivity is not so small and the sheet remains large (despite an apparent X-point on the Poincaré plots), so we should not see any significant acceleration. However the simulations indeed give a very strong acceleration in the bifluid case due to the parallel pressure gradient in Ohm's law. We could check that this acceleration is really due to the electron bifluid term by eliminating separately ion and electron terms in the equations. Hence the simulations are in strong quantitative disagreement with Wang's model, despite the compatibility with the scaling $\mathrm{d}_t W \propto W^2$ during the first half of the reconnection process.

Thus the observed acceleration is still mysterious since the change of scaling when taking the parallel pressure gradient instead of the resistivity does not seem strong enough to explain it.

Finally, comparing again the blue and red curves on Fig. 4.15, it is tempting to conjecture that the first slow phase, $t < 2.32 \times 10^5\ \tau_A$, corresponds to the experimentally seen precursor phase which lasts a few milliseconds, and that the second fast phase, $t > 2.32 \times 10^5\ \tau_A$, corresponds to the sawtooth crash proper. Thus the precursor phase would not be a saturated phase but a very slow growth of the instability, stabilized nonlinearly by the diamagnetic effects, and finally abruptly destabilized (by the very same effect[7]). Checking this hypothesis requires a significant number of simulations, both increasing the Lundquist number toward the experimental value and the amplitude of the $\alpha$ parameter. Such a study is ongoing now but requires a large amount of simulation time. Indeed, increasing $\alpha$ is numerically very demanding because the diamagnetic terms are not well behaved at the centre of the mesh. More precisely, the top right corner of Fig. 3.9 (green triangles) represents XTOR-2F pushed almost at its best in terms of Lundquist number $S$ and $\alpha$ parameters. We see that these points do not even span one order of magnitude in $S$ and only $\alpha = 0.08 - 0.15$, which is very limited for a parametric study. However, with some patience, it would still be possible to carry out this study. It would also reveal if the acceleration is proportional to $\alpha$, as in *Eq.* (4.40). In this case,

[7] We have not insisted on this fact in the text, but notice that the scaling of *Eq.* (4.40) leading to $W \propto 1/(t_c - t)$ implies a very small growth at the beginning, followed by the explosive growth. Hence this is compatible with an apparent stabilization (in the first stage) and then destabilization (in a second stage) of the mode. Notice that since we are in the nonlinear regime, this is not a stabilization/destabilization in the usual linear sense (which would mean that a linear threshold is crossed sooner/later, or that an exponential growth rate is decreased).

it could mean that only numerical factor are missing and that the model is qualitatively correct.

## 4.4 Summary

In this chapter, we have seen how the nonlinear evolution of the kink mode leads to the full reconnection of the magnetic surfaces. Assuming mere conservation of flux, energy and particles, one can compute (numerically in the general case) the post-crash density, temperature and safety factor profiles as a function of the pre-crash profiles. This constitutes Kadomtsev's model. We have noticed that the post-crash density and temperature profiles are not necessarily flat in this model. When the only nonideal effect in Ohm's law is the resistivity, Kadomtsev's model also predicts a reconnection time scale which we will compare to the experiments in the following chapter. Here we have only compared it to the XTOR-2F numerical simulations. Kadomtsev's model, which topology has been precised by Waelbroeck, is in good agreement with the resistive simulations.

A significant acceleration of the crash phase is observed when the parallel electron pressure gradient (related to the Hall term) is retained in the Ohm's law. The model predicted by Wang to explain the acceleration quantitatively disagrees with the simulations, and more investigations are necessary to check if the scaling is correct. The nonlinear time evolution of the magnetic island in the bifluid case gives an interesting trail to improve the understanding of the crash phase of the sawtooth instability.

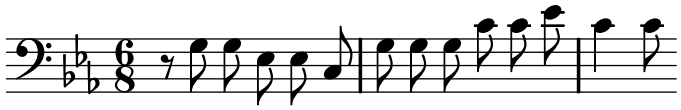

*Qu'à servir mon courroux tout l'Enfer*
*se prépare (Hyppolite et Aricie)*
**Jean-Philippe Rameau**

Chapter 5

# Experimental observations of Sawteeth on the Tore Supra and JET tokamaks

## Contents



In this chapter we will address a number of sawtooth related observations. They will show us the interest of sawteeth from the theoretical as well as operational points of view. From the theoretical point of view, many features of the sawtooth instability, such as the fast crash time, incomplete reconnection or the link with the so-called "snake" instability, remain riddles. From the operational point of view, the capacity of the sawtooth crash to redistribute particles is interesting when it comes to the transport of impurities. Before exploring a few aspects of this issues, we will present the three main diagnostics used here for density and temperature measurements:

- Fast-sweeping reflectometry for density measurements
- Electron Cyclotron Emission (ECE) for electron temperature measurements

- Soft X-ray emission, which gives a line integrated measurement of a quantity which is proportional to the electron temperature, the electron density and the densities of impurities.

## 5.1 Diagnostics

### 5.1.1 Fast-sweeping reflectometry for density measurements

In tokamaks, different diagnostics are used for density monitoring. Density has been measured by interferometry since 1965 [Malamud 1965], Thomson diffusion and more recently by reflectometry [Simonet 1985]. Here we present the principle of the X mode fast-sweeping reflectometry used for Tore Supra and JET measurements, and we detail the technique used to reconstruct poloidal profiles from the equatorial profiles.

Reflectometry is based on the same principle as radar. A wave propagates in a medium until it reaches a cut-off layer where it is reflected. In an unmagnetized plasma, the fundamental frequency involved in this process is the plasma frequency

$$\omega_{pe} = \sqrt{\frac{n_e e^2}{\varepsilon_0 m_e}}. \tag{5.1}$$

The physics is very simple. In the cold plasma approximation with fixed ions, the plasma frequency is the natural oscillation frequency of a layer of electrons displaced with respect to their equilibrium position. The system behaves like a spring. The restoring force is linked to the electric field generated by the displacement, proportional to $n_e e/\varepsilon_0$, hence the expression of this frequency. When the frequency of an electromagnetic wave is above the plasma frequency, it can propagate, while it is damped in the opposite case, where it is evanescent. Thus the plasma frequency is a cut-off frequency: $\omega_c = \omega_{pe}$. In a magnetized plasma with a macroscopic field $\mathbf{B}_0$, the $\mathbf{E} \times \mathbf{B}_0$ drifts associated to the magnetic field modify the response of the plasma to the electromagnetic perturbation, and hence the wave propagation. When the electric field polarization is linear and in the direction of the equilibrium magnetic field $\mathbf{B}_0$, the polarization is said to be ordinary. This is the *O-mode*. In this case the electric drifts vanish and the cut-off frequency is unchanged:

$$\omega_{cO} = \omega_{pe}. \tag{5.2}$$

The case of a polarization in the plane perpendicular to the magnetic field (linear or elliptic) is called *X-mode*, in this case the response of the plasma introduces the electron cyclotron frequency $\omega_{ce} = eB_0/m_e$ in the cut-off frequency. There are upper and lower cut-off frequencies:

$$\omega_{cX\pm} = \frac{\sqrt{\omega_{ce}^2 + 4\omega_{pe}^2} \pm \omega_{ce}}{2}. \tag{5.3}$$

More precisely, *Eqs.* (5.2) and (5.3) are the solutions to $N_O^2 = 0$ and $N_X^2 = 0$, where $N_X$

and $N_O$ are the plasma indexes in O-mode and X-mode, given by

$$N_O^2 = 1 - \frac{\omega_{pe}^2}{\omega^2} \tag{5.4}$$

$$N_X^2 = 1 - \frac{\omega_{pe}^2 \left(1 - \frac{\omega_{pe}^2}{\omega^2}\right)}{\omega^2 - \omega_{pe}^2 - \omega_{ce}^2}. \tag{5.5}$$

Notice that $\omega_{cX\pm} = \omega_{pe}$ is recovered in the $B_0 = 0$ limit, and $\omega_{cX+} = \omega_{ce}$ in the $n_e = 0$ limit.

For typical tokamak plasmas, the cyclotron frequency and plasma frequencies are of the same order, the lower X-mode, O-mode and upper X-mode reflectometers are staggered over the band 20 to 150 GHz. However, in hot plasma, the electron cyclotron frequency and its harmonics are also resonance frequencies. This sets constraints for the accessibility of reflectometry depending on the plasma density and magnetic field[1]. Fig. 5.1 shows a typical Tore Supra density profile and the corresponding cut-offs and cyclotron resonance frequencies. In O-mode, as well as in lower X-mode, the plasma can be probed only from the edge to the gradient region. Both techniques become inaccurate in the core because of the low density gradient. In upper X-mode however, owing to the magnetic field amplitude dependence on the major radius, a reflectometer on the external side of the tokamak can scan almost the whole plasma radius from the outer edge to the inner side. At moderate density, only the edge on the inner side is inaccessible, as shown on Fig. 5.1.

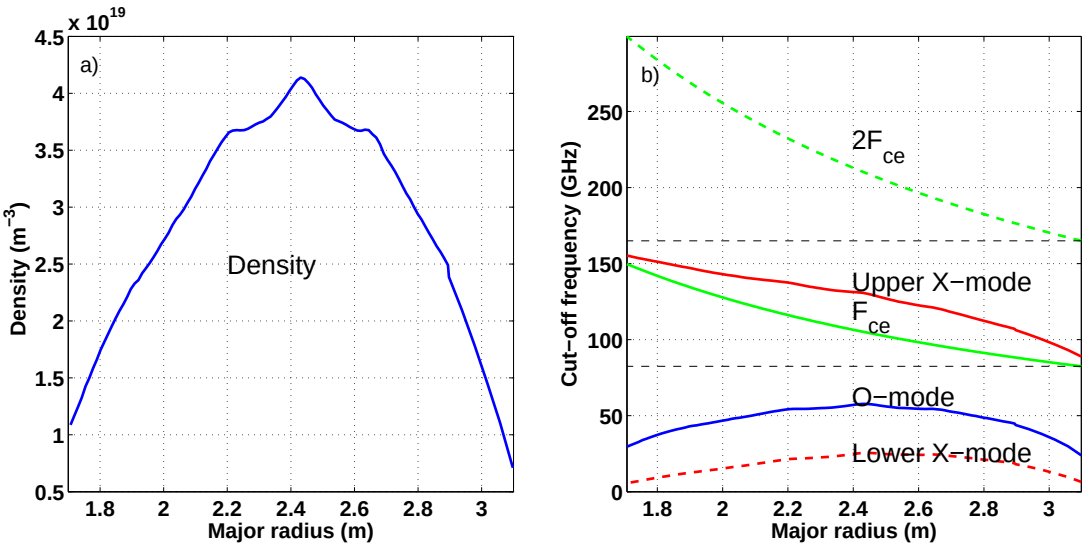


Figure 5.1: Typical ohmic density profile (a) (Tore Supra #44634) with corresponding cut-off frequencies and cyclotron resonance frequencies (b).

Reflectometry measures the phase shift after reflection at the cutoff layer. This phase

[1]ECE absorbtion is deleterious at low magnetic field ($B$<2T) preventing core measurement both in O and X mode.

shift reads:

$$\phi_p = \frac{4\pi}{c} f \int_0^{r_c} N(x, f, t) \mathrm{d}x - \pi/2, \tag{5.6}$$

where $x = 0$ corresponds to the position of the antenna and $x$ increases towards the magnetic axis, until the position of the cut-off layer $x = r_c$. $N(x, f, t)$, the plasma index, varies from $N = 1$ in the vacuum to $N = 0$ at the cutoff.

In the following, we denote by $F_{X+} = \omega_{cX+}/2\pi$ the upper X-mode cutoff frequency. We also have $f_{ce} = \omega_{ce}/2\pi$. At fixed frequency, phase variations are predominantly due to displacement of the cutoff layer and hence give information on the plasma turbulence [Mazzucato 1998].

Frequency sweeping is the standard technique to reconstruct (or measure) the density profile. As for frequency modulated (FM) radar, the variation of the phase with the frequency gives the time delay *i.e.* the propagation time inside the plasma:

$$\tau = \frac{1}{2\pi} \frac{\partial \phi_p}{\partial f} = \frac{1}{2\pi} \frac{\partial_t \phi_p}{\mathrm{d}f/\mathrm{d}t}. \tag{5.7}$$

Contrary to FM radar in air where the time delay is directly proportional to distance, in plasma, the preceding relation should be inverted to recover the reflecting layer position. In O-mode, this inversion is done analytically (Abel inversion):

$$r_c(F) - a = \frac{c}{\pi} \int_a^F \frac{\tau(f)}{\sqrt{F^2 - f^2}} \mathrm{d}f, \tag{5.8}$$

the probing frequency $F$ fixing the density value at the cutoff: $F = \omega_{pe}/2\pi$. This inversion requires a time delay measurement from the edge to the cutoff. However reflectometry cannot measure below ∼20 GHz since the wavelength becomes much larger than the edge density gradient length ($\lambda = 1.5$ cm at $F = 20$ GHz). To reconstruct the density profile, one then requires a density measurement from other diagnostics like Langmuir probes or an assumption on the edge profile shape.

In X-mode, the inversion must be done numerically and recursively. The knowledge of the density profile from the edge to the radius $r_c(F)$ is used to compute the cutoff position at $F + \delta F$. The density is then given by the relation $F_{ux}(r_c(F + \delta F)) = F + \delta F$.

Contrary to O-mode, upper X-mode reflectometry can measure the density profile at very low density since $F_{ux} \sim F_{ce}$ when $n_e = 0$ and the density profile can be reconstructed only from reflectometry data provided a precise evaluation of the magnetic field $B(R)$. Absolute and relative precision of the density profile measured with reflectometry is difficult to evaluate since the reconstruction is recursive: an error will propagate, with some attenuation, throughout the profile. Inaccuracy of the magnetic field, the probing frequency, or the position of inner wall (the reflection on the inner wall is used as a reference to correct the dispersion in the waveguides) produce a global uncertainty of a few centimeters on the radial position of the cutoff layer. Relative uncertainties from profile to profile are much lower (millimetric) and density perturbations lower than 0.5% can be detected.

Tore Supra is equipped with 6 reflectometers for profile and fluctuations measurements. 2 reflectometers covering the band 50-75 GHz and 75-110 GHz are dedicated to

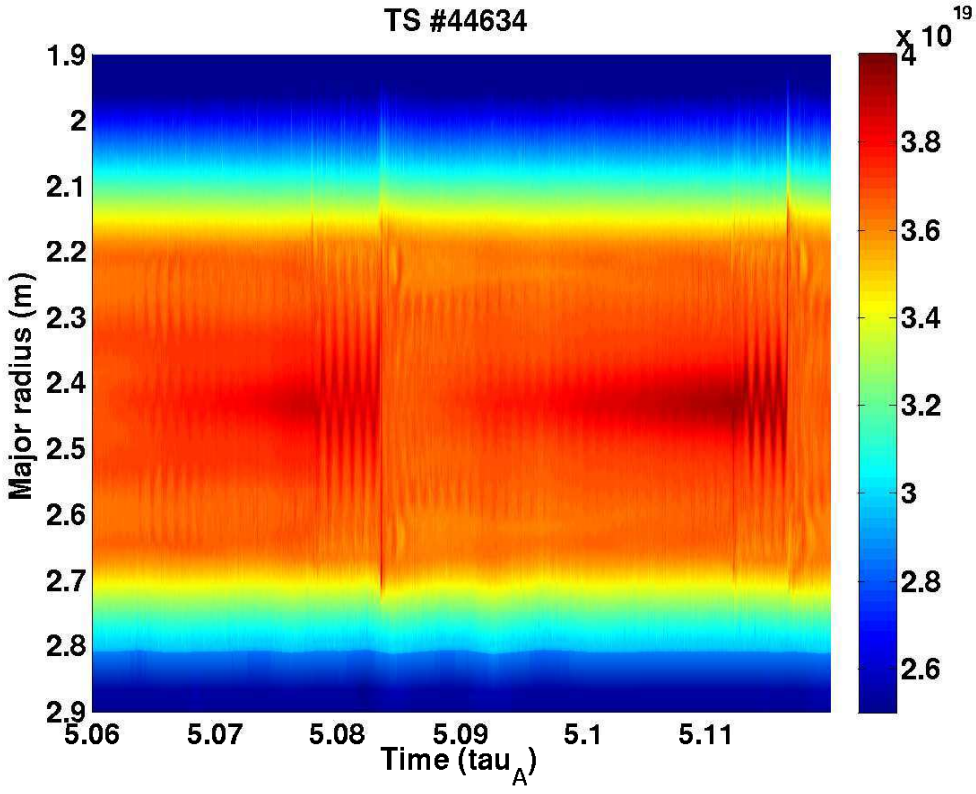


Figure 5.2: Time traces of the density profile obtained using X-mode reflectometry, on Tore Supra pulse #44634

edge profile measurement. They are now swept in a few microseconds [Clairet 2011]. Decreasing the sweeping time improves the precision of the measurement since for short sweeping time (<10-20 $\mu$s), the plasma turbulence is frozen during the measurements [Moreau 2000]. For very short sweeping, one can even observe the radial propagation of structures along the profiles [Hornung 2013]. The core reflectometer, 100-155 GHz can measure the density profiles and density fluctuations (frequency plateaus) during the same shot [Sabot 2006]. The sweeping time varies between 25 and 70 $\mu$s depending on plasma conditions. Up to 10000 profiles can be recorded during a shot, with a rest time as low as 5 $\mu$s. As the lowest frequency is always reflected inside the plasma, knowledge of the edge profile is needed to initialize the reconstruction. This edge profile can come from the 50-110 GHz reflectometers or the interferometry diagnostic.

On JET, 6 reflectometers: 4 X-mode 33 to 150 GHz and 2 O-mode 50 to 110 GHz measure the profiles. The sweeping time varies between 10 and 11 $\mu$s, and a profile can be measured every 15 $\mu$s. Up to 100000 profiles can be stored during a shot. The 6 Gbyte memory can be filled in 1.5 s to record the evolution of the density at full resolution (15$\mu$s), a huge storage very useful to study sawtooth dynamics. Large uncertainties on JET magnetic field estimation ($\delta B/B$ up to 1-2 %) and profile jitters due to pedestal displacement during H-mode deteriorate the accuracy of the profile measurement compared to Tore Supra. However, owing to the short sweeping time and huge memory, filter can

be used to reduce the noise.

To conclude this subsection, Fig. 5.2 shows an example of time trace obtained with the X-mode reflectometer on Tore Supra pulse #44634.

### Tomographic reconstruction of the 2D profiles

In X-mode, a full frequency sweep from the low frequencies to the high frequencies scans the density profile from the LFS to the HFS. A density profile is obtained in a few $\mu$s, which is much less than the typical time scale of profile evolution. On Tore Supra in ohmic regime for instance, the sawtooth period, and hence the characteristic evolution time of the temperature and density profiles, is larger than 10 ms, and the profile obtained during one frequency sweep can be considered as instantaneous (disregarding turbulence). The density outside the equatorial plane of the tokamak is not scanned, but with some assumptions, the 2D poloidal density profile can be reconstructed using a tomography technique. This technique is not a tomography technique in the sense of Abel inversion, but can be used to infer the poloidal structure of a mode with given frequency. Assuming there is a mode with frequency $\omega/2\pi$ present in the plasma, perturbations will appear and disappear with the same frequency on the reflectometry signal in the equatorial plane. For this given mode, it will be as if instead of having the mode rotating in the poloidal plane, the reflectometer was rotating around the poloidal plane, periodically scanning the plasma. We insist that only the perturbations associated with a given mode can be scanned using this technique. Poloidal up-down density asymetries may exist, but they cannot be studied using this technique since only the equatorial plane is monitored. Moreover, it is necessary that the plasma can be considered steady during one rotation of the mode. Again, the characteristic evolution time of the profiles must be compared to the mode frequency. For typical plasma conditions, modes with frequency larger than several hundreds of Hz must be considered. In the Tore Supra pulses we will be looking at, the monitored kink mode frequency is of the order of 1 kHz, allowing the use ot the tomography technique.

We now detail how the tomography technique is carried out. It is explained in Ref. [Nagayama 1990]. The basic principle is very simple. To infer the density at time $t_0$ and point $(r, \theta)$ out of the equatorial plane, the densities in the equatorial plane, namely at $(r, 0)$, $t = t_0 - \theta/\omega$ and at $(r, \pi)$, $t = t_0 + (\pi - \theta)/\omega$ are used for interpolation:

$$n(r, \theta, t_0) = \frac{\pi - \theta}{\pi} n(r, 0, t_0 - \theta/\omega) + \frac{\theta}{\pi} n(r, \pi, t_0 + (\pi - \theta)/\omega). \tag{5.9}$$

Fig. 5.3 presents an example of 2D poloidal profile obtained with this technique. The displacement induced by a kink mode can be seen as the dense core is shifted from the center.

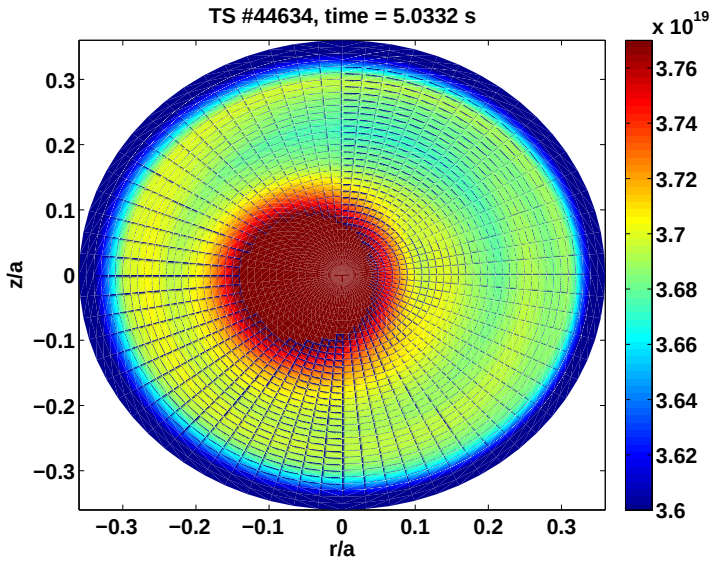


Figure 5.3: Poloidal density profile obtained using tomography of the reflectometry profiles during a kink displacement. The displacement here is about 5 cm.

### 5.1.2 ECE radiometry for temperature measurements

ECE radiometry makes use of the fast gyration motion of the electrons around the magnetic field lines at the cyclotron frequency

$$\omega_{ce} = \frac{eB}{m_e}. \tag{5.10}$$

The acceleration linked with the circular motion is responsible for power losses. The power emitted by the particles is proportional to the square of the acceleration $a = \omega_{ce} v$, and of course since the emission results from a resonant interaction between the particle motion and the electromagnetic field, the pulsation of the emitted photons is also $\omega_{ce}$. For an electron with perpendicular velocity $v_\perp$, the emitted power is

$$P_{cyc} = \frac{e^4 B^2}{6\pi\varepsilon_0 m_e^2 c^3} v_\perp^2, \tag{5.11}$$

In practice, there is reabsorption of the signal along the propagation from the plasma to the detectors outside the plasma. The plasma can be in general assumed optically thick to the electron cyclotron frequencies (in the core), so that radiation is in thermodynamic equilibrium, and the radiated power is actually the black body radiation, which for small frequencies $\hbar\omega \ll T$ (Rayleigh-Jeans approximation), is

$$I(\omega) = \frac{\omega^2 T_e}{8\pi^3 c^2}, \tag{5.12}$$

where $I(\omega)$ is the radiated power per unit area of emitting surface, per unit solid angle and per unit frequency. A layer of plasma located between $R$ and $R+\mathrm{d}R$ emits the power $I(\omega_c)\mathrm{d}\omega$ per unit area and solid angle, with $\omega_c = eB(R)/m$ and $\mathrm{d}\omega = e/m|\mathrm{d}B/\mathrm{d}R| \simeq$

$eB_0/(mR_0)\mathrm{d}R$, since the magnetic field amplitude due to the external coils is proportional to $1/R$. In addition, there is a correction of order $\beta$ to the toroidal field, and a poloidal component of order $\varepsilon = r/R$. The contributions of these terms to the magnetic field amplitude $B$ are not measured but calculated.

The physics of ECE emission is actually a bit more complex due to the relativistic broadening in the tail of the Maxwellian electron distribution, to the plasma not being optically thick at the edge, and to radiation reabsorption at higher harmonics in certain cases. More details can be found in Ref. [Hutchinson 1987].

The detector collecting the light emitted by the plasma and separating it in its different frequency components is called the radiometer. On Tore Supra, the radiometer is divided in 32 channels separated by 1 GHz and with a 500MHz bandwidth, giving 32 radial positions [Ségui 2005]. The signal is sampled every 1 ms in the slow acquisition mode, and every 1 $\mu$s in the fast acquisition mode. The radial separation between each channel is typically $2-3$ cm.

On JET, there are 96 channels separated by 500 MHz with 250MHz bandwidth, giving an improved radial separation of the channels compared to Tore Supra, typically less than 1 cm [De La Luna 2004]. The slow and fast signals are sampled at the same frequency as on Tore Supra.

Slow ECE is extremely useful to observe the evolution of the temperature profile while fast ECE can be used to study MHD mode and some frequency turbulence ($<$ 500 kHz).

### 5.1.3 Soft X-Ray diagnostic

Tokamak plasmas emit a lot of radiation in the Soft X-Ray (SXR) range (from about 100 eV to 5 keV), due to several dynamic atomic processes[2], and it can be used to probe the plasma. On JET, the SXR radiation is observed by one horizontal and two vertical cameras with about a dozen channels each. Each channel collects all the radiation emitted in its own line of sight. Fig. 5.4 shows the layout of the lines of sight for one of the vertical cameras. In the following figures we will use the $12^{th}$ line starting from the right, which goes through the core, closest to the magnetic axis.

The power (in W.m$^{-3}$) radiated by the plasma in the SXR range is called emissivity $\varepsilon_{SXR}$ and depends mainly on the electron density $n_e$, the ion and electron temperatures $T_i$ and $T_e$, and the densities of each impurity $n_X$[3]. Thus it is a very complex quantity, out of which it is difficult to extract the desired information (in general the impurity density). The theoretical dependence on the aforementioned parameters can be quite delicate to compute when heavy impurities are considered because of the huge numbers of interactions in which such particles can take part, which makes the issue even more intricate, not to mention the fact that the measurement along a line of sight convolves the local signals and makes deconvolution by Abel inversion necessary. However they are a very convenient quantity to measure and have been used for a long time (see for instance

[2] Atomic process is to be taken in the wide acceptance, meaning all processes involving excitation, absorption or emission of electrons, that is, all free-free, free-bound or bound-bound interactions.

[3] Note that if impurities are not thermalized with the dominant ion, their temperature must also be taken into account in the dependence of the emissivity.

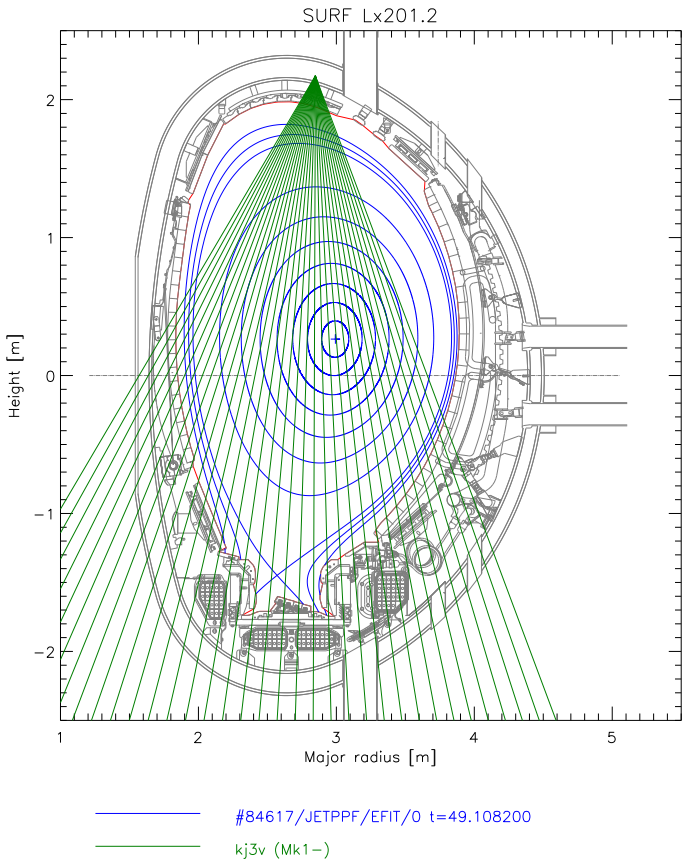


Figure 5.4: Layout of one vertical SXR camera and its lines of sight (green) on the JET tokamak. The flux surfaces are also shown in blue.

the discovery of sawteeth in 1974 using SXR [von Goeler 1974]). The measurements usually have a good time resolution, of the order of the $\mu$s. Because of these difficulties, we will not try to derive a $W$ concentration from the SXR signals (this is the job of specialists), but we will just use the fact that $\varepsilon_{SXR}$ increases with $n_e$, $T_e$, $T_i$ and $n_X$ (impurity) in all the parameter space relevant to tokamak. Since we are interested in sawteeth, we must say a few words before being able to read into the sharp evolution of the signals at the sawtooth crash.

Typically, at a sawtooth crash (and first assuming no impurities), central channels (line of sight going through the core) tend to decrease and outer channels tend to decrease. This is because the emissivity has a quite strong dependence on the temperature. When there are impurities in the plasma, things get more complicated. Recall that the sawtooth crash can in theory lead to either flushing of the impurities or, on the contrary, if their pre-crash profile is hollow, to the penetration thereof. One would like to discriminate between the two (penetration or flushing) by looking at the SXR signals. It is straightforward that a sufficient condition for having penetration is that the central channels increase at the crash instead of decreasing. This is, however, by no means a necessary condition, and in general, a detailed study is necessary.

## 5.2 Phenomenology

The necessity of a $q = 1$ surface existing somewhere in the plasma is one of the only universal features of the so-called sawtooth phenomenon. A plasma discharge is said to have sawteeth if X-ray, temperature or density signals exhibit a sawtoothing behavior. This said, the word "sawtooth" covers a very wide range of different behaviors, some of which are far from being fully understood. As we will see, none of the models we have presented so far is really able to account for all the diversity of behaviors observed. In this section we will simply focus on describing the various aspects of sawteeth on the Tore Supra and JET tokamaks.

### 5.2.1 Period and shape

What is known about the sawtooth triggering mechanism was described in section 2.2.6. Recall that a given energy integral must change sign for the kink mode, precursor of the sawtooth, to be driven unstable. The energy depends on the global configuration in the $q = 1$ surface, and thus what matters is the characteristic time necessary to rebuild the pressure and current profiles, that is, the diffusive and resistive times $\tau_\chi$ and $\tau_{R,s}$:

$$\tau_\chi = \frac{r_s^2}{\chi} \tag{5.13}$$

$$\tau_{R,s} = \frac{r_s^2}{\bar{\eta}}. \tag{5.14}$$

In most tokamaks, the thermal diffusivity is much larger than the resistivity, so that what actually fixes the sawtooth period is the resistive time. In recent, large and hot tokamaks, it can become very large, several tens of seconds. It does not set the sawtooth period to tens of seconds, though. However it indicates that large and hot, less resistive tokamaks tend to have longer sawteeth. When the sawtooth period is long compared to the diffusive time, the overall shape of the temperature signal exhibits a fast rise followed by a longer plateau, until the next sawtooth crash. In the opposite case, the signal assumes a triangular form: a linear ramp followed by a sudden crash. In JET pulses, an ohmic phase precedes the switch-on of additional heating methods, in general Neutral Beam Injection (NBI) and sometimes in addition, Ion Cyclotron Resonant Heating (ICRH). Fig. 5.5 shows the two different shapes of the sawtooth ramp in ohmic regime (b) and during the NBI-heated phase (c). One notes that sawteeth are much longer in the NBI-heated phase, the ratio of the sawtooth periods is roughly 3–4, however the slopes of the rise in the ramp are roughly the same. This is mainly because the plasma is hotter by approximately a factor of 2, resulting in an increase of the resistive time by almost 3[4]. On top of that, as we discussed in section 2.2.6, there is a stabilization of the sawtooth by the fast particles coming from the neutral beam, with energy of the order of 100 keV [Ciric 2011], which further delay the onset of the kink mode and increase the sawtooth period.

[4]Recall that $\eta \propto T_e^{-3/2}$.

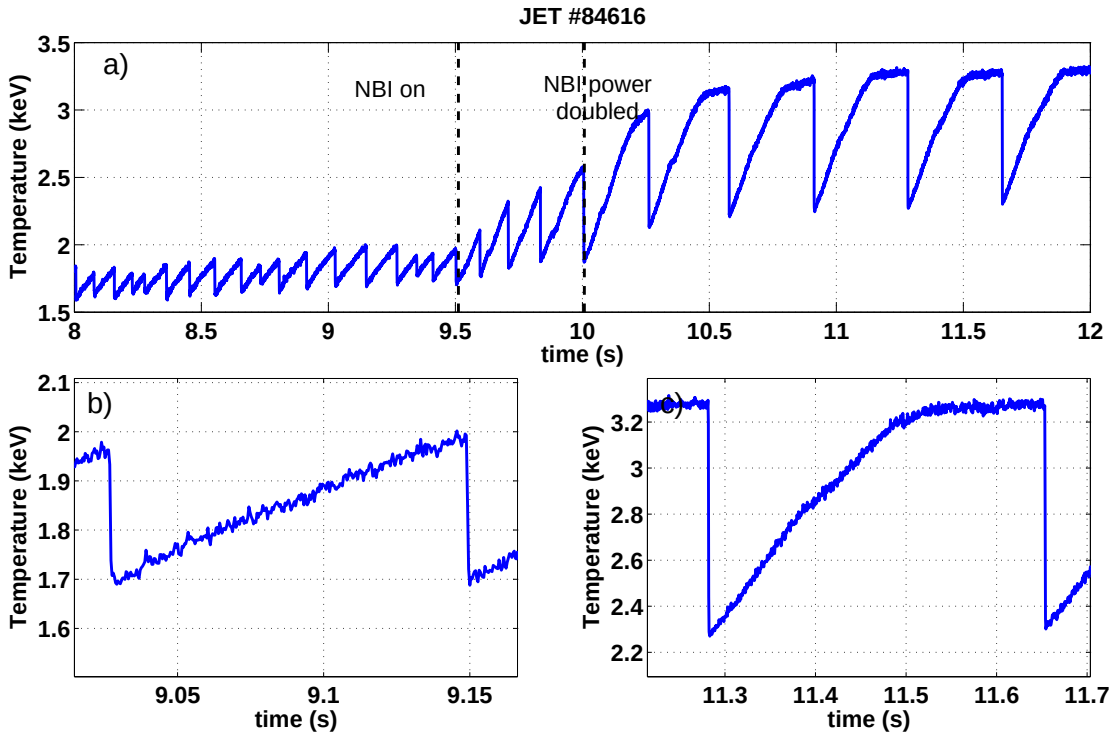


Figure 5.5: Central temperature in JET pulse #44634 obtained with ECE (a). Zoom on a sawtooth ramp and crash in ohmic phase (b) and in NBI-heated phase (c).

### 5.2.2 Precursor/Postcursor behaviour

It has been said previously that sawtooth activity is intimately linked with the $(1,1)$ kink mode instability. It is the linear displacement provoked by the kink mode which leads to the non-linear reconnection process, once the magnetic surfaces have been pushed against the $q = 1$ surface. On the signals, kink oscillations are usually observed inside the $q = 1$ surface prior to the sawtooth crash. This MHD activity is called precursor of the sawtooth. Due to incomplete reconnection[5], there may remain free energy for the mode after the crash, so that a postcursor mode is also often observed. Thus sawteeth come with a wide variety of behaviours according to the duration of the $(1,1)$ pre/postcursor. This is the reason why sawteeth are so complex and diverse, and why it is so difficult to derive a general model. Indeed there is no general experimental behaviour. An excellent review of the different types of precursors can be found in [Udintsev 2005]. We will follow the terminology used in this review and provide some additional examples and remarks.

Two main kinds of sawtooth are distinguished. Other types of behaviour can be encountered, as will be seen in the following, but the two following are the most typical.

[5]section 5.2.6 deals with the support of safety factor measurements to the hypothesis of incomplete reconnection. For now, we will assume that the presence of a postcursor is a strong indication for incomplete reconnection, and that on the contrary, the absence of a postcursor indicates complete reconnection. There are no clear experimental evidence to support this assumption.

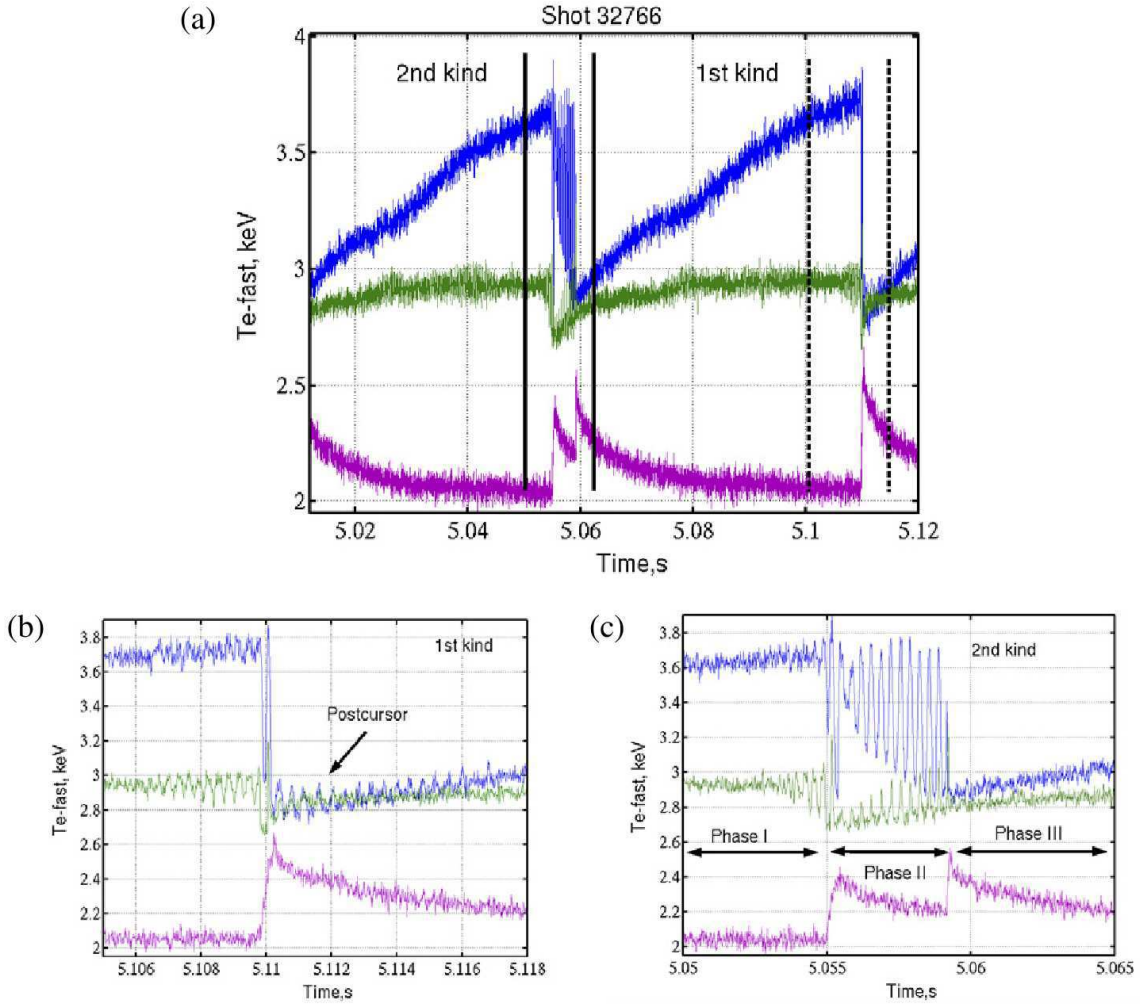


Figure 5.6: The two main kinds of sawtooth behaviour observed in Tore Supra. The blue, green and magenta traces respectively plot the central, close to $q = 1$, and external temperatures. Taken from [Udintsev 2005].

1. In the first kind, the sawtooth crash is triggered very rapidly after the onset of the precursor oscillations. It happens in one fast sequence, and a small amplitude postcursor can be observed afterwards.

2. In the second kind, the sawtooth crash is divided in three phases. In phase I, the oscillations become visible on the signals. In phase II, after a couple of ocillations, a first reconnection[6] event can be infered from the sudden rise in the temperature outside the $q = 1$ surface, whereby the amplitude of the oscillations significantly increases. After a dozen oscillations or so, a second reconnection event, usually

[6] We will see in section 5.2.6 that the presence of a heat pulse does not imply a reconnection event. In other words, the temperature collapse mechanism may not only be due to reconnection. However until section 5.2.6, we will still assume that the heat pulses linked with the sawtooth activity are caused by reconnection.

more violent, is triggered. Phase III consists of the quiescent ramp phase following the sawtooth crash, with some postcursor activity often remaining. This kind of sawtooth behavior reminds what is called compound sawteeth (*cf.* section 5.2.4)

We partially reproduce in Fig. 5.6 the first figure from [Udintsev 2005], which displays the two kinds of behaviours.

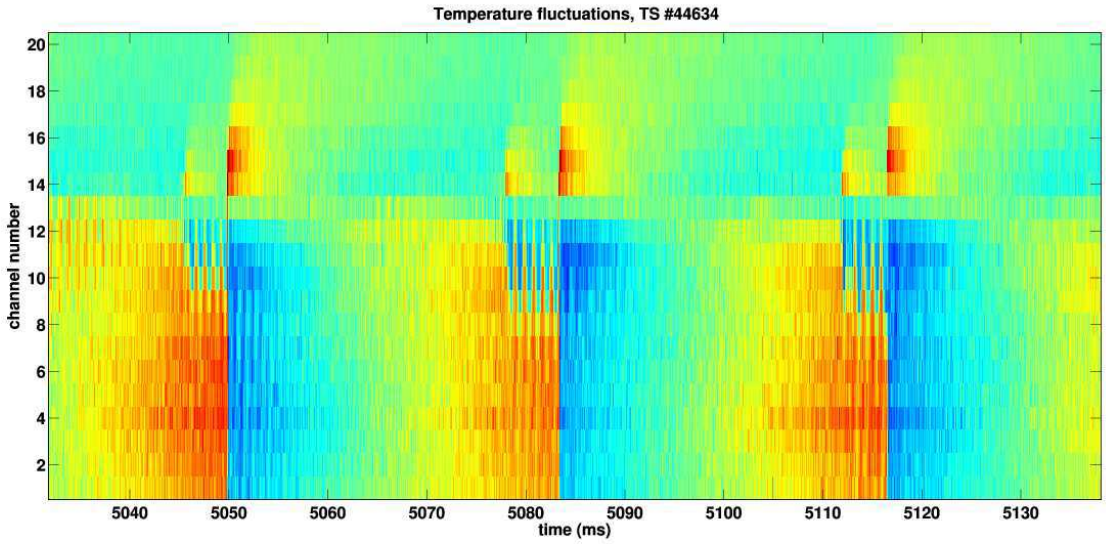


Figure 5.7: Temperature fluctuations during ohmic sawteeth in Tore Supra pulse #44634, obtained with the fast ECE diagnostic

Figs. 5.7 and 5.8 show an example of 3 consecutive sawteeth of the second kind in Tore Supra pulse #44634, where fast ECE data and fast-sweeping reflectometry are available simultaneously. The two different heat pulses are very well seen on the temperature time trace at each crash , at $t = 5.046$ and 5.050 s, $t = 5.078$ and 5.084 s, $t = 5.112$ and 5.116 s. On Fig. 5.8, the second density pulse can be clearly seen, but the first one is more difficult to see. On the image, we increased the contrast to make it apparent, but obviously the second one is more striking.

The most natural interpretation for the second kind of sawtooth is the following. The kink mode destabilization triggers a first thermal collapse, most likely going along with reconnection. For some reason, the reconnection stops before being complete, and we are left in phase II with a saturated magnetic island inside the $q = 1$ surface, which rotates with the mode and produces the very large ($\delta T/T \simeq 20\%$) oscillations of the temperature. Finally, a second trigger is crossed and reconnection starts again, leading to a more quiescent phase III.

This interpretation, however, is not very instructive, since it does not tell us anything on the mechanisms leading to saturation, or on the contrary to the triggering of the second crash, nor the first one.

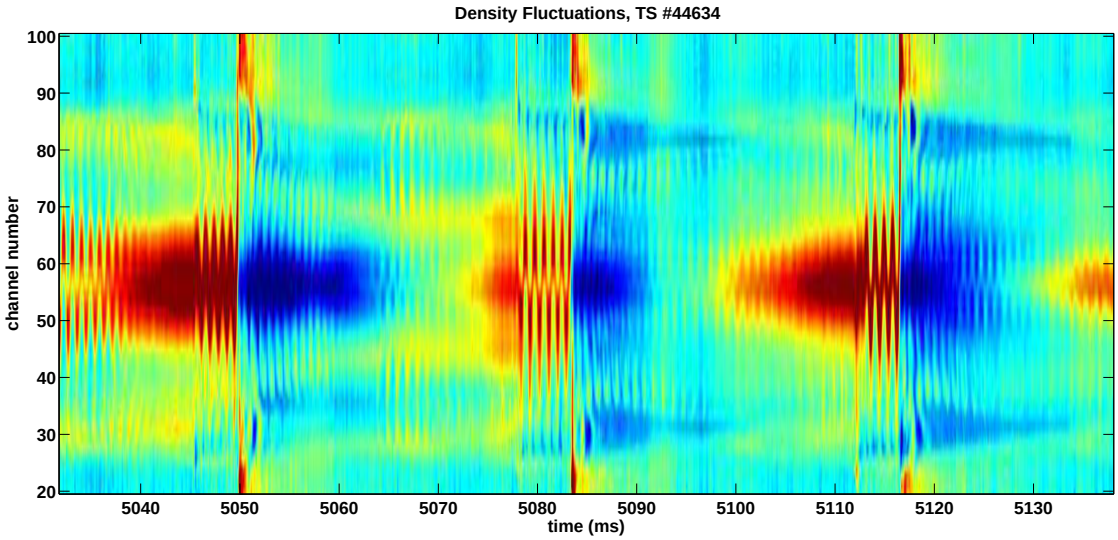


Figure 5.8: Density fluctuations during ohmic sawteeth in Tore Supra pulse #44634 obtained with the fast-sweeping reflectometer

Note that the first kind of sawtooth, which seems to best fit the picture detailed in chapter 2, also raises questions. Indeed, on Fig. 5.6, panel (b), the precursor is actually seen to appear long before the actual crash, namely approximately 4 ms before. Thus the kink precursor most probably saturates at finite small amplitude

We conclude this subsection with an interesting example, Tore Supra ohmic pulse 47126. Fig. 5.9 displays a time trace of the temperature perturbations during a period of a dozen of sawtooth crashes, measured with fast ECE, with a time resolution of 1 $\mu$s. The $y$-axis is the ECE channel number, representing the major radius. On this picture, a sawtooth crash of the first kind is characterized by the abrupt change in the core temperature, without visible oscillations and with a single heat pulse, visible for channel numbers in the intervals $[25, 30]$ and $[2, 7]$ approximately. On the contrary, a sawtooth crash of the second kind is characterized by a first heat pulse and minor change in the core temperature, followed by oscillations lasting a few milliseconds and finally a second heat pulse, larger than the first one. We clearly see that every crash of the first kind is followed by a crash of the second kind. This quite regular behaviour repeats over more than a dozen sawtooth crashes. This is probably not a coincidence, considering the number of crashes during which this behaviour can be observed, and despite the fact that this does not happen in every pulse. Even though this is only a curiosity, it seems to indicate that some information is transported from a crash to another, over quite long periods of time, several tens of milliseconds. For instance, one could imagine that both kinds of sawtooth crash yield different $q$ profiles immediately after the sawtooth crash, say $q_1$ for the first kind and $q_2$ for the second kind. Remembering that resistive evolution is slow and does not converge to equilibrium in a sawtooth period, the profiles can also be different immediately before the sawtooth crash, say $q_1'$ and $q_2'$. It is very likely that the type of crash obtained depends on the precise structure of $q$ just before the crash.

Now if $q_1'$ gives a crash of the second kind and $q_2'$ a crash of the second kind, then such an alternance can occur.

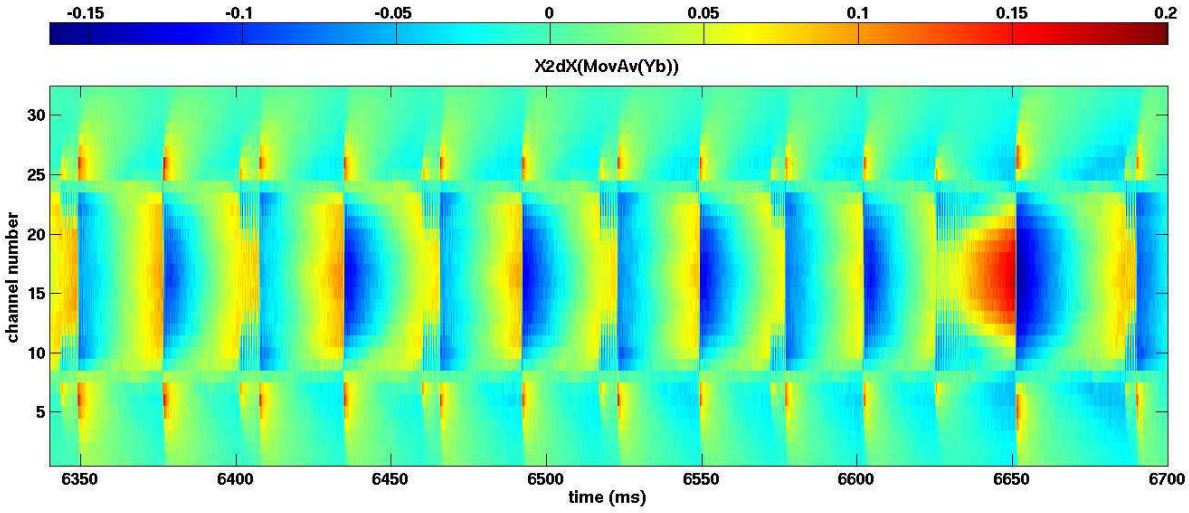


Figure 5.9: Time trace of temperature fluctuations in shot #47126

### 5.2.3 Crash time

In this subsection we will focus on the experimental determination of the sawtooth crash time. We will see that the crash time is always much smaller than the Kadomtsev time, *Eq.* (4.19), especially in the JETtokamak.

We first explore the case of JET.

#### 5.2.3.1 On JET

The characteristic time of the sawtooth crash in JET plasmas was first estimated with good precision in Ref. [Edwards 1986], where soft X-ray (SXR) signals with 5 $\mu$s time resolution are used to perform tomographic inversion of the plasma emissivity. The typical crash time was found to be 100 $\mu$s. The results were confirmed by the fast ECE diagnostic with time resolution 10 $\mu$s. Fig. 5.10 shows typical fast ECE signals with time resolution 5 $\mu$s in sawtoothing regime (a) and during two distinct sawtooth crashes (b) and (c). The signals are averaged over 50 $\mu$s to reduce the noise, without eliminating the relevant frequencies. Superimposed is the slow ECE signal (red). Note that looking at the slow ECE data can be very misleading, since the collapse seems to be much slower, up to 1 ms. It should probably be attributed to the response time of the diagnostic or to filtering treatments applied to the raw signals.

Nonetheless, it is seen that the two sawtooth crashes exhibit different behavior. Following the nomenclature introduced in section 5.2.2, the first one (b) should probably be considered a sawtooth crash of the first kind, since the precursor oscillations are very

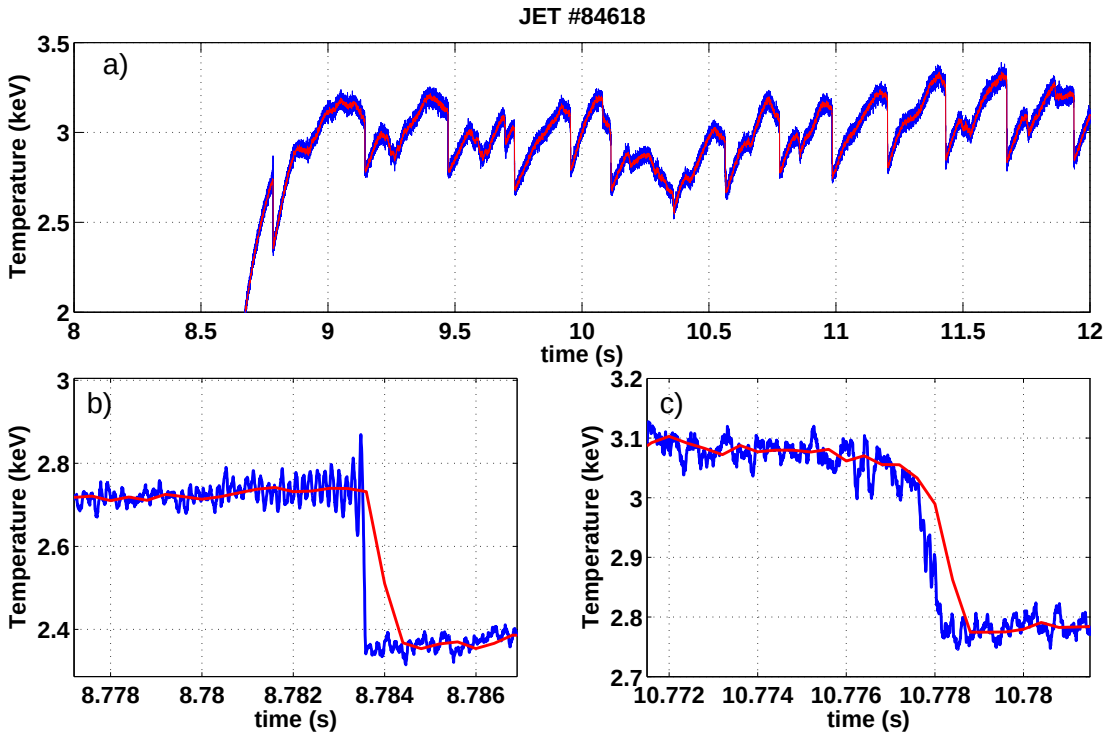


Figure 5.10: Fast (blue) and slow (red) ECE central signals in sawtoothing regime (a) and zoom around two sawtooth crashes showing two quite differnt behaviors (b) and (c). The time resolution is 5 $\mu$s. The signal is seen to drop in a characteristic time of 100 $\mu$s on panel (a), and 800 $\mu$s on panel (b).

small in amplitude. They look like the green signal of Fig. 5.6 b). The second one (c) should probably be called a first kind too, however there are no clear sign of precursor or postcursor oscillations. Also the crash times seem rather different: the first one clearly happens extremely rapidly, in about 100 $\mu$s, in accordance with Ref. [Edwards 1986], however the second one is much slower, almost in agreement with the slow ECE trace. It occurs in about 800 $\mu$s, which is almost an order of magnitude longer. This is still, however, much shorter than the prediction of Kadomtsev's model, *Eq.* (4.28). This scaling, with $B_0 = 2.6$ T, $R_0 = 3$ m, $r_s = 0.25$ m, $T_{e0} = 3$ keV, $n_{e0} = 5 \times 10^{19}$ m$^{-3}$ and $s \sim 0.1$[7], gives $\tau_{\rm rec} \simeq 10$ ms, between one and two orders of magnitude longer than the experimentally observed crash times.

#### 5.2.3.2 On Tore Supra

The same can be done on Tore Supra, where fast ECE is also available. Fig. 5.11 presents the fast ECE signals with 1 $\mu$s time resolution for Tore Supra pulse #44634. It is seen that the characteristic time of the sawtooth crash is 100 $\mu$s, as in JET. Again, the crash

[7] The shear is difficult to evaluate when no precise evaluation of the safety factor profile is available. A satisfactory approximation for the shear is $s \simeq 1 - q_0$, typically of the order of 0.1 – 0.2.

time is not the same throughout a given discharge, and a range of different behaviors can be obtained, however what matters most is the fastest observed crash. The discrepancy with Kadomtsev's model is less pronounced on Tore Supra, but still obvious. The relevant parameters in this discharge are $B_0 = 3.8$ T, $R_0 = 2.4$ m, $r_s = 0.25$ m, $T_{e0} = 2.4$ keV, $n_{e0} = 3 \times 10^{19}$ m$^{-3}$ and we still take $s = 0.1$. This gives $\tau_{\text{rec}} = 5$ ms, slightly shorter than the JET value.

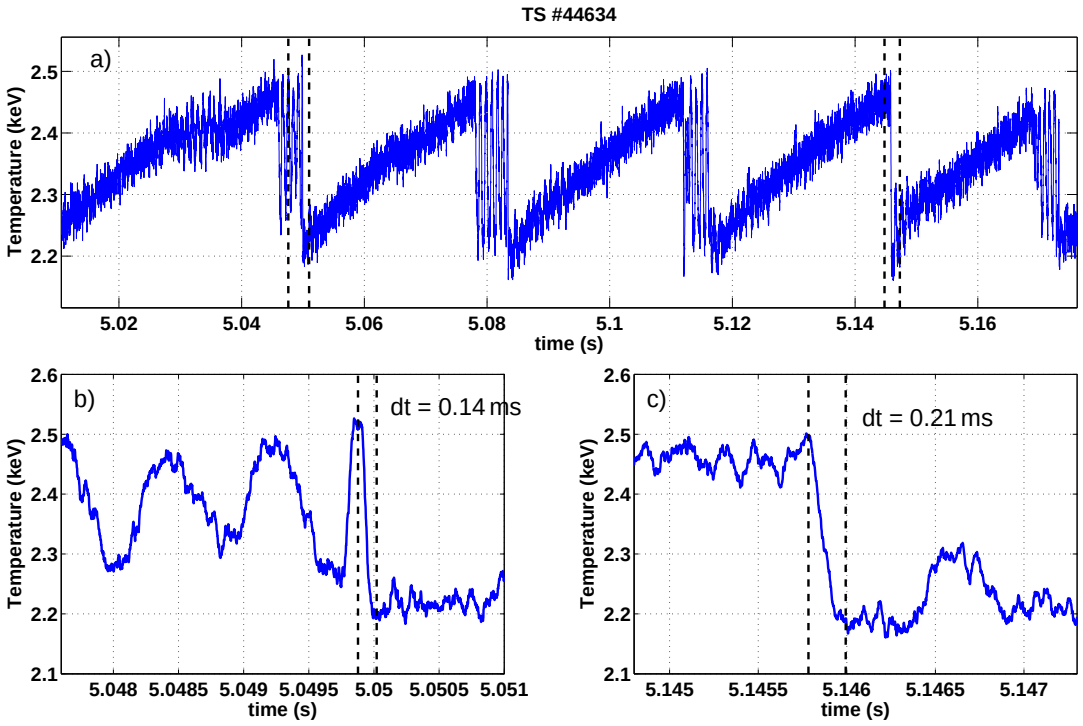


Figure 5.11: Fast ECE central signal in sawtoothing regime (a) and zoom around two sawtooth crashes (b) and (c). The time resolution is 1 $\mu$s. The signals are seen to drop in a characteristic time of 100 $\mu$s.

Hence, be it on Tore Supra or JET, Kadomtsev's model is clearly in disagreement with experiments. The discrepancy is even more pronounced in the larger and hotter JET plasmas. There has been few progress in the understanding of the fast crash mechanism. Reconnection theory has provided different possible causes for enhanced reconnection rates compared to resistive reconnection (an example was studied in section 4.3), but up to date, there has not been any convincing simulation of a sawtooth crash with characteristic time scales in agreement with the experiment. This should be kept in mind when studying the sawtooth simulations with the XTOR-2F code in the following chapters.

Notice, however, that the time scale discrepancy itself does not yet rule out the basic topological hypotheses of Kadomtsev's model. Other observations lead to question them, as we will see in section 5.2.6.

### 5.2.4 Compound sawteeth and partial crash

There are similarities between what we call compound sawteeth and the second kind of crash described above. Fig. 5.12 displays an example of a compound sawtooth in Tore Supra pulse #44634 on the central density. In the middle of the sawtooth ramp, at $t = 5.03$ s, a discontinuity followed by oscillations can be observed. Note that this is the same ramp as the first one of Fig. 5.11 a), where the oscillations can also be seen at $t = 5.03$ s, although the effect seems more dramatic on the central density in this particular case.

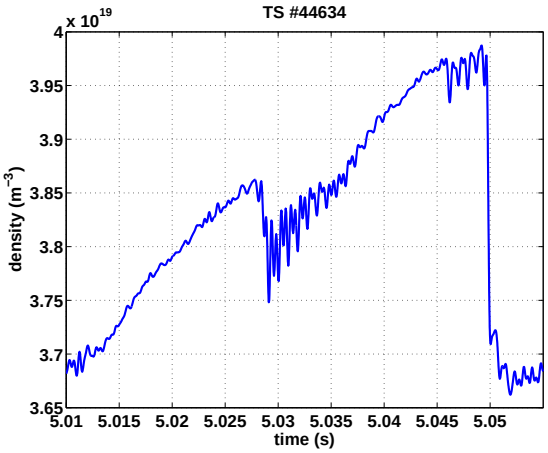


Figure 5.12: Compound sawtooth crash in Tore Supra pulse #44634

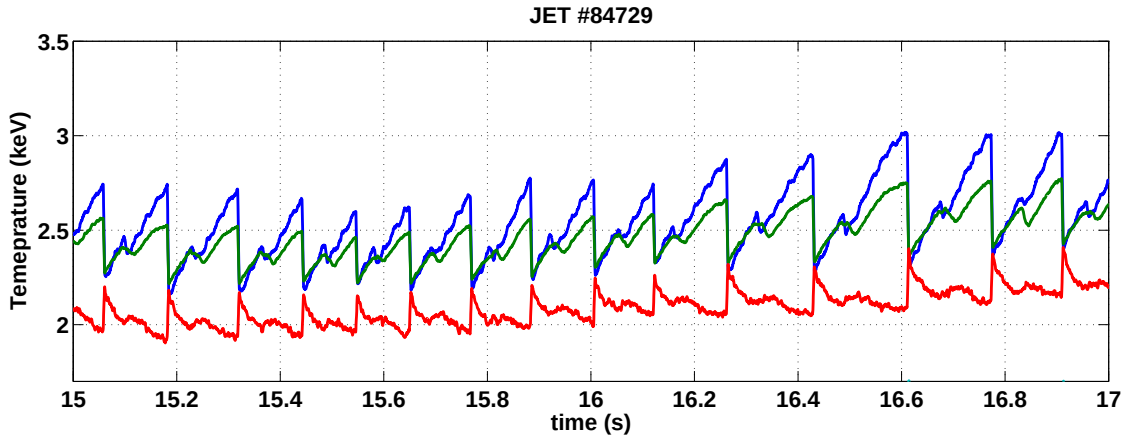


Figure 5.13: Slow ECE signals in JET pulse #84729, showing a compound sawteeth quite regular behavior. The blue and green signals are inside the $q = 1$ surface, while the red one is beyond the $q = 1$ surface.

Fig. 5.13 shows a series of compound sawtooth crashes on JET pulse #84729. This time, it is clearly seen on the ECE signals. We see a quite regular behavior for each

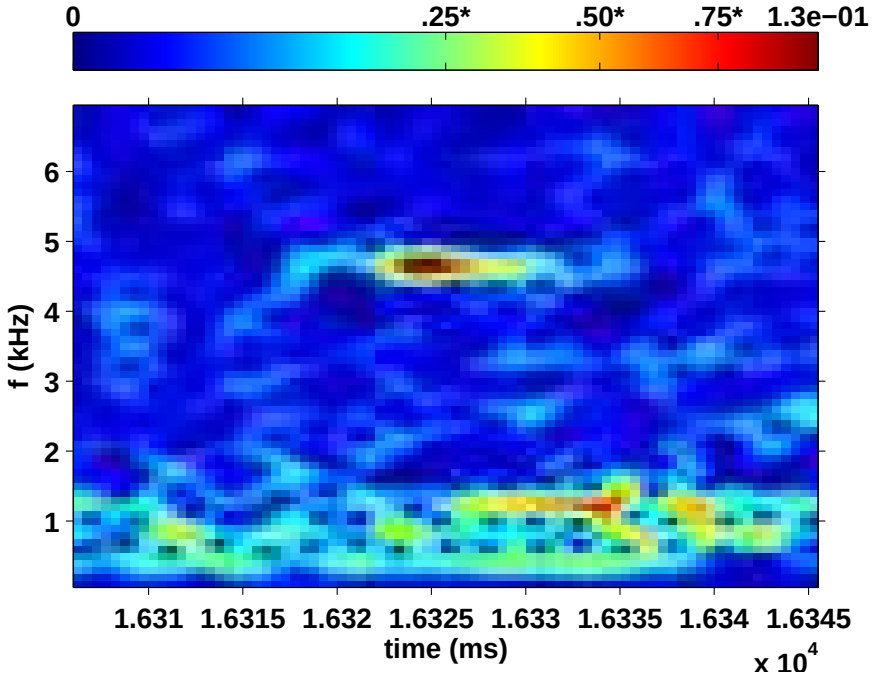


Figure 5.14: Spectrogram of the temperature perturbations during a partial crash in JET pulse #84729, in the time range $t = 16.30 - 16.345$ s.

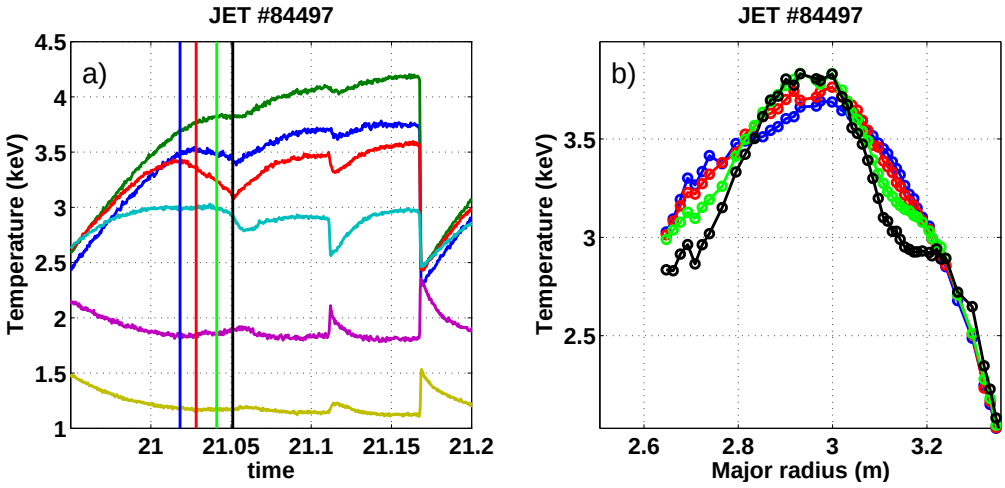


Figure 5.15: Extremely slow partial crash in JET pulse #84497. Slow ECE time traces (left). Profiles corresponding to the vertical lines (right).

sawtooth, with a "partial crash" in the middle of each ramp. The blue and green signals are inside the $q = 1$ surface and the red one outside. However the magnetic axis is not available in this pulse. The temperature drop at each partial crash is quite small, of the order of 0.1 keV, but clearly visible. It should be noticed that the characteristic time of this drop is very different from the regular sawtooth crash. It can be confirmed using

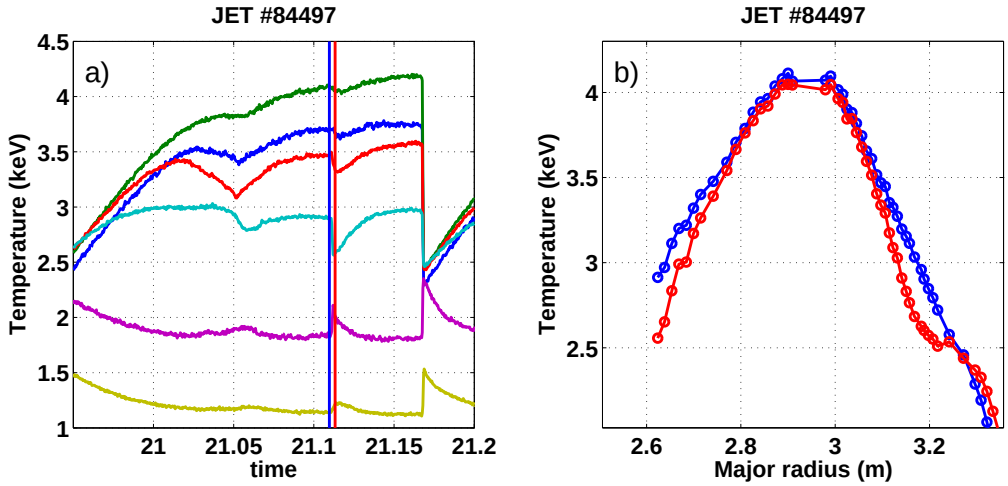


Figure 5.16: Fast partial crash in JET pulse #84497. Slow ECE time traces (left). Profiles corresponding to the vertical lines (right).

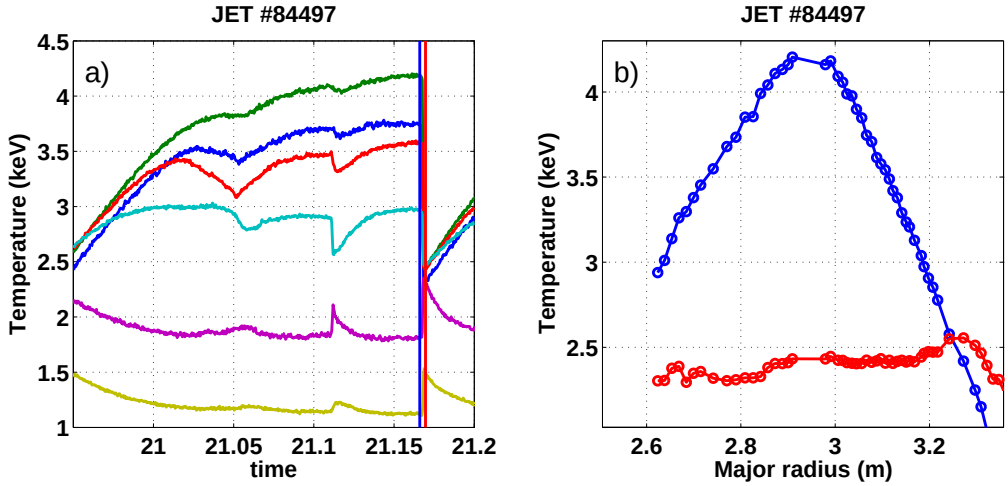


Figure 5.17: Regular sawtooth crash in JET pulse #84497. Slow ECE time traces (left). Profiles corresponding to the vertical lines (right).

the fast ECE signals that this time is of the order of several milliseconds, almost 10 ms. The green signal exhibits an even slower drop, in more than 15 ms. Also, it should be noticed that the event can be observed only on the most central signals, and not on the signals from outside the $q = 1$ surface, while usually these chords exhibit a clear rise indicating the presence of a heat pulse[8]. The mode responsible for this partial crash is most probably an $\mathsf{m} = 1$ kink mode, like the sawtooth precursor. Fig. 5.14 shows the spectrum of the temperature perturbations obtained with the fast ECE diagnostic, in the range $t = 16.30 - 16.345$ s. It is seen that a short-lived mode at 5 kHz develops at the

[8] Actually, something can be seen on the red trace of Fig. 5.12, but this is extremely weak and with an even longer time scale.

time of the partial crash. This is the typical frequency of the m = 1 sawtooth precursor in JET.

Yet a different behavior can be observed in JET. Two different types of partial crashes are displayed on Figs. 5.15 and 5.16 for JET pulse #84497. One can see on the left panel some slow ECE traces in the core and outside the $q = 1$ surface, as well as the corresponding profiles on the right panel. For comparison, Fig. 5.17 shows what happens to the temperature at the following regular sawtooth crash. The case of 5.15 is particularly striking. It shows a flattening almost 10 cm wide developing on an extremely long timescale, here about 30 ms. Such a flattening of the profile in general indicates the presence of a magnetic island. Indeed when a magnetic island is present, the fast parallel diffusivity of the temperature homogenizes the profile over the whole island, leading to the observed flattening. On this case, it develops so slowly that its effect can be seen only on the ECE channels located on the island, like the red time trace on Fig. 5.15 (left). The right panel shows that indeed the flattening develops very progressively.

On Fig. 5.16, we see a much faster development of a similar phenomenon, a clear flattening of the temperature a few centimeters wide. Looking at the time traces, in particular the purple one, outside $q = 1$, the sequence is reminiscent of a sawtooth crash of the second kind. However we do not observe the oscillations following the first small crash so typical of the second kind of crash described above. Thus the phenomenology is still a bit different.

### 5.2.5 Monster sawteeth, NTMs and mode locking

Here we present a quite common feature of sawtoothing plasmas, which may actually be the main source of concern, well before the concern about the flushing of impurities and He ash. We have already mentioned the Neoclassical Tearing Mode (NTM) in chapter 1, and the fact that it can be triggered by sawtooth crash. Here we give an example.

The NTM typically occurs after large sawteeth. The denomination monster sawtooth is somewhat loose, but it generally refers to sawteeth which have a long period, comparable to or longer than the energy confinement time $\tau_E$ [Bhatnagar 1989]. On JET, the amplitude in the core is often of the order of 2 keV or more and the period is longer than neighbouring sawteeth, reaching between several hundreds of milliseconds and up to 3s [Bhatnagar 1989]. The link with NTMs has been noticed from the start, at their discovery [Campbell 1988], and a detailed study of the interaction between the two can be found in Ref. [Maget 2005]. We can see such a crash on Fig. 5.18. We see that the amplitude is 2.4 keV and the sawtooth period, 350 ms, is indeed almost twice the period of the preceding and next sawteeth, about 200 ms. The crash time is fast, 100 $\mu$s.

Fig. 5.19 shows a spectrogram of the magnetic coil signal, on which the evolution of the NTM frequency can be seen. There are several such coils on the JET tokamak, which are able to probe the plasma for the magnetic perturbations. The coils deliver a current proportional to the time derivative of the perturbation. On the figure, the mode is clearly seen to be triggered immediately after the sawtooth crash at $t = 20.93$ s. This has been frequently reported in the literature, see for instance Refs. [Chapman 2010a, Chapman 2010b, Graves 2012, Maget 2005, Sauter 2002]. The mode frequency stagnates

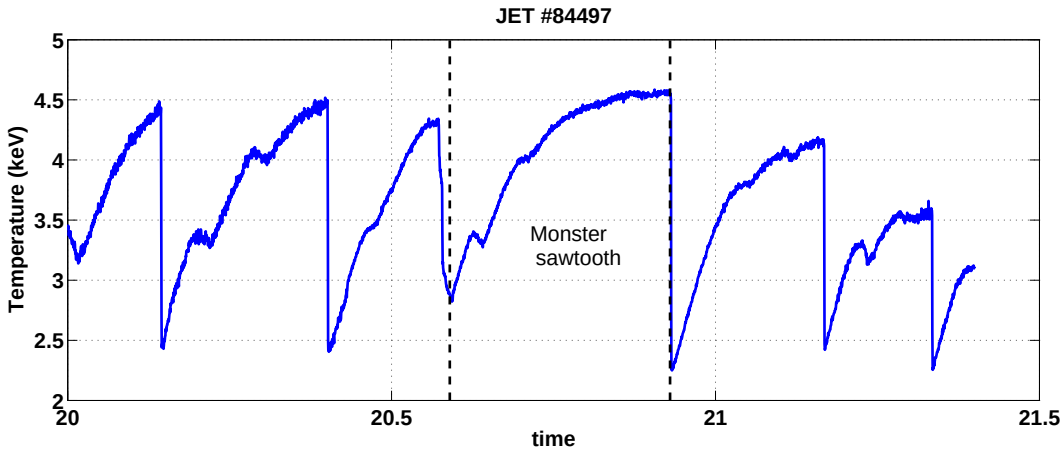


Figure 5.18: Monster sawtooth crash followed by the triggering of an NTM in JET pulse #84497. The crash is at $t = 20.93$ s and it seen that the sawtooth period is longer than neighbouring sawteeth.

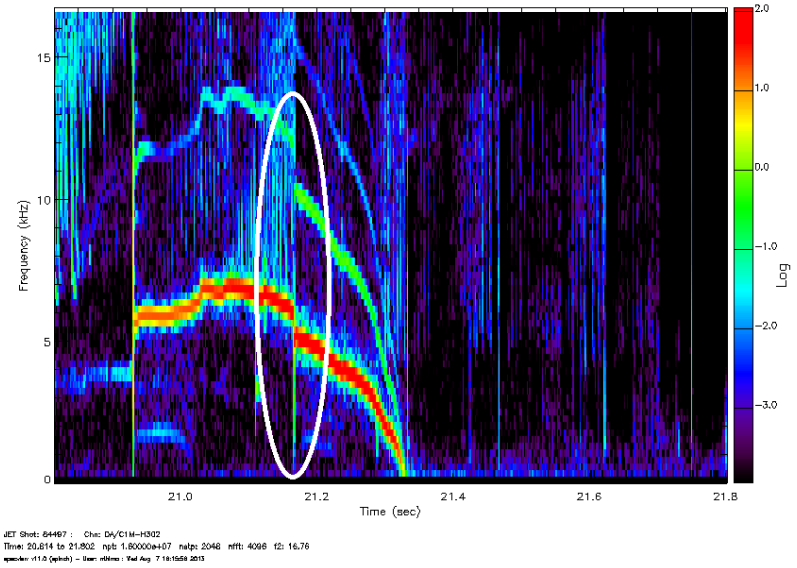


Figure 5.19: Spectrogram of the magnetic coil signal after the triggering of the NTM. Mode locking can be seen to occur at $t = 21.33$.

a little while until it suddenly drops to zero. One could think that the mode has faded away but looking at Fig. 5.20 at $t = 21.906$, long after the drop of the frequency to zero, we still see a 5 cm wide flattening of the temperature[9]. It means the mode and the associated magnetic island is still present in the plasma. The drop of the frequency is due to the fact that the mode has locally completely stopped the plasma flows. This is called "mode locking" and it happens because of the island coupling to the error fields due to

[9] It is not seen on the magnetic coil signal anymore because the latter is sensitive to the time derivative of the magnetic perturbation. When the mode is locked, the associated magnetic perturbation is static, thus not detected by the diagnostic.

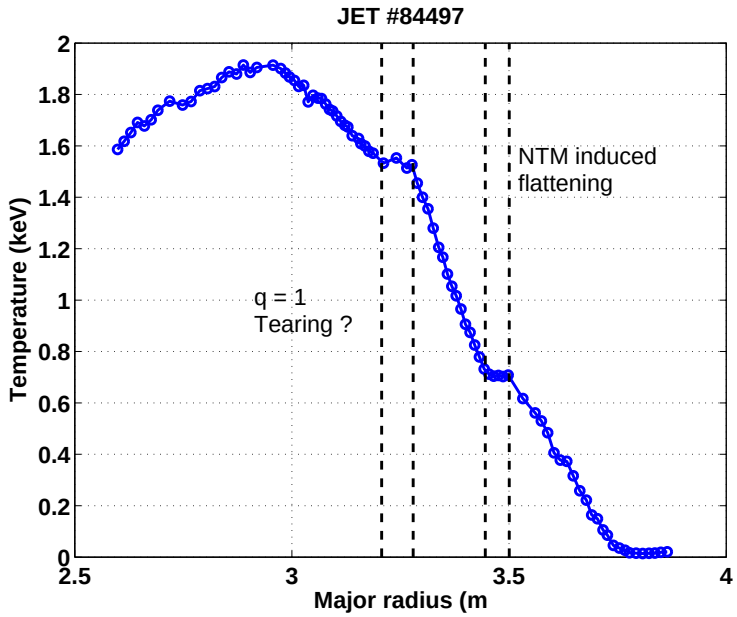


Figure 5.20: Temperature profile at $t = 21.906$ s, at the top of a sawtooth ramp, showing the flattening on the $q = 3/2$ surface still present even after the mode is locked. Also shown is a flattening on the $q = 1$ surface.

a misalignment of the toroidal field coils (see Refs. [Fitzpatrick 1995b, Fitzpatrick 1991, Wang 1997]). A pedagogical review of the associated physical mechanism can be found in Ref. [Fitzpatrick 1995a].

Another phenomenon is very interesting on Fig. 5.20, at $R = 3.25$ m, the location of the $q = 1$ surface, (or at least the location of the sawtooth inversion radius in most of the discharge). One observes an important flattening here too, similar to the one caused by the NTM. It also resembles the flattening caused by partial crashes, as in Fig. 5.16, however no trace of partial crash can be found during the corresponding sawtooth ramp. The spectrogram (not shown) at the same time shows no mode, so that this one is possibly locked like the NTM. It is very interesting that this is observed at the top of the sawtooth ramp, and repeats over a large number of successive sawtooth crashes. In other words, the island seems to survive the sawtooth crash. However it could also be destroyed by the sawtooth crash and reform in the middle of the ramp. It is impossible to discriminate between the two since the large scale flattening of the sawtooth crash prevents from seeing the possible effect of the island immediately after the crash. This behaviour starts to be observed shortly after the onset of the NTM, which reinforces the evidence of a coupling between the two. Related issues are discussed in section 5.2.6.

As seen on Fig. 5.20, the NTM has a severe effect on the confinement, and the island is sometimes seen to grow quite freely after the mode locking, which can lead to a disruption. When mode locking is detected on JET, there is a feedback from the real time controllers to try to avoid a disruption and lead the discharge to a smooth end. This implies in particular a reduction of the energetic content by progressively switching off additional heating. Since disruptions are such a big source of concern for ITER, so are

NTMs and monster sawteeth. This is the reason why some strategies have been imagined to artificially reduce the sawtooth period, in using the fact that the sawtooth period is sensitive to the populations of energetic particles (see section 2.2.6).

Also highlighted on Fig. 5.19, in the white ellipse, is a sawtooth crash occurring a bit later (it is actually the same as in Figs. 5.15, 5.16 and 5.17). This crash is seen to have a quite significant effect on the mode frequency, which seems to indicate that sawtooth crashes modify the plasma momentum. Since momentum is conserved, this means that there is generation of a momentum dipole, which locally modifies the rotation. Note that depending on the radial propagation of the two parts of the dipole, this can lead to a net modification of the plasma momentum. The effect of sawteeth on plasma rotation has been studied on the TCV tokamak [Duval 2010].

On Fig. 5.21, we show an other example of the link between mode locking and the sawtooth crash, where it even seems that the mode locking is triggered by the sawtooth crash. Indeed the mode frequency starts dropping just after the sawtooth crash occurs (again highlighted in white). This possible interaction between mode locking and sawteeth probably requires some attention.

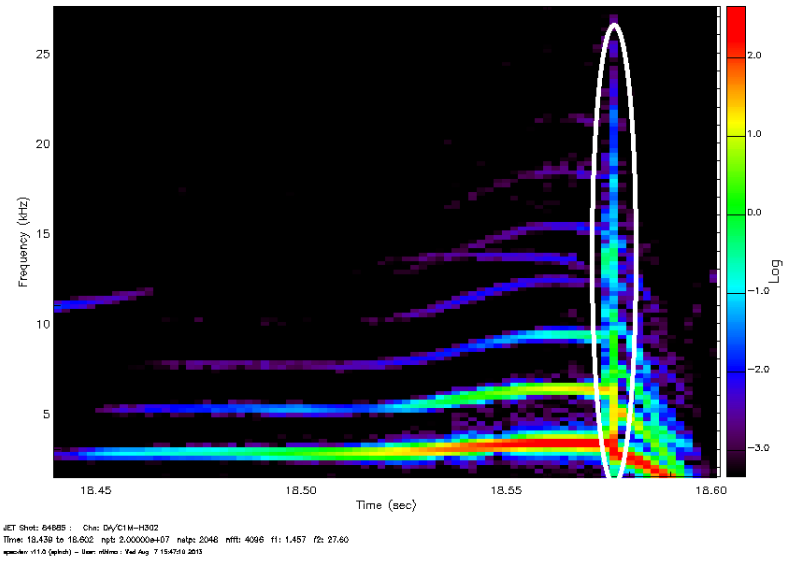


Figure 5.21: Mode locking in JET pulse #84685, where it seems the locking is triggered by the sawtooth crash occurring at $t = 18.57$ s.

### 5.2.6 Incomplete reconnection

We now come to one of the most counter-intuitive aspects of the sawtooth instability. It is the fact that reconnection is usually incomplete during the sawtooth instability. By this we mean that the reconnection process is stopped at some point, and not all flux surfaces reconnect up to the mixing radius. The evidence for this conclusion mainly come from core safety factor measurement, which have shown that $q$ in general does not rise

to 1 after the crash (see section 5.2.6.1). A confirmation comes from the study of the so-called "snake" instability, this is mentioned in section 5.2.6.2.

First recall that in the framework of section 4.1 about Kadomtsev's model, the magnetic surfaces remain well-defined during the whole duration of the reconnection process (although the topology is changed), and the magnetic flux is conserved. This implies that if all magnetic surfaces reconnect up to the mixing radius, then the central value of the safety factor after the crash should be 1. If it is not the case, it means one of the following:

- (i) Magnetic surfaces are well defined and magnetic flux is conserved but reconnection is not complete.
- (ii) Reconnection is complete but the magnetic flux is not conserved.
- (iii) Reconnection is complete but the magnetic surfaces are not well defined during the evolution, and the analysis of section 4.1 does not make sense.
- (iv) Reconnection is not complete, and magnetic surfaces/flux are not well-defined/conserved quantities.

The first proposition is the most simple conceptually because it remains attached to the convenient concepts of magnetic surfaces and magnetic surfaces. It basically means that a magnetic island is destabilized at some point, and grows until it saturates at a finite amplitude. The third proposition probably goes along with the second one. The fourth one may be the closest to reality, although it does not get us very far, since it says that nothing is defined and understood. We will return to these propositions after presenting the experimental results of a few machines, including JET and Tore Supra.

#### 5.2.6.1 Safety factor measurements

The most intense activity regarding core safety factor measurements took place at the end of the 1980s/beginning of the 1990s. The two most common methods for this measurement are the Motional Stark Effect (MSE) polarimetry and the Far Infrared Interferometry to estimate the Faraday rotation effect. MSE measures the polarization of the Balmer-alpha light emitted by a probing beam of neutral hydrogen atoms. The beam propagating at the velocity $\boldsymbol{v}$ experiences in its reference frame an electric field $\mathbf{E}' = \boldsymbol{v} \times \mathbf{B}$, which splits the line in nine sublines (Stark effect), and also polarizes these lines [Levinton 1989]. The polarization is parallel to the local magetic field for certain transitions, and thus measuring the polarization of the emitted light yields the tilt angle of the magnetic field [Levinton 1989]. The Faraday effect uses the fact that the magnetic field causes the circular left-handed and right-handed waves to propagate at different velocities. Thus measuring the phase shift by interferometry of an adequately polarized laser beam yields a measure of the magnetic field tilt angle. The advantage of far infrared interferometry over MSE polarimetry is that the latter may not be applicable to ITER [Bergerson 2012]. The first measurements at the end of the 80s led some authors to find the safety factor close to 1 during all the sawtooth cycle, and others to find it

below 1 outside of experimental error bars (see the introduction of Ref. [O'Rourke 1991] for an exhaustive list of references). However these first measurements were poorly time-resolved so that they could not discriminate between a situation where $q$ indeed stays below 1 and a situation where it increases to 1 at the sawtooth crash but drops rapidly to lower values, in a time shorter than the capabilities of the measurement system. In the beginning of the 90s, increased time resolution for MSE and far infrared interferometry (reaching up to 1 ms time resolution [O'Rourke 1991, Wróblewski 1993]), as well as coherent signal averaging [Soltwisch 1988] allowed much more reliable measurements of the change of $q_0$, denoted $\Delta q_0$. Note that in stationary regime, $\Delta q_0$ is not only the change of $q_0$ at the sawtooth crash, but also minus the diffusive change of $q_0$ during the sawtooth ramp. Thus the measurements can also be compared to current diffusion models.

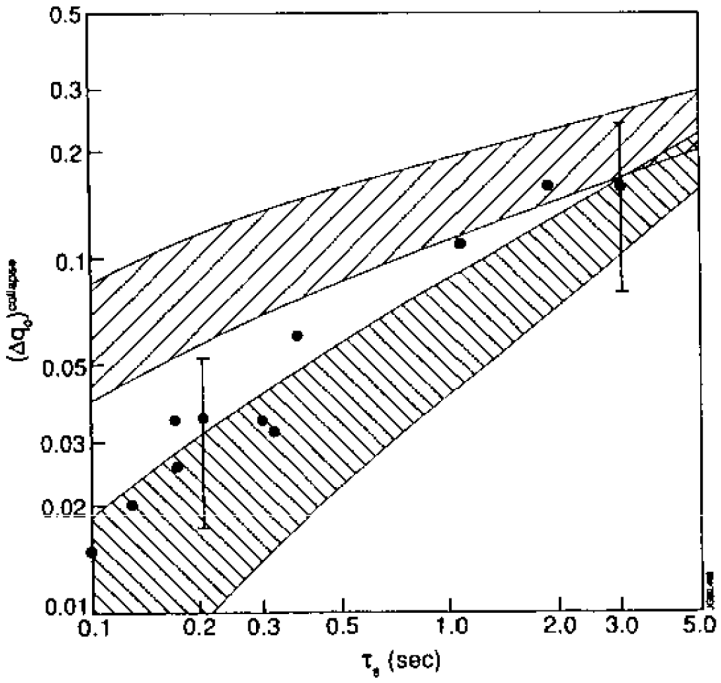


Figure 5.22: Measurements of $\Delta q_0$ in JET. The circles are the experimental data, the upper band results from current diffusion assuming complete reconnection, the lower band from calculations assuming $q_0 = 0.75$ after the sawtooth crash. From Ref. [O'Rourke 1991].

On JET, $q_0$ is found to be around 0.75 and $\Delta q_0 \sim 0.01 - 0.1$, as seen on Fig. 5.22. On the figure, the circles represent the experimental data points as a function of the sawtooth period. The two bands represent the estimation of $\Delta q_0$ following two assumptions: complete reconnection, meaning $q_0 = 1$ after the crash (upper band), or $q_0 = 0.75$ after the crash (lower band), as found in the experiment. The point to understand here is that relative measurements are more reliable than absolute measurements. Hence, the absoulte value of $q_0$ could be questioned, but the measurements $\Delta q_0$ are more precise. However, the figure shows that the data points best fit the lower band, corresponding to the measured value of $q_0 = 0.75$ at the center.

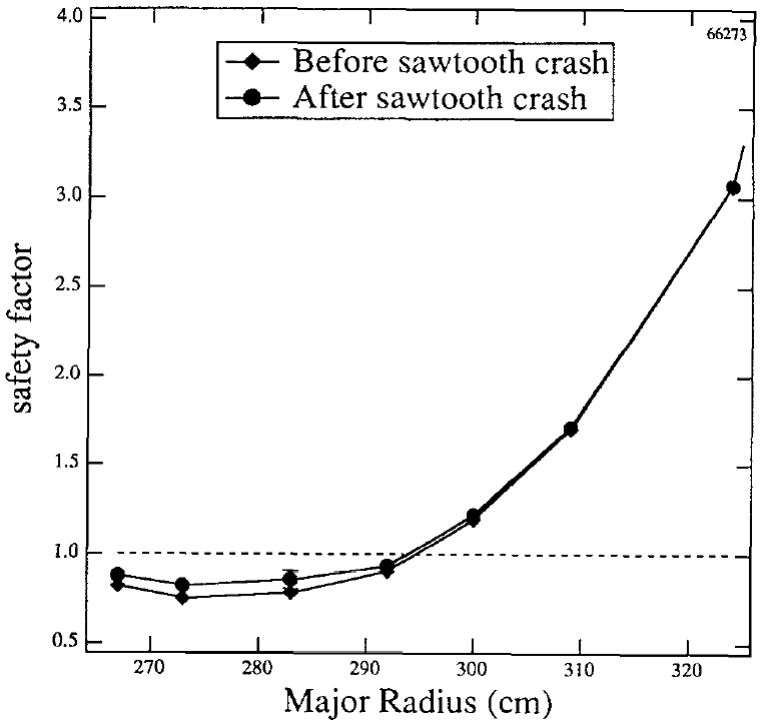


Figure 5.23: Typical evolution of the $q$ profile at a sawtooth crash in TFTR. From Ref. [Yamada 1994].

The results of many tokamaks, like TEXTOR [Soltwisch 1988], TFTR [Levinton 1993, Yamada 1994] or PBX-M [Levinton 1989] agree with this result, and usually find a similar value, $0.7 - 0.8$ for the central safety factor. For instance, Fig. 5.23 shows the typical evolution of the safety factor at the sawtooth crash in TFTR.

However, contrary to these results, in DIII-D the safety factor is found to be very close to 1 [Wróblewski 1993], with $\Delta q_0$ of the order of 0.05, in a wide range of plasma parameters. This suggests complete reconnection happens, but is also compatible with Wesson's model (see section 4.1.5).

#### 5.2.6.2 The "snake" instability

Even though one could criticize the aforementioned safety factor measurements, which are quite old and suffer from large uncertainties, an other phenomenon, known as the "snake" instability, adds to the body of evidence toward incomplete reconnection at the sawtooth crash. The snake was first discovered in 1987 on JET [Weller 1987], most often after pellet injection[10]. Fig. 5.24 shows the observation of a snake using the SXR diagnostic. The terminology is readily understood from the shape of the signal. Generally speaking, snakes are very stable structures. On JET the snake is usually located at the $q = 1$ surface and its helicity is $(\mathsf{m}, \mathsf{n}) = (1/1)$, it is a region of significant enhancement

[10]Pellet injection consists in injecting high velocity frozen deuterium chunks in the machine as a way to fuel the plasma.

of the density (up to a factor of 2), and accumulation of impurities inside the snake structure is also thought to play an important role in their stability. They are also

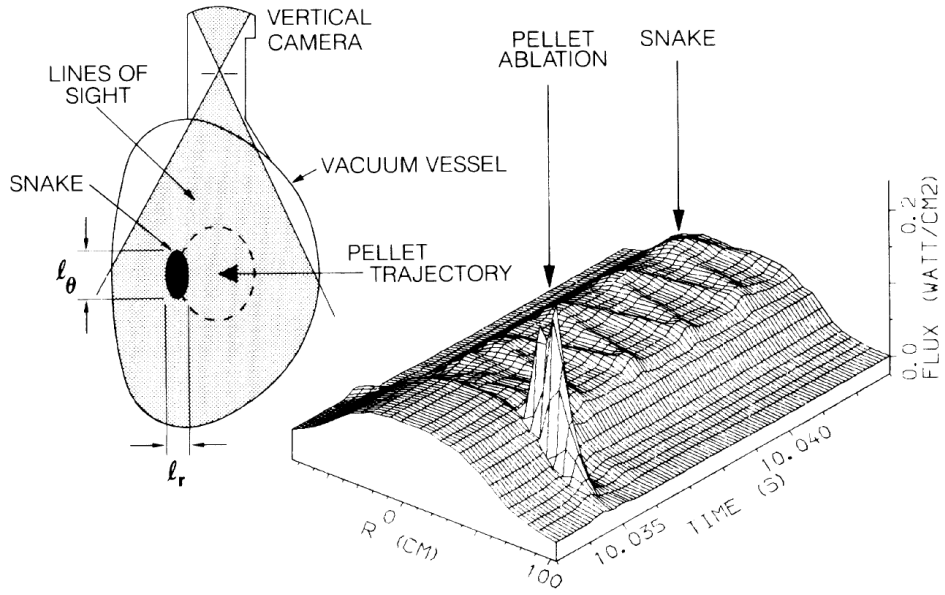


Figure 5.24: Observation of a snake on JET, figure taken from [Weller 1987].

observed on other machines, in particular Tore Supra [Pecquet 1997] and Alcator C-mod [Delgado-Aparicio 2013]. On Tore Supra, an important difference with JET is that the snake is not observed on the $q = 1$ surface, but at roughly $r_{snake}/r_{q=1} = 0.5$. This is interpreted as being the indication for a second $q = 1$ surface inside the most external $q = 1$ surface, or a very flat safety factor inside the $q = 1$ surface. However, in all cases, the snake is thought to be caused by a (1/1) magnetic island, which remains stable for a very long time. The stability of the snake is so good that they can last several seconds, sometimes they disappear only with the end of the discharge. This means they are not destroyed by sawtooth crashes. Rather, their radius is observed to shrink by a few centimeters at the sawtooth crash, as shown on Fig. 5.25 taken from [Weller 1987]. The poloidal structure can also be transiently distorted [Delgado-Aparicio 2013].

If the snake's position is a good indication of the $q = 1$ surface position, the latter observation strongly supports the theory of incomplete reconnection at the sawtooth crash. Indeed, otherwise, the snake should die away and possibly reform once a new $q = 1$ surface is present. Here instead the position of the $q = 1$ surface is only seen to move towards the center, as would be the case if there is only a small rise of the central safety factor in the $q < 1$ region. The fact that the snake is almost unaffected by the crash is really striking when one considers the usual interpretation of the sawtooth crash as a large scale reorganization of the magnetic field and redistribution of particles and energy. Also, if the crash involves the non-linear evolution of a (1/1) magnetic island, it would seem natural to assume that the snake's magnetic island be the initial "seed" of the sawtooth's island. But it does not seem to be the case as the snake's island survives the sawtooth crash. Given this, it would be tempting to advance that the thermal collapse

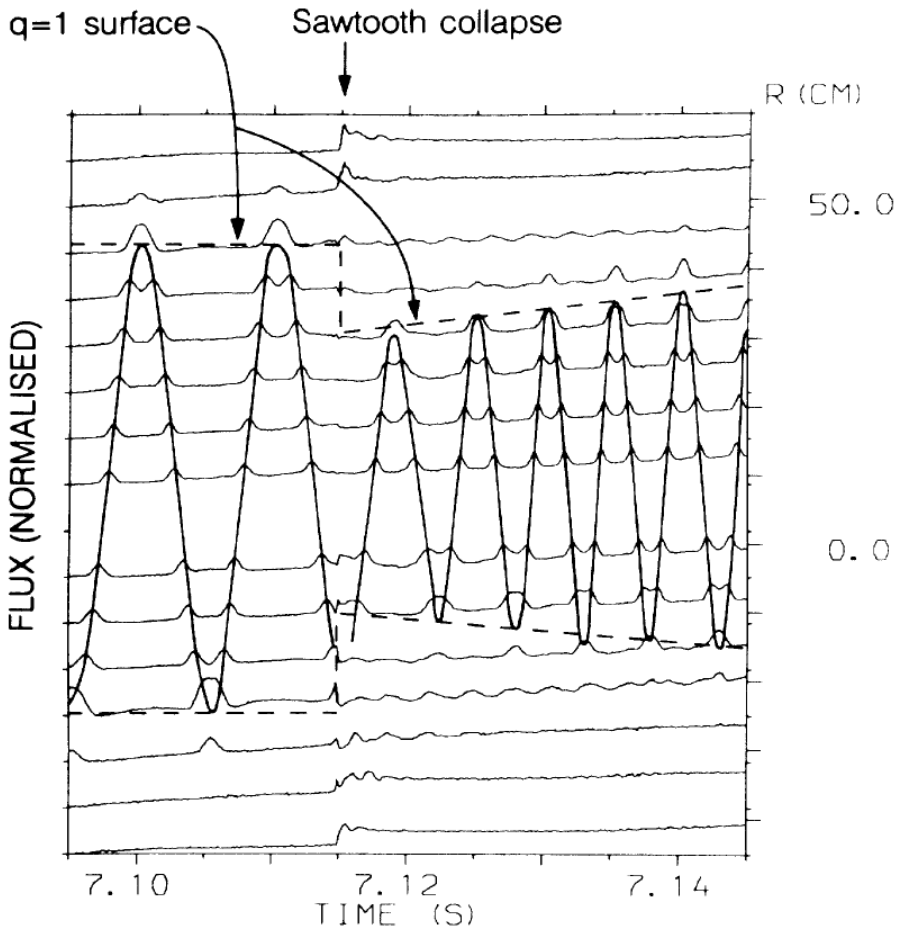


Figure 5.25: Shrinking of the snake's size at the sawtooth crash, figure taken from [Weller 1987].

observed at the sawtooth crash is not determined by pure (1/1) magnetic reconnection. Or it could be that the resonant surface of the snake is distinct from the resonant surface of the sawtooth, which seems to be backed up by the observation of a snake inside the $q = 1$ surface on Tore Supra. At the very least, the snake instability, its long stability[11], its link with the $q = 1$ surface and its resistance to sawteeth are baffling, and well in favour of incomplete reconnection.

Before coming to the possible explanations for incomplete reconnection, there are a few facts that can soften a little bit the preceding arguments. First, it may be that the presence of the snake modifies the core properties in such a way that only incomplete reconnection is possible, whereas full reconnection applies in the absence of snake. For instance on Tore Supra, it seems that the full thermal collapse characteristic of the sawtooth crash is not observed when the snake is present [Cristofani 1996]. Only the triggering of an island is observed. Hence the statement that the snake survives the

[11] Even though it seems paradoxical that an instability be stable, we mean that the saturated state is stable over time.

sawtooth crash is incorrect in this case, or at least exaggerated. Also, recent results about 3D, snake-like equilibria with an axisymmetric boundary [Cooper 2011] indicate that such equilibria can exist even if the minimum value of $q$ is slightly above 1. Thus there is a body of evidence in favour of the hypothesis of incomplete reconnection, but an extremely rigorous and careful reexamination, backed up by more recent safety factor measurements, would probably be required to be fully conclusive. In the following still, we assume incomplete reconnection to be generally verified and investigate possible explanations.

### 5.2.7 Possible explanations for incomplete reconnection

To bring back together our basic understanding of the sawtooth/reconnection phenomenon with the measurements of $q$ profile and snakes, several attempts have been made. In the following we briefly present 4 interesting attempts.

#### 5.2.7.1 Diamagnetic stabilization

We have seen in the preceding chapters that the diamagnetic effects have a significant effect on the dynamics of the kink mode. Namely, they are linearly stabilizing, and non-linearly, they can be either stabilizing (in the first stages of reconnection in the XTOR-2F case) or destabilizing (significantly increasing the growth rate in the far non-linear stage). In the literature, bifluid simulations are reported where the diamagnetic effects completely suppress reconnection [Swisdak 2003, Beidler 2011]. In these papers, it is argued that the compression of flux at the reconnection site goes along with plasma compression, hence a large increase in the pressure gradient. The plasma flows are significantly affected by the resulting diamagnetic flows. On each side of the reconnection layer, the ion or electron diamagnetic velocity (depending on which side one is looking at) is opposing the fast reconnection outflow related to the electric drift $v_E$. As a result, reconnection is stopped when the amplitude of the diamagnetic velocity exceeds the amplitude of the Alfvénic outflow. This suppression of reconnection is observed in their simulations and may be related to the measured incomplete reconnection after the sawtooth crash in tokamaks. However, we remark that in our own bifluid simulations with the XTOR-2F code, no such suppression of reconnection is observed, even though the diamagnetic flow during the reconnection phase and the reconnection outflow are of the same order of magnitude. On the contrary, we observe a large increase in the reconnection rate of the far non-linear stage when the Hall term is included in the Ohm's law, that is, when the magnetic flux is advected by the total electron velocity, including the electron diamagnetic velocity (see chapter 4). Hence this hypothesis still requires more investigation.

#### 5.2.7.2 Double current-sheets

In 1992, Kolesnichenko *et al.* [Kolesnichenko 1992] proposed that even Kadomtsev's model could be compatible with incomplete reconnection, in the case where two instead of one current layers are present in the plasma. In this case, the resulting relaxed state obtained using Kadomtsev's rules can indeed have $q_0 < 1$. The plasma motion involved is some

kind of mixing between Kadomtsev reconnection followed by a Wesson-like motion (see section 4.1.5), as shown on Fig. 5.26 reproduced from the article. In 1994, Biskamp and

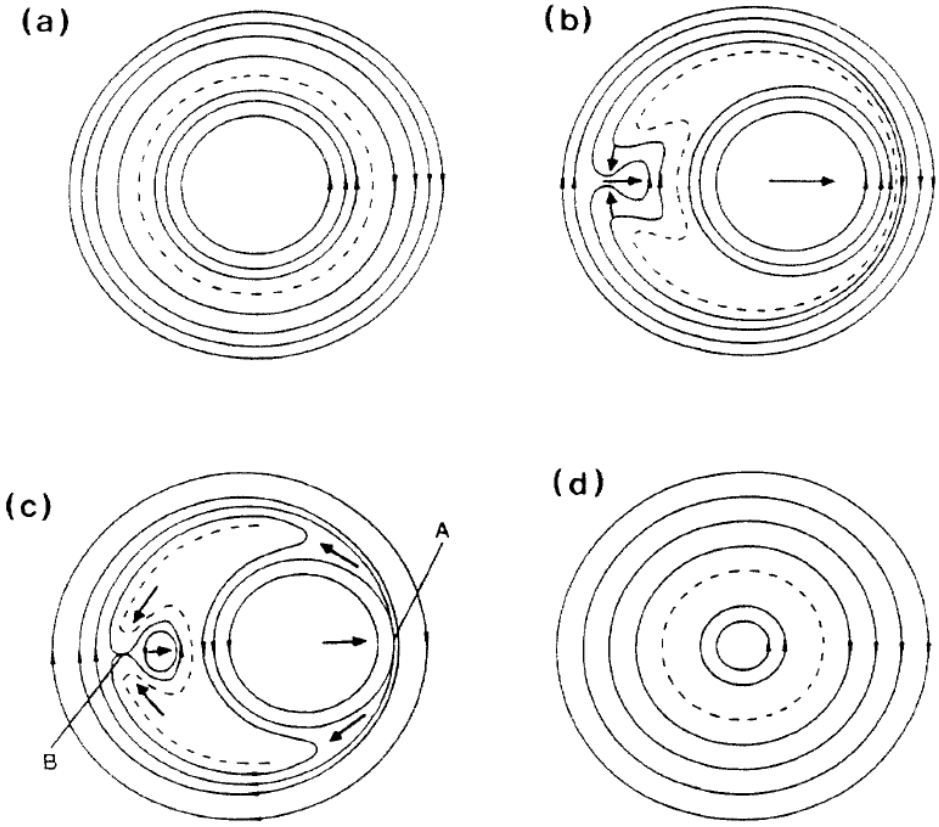


Figure 5.26: Evolution of the field lines of the reconnecting field during a mixed Kadomtsev/Wesson-like reconnection. (a) initial state, (b) shift of the large hot plasma core and formation of a small cold bubble, (c) the hot core is enclosed by a cold crescent which is perturbed by a colder island with $q < 1$, (d) the final axisymmetric state with a cold plasma core and $q_0 < 1$. Figure taken from [Kolesnichenko 1992].

Drake [Biskamp 1994] carried out simulations which back up this hypothesis. Instead of resistivity, they used hyperresistivity (which can also be viewed and justified physically as a viscosity on the electron flow) and most importantly electron inertia in Ohm's law: $(m_e/ne^2)\mathrm{d}_t j$. The problem with the reconnection being dominated by a purely resistive process is that the scalings of outflow versus inflow, sheet thickness and energy dissipation in the sheet let no kinetic energy available at the end of the reconnection process. In the case where it is dominated by electron inertia, the kinetic energy remaining in the relaxed state is sufficient to drive a Wesson-like motion, which drives the external surfaces back inside the core (as shown on Fig. 5.26). The resulting safety factor is below in the core, and Biskamp also says that the resistance of snakes to the sawtooth crash could be explained by this model.

Note that it is a bit inappropriate to denote this model as incomplete reconnection since the first Kadomtsev-like phase indeed leads to complete reconnection of the flux.

The restoration of a safety factor below 1 is established by the following Wesson-like motion of the plasma.

#### 5.2.7.3 Magnetic stochasticity

In 1984, Lichtenberg [Lichtenberg 1984] proposed a sawtooth crash mechanism mediated by large scale stochasticity. The purpose of the study was to explain the rapidity of the crash (it was a few years before the safety factor measurements and the observation of the snake). However, it also gives a nice framework for incomplete reconnection.

The physical picture is that after the primary destabilization of the (1,1) island, the mode couplings due to the toroidal curvature can destabilize higher order modes. When these modes are in sufficient number and sufficiently large, their overlapping leads to the destruction of the magnetic surfaces and to a region of large stochasticity, in the spirit of Fig. 3.4 (c) and (d). When the stochasticity is widespread, the temperature, which is transported along the field lines, can be relaxed rapidly in a quasi-linear diffusion time. The minimum quasi-linear time is below the experimental observed crash time, which speaks in favour of the model. During this phase, the (1/1) magnetic island cannot be observed because of magnetic surface destruction, but it is still present. The higher order modes are expected to diffuse away after the thermal collapse, possibly leaving the (1/1) island subsisting. At the least, since the collapse is fast compared to the characteristic evolution time of the island observed experimentally before the crash (the precursor is in general in a saturated state), the island could be only slightly affected by the crash. The current would also diffuse along the stochastic field lines, but at a slower rate, leading to a small modification of the safety factor. In order for the model to be realistic, a quite strong magnetic shear $s$ is required. Indeed, the distance between the islands is proportional to $1/s$, while their width is proportional to $1/\sqrt{s}$, so that there is more island overlapping with increasing shear (the islands are smaller, but they are even more close).

This model has the advantage that it can explain both the fast crash time and incomplete reconnection in a quite elegant manner. However it has not been backed up by nonlinear MHD simulations yet.

#### 5.2.7.4 Secondary ballooning instability

In 1987, Bussac *et al.* proposed that the sawtooth crash happens in two distinct phases. The first one is, as usual, a kink like displacement evolving toward a neighbouring helical equilibrium (or saturated state). In this helical state, due to the rigid displacement, the pressure gradient is significantly enhanced at the $q = 1$ surface. Some part of this pressure gradient is located on the bad curvature size of the tokamak which is unstable to ballooning modes[12]. The ballooning mode is then responsible for the final thermal

[12] Ballooning modes are interchange pressure gradient modes located on the outboard (LFS) of the tokamak and destabilized by the toroidal curvature. This means they do not have given poloidal and toroidal mode numbers, but are a mixing of several modes with high m and n which combine to give a "ballooning" on the outboard size. This unstable region is called the bad curvature region.

collapse. This has not been backed up by nonlinear MHD simulations yet.

There have been other attempts to reconcile measurements and the basic theory of the sawtooth crash, but we will not cover them all. We now turn to an important issue which is the link of the sawtooth crash with impurity transport, one of the focus of this thesis.

### 5.2.8 Interaction between sawteeth and impurities in JET

One of the most stringent issues for the control of a burning plasma is the penetration of impurities, as mentioned in the introduction, chapter 1, especially heavy impurities coming from the wall. Indeed, recall that the power radiated by an impurity scales with the square of the charge $Z$ of the impurity. In particular, Tungsten ${}^{74}_{183.8}W$ is particularly preoccupying for the operation of the ITER tokamak, since at the temperatures reached in the core, $T_i > 20$ keV, the charge number of W exceeds 60. This implies that the maximum relative concentration which can be tolerated in the core of ITER plasma to be able to reach the ignition condition is of the order of $2 \times 10^{-4}$ [Pütterich 2010]. Several machines, including JET, now have W plasma facing components (the divertor plates in the JET case) in order to test the operation of a hot plasma with heavy impurities generated at the edge due to physical sputtering, melting, *etc.* We will see in this subsection that W can indeed significantly affect the plasma and sometimes lead to a radiative collapse.

#### 5.2.8.1 Core penetration of W due to a sawtooth crash

A very "nice" example of impurity penetration due to a sawtooth crash can be found in JET pulse #84617. Fig. 5.27 shows the time traces of injected power (NBI and ICRH), the central temperature, the line V12 of the vertical camera displayed on Fig. 5.4, the total radiated power obtained with bolometry[13] and a spectroscopic diagnostic for W[14]. It is seen that when NBI (11 MW) is switched on, at $t = 8.56$ s, the temperature increases rapidly, as expected, to reach almost 4 keV. The sawtooth period increases but after the third sawtooth at $t = 9.43$ s, just after the ICRH power is switched on, the temperature is seen to drop down to 1 keV. It is seen to coincide with a significant and fast increase of the time traces of panels (d), (e) and (f). Panel (d) is the SXR vertical line of sight which goes through the center, and as said above, an increase of this line at the sawtooth crash means impurity penetration. This suggests that the sawtooth crash has led to W penetration in the core, and that the induced radiation overcomes the additional heating and leads to a cool down of the plasma. This is confirmed and precised by a zoom on the relevant region (between the dashed lines), as seen on Fig. 5.28.

On this figure, the chronology is obvious. Between $t = 9.35$ and 9.4 s, panel (f) indicates that somehow, W is generated and enters in the plasma. This is confirmed by

[13] Bolometers collect all radiation emitted from the plasma without distinction, and deduce the total radiated power.

[14] This time trace is obtained from an energy resolved diagnostic, for which the wavelength range 16.5-25 nm has been identified as coming mainly from W. The plotted time trace is just the integration of the signal across this wavelength range. The emission is thought to come from the 1-2 keV region. We will not use it as a quantitative tool but as a confirmation that there is some W in the plasma.

the sudden rise of the total radiated power on panel (e). Starting from this time, the SXR time trace is seen to increase very smoothly, until the sawtooth crash at $t = 9.43$ s, where it undergoes a sudden rise, while the temperature naturally drops. The bolometry indicates that the total radiated power is of the order of 15-20 MW in this phase, that is, larger than the total heating (11 MW NBI plus $\sim$ 1 MW ICRH plus $\sim 1-2$ MW ohmic heating), which leads to a fast cooling down of the plasma temperature. It can be observed that this "W event" appears shortly after the ICRH antenna has been switched on. This may be not be a coincidence, as the link between ICRH power and W erosion has been reported in the literature, see for example Refs. [Dux 2007, Dux 2005]. The standard interpretation is that the coupling of the antenna to the plasma increases the sheath potential[15] and thus the ions are accelerated at higher energies, which enhances the sputtering at the wall.

[15] The sheath is a small (a few Debye lengths wide) charged region at the plasma-wall interface. Because of their small inertia, the electron flux would be larger than the ion flux along the open field lines in the scrape-off-layer in the absence of sheath. The sheath thus establishes as a result of the excess of electrons at the wall, to accelerate the ions and slow down the electrons.

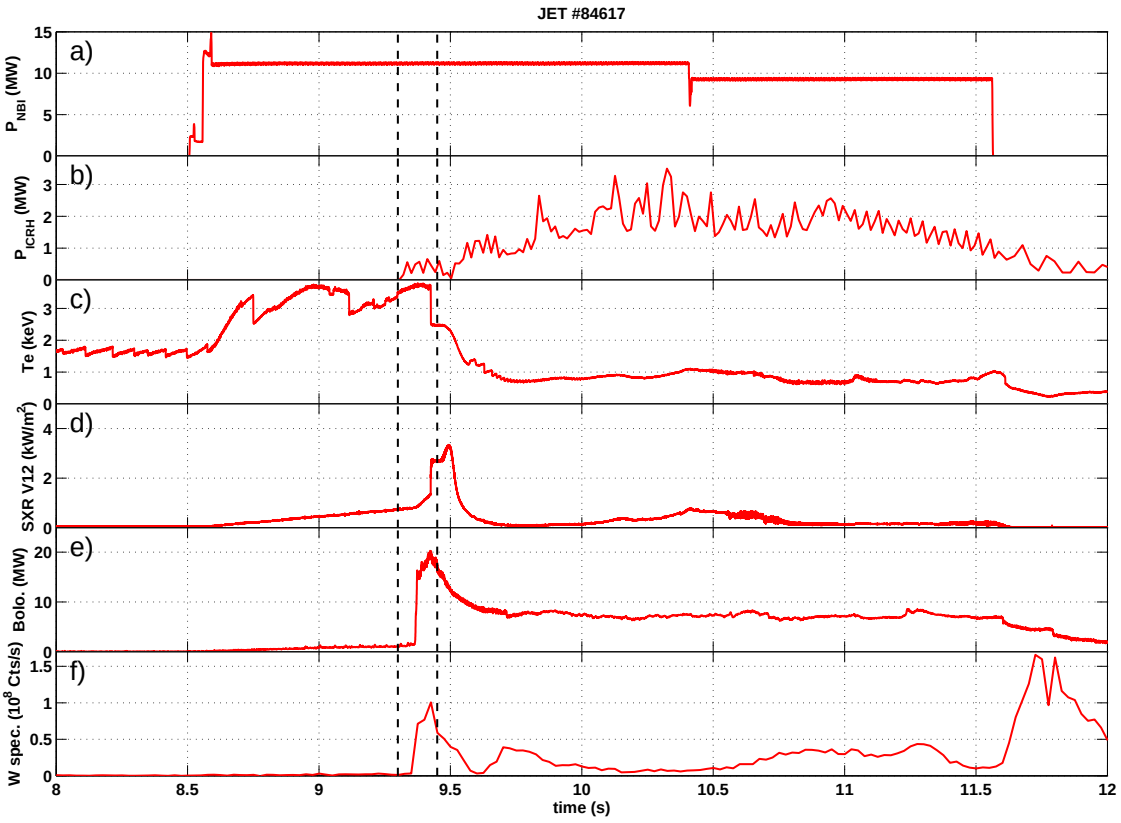


Figure 5.27: JET pulse #84617. NBI total power (a), ICRH total power (b), central electron temperature (c), Vertical SXR camera, line V12, (d), total horizontal radiated power from bolometry (e) and W spectroscopy signal (f).

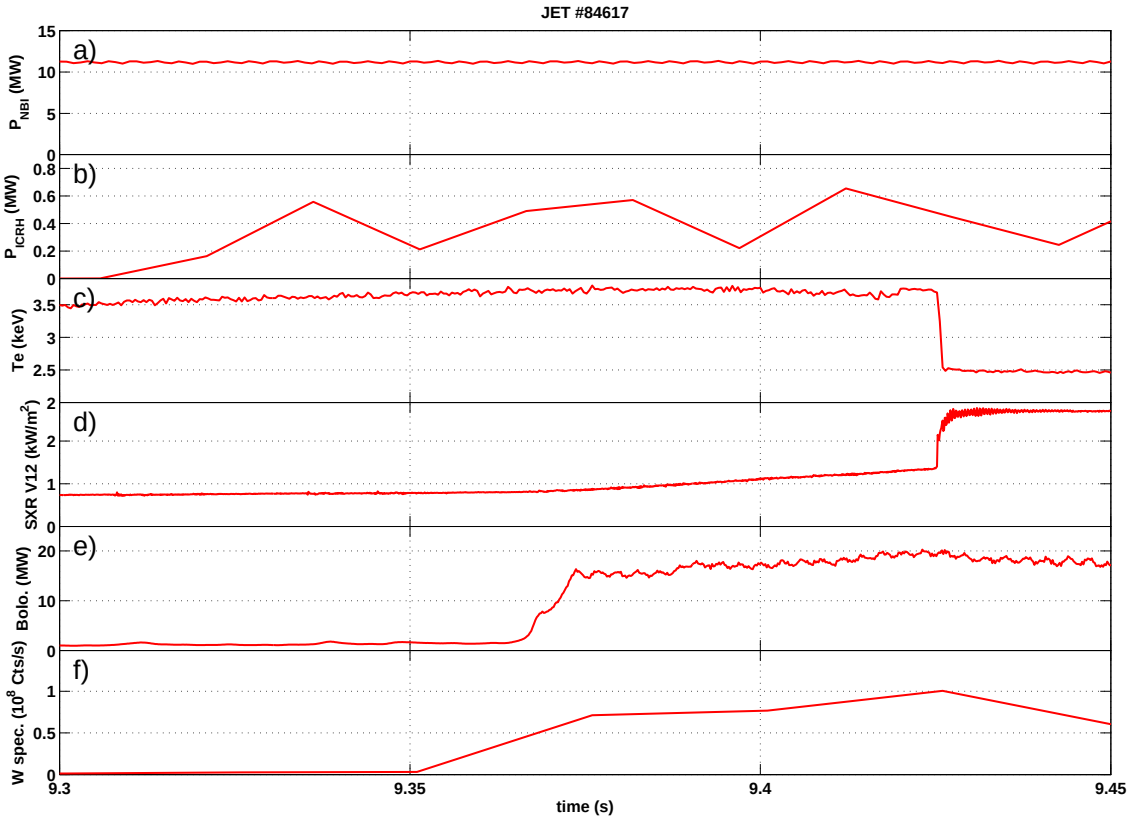


Figure 5.28: JET pulse #84617 (zoom of the preceding figure between $t$ =9.3 s and $t$ =9.45 s). NBI total power (a), ICRH total power (b), central electron temperature (c), Vertical SXR camera, line V12, (d), total horizontal radiated power from bolometry (e) and W spectroscopy signal (f).

#### 5.2.8.2 Radiative collapse due to impurities

In the preceding example, W leads to a dramatic cooling of the plasma after it is suddenly injected in the plasma. Radiative collapse of the discharge can also occur on longer time scales, when the penetration of the impurities and their accumulation in the center is not controlled. Fig. 5.29 shows an example of this in JET pulse #81913. It is thoroughly detailed in Ref. [Pütterich 2012].

On the figure, one sees first a slow rise of the radiated power from $t$ = 8.5 s to $t$ = 11.5 s, where the power starts to rise very rapidly and starts to overcome the NBI heating power, which leads to the collapse of the temperature in about 500 ms. This is similar to the previously analized case, but the chronology is a bit different. Instead of identifying a precise impurity event on the SXR signal, we see that the latter (panel (c), still looking through the core) increases on average despite frequent sawteeth. Notice that each sawtooth crash leads to a drop of the SXR signal, contrary to the preceding case. This suggests that in this case a small amount of impurities is already present

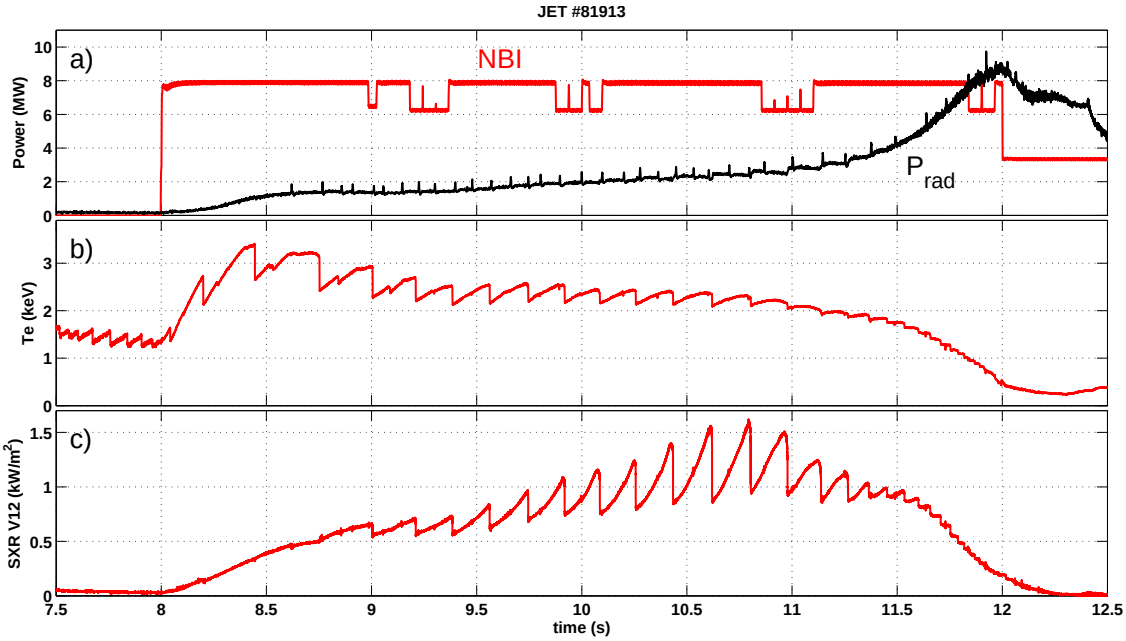


Figure 5.29: JET pulse #81913. NBI total power and radiated power (bolometry) (a) Core temperature (b) and vertical SXR camera, line V12 (c).

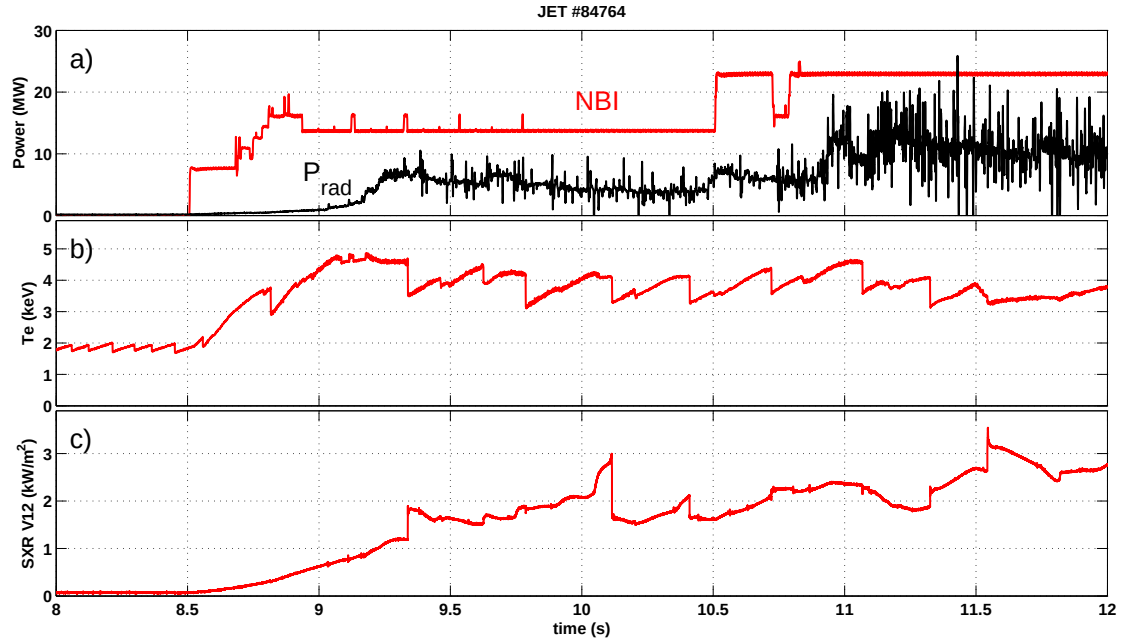


Figure 5.30: JET pulse #84764. NBI total power and radiated power (bolometry) (a) Core temperature (b) and vertical SXR camera, line V12 (c).

everywhere in the plasma, including close to the magnetic axis. Since in the meantime, the core temperature decreases, it is very likely that the core impurity content increases

on average[16]. The nature of the impurities is quite difficult to establish in this case but thorough analysis reveals that it is, again, mainly W (see Ref. [Pütterich 2012]).

Thus the two preceding examples indicate that uncontrolled impurity content in the plasma can be extremely deleterious and prevent adequate plasma operation. In the first case, W is suddenly generated in the plasma and the sawtooth crash leads to a fast penetration of the impurity until the very core of the tokamak, which causes the radiative collapse. In the second case, the impurity has an overall tolerable concentration but it is seen to accumulate in the core (probably because of a pinch velocity), which finally leads to the radiative collapse on longer time scales. Notice that in this case, the frequent sawtooth crashes are not sufficient to efficiently flush the core from the impurities. We will keep these two examples in mind when examining the impurity transport by the sawtooth crash in chapter 7.

We close this subsection with a last puzzling example, in JET pulse #84764, with NBI power up to 23 MW. The NBI power, central electron temperature and same SXR channel as above are plotted for this pulse on Fig. 5.30. A rather complex behavior can be observed on the SXR time trace, where the sawtooth crashes are seen to either increase or decrease the SXR emission. Namely, from NBI switch-on at $t = 8.5$ s until approximatively $t = 10$ s, each sawtooth crash leads to an increase of the emission. Then the crashes lead to a decrease of the emission until NBI power is increased up to 23 MW at $t = 10.5$ s, where the emission starts to increase again at each crash. Overall a very irregular behavior can be observed and the analysis is not straightforward. A tomography of the emissivity and decorrelation from the different contributions to $\varepsilon_{SXR}$ would be very instructive for this case.

### 5.2.9 Two specific structures observed on Tore Supra

We have already covered a quite broad range of experimental characteristics of the sawtooth phenomenon. We will now focus on the density structures which were first observed with the fast-sweeping reflectometer in 2010 [Sabot 2010]. The following physical and numerical analysis of chapter 6 will be concerned with providing a mechanism for the formation of the two structures described in this subsection.

Fig. 5.31 represents, for Tore Supra pulse #44634, the time trace of the core temperature obtained from ECE measurement (a), the time traces of the density profiles obtained with reflectometry (b), together with several tomography snapshots where the evolution of the density before and after a sawtooth crash is visible (c). In this ohmic pulse, the plasma parameters are as follows: magnetic field on axis $B_0 = 3.8$ T, minor radius $a = 0.72$ m, major radius $R_0 = 2.4$ m, core density $n_0 = 3.8 \times 10^{19}$ m$^{-3}$, core electron temperature $T_{e0} = 2.4$ keV, plasma current $I_P = 1.2$ MA. The sequence A – F can be described as follows:

[16] Actually, the core electron density also increases during the same time, while the edge density remains constant, so one should be careful. However the core density increase reveals the existence of a significant inward pinch, and the impurities may also have such an inward pinch. The average increase of the core SXR line of sight is hence probably due to the combined increase of the electron density and impurity density.

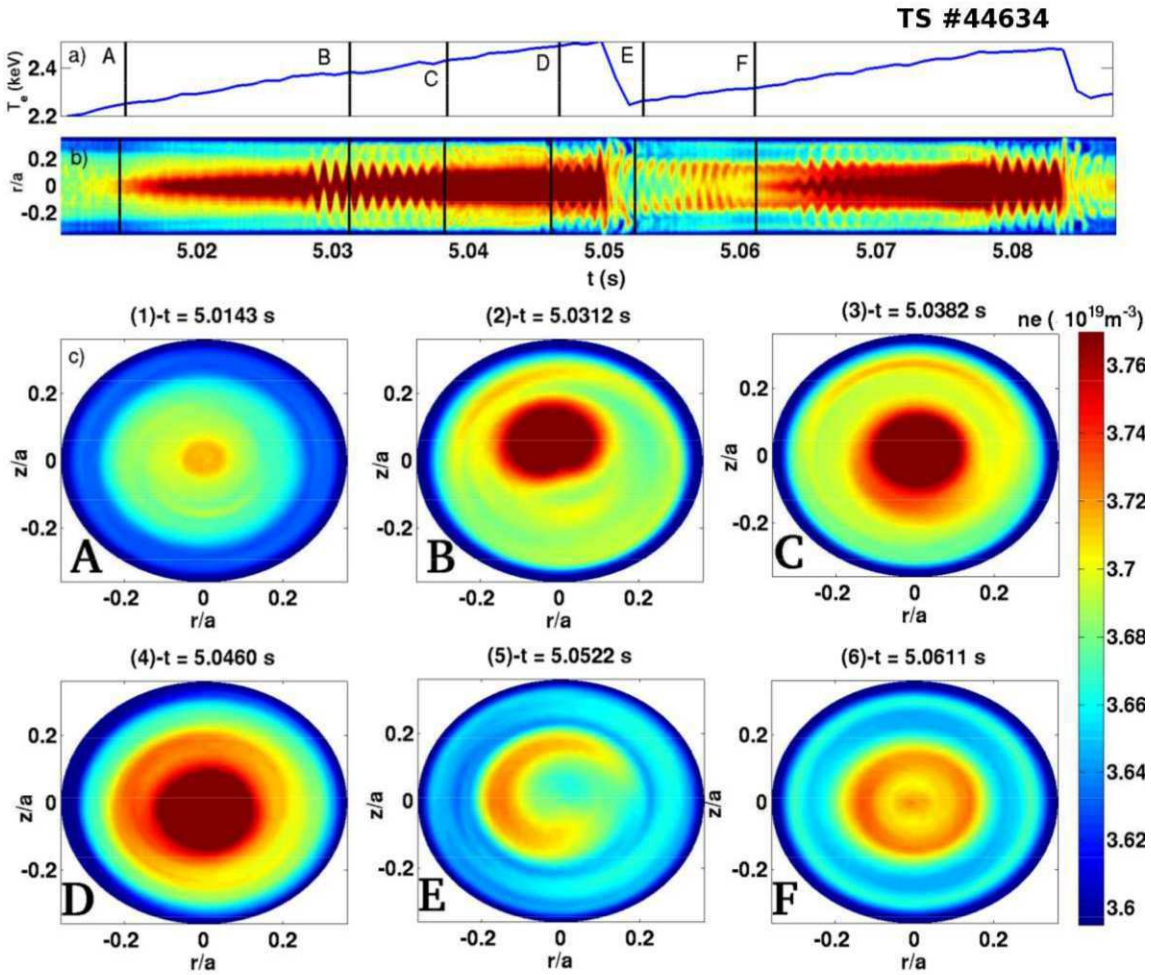


Figure 5.31: Time trace of core temperature (a), density profiles (b) and snapshots of the tomographically reconstructed density (c).

- A: After a crash, the density is almost flat inside the $q = 1$ surface and a peaking is seen to appear in the deepest core.
- B: A kink oscillation appears and the peaked core is displaced.
- C: The kink does not lead to a sawtooth crash but is later stabilized. The peak thus continues to grow.
- D: The peak is highest just before new kink oscillations appear in the core, this time leading to a sawtooth crash.
- E: After the sawtooth crash, a very distinct crescent-shaped density structure can be observed inside the $q = 1$ surface. It seems to have formed during the reconnection phase because it is present immediately after the crash.
- F: After a few milliseconds, the crescent-shaped structure is seen to homogenize

poloidally, while the peaking reappears in the center of the image. The main ring (orange) is encircled by a secondary ring (light blue).

The density structure in A – C is very striking because the peaking gives the profile a sombrero, or Mexican hat, shape. See Fig. 5.32 for a surface plot of the density at the time of image C, $t = 5.0382$ s, where the shape is clearly visible. Thus we will call this structure the Mexican hat.

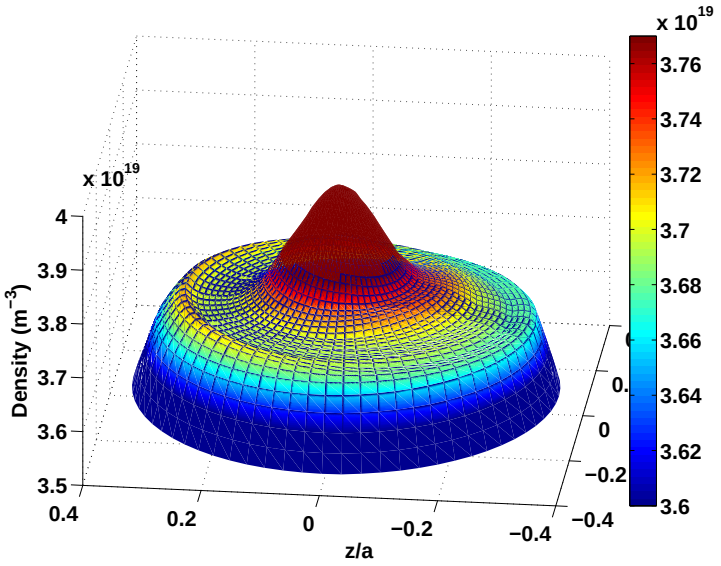


Figure 5.32: Surface plot of the Mexican Hat at $t = 5.0382$ s, Tore Supra #44634.

After the crash, the striking structure is the crescent inside the $q = 1$ surface (image E on Fig. 5.31). It is surprising because conventional wisdow, motivated in part by the Kadomtsev model, expects the density profile to be very flat following the crash. This significant deviation from flatness, and the difference in behaviour compared to the temperature, which is well flattened, requires more investigation.

These two structures have been observed first on Tore Supra in ohmic regime, but as we will see, they are recovered in JET ohmic regime as well. The physical and numerical analysis follows in chapter 6.

## 5.3 Summary

At the end of this chapter, we have acquired a much more detailed knowledge of the sawtooth instability, but also revealed in what extent it constitutes a rich, diverse and sometimes mysterious phenomenon with still a lot of unsolved issues.

- We have seen that precursor oscillations can be observed or not before the crash, which defines two main types of sawtooth crash. When the oscillations are observed, they come with a small particle and heat pulse crossing the $q = 1$ surface, followed by a larger pulse at the crash proper. Sometimes a back and forth transition between the two types of sawteeth is observed.

- The crash time measured with the fast ECE diagnostic reveals the strong discrepancy between Kadomtsev's resistive scaling and the experiments. In this regard, the acceleration of the crash by the electron parallel pressure gradient in Ohm's law studied in chapter 4 is particularly interesting. In the literature, other effects, like electron inertia, are considered good candidates for accelerated reconnection, but they cannot be studied with XTOR-2F for the moment.

- The observation of compound sawteeth seems to correspond to the destabilization of a small amplitude (1,1) island on the $q = 1$ surface. It can be quite fast or very slow, we have indeed reported on example on the JET tokamak where this takes 30 ms, even longer than Kadomtsev's time scale.

- The triggering of an NTM by long sawteeth has been observed.

- There seems to be an interaction between sawtooth crashes and rotation, as seen when a long-lived mode is present in the plasma. The influence of sawteeth on plasma rotation has been observed on a few other tokamaks, in particular TCV.

- The problem of incomplete magnetic reconnection has been documented. This is the most puzzling and counter-intuitive experimental result on sawteeth. In fact, without this, our understanding of the sawtooth instability would be quite good, and the only important discrepancy between models and experiments would be the prediction of the crash time. All nonlinear MHD simulations predict complete reconnection and in general the redistributed particle and density profile are in good agreement with the experiments. Only the safety factor seems to present a clear discrepancy. If measurement errors cannot be completely excluded, the observation of the snake instability still speaks in favour of incomplete reconnection, even though it does not really help to shed light on the problem given the wide range of different observations across machines and the possible multiple $q = 1$ surfaces in the plasma. To resolve the issue, the most attractive model in my opinion is Biskamp's model [Biskamp 1994], which states that due to the reconnection being dominated by electron inertia, there is enough kinetic energy after Kadomtsev reconnection to drive the reconnected field lines back well inside the core, restoring a $q = 1$ surface. In this model, reconnection would actually be more than complete, instead of incomplete, and possibly in agreement with safety factor measurements.

- The interesting interaction of the sawtooth crash with impurity transport, and in particular W penetration at the crash has been observed on the JET tokamak. This will be the subject of chapter 7.

- Finally the structures observed on Tore Supra using fast-sweeping reflectometry tomography have been presented. The study of these structures and their importance is the subject of the next chapter.

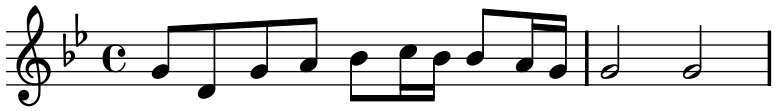

*Dixit Dominus (HWV 232)*
**George Frideric Handel**

Chapter 6

# Numerical and physical analysis of Tore Supra and JET density measurements

## Contents



We now use our numerical tools to give a physical analysis of the two structures observed experimentally and described in section 5.2.9. This chapter is mainly a compilation of the papers [Nicolas 2012] and [Nicolas 2013].

## 6.1 The Mexican hat

### 6.1.1 Detail of experimental observations

Fig. 6.1 displays the core density profiles together with the electron temperature measured using electron cyclotron emission, in pulse #44634, for $t = 5.15 - 5.17$ ms.

These measurements deserve several comments. The density behaviour may seem unusual, compared to typical density profiles, as seen for instance with interferometry. Recall, however, that the discharge is ohmic, with no additional heating or non-inductive current drive, hence there is a significant Ware pinch effect [Ware 1970] due to the significant inductive toroidal electric field, responsible for density peaking inside the $q = 1$ surface. The Ware pinch is an inward radial velocity linked with the conservation of the canonical toroidal momentum and the under the hypothesis of axisymmetry (see appendix E). After the sawtooth crash, the density profile is flat, up to a few percents (*cf.* Fig. 6.1 c), blue profile). The growth of the peaking can be observed while the density rebuilds on Fig. 6.1 c). It was shown in ref. [Guirlet 2010] that indeed the measured pinch velocity essentially agrees with the neoclassical calculation, obtained with the NCLASS

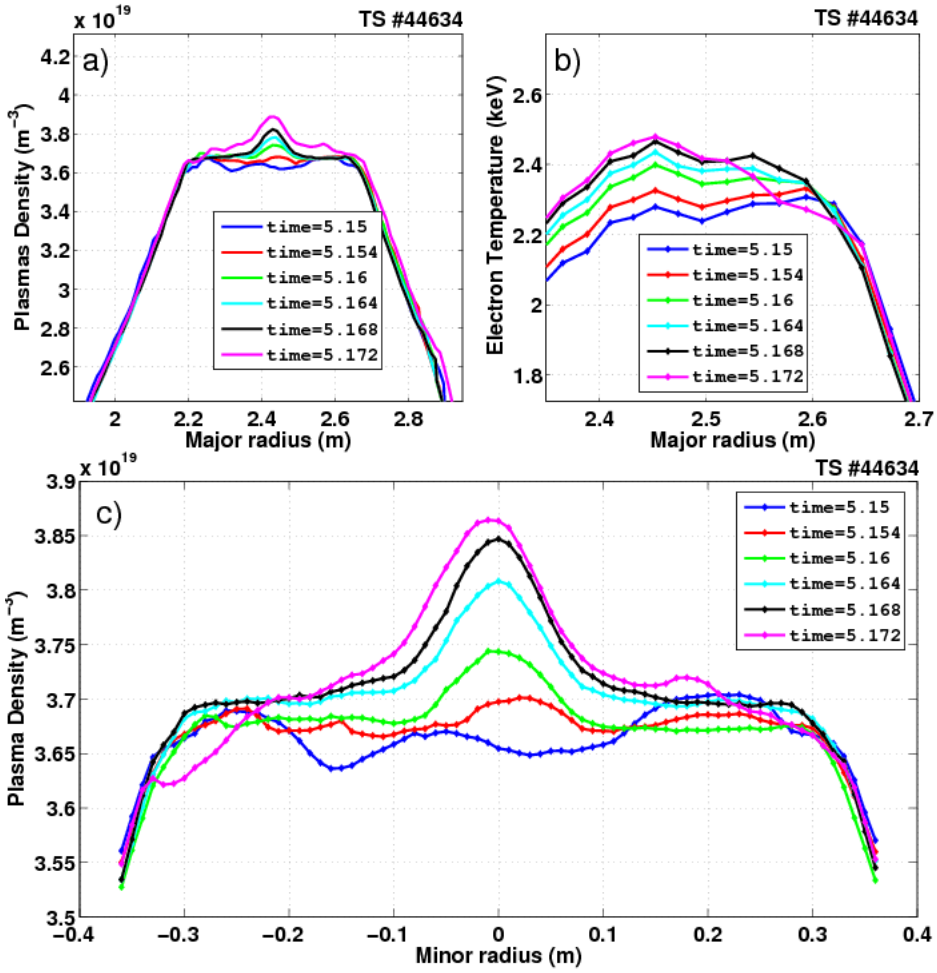


Figure 6.1: Density profiles Temperature profiles versus major radius in TS # 44634, for $t = 5.15 - 5.17$ ms, during the ramp phase of the sawtooth (a), corresponding electron temperature profiles obtained by ECE measurements (b). Zoom on the core density inside the $q = 1$ surface (c).

code [Houlberg 1997]. Ref. [Guirlet 2010] simultaneously measures the pinch velocity and diffusion coefficient inside the $q = 1$ surface by locally measuring the radial electron flux $\Gamma_e(r) \equiv -1/r \int_0^r r' \partial_t n_e(r') \mathrm{d}r'$ and plotting $\Gamma_e/n_e$ versus $-\partial_r n_e/n_e$. When the particle source is negligible, this yields a straight line with slope $D_\perp$, the particle diffusion coefficient, and intersect $V_{\mathrm{pinch}}$, the radial velocity pinch. The coefficients can be seen on Fig. 6.2. The radial velocity is measured to be of the order of 0.1 m.s$^{-1}$, and can be considered as a constant except in the center where it drops to zero, thus avoiding a singularity on the magnetic axis. The diffusion coefficient is of the order of 0.05m$^2$.s$^{-1}$.

As said in section 5.2.9, the shape of the building profile is remarkable: the profile is significantly more peaked deep inside than close to the $q = 1$ surface. Together with the steep gradients outside $r_s = r(q = 1)$, it yields the shape of a mexican hat. This general shape can readily be explained. To simplify the discussion, we take a constant radial pinch velocity profile, which is realistic for $r > 0.05$ m. The evolution of the electron

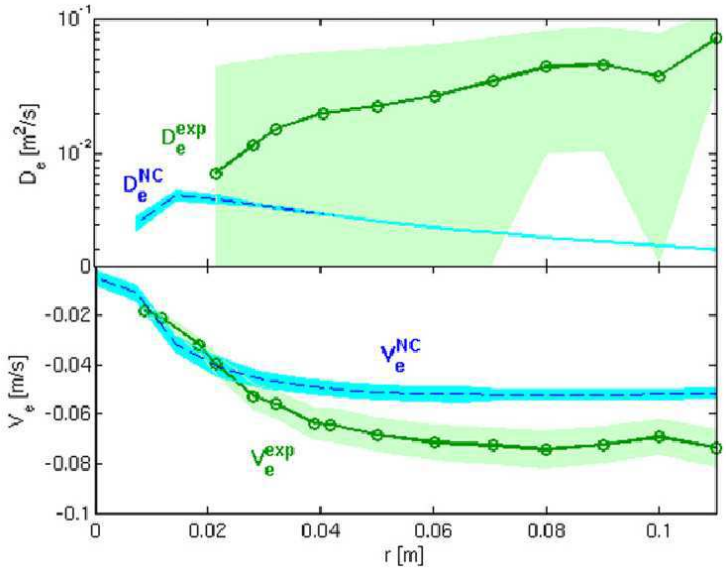


Figure 6.2: Pinch velocity and $D_\perp$ in the core for Tore Supra pulse #35035. Figure taken from [Guirlet 2010]. The blue curve represents a neoclassical calculation with the NCLASS code [Houlberg 1997].

density $n_e$ is modeled with a convection diffusion equation:

$$\partial_t n_e = -\nabla \cdot (n_e V_{\text{pinch}} \hat{\boldsymbol{r}} - D \nabla n_e) \,, \tag{6.1}$$

where $V_{\text{pinch}}$ is the constant pinch velocity and $D$ the constant diffusion coefficient. Equilibrium yields the slope $|\nabla n_e / n_e| = |V_{\text{pinch}}/D|$, which is constant. However in cylindrical geometry, the evolution towards this equilibrium is not uniform. Indeed volume effects yield an additional term $-n_e V_{\text{pinch}}/r$, in addition to advection $-(V_{\text{pinch}}\hat{\boldsymbol{r}}) \cdot \nabla n_e$, which enhances the effect of the pinch close to the magnetic axis. As a result, the profile is more peaked in the center. This can be verified numerically: feeding the experimental parameters of Fig. 6.2 to the 1D advection diffusion code, with fixed (Dirichlet) boundary conditions, yield the result displayed on Fig. 6.3. The normalized experimental profiles of Fig. 6.1 and the simulated profiles are juxtaposed, and we see a quite good agreement in the general shape of the profiles.

However there is more to this than radial convection only. The previous simple model would be sufficient to describe the evolution of the profile if the latter was already flat immediately after the crash. However the crash does not flatten the density profile completely. Structures of amplitude in the range 1-2% and of typical radial size equal to 0.2 m are obtained at the end of the reconnection phase, as seen on the blue profile, Fig. 6.1 c). The first steps of the profile evolution are dominated by the disappearance of these structures, leading to the green profile. Fig. 6.4 shows a surface plot of the density at the time where the green profile is taken. This flattening process lasts 10 ms, so that a high diffusion of 4 m.s$^{-2}$ is required for a diffusive process to explain this flattening. Furthermore, if some turbulent process were responsible for such a rise in the perpendicular particle diffusion coefficient (compared to the aforementioned value of 0.05 m.s$^{-2}$), the temperature

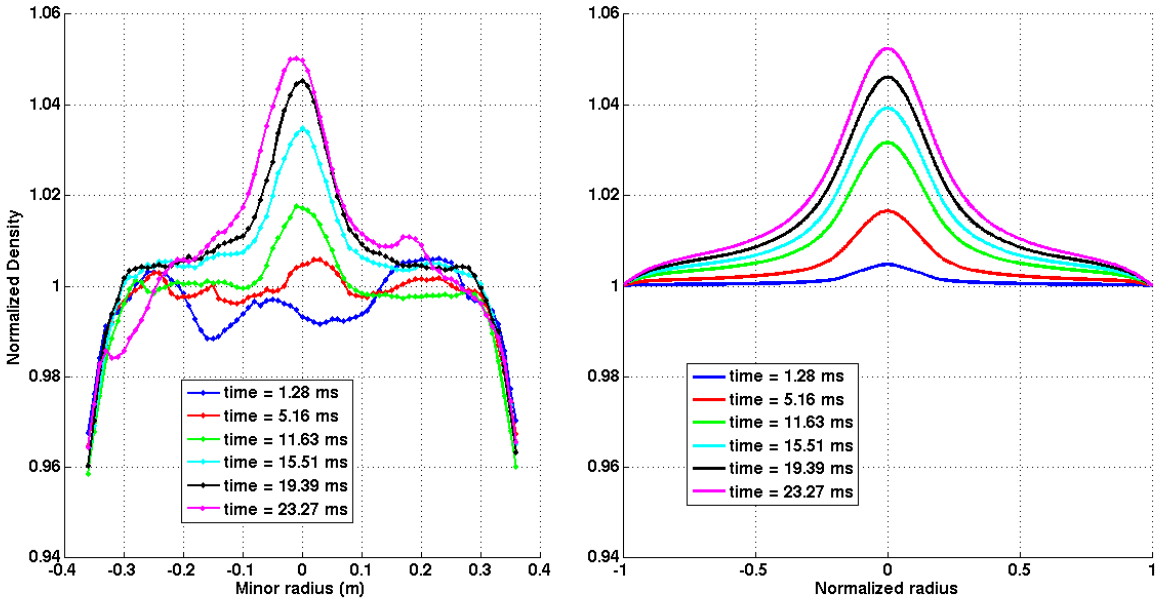


Figure 6.3: Normalized experimental density (left panel) and profile evolution simulated using transport coefficients inferred from Ref. [Guirlet 2010]. (right panel)

diffusivity $\chi_\perp$ would also undergo a dramatic rise. As a result, the temperature profile would flatten significantly. Fig. 6.1 b) shows however that the smooth reconstruction of the temperature profile is not affected during this density event. Finally, it is important to note that a magneto-hydrodynamic mode with mode numbers $m = n = 1$ is observed during the flattening. Fig. 6.5 a) displays the time trace of the density, and Fig. 6.5 b) the corresponding average power spectra, exhibiting the frequency of the mode preceding and following the crash. It is observed that the postcursor frequency ($t = 5.146 - 5.150$ s) is very close to the precursor frequency ($t = 5.140 - 5.146$ s). The precursor is a kink mode with frequency of the order of half the ion diamagnetic frequency $\omega_i^\star$, according to Ref. [Ara 1978], and as we have seen in section 2.2.4. The frequency of the plasma flows are also of the order of the diamagnetic frequency, so we can conjecture that both mode frequency and Doppler shift play significant roles in the total frequency in the laboratory frame. This conjecture will be checked later on. Since the frequency of the postcursor is not different from that of the precursor, we can conclude that it is not the result of the mere convection of a residual density perturbation by the plasma rotation, but really the signature of kink type MHD activity following the crash. Such MHD activity can be due to incomplete reconnection. It is important to note this fact because the flows affecting the density are very different in presence or in absence of MHD activity, as we will readily see.

The experimental results of Fig. 6.1 suggest that density and temperature behave differently. Namely, the temperature evolves smoothly after the crash while the den-

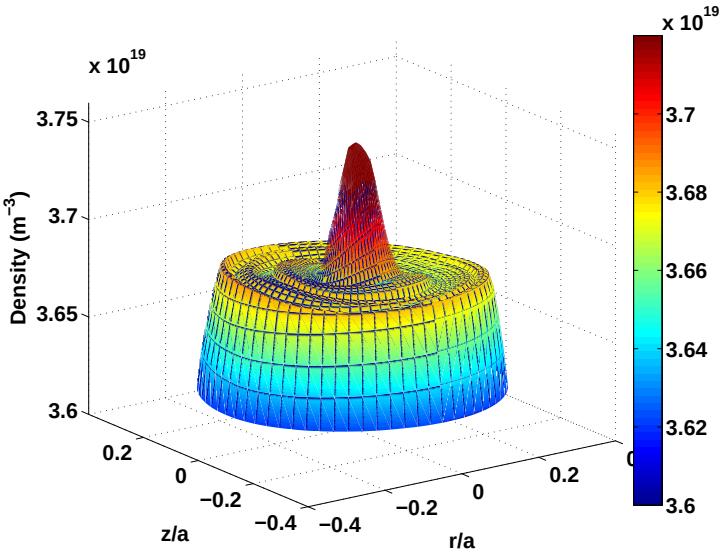


Figure 6.4: Surface plot of the density with a very strong flattening

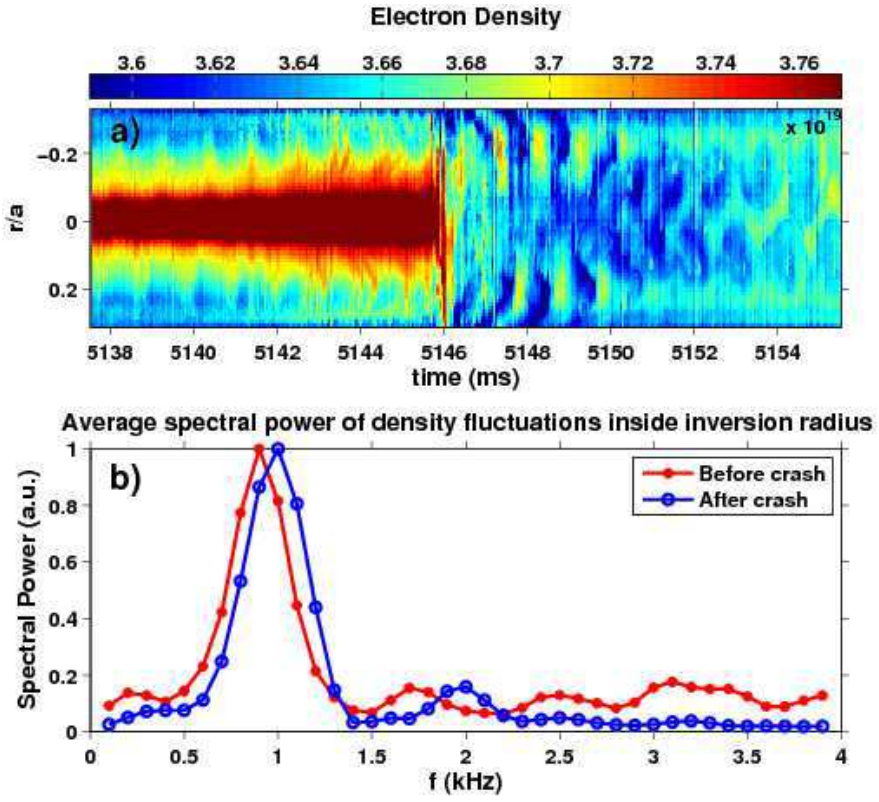


Figure 6.5: Time trace of the equatorial density in Tore Supra ohmic shot #44634, obtained with fast-sweeping reflectometry (a), Average spectral power of density fluctuations inside inversion radius (b).

sity is found to exhibit very specific structures[1], and a more complex behaviour, with a

[1]It must be noted, however, that the density diagnostic is more precise than the temperature diag-

strong sudden flattening is observed. This fact can be surprising considering the typical assumption that the temperature and the density are both flux functions in ohmic plasmas: $T_e = T_e(\Psi^\star)$, $n = n(\Psi^\star)$, where $\Psi^\star$ is the helical flux we are now familiar with, *Eq.* (2.141). This assumption generally holds in a steady-state fusion plasma. However it does not hold in the regions subject to important MHD activity, for instance close to the $q = 1$ surface during a sawtooth precursor or postcursor kink, not to mention during the crash itself.

### 6.1.2 Conditions for $T_e$ and $n_e$ to be flux functions

Let us briefly review the arguments leading to the conclusion that $n$ and $T_e$ are flux functions. Working again with the high aspect ratio approximation, we use the results obtained in section 2.2.3, writing ideal Ohm's law:

$$\partial_t \psi = \frac{\hat{\mathbf{z}}}{B_0} \cdot (\nabla \Psi^\star \times \nabla \phi)\,, \tag{6.2}$$

still in a high aspect ratio framework, and with $z = R_0\varphi$.

The equilibrium flux is denoted by $\psi_0$, and perturbed quantities are denoted by a tilde, and depend on $\psi_0$ (or $r$) and the variable $\zeta = \theta - \varphi + \omega t$. When the equilibrium is perturbed, $\psi = \psi_0 + \tilde{\psi}$, the flux surface label is the helical flux

$$\Psi^\star = \int^{\psi_0} (1 - q(\psi))\mathrm{d}\psi + \tilde{\psi}. \tag{6.3}$$

Indeed, it can be checked that $\mathbf{B} \cdot \nabla \Psi^\star = 0$. Equation (6.2) implies that the potential $\phi$ is such that

$$\phi = \phi_0 + F(\Psi^\star), \tag{6.4}$$

where $F$ is an arbitrary function and $\phi_0(r)$ is solution to

$$\partial_t \psi = \frac{\hat{\mathbf{z}}}{B_0} \cdot (\nabla \Psi^\star \times \nabla \phi_0) \tag{6.5}$$

Using $\partial_t \psi = \partial_t \tilde{\psi}$, we find

$$\phi_0 = -\frac{1}{2}\omega B_0 r^2. \tag{6.6}$$

We will see that this offset electric potential corresponds to the Doppler shift induced by a change of rotating frame at the pulsation $\omega$.

Now let us apply this formalism to the temperature and density evolution in the plasma. The argument for the temperature is straightforward. The parallel diffusion coefficient is large, so that the fluid pressure equation, *Eq.* (2.87), after expanding in terms of density and temperature, and using the continuity equation, the equation of evolution of the temperature at lowest order reduces to

$$\partial_t T_e = \chi_\parallel \nabla_\parallel^2 T_e \tag{6.7}$$

nostic.

yielding $T_e = T_e(\Psi^\star)$. The other terms in the evolution of the temperature are perpendicular transport terms that control the details of the temperature profile across flux surfaces. To be more precise, *Eq.* (6.7) holds because the parallel diffusion time, $\tau_\parallel \sim 4\pi^2 R_0^2/\chi_\parallel$, is very short compared with the other time scales. Specifically, $\tau_\parallel$ must be small compared with the period of the mode, to guarantee the adiabatic alignment of $T_e$ on $\Psi^\star$. Typically, the ordering $\tau_\parallel^{-1} \gg \omega/2\pi$ holds, with $\omega$ the typical frequency of the mode. The other terms are either small curvature terms, either perpendicular diffusion terms, with characteristic time $\tau_\perp \sim a^2/\chi_\perp$, either terms related to drift advection with time $\tau_{ad} \sim a/V_E$. Since $V_E \sim 1$ km.s$^{-1}$, $\chi_\parallel \sim 10^8$ m$^2$.s$^{-1}$, $\chi_\perp \sim 1$ m$^2$.s$^{-1}$, we have $\tau_\perp/\tau_\parallel \sim 10^5$ and $\tau_{ad}/\tau_\parallel \sim 10^2$.

The argument for the density is slightly more subtle, because homogenization on flux surfaces can arise from two processes: parallel homogenization by sound-waves or by $\mathbf{E}\times\mathbf{B}$ drift convection. To simplify the discussion, we neglect curvature terms in a low inverse aspect ratio limit. The source vanishes in the center. Then *Eq.* (2.85) can be recast at lowest order in $\varepsilon$ into:

$$\partial_t n + \frac{\hat{\mathbf{z}}}{B_0}\cdot(\nabla\phi\times\nabla n) + v_\parallel\nabla_\parallel n + n\nabla_\parallel v_\parallel = \nabla\cdot D_\perp\nabla n. \tag{6.8}$$

The advection by $v_\parallel$ is usually negligible, the right hand side corresponds to slow dynamics, so we are left with two terms, the advection by the electric drift velocity and the parallel compressibility.

If the latter is dominant, then coupling with the momentum equation yields the physics of sound waves with dispersion relation $\partial_t^2 n = c_s^2\nabla_\parallel^2 n$, with $c_s = \sqrt{T_e/m_i}$ the ion sound velocity. In the case of non perturbed flux surfaces, the latter equation yields the dispersion relation $\omega^2 = k_\parallel^2 c_s^2$, where $k_\parallel = 1/R(1/q-1)$. Thus the density tends to become a flux function, if the wave is sufficiently fast compared to the frequency of the mode. Any perturbation with non-vanishing parallel wave-number is propagated along the field line and homogenization on the flux surface occurs.

If, however, the advection by the electric drift velocity dominates, then $n$ will be constant on the streamlines of the flow. Here it is important to note that the stream function is not $\phi$. Indeed, to be an acceptable stream function, the potential $\phi'$ involved in the electric drift needs to be time independent. Thus the stream function is obtained in the frame moving with the perturbation at the pulsation $\omega$. This change of frame introduces a Doppler shift in the potential: $\phi' = \phi + r^2\omega B_0/2$. We have indeed with this definition, up to $\mathcal{O}(\varepsilon)$ term:

$$(\mathbf{B}\times\nabla\phi')/B_0^2 = (\mathbf{B}\times\nabla\phi)/B_0^2 - r\omega\hat{\boldsymbol{\theta}}, \tag{6.9}$$

and $\phi'$ is independent of time because the new poloidal variable is $\theta' = \theta - \omega t$. If ideal MHD is valid, *Eqs.* (6.4) and (6.6) imply that

$$\phi' = \phi + r^2\omega B_0/2 = \phi - \phi_0 = F(\Psi^\star). \tag{6.10}$$

This means that when advection dominates, the density tends to being a function of $\phi'$, which is a flux function, and the density ends up being a flux function. This can be seen

as an expression of the frozen-in-law. The time it takes to homogenize is at maximum the particle diffusive time $a^2/D$, and at minimum the characteristic time of the motion on the vortex, $L/v_E$, where $L$ is the size of the vortex and $v_E$ denotes here the typical velocity of the flow. We will see that the latter, usually much faster time, is indeed relevant.

When there is significant MHD activity in the plasma, the previous arguments for the density break down for different reasons. First, non-ideal MHD effects become important in a narrow layer around the radius of the $q = 1$ surface, where the assumption $\phi = F(\Psi^\star)$ breaks down. More importantly, it takes some time for a scalar to homogenize on flux surfaces. If the time scales of evolution of the MHD instability (which can be very short in the non-linear phase of the sawtooth for example) are faster than typical homogenization time, then the final state of the scalar can be significantly different from a flux function. In particular, the parallel diffusivity is in general fast enough so that the temperature remains a flux function even during the reconnection phase, to a good approximation. However it is not true at all for the density, since sound-waves are not fast enough, and the non-linear evolution of the flow pattern is too fast for the density to follow during the crash phase. Hence the density following the crash is usually not a flux function. Nonetheless, in the presence of a saturated postcursor mode, as is the case during the flattening phase, *cf.* Fig. 6.5, the preceding analysis makes sense, and we will exhibit the flattening mechanism, showing that the flattening time can indeed be much shorter than the particle diffusion time on the vortex.

### 6.1.3 Flattening by the postcursor mode

In this subsection, a standard non-ideal single fluid MHD model is assumed, even if the mode is supposed to have a frequency of the order of the diamagnetic frequency. The nature and structure of the flow associated with a saturated kink mode is described. The bifluid effects are important only in the next subsection where the crescent-shaped structure is studied with the XTOR-2F code.

As noted above, the strong flattening observed on the density profile occurs simultaneously with a saturated kink type $m/n = 1/1$ MHD mode. We do not discuss the reasons that may lead the kink mode to saturation rather than crash. We have seen in chapter 3 that the kink mode can evolve to a saturated 3D helical state, however this is obtained with unrealistic parameters. It could also be that the non-linear stabilization by the diamagnetic effects occurring at the beginning of the nonlinear phase is sufficiently strong in some instances to lead to saturation rather than to a crash[2]. This will be further developed in chapter 4.

Here we use the MHD displacement $\boldsymbol{\xi}$ which characterizes the mode. It is of the form $\boldsymbol{\xi}(\boldsymbol{x}) = \boldsymbol{\xi}_{1,1}(r)e^{-i(\omega t-\theta+\varphi)}$, together with the condition $\nabla\cdot\boldsymbol{\xi} = 0$. In the frame where $\boldsymbol{\xi}$ is defined, the equilibrium radial electric field vanishes, at least locally, and the flow associated with the mode has a velocity $\boldsymbol{v} = \mathrm{d}\boldsymbol{\xi}/\mathrm{d}t = \partial_t\boldsymbol{\xi} = -i\omega\boldsymbol{\xi}_{1,1}e^{-i(\omega t-\theta+\varphi)}$, where $\omega$ is

[2]Notice that in section 3.2.3, we have mentioned only the acceleration of the crash by the diamagnetic effects. It happens actually that the acceleration phase is preceded by a nonlienar phase where the growth rate is smaller than in the pure resistive case due to the diamagnetic effects.

the frequency of the mode. Let us note that the toroidal component of the displacement is $\mathcal{O}(\varepsilon)$ and contributes in $\nabla\cdot\boldsymbol{\xi}$ only at order $\mathcal{O}(\varepsilon^2)$. Thus it is neglected. Again, we use the electric potential $\phi = \phi_{1,1}(r)e^{-i(\omega t-\theta+\varphi)}$ associated with this flow, in a low inverse aspect ratio limit. Up to $\mathcal{O}(\varepsilon)$ curvature terms, $\boldsymbol{v} = 1/B_0^2\mathbf{B}\times\nabla\phi = i/(rB_0)\phi\hat{\boldsymbol{r}} + 1/B_0\partial_r\phi\hat{\boldsymbol{\theta}}$, so that $\phi_{1,1}(r) = r\omega B_0\xi_r(r)$. Consistency is ensured by the vanishing divergence conditions for both $\boldsymbol{v}$ and $\boldsymbol{\xi}$. Thus the flow is entirely determined by the shape of the MHD radial displacement. Recall from chapter 2 the typical form for $\xi_r$: at lowest order it is a step function, constant for $r < r_s$ and vanishing for $r > r_s$, with a smooth transition in the nonideal region, which depends on the physics taken into account.

With the previously described shapes for $\xi$, $\phi$ has the structure of two vortices in the poloidal plane, as seen on Fig. 6.6 a), which represents the $m/n = 1/1$ electric potential structure obtained with XTOR-2F in linear single fluid regime. In this case, the smoothing in the inertial region is due to the resistivity. Fig. 6.6 a) is misleading because $\partial_t\phi = -i\omega\phi \neq 0$. By this we mean that since the vortices are rotating in the poloidal plane, they cannot represent the streamlines, that is, the trajectories of the particles. As explained in the preceding subsection, the relevant stream function is obtained by moving to the frame where the perturbation is stationary, and adding the corresponding Doppler shift $r^2\omega B_0/2$. The streamlines are represented on Fig. 6.6 b). They have indeed the same structure as the perturbed magnetic surfaces, confirming the results of section 6.1.2.

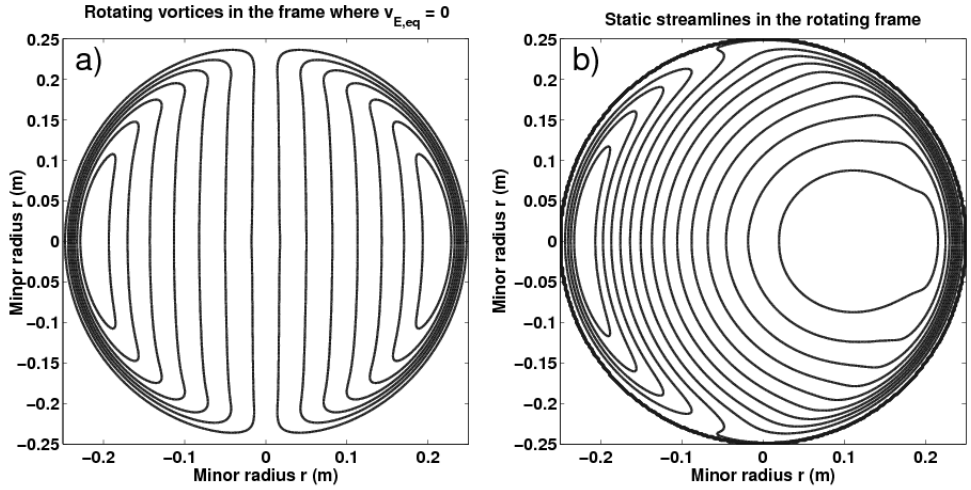


Figure 6.6: Potential structure in the frame where $\boldsymbol{v}_{E,eq} = 0$ (a) and corresponding static streamlines of the flow in the rotating frame (b). The streamlines describe rotation around the displaced core, accelerated in the region of the $q = 1$ surface.

The amplitude of the flow is of the order of $\omega\xi_r$. Recall that here $\omega$ is the frequency of the mode and not its measured frequency $\Omega$ which is the sum of $\omega$ and of the Doppler shift due to the equilibrium $\mathbf{E}\times\mathbf{B}$ drift velocity. However only the frequency in the laboratory frame $\Omega$ is measured. There are some measurements of the equilibrium radial electric field in Tore Supra using Doppler-shift measurements but they do not provide information below $r < 0.6$ m. Since we are interested in the electric field at the $q = 1$

surface, here $r \sim 0.3$ m, this is of no practical use. We could also estimate $\omega$ using *Eq.* (2.160), giving a numerical resolution for $\omega$ as a function of $\omega_i^\star$ and $\omega_e^\star$. However, these quantities are also difficult to evaluate on the $q = 1$ surface because this corresponds to the radius where the profile turns flat, coming from the outside of the resonant surface. Thus the computation of the gradient of the pressure profile involved in the evaluation of the diamagnetic frequencies is very inaccurate.

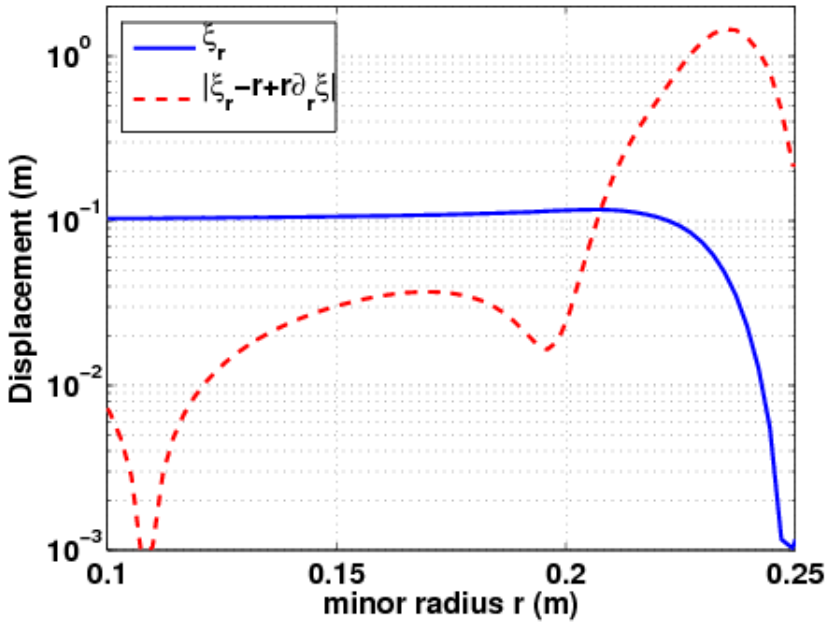


Figure 6.7: Comparison between the radial displacement $\xi_r$ and $|\boldsymbol{v}/\omega| = |\xi_r - r + r\partial_r\xi|$ on the line $\theta' = 0$.

Nonetheless there is a way to get round this difficulty. First note that in the shot we are interested in, the density at the $q = 1$ surface is much flatter than the temperature, thus $\omega^\star_{(i,e)} \simeq \omega^\star_{T,(i,e)} = \left(\mathbf{B} \times \nabla T_{(i,e)}\right)/(eB_0^2)$. Theoretical neoclassical results can be used to predict the value of the electric field as a function of the temperature gradient. Neoclassical theory in axisymmetric configurations does not allow to dissociate the electric field from the toroidal velocity in the force balance equation. In other words, only the quantity $E_r - v_\varphi B_\theta$ can be computed, because the ambipolarity of the radial particle fluxes is automatically verified in this formalism. Neoclassical theory with magnetic ripple effects (the ripple is high in Tore Supra) removes this degeneracy and leads to the computation of the factor $k_E$ of proportionality between the radial electric field and the ion temperature gradient: $E_r = k_E \partial_r T_i$. In other words, the Doppler shift $\boldsymbol{k}\cdot\boldsymbol{v}_E = -k_E\omega_i^\star$. This factor of proportionality is determined by the competition between turbulence effects and ripple effects. The ripple plays an important role because it breaks axisymmetry and because it is responsible for local particle trapping leading to radial non-ambipolar particle fluxes. The electric field adjusts to compensate for this non-ambipolarity. In Tore Supra, it was found that ripple dominates, so that $k_E = 1.5$ (ripple plateau regime) [Garbet 2010, Garbet 2009]. This result was checked experimentally in

Ref. [Fenzi 2011]. Secondly, we have seen that *Eq.* (2.160) allows straightforward evaluation of the kink pulsation in the limiting case where $\gamma\tau_I(\tau_R/\tau_I)^{1/3} \gg 1$, with $\tau_I = \tau_A/\hat{s}$. In this case $\omega = \omega_i^\star/2$. In section 2.2.4 (*Eq.* (2.167)), we have seen that this condition is not really satisfied. The ideal drive of the mode must be strong as well for this result to be valid, and this parameter is not easily known from the experiment. Thus we make the strong assumption that $\omega_i^\star/2$ is indeed a good estimate for the mode's frequency, and we cannot easily check this assumption. Finally we can write $|\Omega| = |\omega_i^\star/2 - k_E\omega_i^\star|$, so $k_E = 1.5$ yields $\Omega = -\omega_i^\star$ and $\omega = -\Omega/2$. Thus the kink pulsation is expressed without explicitly referring to the diamagnetic pulsation. This shows that the Doppler shift and the frequency of the mode play comparable roles in the measured pulsation $\Omega$ of the mode. The Doppler shift and the mode frequency have opposite signs, and the existence of the mode reduces the pulsation to 2/3 of its value without kink activity. This shows that the 1 kHz frequency of the postcursor cannot be attributed to plasma rotation only, but that the mode's own frequency is of the order of 0.5 kHz, while the plasma rotates in the opposite (electron diamagnetic) direction at a frequency of the order of 1.5 kHz.

The preceding argumentation should not be seen as a demonstration, because of the many unknowns and assumptions which are not properly checked, namely the $\omega_i^\star$ dependence of the mode pulsation, and the result that $k_E = 1.5$, which has indeed been checked, but not with sufficient precision and not for this particular plasma. It shows how difficult it is actually to disentangle the plasma rotation from the mode pulsation. At the very least, it is reasonable to assume that plasma and mode rotation are both proportional to the diamagnetic frequency, and thus are of the same order of magnitude. This means that the mode frequency of 1 kHz should at least give the good order of magnitude for the mode frequency.

There is also some difficulty in estimating experimentally the amplitude of the radial displacement. It is straightforward only when the profiles are peaked since $\xi_r$ is directly measurable as the displacement of the core. A typical core displacement for the saturated kink oscillation in Tore Supra ohmic shots is 0.1 m. At the onset of the crash, the core is displaced up to the $q = 1$ surface. The position of this surface $r_s$ depends mainly on $I_P$. In the Tore Supra shot #44634, which characteristics are studied here, $I_P = 1.2$ MA, resulting in the $q = 1$ surface located at $r_s \simeq 0.3$ m. For the postcursor mode, there is usually no peaking in the core allowing to trace back the amplitude of the displacement. However in our case, the peaking is seen to reappear while the kink oscillations are still present, so that its amplitude can be evaluated. It is of the order of 0.1 m, making the typical velocity of the order of 300 m.s$^{-1}$.

However, the effective convection velocity can be much larger. The velocity along the line $\theta' = 0$ is given by the expression:

$$|\boldsymbol{v}| = |\boldsymbol{v}_\theta| = \omega|\xi_r - r + r\partial_r\xi_r|, \tag{6.11}$$

as can be seen from *Eq.* (6.9). Thus the velocity is dominated by the term $\partial_r\xi$ near the $q = 1$ surface where the radial variations of $\xi_r$ (and $\phi$) are fast. This originates from the condition $\nabla \cdot \boldsymbol{\xi} = 0$. This can be seen on Fig. 6.6 a) and b) where on the edges the streamlines are very close to each other, meaning significant acceleration of the flow.

Fig. 6.7 represents the functions $\xi_r$ versus $|\xi_r - r + r\partial_r \xi_r|$. It appears that the velocity is enhanced by a factor of 10 next to the $q = 1$ surface, compared with the rough estimate $v \sim \omega \xi_r$.

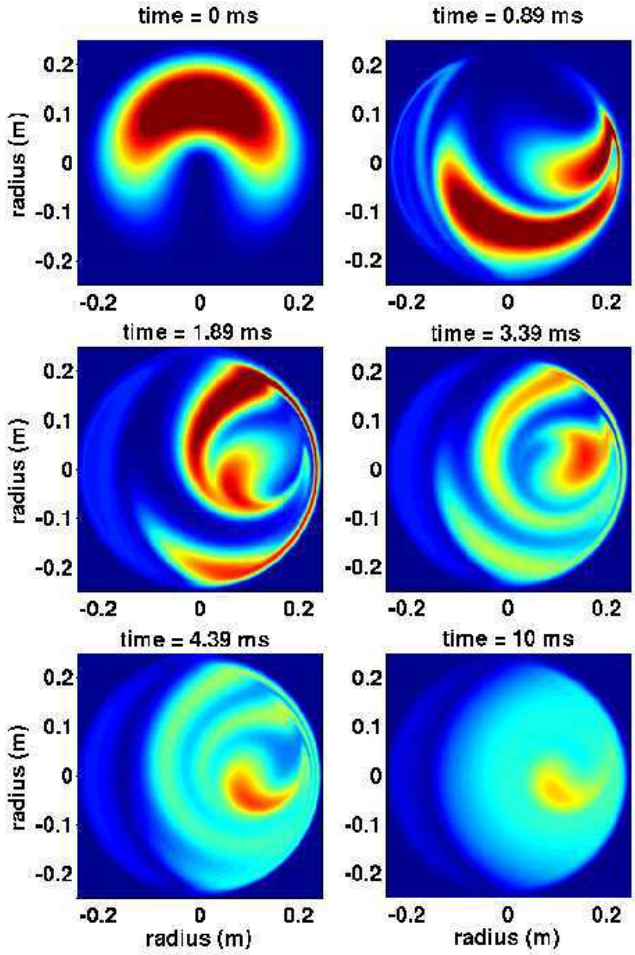


Figure 6.8: Advection diffusion simulation with $r_s = 0.25$ m, $D = 0.05$ m$^2$.s$^{-1}$, $f = 400$ Hz, $\xi_r(r = 0) = 0.1$ m. Homogenization occurs in less than 10 ms.

Now let us use the advection-diffusion code described in section section 3.3 to study the effects of this flow during 10 ms on the poloidal density profile. The stream function $\phi$ is obtained from XTOR-2F as the dominant $m/n = 1/1$ component of the potential in linear regime and without bifluid effects. The pinch velocity is set to zero in the 2D code because it does not play a role in the process, and $\phi$ is rescaled to be consistent with the measured MHD displacement. We take $r_s = 0.25$ m, $D = 0.05$ m$^2$.s$^{-1}$, $f = 400$ Hz, $\xi_r(r = 0) = 0.1$ m, the time step is 1 $\mu$s and the computation is done on a 256×256 cartesian grid. In order to reproduce the experimental results, we simply take an initial perturbation defined analytically by a smooth function of the form

$$n(r, \theta) = 1 + P(r)\frac{1 + \cos(\theta - \theta_0)}{2},$$

with $P(r) = 16(r^4 - 2r^3 + r^2)$. The precise expression of the initial perturbation is unimportant. The experimental perturbation could have been interpolated on the numerical mesh, but it would not have changed the discussion. Only a perturbation which is not a function of the potential is needed. The same simulation was done with other profiles and the results were similar.

The results of the advection simulation is presented on Fig. 6.8. It is seen that a frequency of 400 Hz and an MHD displacement of 0.1 m is sufficient to homogenize the density in the poloidal plane in 10 ms. The reason is that the velocity pattern enforces the density to enter the very thin zone where $\partial_r \phi$ is large, stretching the density profile. The characteristic width of the density filaments generated by this process is small enough to be erased even by a small diffusion coefficient. By comparison, the purely diffusive evolution would have required a time of the order of 1 s to reach the same level of flatness.

## 6.2 The crescent-shaped structure

Here the nature and the origin of the crescent-shaped structure observed after a sawtooth crash and described in section section 5.2.9 are investigated, using XTOR-2F sawtooth crash simulations. To model the effect of the sawtooth crash on the density observed on the experiment, a pinch velocity is added in the continuity equation, which thus reads

$$\frac{\partial \rho}{\partial t} + \nabla \cdot (\rho \boldsymbol{v}) + \alpha \nabla p_i \cdot \nabla \times \frac{\mathbf{B}}{B^2} = \nabla \cdot (D_\perp \nabla \rho - \rho V_{\text{pinch}} \hat{\boldsymbol{r}}) + S, \tag{6.12}$$

This simulates the buildup of the peaked core density profile in the quiescent ramp of the sawtooth. The aim of the simulation is to provide a comparison with the experiment. This comparison will be only qualitative, because as we will see, many features of the simulation are in discrepancy with the experiment. First of all, the resistivity is much larger. In Tore Supra #44634, the Lundquist number as defined in XTOR-2F is $S_{TS} = 2 \times 10^8$, while we have used $S = 10^7$ in the simulation. This has two effects: firstly it reduces the time between two consecutive sawteeth. Indeed the sawtooth period is closely related to the resistive time, which determines the rate at which the safety factor relaxes to its equilibrium value. In our simulations, the sawtooth period indeed seems to be roughly proportional to the Lundquist number. Secondly it changes the size and features of the reconnection layer, in the limit where resistive effects are dominating the physics of reconnection. Regarding this last point, the diamagnetic effects do play a very important role and may be dominating resistive effects in the reconnection, as we will see in chapter 4. So this discrepancy with the experiment may not be a big source of concern in this regard.

To accomodate with the shorter sawtooth period in the simulation, the time scales of the other diffusive processes are also accelerated. Namely, we try to keep the product $S\chi$, where $\chi$ is any diffusive coefficient apart from resistivity, as close to its experimental value as possible. With a perpendicular diffusivity of the order of $1\,\mathrm{m}^2.\mathrm{s}^{-1}$ in the code, the experimental value of $S\chi_\perp$ is 80. We have used $S\chi_\perp = 30$, which is of the right order of magnitude. The ratio between parallel and perpendicular diffusivities is of the order

of $10^8$ in the experiment. In our simulation, this ratio is only of $3 \times 10^6$. This allows to reduce the numerical difficulty of the simulation, while having a still quite large $\chi_\parallel$ allowing to have adiabaticity between the temperature and the magnetic flux to a good approximation.

In order to reproduce the experimental density peaking, a pinch the two ratios $a|V_{\text{pinch}}|/D_\perp$ and $|V_{\text{pinch}}|/(a\tau_{ST})$, where $\tau_{ST}$ is the sawtooth period, should be set to their experimental values. In Tore Supra #44634, the sawtooth period is of the order of 30 ms, $a = 0.7$ m, which sets these ratios respectively to 1.4 and 0.004. Thus we should take for $|V_{\text{pinch}}|$ and $D_\perp$ the values

$$|V_{\text{pinch}}| = \frac{0.004}{\tau_{ST,XTOR}} \tag{6.13}$$

$$D_\perp = \frac{V_{\text{pinch}}}{1.4}. \tag{6.14}$$

With the sawtooth period in XTOR-2F, $\tau_{ST,XTOR}$, expressed in Alfvén time unit. In our simulation, this period is $40000\tau_A$, so that we should take $|V_{\text{pinch}}| \simeq 10^{-7}$ and $D_\perp \simeq 7.5 \times 10^{-8}$. However these values are numerically quite challenging, because, as expected, they produce a very sharp peaking of the density profile. This increases significantly the effect of diamagnetic terms, for a given value of the parameter $\alpha$. Yet diamagnetic terms do not behave very well numerically when they are too large, especially in the center of the mesh. Therefore we have used values which make the density peaking less sharp, but still significant: $|V_{\text{pinch}}| = 6 \times 10^{-8}$ and $D_\perp = 3 \times 10^{-7}$.

The experimental value of the parameter $\alpha$ is 0.08. In theory, it should be rescaled too since it determines the frequency of the sawtooth precursor, or equivalently, the rotation frequency of the island in the poloidal section during the reconnection. However the value of $\alpha$ is extremely constrained, as can be seen on Fig. 3.9. At a Lundquist number of $S = 10^7$, the minimum value required to reach the sawtooth cycling regime is very close to 0.08, and the code cannot be run with $\alpha$ exceeding 0.15. Above, numerical instabilities in the core are too strong and can lead to a crash of the simulation. We have used the value $\alpha = 0.1$, which allows to be "safe" in terms of being in the sawtooth regime or not, and which is sufficiently small to limit the effects of numerical instabilities in the core.

Regarding the stability of the initial configuration, the safety factor is not fitted to the experiment, but we take a monotonic profile with core and edge values, and $q = 1$ surface position, consistent with the experiment, in a loose sense. The edge value $q(a) \simeq 5$, while experimental values are rather in the range $3 - 4$. The core initial value is $q(0) = 0.77$. However this value is irrelevant since in the regime of sawtooth oscillations, the safety factor profile evolves self-consistently and never recovers its initial value in the core. During the oscillations, the lower value reached by the safety factor is $q(0) = 0.92$. The $q = 1$ surface is located a little before mid-radius, for $r = 0.4$, in accordance with the experiment, where it is approximately at $r = 0.3$ m for a minor radius of $a = 0.7$ m.

To sum up the numerical set up, we have in no way tried to fit the equilibrium on the experiment. Instead, we have put the system in a point of the space parameters where the best sawteeth are obtained, in terms of separation of time scales and relevance of the physics at stake (here, the diamagnetic effects, that is, the value of $\alpha$), and where a

significant peaking of the density profile is present before each sawtooth crash. The idea is that the final structures depend quite strongly on the initial profile. When there is no peaking at all before the crash, we do not expect any structure to be generated by the reconnection phase. We will see in more details in chapter 7 the influence of the initial profile on the post-crash structures.

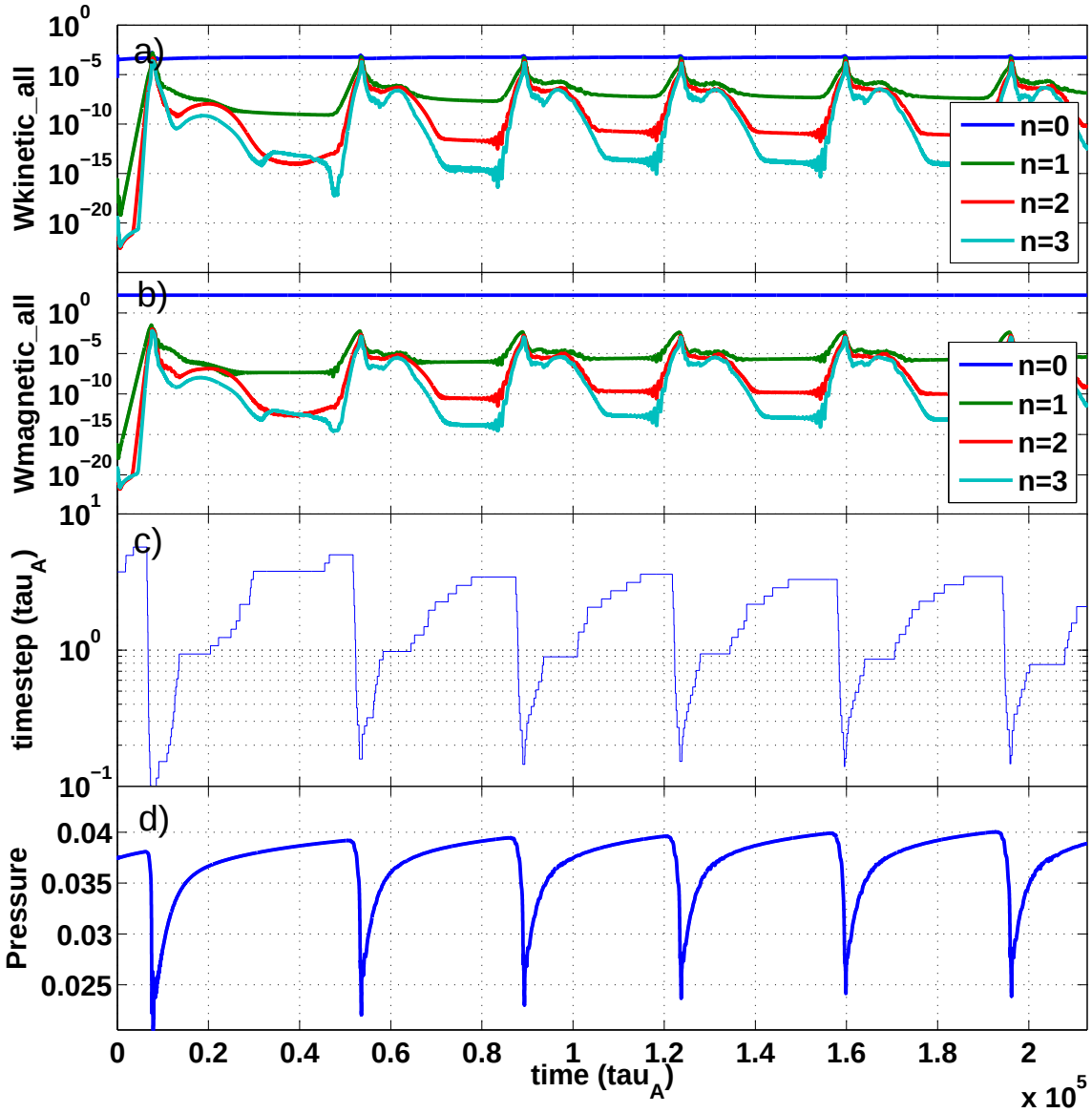


Figure 6.9: Evolution of different quantities during the simulation: Kinetic energy (a), Magnetic energy (b), time step (c), central pressure (d).

The results of the simulation are presented on Figs. 6.9 and 6.10. Fig. 6.9 shows the

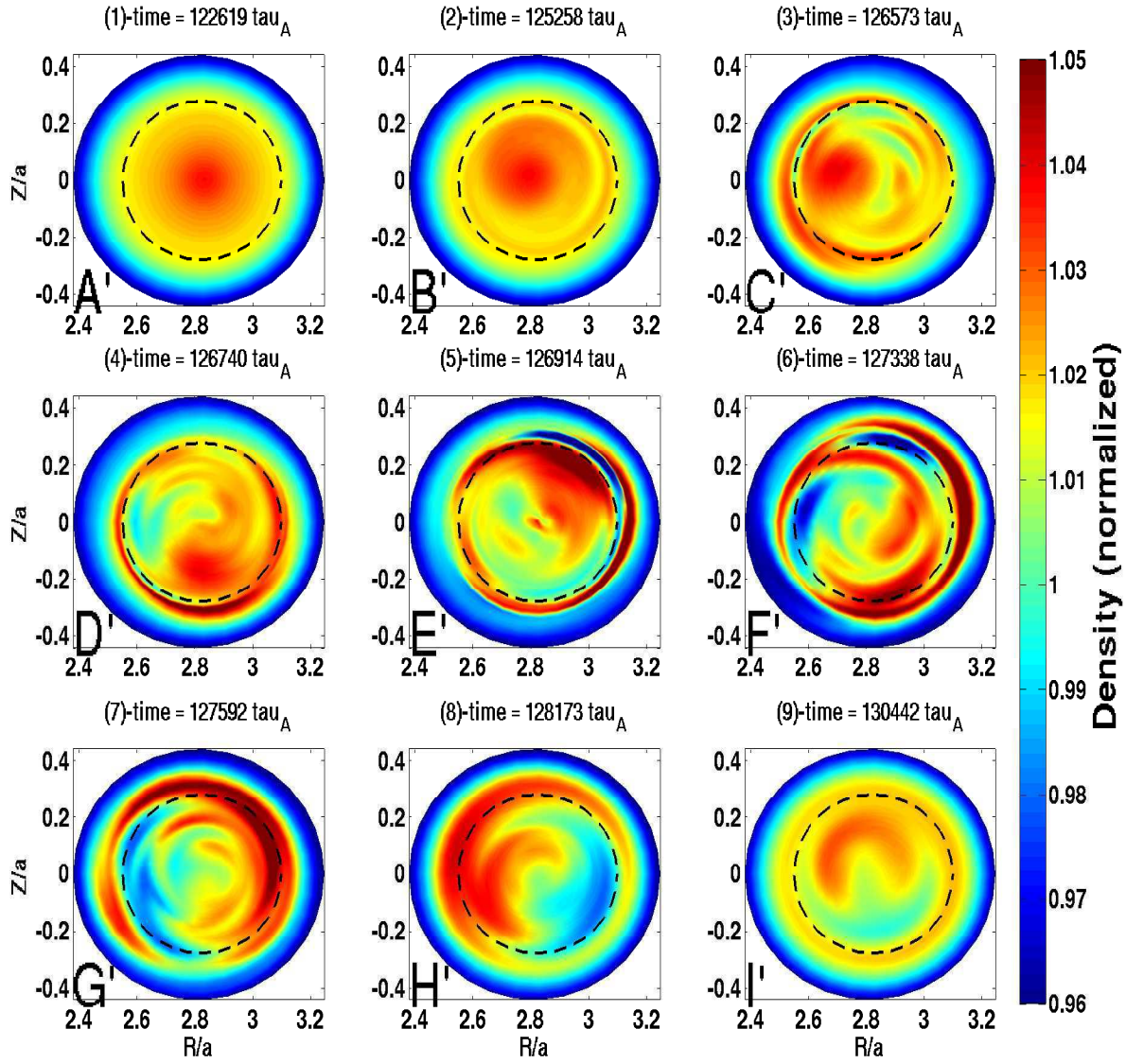


Figure 6.10: Colour plots of the density in an XTOR-2F sawtooth crash simulation. The crescent-shaped structure is recovered and forms during the crash. Rotation is counter-clockwise. The dotted black circle figures the position of the initial $q = 1$ surface. It should not be confused with the separatrix which moves outward during reconnection.

cycling evolution of different quantities in the simulation: kinetic and magnetic energies, numerical time step and central pressure. Notice that in XTOR-2F, the time step is adaptive. When too many iterations are necessary to resolve the time advance, it is decreased, and then increases again when a small number of iterations is necessary. The time step is typically between 1 and $10\tau_A$ in the quiescent phase of the sawtooth ramp, and drops to between typically 0.01 and $0.1\tau_A$ during the reconnection phase. The similarity of Fig. 6.10 with Fig. 5.31 is striking. The same crescent-shaped structure is obtained at

the end of the reconnection phase. As in the experiment, it is encircled by a secondary ring-shaped structure. Namely, frame I' of Fig. 6.10 looks much like frame E of Fig. 5.31. The two are displayed as surface plots on Fig. 6.11. It is possible to trace back the apparition of the density structures using the outputs of the code.

- A': The density poloidal profile before kink destabilization.
- B': Initial core displacement pushing the core toward the $q = 1$ surface. A thin density structure is already distinguishable in the right part of the image.
- C' and D': Formation of circular structures is clearly visible while the dense core shrinks at the reconnection layer.
- E': Reconnection rate is enhanced due to diamagnetic effects and leads to a gap (dark blue) and bump (dark red on the right edge of the image) structure.
- F' and G': The process continues and finally reconnection stops. The result is that the core density has been remapped on a circular zone close to the separatrix.
- H': The density structure homogenizes poloidally to form a ring and feeds a more internal crescent-shaped structure.
- I': While the external ring structure slowly diffuses, the remaining dominant density structure is crescent-shaped.

Figure 6.11: Surface plot of the crescent-shaped structure as observed in the experiment (a) and in the simulation (b). The experimental density is normalized to the value at the $q = 1$ surface.

The origin of this density redistribution can be understood using the same kind of arguments as in the previous subsection. Indeed the poloidal perpendicular flows are, again, the key to understand this phenomenon. The sequence displayed on Fig. 6.10 corresponds to one magnetic reconnection event. As noted before, the kink displacement is accompanied by rapid flows emerging from the reconnection layer, located at $r_s$. When reconnection occurs,these flows are Alfvénic. However the corresponding Alfvén speed is composed using the reduced helical field, $\mathbf{B}^\star \equiv \mathbf{B}_\theta(1-q)$, $|\mathbf{B}^\star| \simeq rB_0(1-q)/(Rq)$.The maximum value of $|\mathbf{B}^\star|/B_0$ inside the $q = 1$ surface is of the order of $3 \times 10^{-3}$, given that $(1 - q_0) \simeq 0.1$ and $r_s/R_0 \simeq 0.1$. Actually, the velocity of the jet generated at the separatrix reaches the value of $0.01V_A$ when reconnection is at its maximum rate. It is a very fast velocity, considering that the Alfvén velocity is of the order of $10^7$ m.s$^{-1}$. To understand how the density is transported by the flows, it is necessary to evaluate the different terms in *Eq.* (6.12) during the simulation, while the structure develops. However this must be done in the rotating frame, because in the laboratory frame a significant part of the time derivative of the density is due to the term $r\omega\hat{\boldsymbol{\theta}} \cdot \nabla n$, which overrides important information. Since the simulations presented here have bifluid effects included,

we must take into account the total velocity $\boldsymbol{v}_i = \tilde{\boldsymbol{v}}_E + \boldsymbol{v}_{\|i} + \boldsymbol{v}_i^\star$. Here $\tilde{\boldsymbol{v}}_E = \boldsymbol{v}_E - r\omega\hat{\boldsymbol{\theta}}$, but we will further remove the tilde notation for clarity. Recall that in a cylindrical plasma, the diamagnetic flux does not advect the density at all, $\nabla \cdot (n\boldsymbol{v}_i^\star) = 0$. In a toroidal plasma however, the compressibility of the diamagnetic velocity does not totally compensate the advection, $\nabla\cdot(n\boldsymbol{v}_i^\star) = 1/e\nabla p_i\cdot\nabla\times(\mathbf{B}/B^2) \neq 0$. This term actually turns out to be dominant in the continuity equation, especially in the singular layer, where the pressure gradient is significantly enhanced. It is mainly compensated by the divergence of the electric drift velocity, that is, we have:

$$1/e\nabla p_i \cdot \nabla \times (\mathbf{B}/B^2) \simeq -n\nabla\phi \cdot \nabla \times (\mathbf{B}/B^2), \tag{6.15}$$

except in the resonant layer. *Eq.* (6.15) is an expression of the fact that ion confinement is electrostatic.

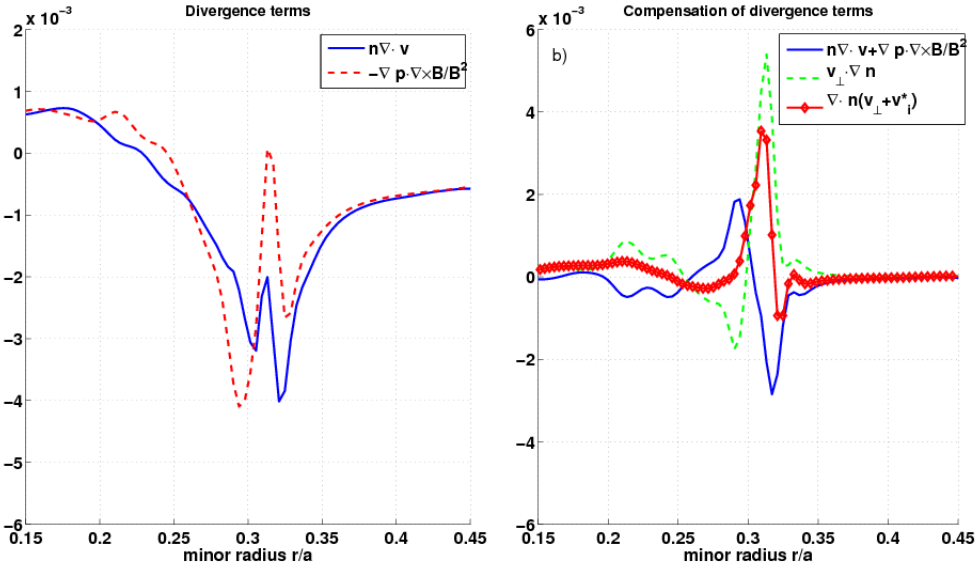


Figure 6.12: Plot of the different terms in the continuity equation, for $\theta = \pi/4$, $t = 126914\,\tau_A$.

The sum of these two terms are curvature terms. The next dominant term in the continuity equation is the electric drift advection $\boldsymbol{v}_E \cdot \nabla n$. In the following, the contributions of the curvature terms and of the electric drift advection during the reconnection phase are compared. The different dominant terms in the continuity equation are plotted on Fig. 6.12 across one minor radius, for one given angle, here $\theta = \pi/4$ at $t = 126914\,\tau_A$, corresponding to frame E' in the region of the growing perturbation ($\theta = 0$ is on the equatorial plane). On Fig. 6.12(b) the sum of the two terms from Fig. 6.12(a) is plotted in blue. The electric advection term is also represented in green, while the red curve represents the sum of the blue and green curves, representing the dominant term in the time derivative of the density in the rotating frame.

It can be concluded from Fig. 6.12(b) that in the reconnection region, the density evolution is driven by the electric drift, which is not surprising given the amplitude of

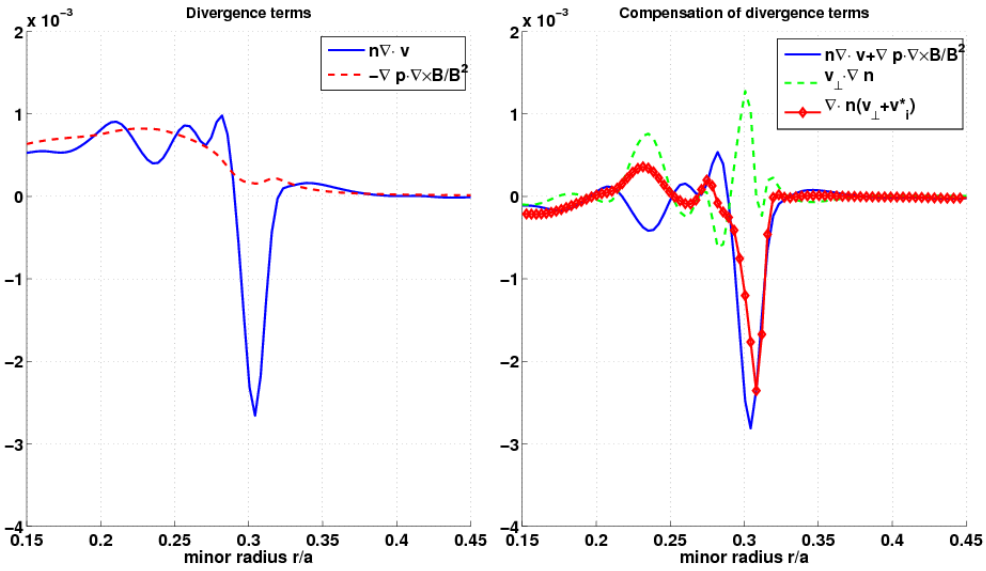


Figure 6.13: Plot of the different terms in the continuity equation, for $\theta = 0$, $t = 126914\,\tau_A$.

the flow. Indeed the main contribution to the red curve is the green curve, and it adds positively in the l.h.s. of *Eq.* (6.12), that is, it is a density sink, at the origin of the deep gap observed on frame E'. The same curves can be plotted for any angle $\theta$. Fig. 6.13 is at the angle $\theta = 0$, which corresponds to the right end of the reconnection layer. Here it is seen that the dominant term comes from curvature, or compressibility effects, and adds negatively to the density balance equation. It is a source of density and leads to the formation of the bump observed on frame E'.

Fig. 6.14 helps summarizing the process described using Fig. 6.12 and Fig. 6.13. The stream function of the flow is displayed together with the separatrix at $t = 126914\,\tau_A$, when the reconnection flows are the largest, and it is compared with a Poincaré plot of the magnetic surfaces.The stream function adopts the same general structure as the magnetic flux surfaces, a bubble-shaped old core and a wide island encircling it, with a few secondary islands denoting $m/n = 2/2$ and $m/n = 3/3$ activity. It is clearly seen on Fig. 6.14 a) how advection lets the density cross the separatrix to map the dense core on a circular zone outside the $q = 1$ surface.

The analysis of Fig. 6.12, Fig. 6.13 and Fig. 6.14 leads to the following conclusions:

- The particles are mainly advected by the fast electric drift velocity jets generated at the reconnection layer.
- After crossing the separatrix, finite compressibility leads to a density build-up producing the observed ring-shaped structure.

It is more difficult to understand how the more central crescent-shaped structure is generated. A first guess would be that it corresponds merely to an $m = 1$ perturbation of the density profile, thus uninteresting when looking at the radial transport properties

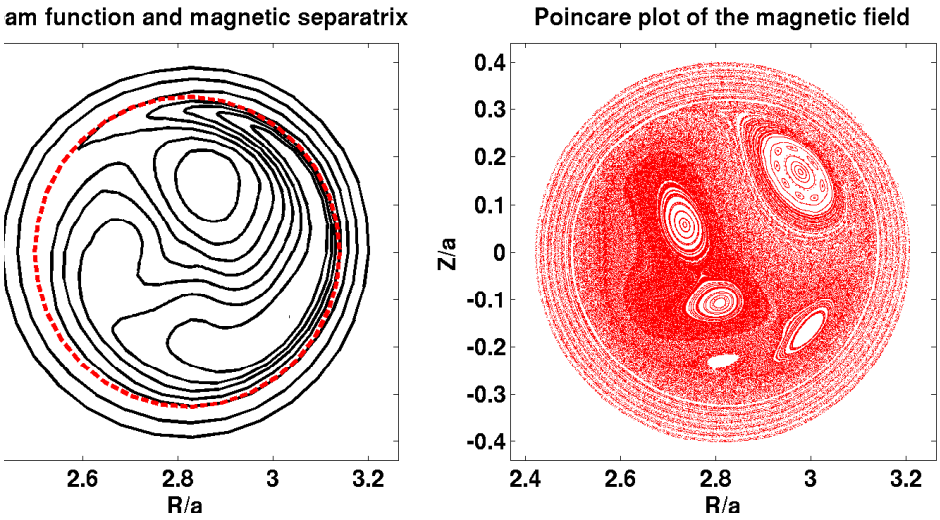


Figure 6.14: Contours of the potential function in the rotating frame during the crash, with the magnetic separatrix shown in red at time $t = 126914\,\tau_A$ (left panel). It is compared with the magnetic surfaces obtained as Poincaré plots (right panel). The stream function and the flux label display similar structures.

linked with the sawtooth crash. However, the structure remains visible on the poloidally averaged profiles (as seen on Fig. 6.16), so this possibility is ruled out. Instead, the structure really seems to be fed by the outer ring (frame H'). There is a possibility that it be generated by the small flows remaining at the end of the crash, and linked with the final reorganization of the poloidal flux surfaces. Indeed, following the end of the reconnection phase, the magnetic island occupying the volume inside the separatrix must become a new magnetic core. Thus magnetic surfaces must recenter, carrying with them the plasma in a radial motion. In chapter 7, we will also see that ion inertia seems to be necessary to obtain the crescent-shaped structure.

Finally, note that during reconnection, the structure and position of the magnetic island approximately corresponds to the structure seen on the stream function, as shown on Fig. 6.14. Following the arguments of section 6.1.3, one could expect to see flattening occur on the magnetic island, resulting in a final flat density profile, in accordance with the most common sawtooth model (see for example [Porcelli 1996]). However there is a major difference between the situation studied presently and section 6.1.3: while the flattening process was due to the existence of a long-lasting potential structure, giving the density enough time to whirl several times around the vortex, now the whole process lasts only one reconnection time. The most significant part of the reconnection phase happens in less than $2 \times 10^3\,\tau_A$, with a typical period of rotation around the vortex of $10^3\,\tau_A$ (only immediately in the reconnection layer and for a short time does the velocity reach the value $0.01 V_A$), so homogenization does not have time to occur. Also, the flow pattern itself evolves on the reconnection time scale, so we do not expect to obtain the result $n_e = n_e(\phi) = n_e(\Psi^\star)$, neither during the reconnection phase, neither as a result of the process. Fig. 6.15 shows that indeed the contours of the density and the stream

function are quite different, both during the reconnection process (panels a) and b)) and at the end of the reconnection phase (panels c) and d)).

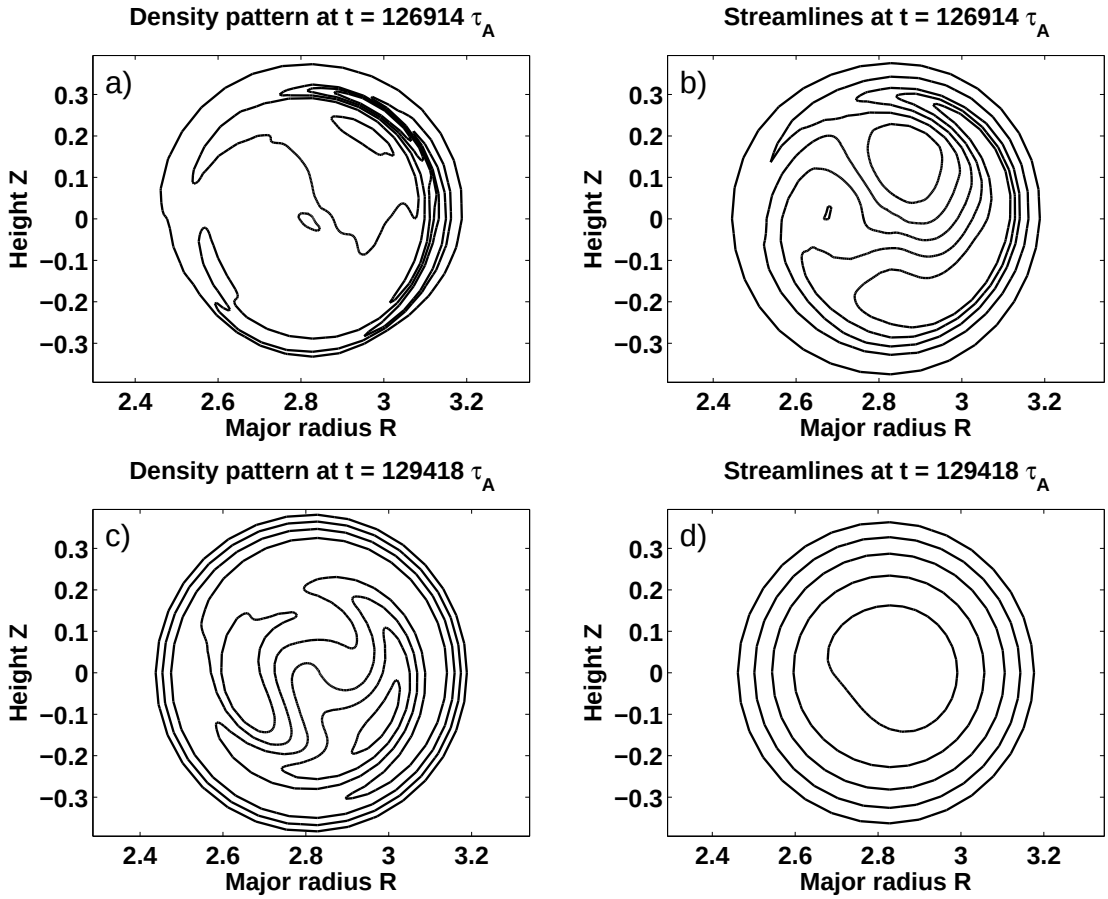


Figure 6.15: Density contours at $t = 126914\,\tau_A$ (a) and $t = 129418\,\tau_A$ (c), compared to the streamline pattern at the same times (b) and (d).

We can push a little further the comparison between XTOR-2F results and the experimental results. Frames E and F of Fig. 5.31 show that the crescent-shaped structure homogenizes in a few milliseconds. The external structure also homogenizes, and two rings remain. This is consistent with sound-wave homogenization, occurring on a time scale $\tau_s = (k_\parallel c_s)^{-1}$. Given the post-crash temperature of 2.2 keV, a homogenization time of a few milliseconds is consistent with a $\delta q \equiv |q - 1|$ in the range $[10^{-2}, 10^{-1}]$. In the experiment, the safety factor is not known with a sufficient precision to conclude definitively, even if such values correspond to commonly observed magnetic shearing rates. In XTOR-2F, reconnection is complete, so that the safety factor is above 1 in all the plasma after the crash. Fig. 6.16 shows the safety factor and the flux surface averaged density at the time $t = 130442\,\tau_A$, frame I' of Fig. 6.10. It is seen that $q - 1$, and hence $k_\parallel$, is approximately 5 times bigger on the external structure than on the crescent. Hence it homogenizes poloidally 5 times faster, in a few $\tau_s$, $\tau_s \sim 0.5 \times 10^3 \tau_A$. Thus the transition from crescent to ring is not observed for the more central structure because since the

Lundquist number is lower than in the experiment, the sawtooth cycle dynamics is faster and the next crash occurs before homogenization is complete.

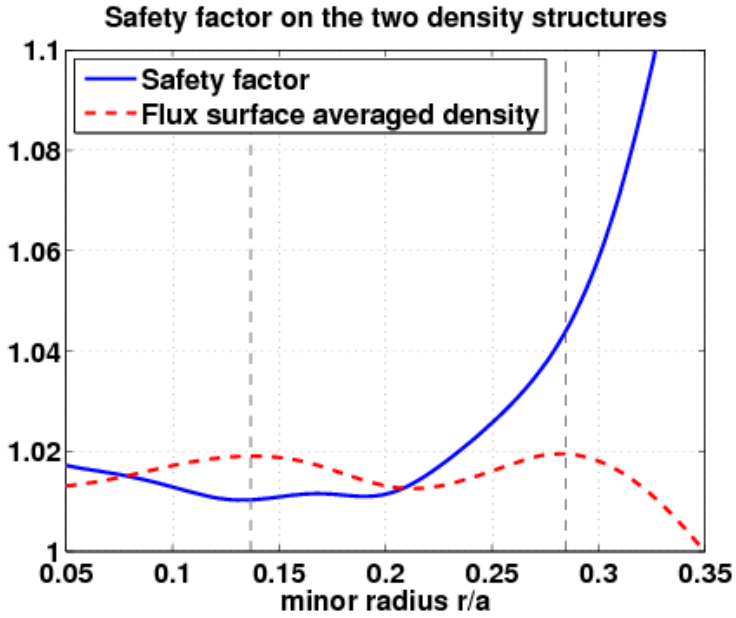


Figure 6.16: Safety factor and density on the line $\theta = \pi$ at $t = 130442\,\tau_A$. The dotted vertical lines show the radial location of the two structures. Safety factor and normalized density have same units on the y-axis.

A difference with the experiment is the amplitude of the final structures. In the experiment the crescent amplitude is of the order of 2% of the total density, while the amplitude of the circular structure is less than 1%. In XTOR-2F, these amplitudes are both slightly below 1% (after flux surface average). In both cases, the circular structure in the final state is located very close to the $q = 1$ surface.

It is crucial to note that the experimental results imply that a significant part of the density in excess of the density at the $q = 1$ surface is not expelled, contrary to what is usually assumed [Porcelli 1996]. The crescent-shaped structure is the trace of a reinjection mechanism. It does not matter much for the electron density because the structure represents a very small part of the total density. However, one is tempted to apply this model to impurities like Tungsten or Helium, which have different profiles. A typical Helium profile almost vanishes at the $q = 1$ surface, if one assumes efficient pump out, while the Helium produced by fusion reactions in the deepest core builds up inside the $q = 1$ surface. If a significant part of the particles are not expelled but reinjected by the flows inside the $q = 1$ surface, it could lead to insufficient Helium (and/or Tungsten) exhaust. The following simplistic model clarifies this point. In theory one can measure the reinjection ratio of a species $s$, $f_s$, defined by the ratio

$$f_s = \frac{N_{p,s}(r_{inv}, t_1)}{N_{p,s}(r_{inv}, t_0)},$$

where

$$N_{p,s}(r,t) = \oint\!\!\iint_0^r (n_s(\boldsymbol{r},t) - n_s(r_{inv},t_0))\,\mathcal{J}\mathrm{d}r\mathrm{d}\theta\mathrm{d}\varphi$$

($\mathcal{J} = [\nabla r \cdot (\nabla\theta \times \nabla\varphi)]^{-1}$ is the jacobian), is the number of particles inside the surface of radius $r$, in excess of $n_s(r_{inv},t_0)$, $t_0$ and $t_1$ are two instants immediately before and after the crash. Here $n_s(r_{inv},t_0)$ designates the density of the species $s$ at the inversion radius of the sawtooth at $t_0$. In general $0 < f_s < 1$, since 0 corresponds to full flattening, and 1 corresponds to no net particle flux through the inversion radius between the beginning and the end of the crash. If one assumes similar density redistribution mechanisms for electrons and minority ions, then the ratios $f_e$ and $f_{He}$ are the same. A number $N^0_{He}$ of $\alpha$ particles is produced in the core between two sawtooth crashes. If we denote by $N_{He}(n)$ the number of $\alpha$ particles inside the $q = 1$ surface immediately after the $n^{th}$ sawtooth crash, then, neglecting transport, $N_{He}(n+1) = f_{He}(N_{He}(n) + N^0_{He})$. It follows that

$$\frac{N_{He}(n)}{N^0_{He}} \underset{n\to\infty}{\longrightarrow} \frac{f_{He}}{1-f_{He}} > f_{He}.$$

Hence for non-negligible ratio $f_{He}$ the density inside the $q = 1$ surface can be significantly enhanced by the $1/(1 - f_{He})$ factor.

The most important caveat to this model is that it neglects transport and any other source of He density change apart from the fusion source and the sawtooth crash. Obviously the inter-sawteeth radial transport due to the neoclassical/turbulent pinch and diffusion plays a comparable role and could either mitigate or exacerbate the preceding conclusion, depending on the precise nature of the transport. What remains is that if one wants to expel particles from the core, then the net loss of particles trough the $q = 1$ surface should be estimated and as large as possible. The choice of the $q = 1$ surface could seem somewhat arbitrary, since what matters is the plasma region where the particles are generated (for the He case), or where impurities have significant radiation (for the heavy impurities case, like W). These regions may be in general different from the $q = 1$ surface. However since the redistribution mechanism studied here is the sawtooth crash, characterized by its $q = 1$ surface, it makes sense to use it.

Also, note that the reinjection ratio $f_s$ is not a well-defined quantity. Indeed it is very sensitive to the choice of $t_0$ and $t_1$, and to the measurement of the position of the inversion radius. In particular, it is difficult to define a density inversion radius in our simulations. Indeed the concept is most easily defined if the profile following the crash is flat in the region of the $q = 1$ surface, however in our case the circular structure ends up in the region of the $q = 1$ surface, as seen on frame I' of Fig. 6.10, and has the same amplitude as the crescent. Thus it is meaningless to compute $f_e$ in this case. However in the experiment the crescent largely dominates over the ring, which is consistent with the experimental results of Ref. [Guirlet 2010] showing that the fluctuation level $\delta n/n$ is reduced inside the $q = 1$ surface. Remembering that the ring originates from the density circular pulse following the separatrix, it is more affected by diffusion, which explains its diminished size. Also the inversion radius is easier to define and the time scales of sawtooth global dynamics and sawtooth crash are well separated, allowing a reasonable choice of $t_0$ and $t_1$ for each crash. The measured ratio $f_e$ depends on the crash. The

sequence in Fig. 5.31 is part of a sequence of 5 tomographically analyzed crashes. The ratios $f_e$ measured for this subsequence are plotted on Fig. 6.17. It is seen that typically, $0.2 < f_e < 0.5$. Given that the redistribution mechanism is dominated by the flows coupled to diffusion, the ratios of the different species are likely to be similar, except if the turbulent diffusion coefficients are very different. These results imply that impurity transport in sawtooth regime is a serious issue which deserves closer investigations.

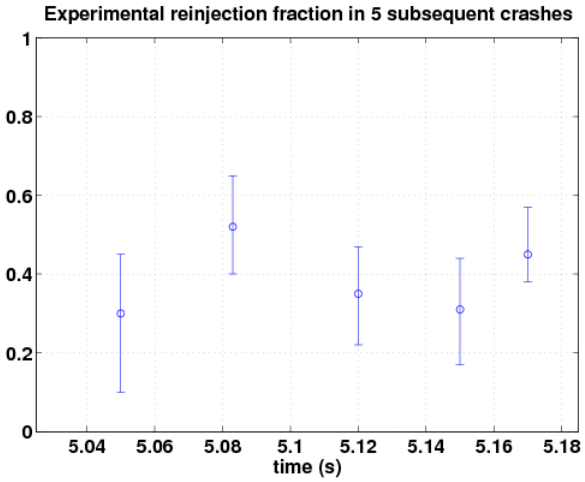


Figure 6.17: Reinjection ratios in the experiment for 5 subsequent sawtooth crashes. They are plotted at the time of the corresponding crash.

### Comparison with Kadomtsev's model

We now compare the profile obtained after the sawtooth crash with the profile obtained with Kadomtsev's model as derived in section 4.1. Fig. 6.18 shows the initial profile (blue), the flux surface averaged profile as obtained after the crash by XTOR-2F (dashed red) and the profile obtained using Kadomtsev's model (dashed black). Recall that the basic mechanism in this model is the fast transport along field lines. We have just demonstrated using the simulations that the mechanism is actually quite different and involves the fast flows generated at the reconnection layer. Fig. 6.18 clearly shows in this case the discrepancy between the two models. Kadomtsev's model does not produce the crescent-shaped structure we have been studying in this section. It is in fact almost completely flat except very close to the mixing radius. Overall, the two profiles are quite different.

We will do more comparisons with Kadomtsev's model in the next chapter, where we carry out simulations of impurity transport during the sawtooth crash. However, in order to understand the conclusions of this next chapter, we must now do the following important remark: in the present section we have been interested in very small structures. The amplitude of the density peak in the core represents less than 10% of the total density, and the post-crash structures have an amplitude of the order of 1%. Thus we are looking at very small details, which may proove irrelevant in the end. The reason why we are

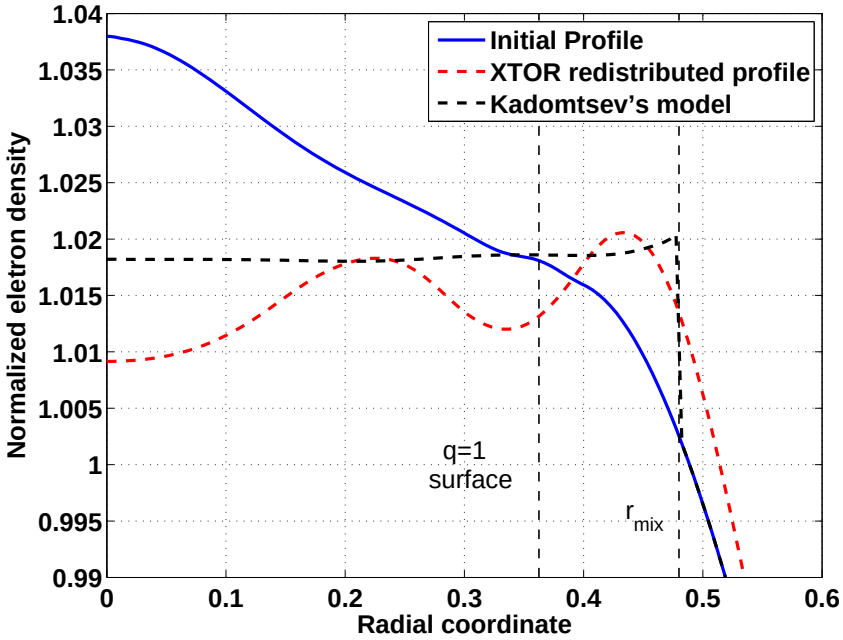


Figure 6.18: Initial profile (blue), the flux surface averaged profile as obtained after the crash by XTOR-2F (dashed red) and the profile obtained using Kadomtsev's model (dashed black). The $q = 1$ and mixing radii are displayed as the dashed vertical lines.

still a bit concerned by the observed crecent-shaped structure is that, as said above, the proportion of particles contained in this structure compared to the initial peak is important (Fig. 6.17), and one could naively expect that this ratio will remain constant for any kind of pre-crash profiles. This means that there could be cases where the absolute amplitude (not the mere relative amplitude) of these post-crash structures will be important, implying a poor efficiency of the sawtooth flushing mechanism. Without uncovering too much of it, the next chapter will show that for more peaked profiles, the redistribution obtained with Kadomtsev's model is actually in good quantitative agreement with the one obtained with XTOR-2F. This result seems paradoxical in regard of what we have just said, but we will attempt to explain it.

## 6.3 Summary

At the end of this chapter we are able to reconstruct a full story of the evolution of the density, and how it is coupled to the sawtooth evolution. The experimental results, confirmed qualitatively by non-linear MHD simulations, lead to the following conclusions:

- At the onset of the sawtooth crash, the hot and dense core is driven toward the $q = 1$ surface, where it is advected by fast electric drift velocity jets on the separatrix. Its evolution is dominated by these drifts. The temperature is also advected by the electric drift, however its evolution is dominated by a large parallel diffusivity, so

that it remains constant on the magnetic surfaces.

- After the crash, about one third of the particles have been reinjected inside the $q = 1$ surface in the form of a crescent-shaped structure. Depending on the amplitude of the remaining MHD activity, two evolutions are possible:
  - When there is low activity after the crash, there is a smooth evolution dominated by sound waves, which homogenize the density in the poloidal direction and lead to a double ring-shaped density structure, on top of which the pinch term builds a peaking of the profile.
  - When a long-lived MHD mode with frequency comparable to the kink frequency persists after the crash, the potential pattern drives a rapid flattening of the profiles because of the existence of a strong velocity shear zone next to the $q = 1$ surface. This flattening occurs because initially the density is not a flux function. Thus the flows, which are tangent to the potential and magnetic surfaces, redistribute the density to make it a flux function, and at the end of this convection process the density ends up to be flat. However the temperature, which is already a flux function, is not significantly affected by these flows.

The experimental results and the interpretation using MHD simulations clearly show that the redistribution mechanism for the electron density is essentially different from Kadomtsev's mechanism (transport along field lines). In addition, these results raise a concern about the efficiency of the sawtooth crash to flush the impurities from the core (heavy impurities like Tungsten or He ash). The following chapter addresses this issue.

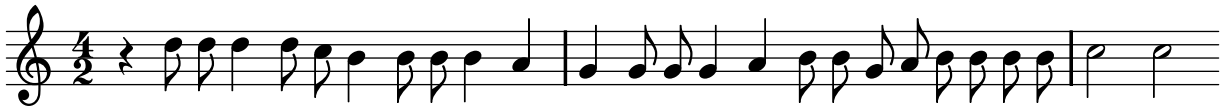

*Lauda Jerusalem a 5 voci da Cappella*
**Claudio Monteverdi**

Chapter 7

# Impurity transport by the sawtooth crash

## Contents



## 7.1 Introduction

As has already been said several times throughout this thesis, the presence in the plasma of heavy impurities like Tungsten (W) is a serious issue the fusion community has to face. In recent machines with W wall and ITER, W can be injected in the plasma because of physical sputtering at the strike points of the divertor [Pütterich 2012]. Regarding W, a maximum relative concentration of $1.9\times10^{-4}$ can be tolerated in the core of ITER plasma to be able to reach the ignition condition [Pütterich 2010]. It has been reported[Nave 2003, Belo 2004, Nakano 2009] that sawteeth can help avoiding accumulation of impurities in the core. This is an important motivation for carrying out modelling of impurities by sawtooth crashes.

Furthermore, fusion reactions, in the Deuterium-Tritium case, produce energetic $\alpha$ particles which contribute to heat the plasma. After power deposition is done, He must be continuously extracted in order to give place to fresh D-T fuel, otherwise the efficiency of the reaction decreases by fuel dilution until the reactions stop. Since the pumps are located under the divertor plates [Tomabechi 1991] and He is produced in the core, there must be some mechanism to efficiently transport it from the core to the edge of the plasma. Sawteeth have been proposed as a possible mechanism for such a transport[Redi 1991,

Chang 1998] in the $q < 1$ region, while turbulence is supposed to take over in the $q > 1$ region.

In this chapter, we will address the question of the transient bursts of transport caused by the sawtooth crash, bearing in mind the results of the preceding chapter. That is, we want to know if large amplitude structures are observed inside the $q = 1$ surface after the sawtooth crash, thus indicating a poor efficiency of the sawtooth flushing mechanism. The cases of peaked profiles (He-like) and hollow profiles (corresponding to an impurity, *e.g.* W, generated at the edge and slowly reaching the $q = 1$ surface) are investigated. We will see that crescent-shaped structures can indeed be sometimes observed, but they have a small amplitude and do not seem to constitute a source of concern for the redistribution by the crash. The results are also compared to a 1-D transport model deduced from Kadomtsev's conservation rules [Kadomtsev 1987, Furno 2001, Porcelli 1999] studied in section 4.1.

## 7.2 Impurity modelling with XTOR-2F

To simulate impurity transport by the sawtooth crash, passive scalars are introduced in the simulation. Even though impurities are passive, we do not simulate pure advection. Indeed, simulating pure advection by $\boldsymbol{v} = \boldsymbol{v}_\perp + v_\parallel \mathbf{b}$ would imply losing particle conservation, since in our simulations $\nabla \cdot \boldsymbol{v} \neq 0$ is a large curvature term. Compressibility must be added, hence the total impurity velocity $\boldsymbol{v}_{Z,tot}$ of an impurity ${}^Z_A X$ is used. To clarifiy the following, we adopt the following notations

$$\boldsymbol{v}_{Z,tot} = \boldsymbol{v}_Z + \boldsymbol{v}_Z^\star, \text{ with} \tag{7.1}$$

$$\boldsymbol{v}_Z = \boldsymbol{v}_\perp + v_{\parallel Z}\mathbf{b}, \tag{7.2}$$

$$\boldsymbol{v}_Z^\star = \frac{\mathbf{B} \times \nabla p_Z}{Z n_Z e \mathbf{B}^2}, \tag{7.3}$$

$$p_Z = n_Z T, \tag{7.4}$$

where $T$ is the main plasma temperature ($T_e = T_i$), thus impurities are assumed to be thermalized, $n_Z$ is the impurity density and $v_{\parallel Z}$ is given by an additional equation. Indeed, $v_{\parallel Z}$ cannot be equal to the plasma parallel velocity, otherwise the difference in the diamagnetic compressibility implied by $Z \neq 1$ and $p_Z \neq p$ would lead to large poloidal asymmetries. The $m = 1$ component of the impurity parallel velocity thus relaxes to a value given by its own Pfirsch-Schlüter equilibrium, hence the need for an additional equation. Thus the impurity velocity is the sum of the electric drift, common to all species, its own diamagnetic velocity and its own parallel velocity.

An *ad hoc* turbulent flux $\Gamma = -D_Z \nabla n_Z + n_Z \boldsymbol{v}_{pZ}$ can be added, where $D_Z$ is a diffusion coefficient and $\boldsymbol{v}_{pZ}$ a pinch velocity, not necessarily constant radially. In this study we made use of the pinch velocity only to benchmark the numerical model, but not for the impurity studies themselves, so we will remove it hereafter. In addition, a restoring source $S_{n_Z}$ is added,

$$S_{n_Z} = -\nabla \cdot (D_Z \nabla n_{Z0}), \tag{7.5}$$

where $n_{Z0}$ is the initial impurity density profile.

Regarding the parallel velocity equation, we take the parallel component of the following impurity momentum equation, adopting the same assumptions as for the main plasma momentum equation:

$$\rho_Z \left(\partial_t \boldsymbol{v}_Z + \boldsymbol{v}_Z \cdot \nabla \boldsymbol{v}_Z + \boldsymbol{v}_Z^\star \cdot \nabla \boldsymbol{v}_\perp\right) = -\nabla p_Z ... \\ + n_Z Z e \left(\mathbf{E} + \boldsymbol{v}_Z \times \mathbf{B}\right) + \mathbf{R}_Z, \tag{7.6}$$

where $\rho_Z = m_Z n_Z$, ($m_Z = A m_p$, where $m_p$ is the proton mass), and $\mathbf{R}_Z$ is a dissipative force. In our study, we take the parallel component of $\mathbf{R}_Z$ to be a viscosity, implemented as a diffusion on $v_{\parallel Z}$ with a coefficient $\nu$, which is the same as in the momentum equation, *Eq.* (3.21). This has the advantage that preconditioning of such diffusive terms is directly available and robust in XTOR-2F. Since we are in a regime where reconnection is dominated by the thermal force, that is, the parallel electron pressure gradient in Ohm's law, we take $E_\parallel = -\nabla_\parallel p_e / n_e e$. Note also that the parallel contribution of $\partial_t \boldsymbol{v}_\perp$ (not vanishing when $\mathbf{B}$ depends on time), is neglected.

Thus the code solves the following set of coupled equations (in unnormalized form):

$$\partial_t n_Z = -\nabla \cdot (n_Z \boldsymbol{v}_{Z,tot}) + \nabla \cdot D_Z \nabla (n_Z - n_{Z0}), \tag{7.7}$$

$$\partial_t v_{\parallel Z} = -\frac{1}{m_Z n_Z} \left(\boldsymbol{v}_Z \cdot \nabla \boldsymbol{v}_Z + \boldsymbol{v}_Z^\star \cdot \nabla \boldsymbol{v}_\perp\right)_\parallel \dots \\ - \frac{\nabla_\parallel p_Z}{m_Z n_Z} - Z \frac{\nabla_\parallel p_e}{m_Z n_e} + \nabla \cdot \left(\nu \nabla v_{\parallel Z}\right). \tag{7.8}$$

Developing the total impurity velocity $\boldsymbol{v}_{Z,tot}$, *Eq.* (7.7) can be recast into

$$\partial_t n_Z + \boldsymbol{v}_\perp \cdot \nabla n_Z + v_{\parallel Z} \nabla_\parallel n_Z = \nabla \cdot D_Z \nabla (n_Z - n_{Z0}) \dots \\ - n_Z \left[\nabla \cdot \left(\boldsymbol{v}_\perp + v_{\parallel Z} \mathbf{b}\right) + \frac{\nabla p_Z}{Z n_Z e} \cdot \nabla \times \frac{\mathbf{B}}{B^2}\right]. \tag{7.9}$$

The perpendicular velocity $\boldsymbol{v}_\perp$, the electron density $n_e$ and the electron pressure $p_e = n_e T$ come from the resolution of the main plasma bifluid MHD equations. This form highlights the dominant mechanism, which is the advection by $\boldsymbol{v}_\perp + v_{\parallel Z}\mathbf{b}$ and the diffusion. The role of the second term on the r.h.s. is to restore particle conservation, and it plays also an important role during the nonlinear phase because of the generation of parallel velocity sheets. The equations are linear in $n_Z$ and $v_{\parallel Z}$ so that normalization is not an issue. $n_Z$ is normalized so that its values are of the order of 1. Also, notice the $n_Z$ at the denominator in the two first terms of *Eq.* (7.8). Because of this term, the simulation diverges when $n_Z$ vanishes. To avoid this scenario, we offset the profiles by a value of order unity, dictated by experience.

In theory, we could add a friction force $-\mu(v_{\parallel Z} - v_{\parallel i})$ between the parallel velocity of the ions and of the impurity. However this would generate poloidal asymmetries in the impurity density, as explained in appendix H. These asymmetries are physical but do not bring much to the present problem so we chose to avoid them by removing the friction. Appendix G, which explains how the equilibrium electric field establishes, should be read before appendix H.

In this setup, the final impurity profile, after the sawtooth crash, depends mainly on the initial profile and diffusion coefficient, since the perpendicular flow is given by the main plasma evolution, which is fixed and is exactly the same throughout this study, and the impurity parallel velocity during the crash exhibits the same structure as that of the main plasma. Three kinds of initial profiles are presented in this study, to illustrate the effect of the crash on radial transport.

- Case 1 (Peaked impurity): A very peaked profile, where all gradients are confined inside the initial $q = 1$ surface. This unphysical configuration has a pedagogical interest since it helps to assess the quantities of impurities ejected by the sawtooth crash.

- Case 2 (W-like): A hollow profile, flat inside the $q = 1$ surface and flat outside the $q = 1$ surface, with a gradient in the region of the $q = 1$ surface. Physically this corresponds either to the case of an impurity with an outward pinch velocity creating a hollow profile, or to a more complex scenario where an impurity, say, W, is generated at the boundary of the plasma, and slowly penetrates until it reaches the $q = 1$ surface. This can happen either at a W event [Krieger 2011], during laser blow-off or supersonic beam injection experiments aiming at determining coefficient transport of impurities [Mattioli 1998, Guirlet 2009], or in impurity gas puff experiments (*e.g.* [Nave 2003, Puiatti 2003, Belo 2004]. The simulation thus helps to determine how the sawtooth crash impacts the penetration of impurities. The offset value used in this case to prevent the impurity density from going to zero during the crash was 1, due to large gradients generated in this phase.

- Case 3 (He-like): A peaked profile, designed as to mimic the Helium (He) ash produced by the fusion reactions. The fusion power $P_{fus}$ is proportional to the square of the plasma density and to a certain power $\gamma$ of the temperature, $P_{fus} \propto n_e^2 T^\gamma$, where $\gamma(T)$ is close to 2 for typical fusion temperatures. In particular, $\gamma(13.5\,\mathrm{keV}) = 2$, $\gamma(7.5\,\mathrm{keV}) = 3$ and $\gamma(26.6\,\mathrm{keV}) = 1$. See Ref. [Huba 2007] for the Deuterium-Tritium (D-T) fusion cross-sections and $\langle\sigma v\rangle$. Thus it is a fair approximation to use $P_{fus} \propto p^2$ for a burning plasma, given that ITER volume average temperature should be around 13 keV, with peaks up to more than 25 keV [ITER 1999a]. Fig. 7.1 shows the pressure profile and the corresponding He source. The source is taken constant over time, even though pressure is modified by the sawtooth crashes. Also note that in the case of He, the hypothesis $T_Z = T$ does not hold since the $\alpha$ particles are generated with an energy of 3.5 MeV. However the energetic particles are supposed to deposit their energy on the electrons before being removed from the plasma, so we can assume that at the sawtooth crash, the major part of the He content is thermalized. In other words, we assume the slowing down time of the $\alpha$ particles distribution is small compared to the transport time scales and the sawtooth period.

The pre-crash profiles for the three cases can be seen as the blue profiles of Figs. 7.7, 7.9 b) and 7.12.

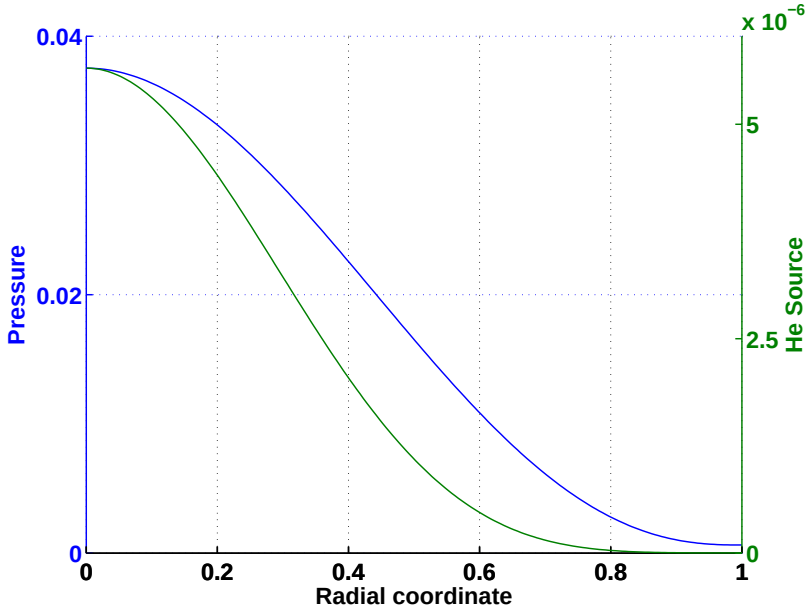


Figure 7.1: Pressure profile in $\rho_0 V_A^2$ units (blue) and corresponding He source, normalized so that $n_{Z0}(0) - n_{Z0}(a) = 1$ (green) for Case 3.

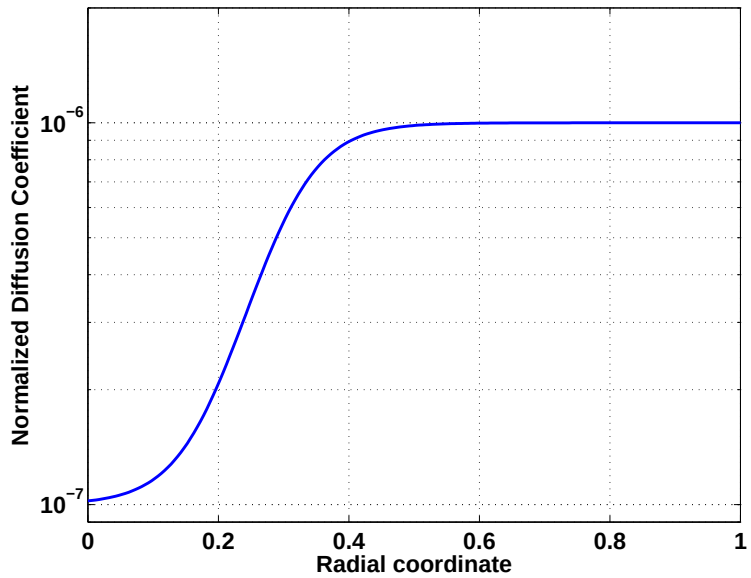


Figure 7.2: Profiles of the diffusion coefficients used in the impurity simulations.

For the charge and mass numbers of the impurities, we have taken $Z = 1$ and $A = 2$ for case 1, $Z = 2$, $A = 4$ for case 3 (Helium), and different values for case 2, showing that it has little influence on the results.

The profile of the diffusion coefficient used in all three simulations is shown on Fig. 7.2. It increases by a factor of 10 between the core and the edge, with a transition located

around the $q = 1$ surface. This mimics the experimental result that turbulence is much lower inside the $q = 1$ surface [Guirlet 2010], and is also qualitatively consistent with critical gradient models, for instance Ref. [Garbet 2004]. The absolute value in the core is taken to be of the same order of magnitude as the measured diffusion coefficient for the electron density. Notice that in this study, we are mainly interested in the transport induced by the sawtooth crash, which is sufficiently fast so that the details of the transport coefficients does not matter much.

In cases 1 and 2, the density is given analytically and the source determined from *Eq.* (7.5). In case 3, the direct implementation of $S_{n_Z} \propto p^2$, with $p$ constant on flux surfaces, leads to poloidal asymmetries due to the equilibrium metric, thereby making interpretation harder. Therefore the density $n_{Z0}$ is determined by a 1-D diffusion code assuming circular and concentric flux surfaces. The density obtained by this means, constant on flux surfaces, is plugged into XTOR-2F and once again the source is determined from *Eq.* (7.5).

We now present a benchmark of the impurity model. To check the model, we simulate an impurity which has the same initial profile, mass and charge numbers, and transport coefficients as the plasma density. Thus the density equations are the same, and the only difference is the expression for the parallel velocity because of the viscosity term. Indeed recall the plasma density and momentum equations:

$$\partial_t \rho + \boldsymbol{v} \cdot \nabla \rho + \rho \left[ \nabla \cdot \boldsymbol{v} + \frac{\nabla p_i}{\rho e} \cdot \nabla \times \frac{\mathbf{B}}{B^2} \right] = \nabla \cdot D_\perp \nabla \left( \rho - \rho_0 \right) \tag{7.10}$$

$$\rho \left( \partial_t \boldsymbol{v} + \boldsymbol{v} \cdot \nabla \boldsymbol{v} + \boldsymbol{v}_i^\star \cdot \nabla \boldsymbol{v}_\perp \right) = \mathbf{J} \times \mathbf{B} - \nabla p + \nabla \nu \nabla \left( \boldsymbol{v} + \boldsymbol{v}_i^\star \right), \tag{7.11}$$

with $\boldsymbol{v} = \boldsymbol{v}_\perp + v_\parallel \mathbf{b}$ and $\nabla \nu \nabla \boldsymbol{v} \equiv \nabla \left( \nu \nabla \cdot \boldsymbol{v} \right) - \nabla \times \left( \nu \nabla \times \boldsymbol{v} \right)$.

The density profile before the sawtooth crash is peaked because of the pinch velocity (not used in the following impurity study) and is the same as in chapter 6. The results of the simulation are presented in Fig. 7.3, where the flux surface average of the density obtained with *Eq.* (7.10) and with *Eqs.* (7.7 – 7.8) are compared. The density profiles agree within 1%, and the density perturbations with respect to the precrash state agree within 30%. It can be verified that the non-linear evolution of the full profiles are virtually identical. The small difference that remains must come from the different implementation of the viscosity in both cases, whereby the parallel velocity sheets generated during the nonlinear evolution of the sawtooth crash are slightly different.

This benchmarking has an other merit in that it helps to highlight the physics involved in the generation of the post-crash crescent-shaped structure detailed in the preceding chapter. Fig. 7.4 shows a comparison between the post-crash poloidal profiles of two simulations, one (a) in which *Eqs.* (7.7 – 7.8) are used, and one (b) in which pure advection is simulated, that is, the density verifies the following equation:

$$\partial_t n_Z + \boldsymbol{v} \cdot \nabla n_Z = \nabla \cdot \left( D_Z \nabla (n_Z - n_{Z0}) \right), \tag{7.12}$$

where $\boldsymbol{v} = \boldsymbol{v}_\perp + v_\parallel \mathbf{b}$ is the plasma velocity. The first simulation clearly exhibits a crescent-shaped structure well inside the $q = 1$ surface, while the second one does not display any crescent structure, showing that the physics of compressibilty and in particular parallel

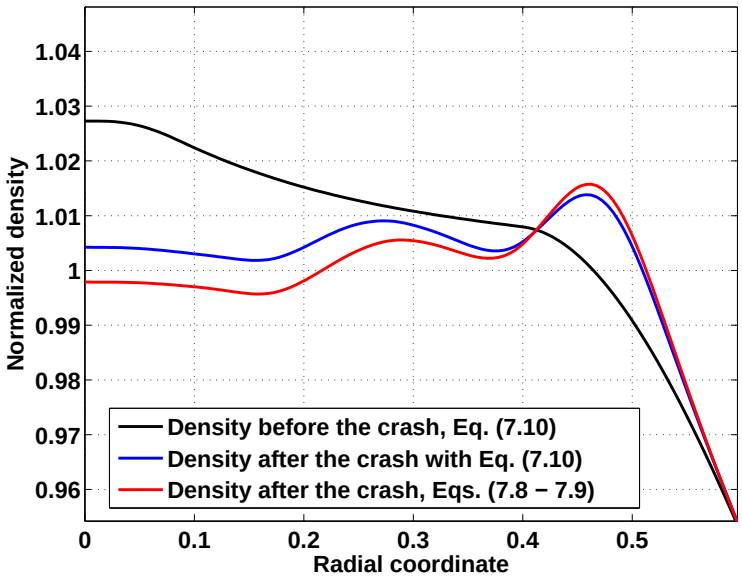


Figure 7.3: Comparison of the flux surface average of the density towards the end of the reconnection phase, obtained with *Eq.* (7.10) (blue) and with *Eqs.* (7.7 – 7.8) (red). The pre-crash density profile is shown as the black curve.

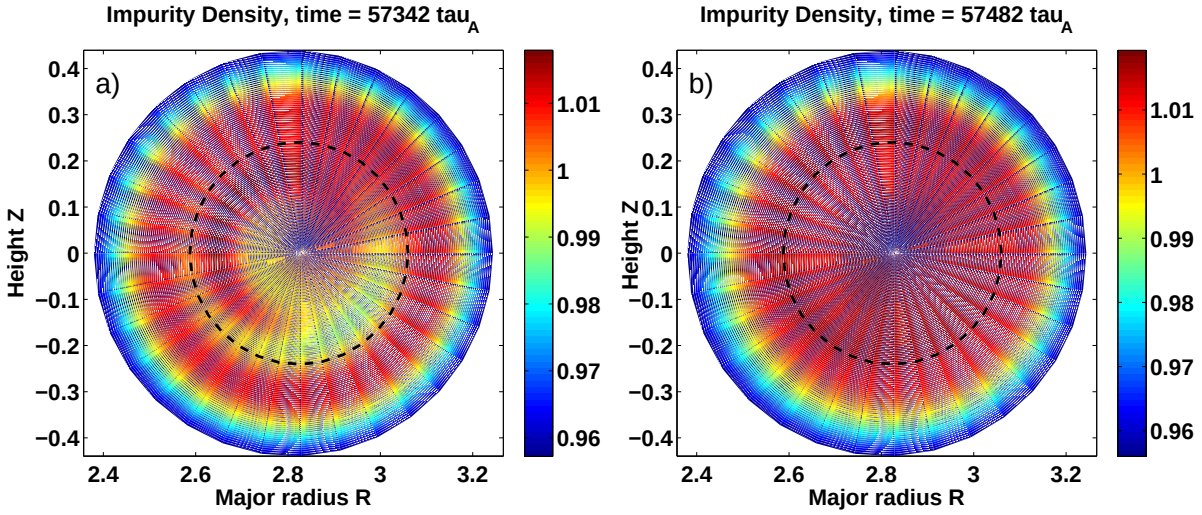


Figure 7.4: Comparison between two simulations of electron density using the impurity model, one with a separate impurity parallel velocity equation (a), and one with pure advection (b).

compressibility is crucial to obtain this structure. In the following impurity study, we will keep in mind that the crescent-shaped structure of Fig. 7.4 a) raises the question of the particle redistribution and seems to indicate that a significant part of the core density is reinjected inside the $q = 1$ surface. On the electron density this is not a concern since

it represents a very small amount of the total density. The concern is that with more peaked profiles, like He for instance, which is produced in the core, the effect could be enhanced and lead to a higher He concentration on average.

## 7.3 Results

### 7.3.1 Case 1 (Peaked Impurity)

We now proceed with the analysis of case 1. To assess the quantity of impurity that leaves the $q = 1$ surface, we compute the quantity $N_{Z1}(t)$ defined by the folowing integral,

$$N_{Z1}(t) = \int_{\mathcal{V}_{q=1}} (n_Z(\mathbf{r}, t) - n_Z(r = r_s, 0))\, \mathrm{d}^3\mathbf{r}, \tag{7.13}$$

where $\mathcal{V}_{q=1}$ is the volume bounded by the magnetic axis and the flux surface located at $r = r_s$, the radius of the initial $q = 1$ surface. We express it in percentage of the initial value, $N_{Z1\%}(t) = 100 N_{Z1}(t)/N_{Z1}(0)$, where $t = 0$ refers to the beginning of the pressure drop corresponding to the shift of the core due to the internal kink mode. Fig. 7.5 shows the evolution of the quantity $N_{Z1\%}$ during a sawtooth crash. The reference time is the time at which the curve starts to decrease.

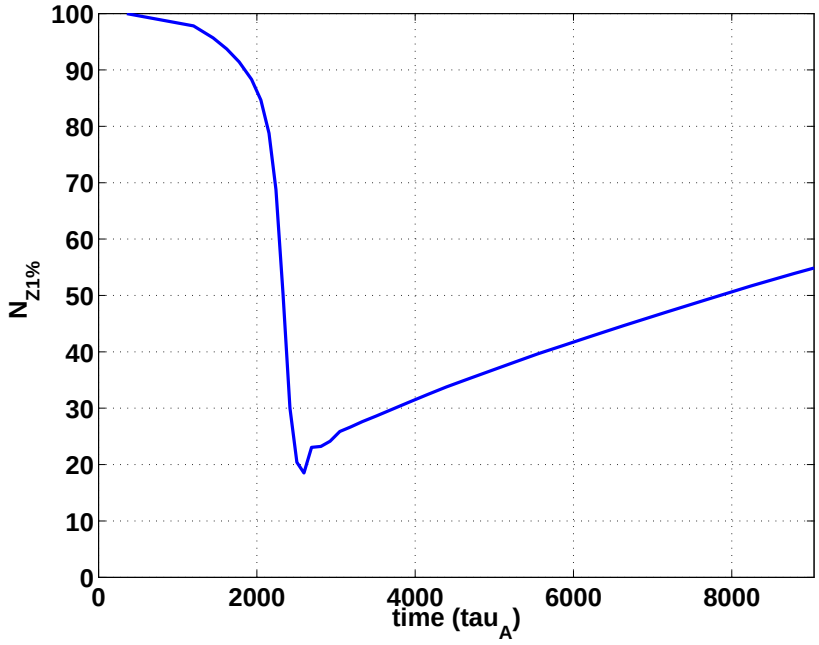


Figure 7.5: Evolution of $N_{Z1\%}$ during a sawtooth crash for case 1.

It is seen that the curve goes to a minimum of around 20% at the end of the reconnection phase. There is a small fast rise of approximately 5% before diffusive evolution (diffusion and source) takes over to rebuild the profile until the next sawtooth crash. The 5% rise at the end of the reconnection phase is due to the small remaining flows necessary

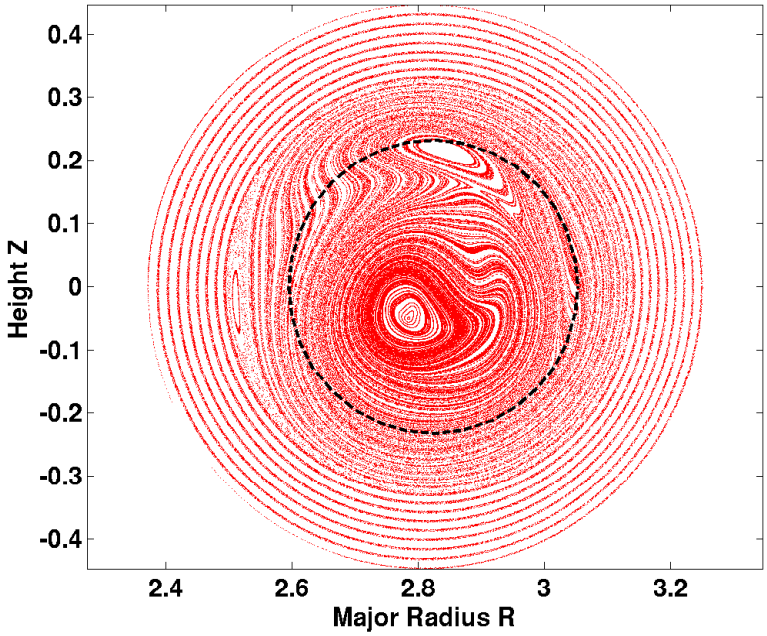


Figure 7.6: Poincaré plot at the end of the reconnection phase. The small remainder of the reconnecting core can be observed at the left of the figure, well beyond the initial $q = 1$ surface location (dashed circle), at a location corresponding to the mixing radius.

to restore the initial topology of the flux surfaces. Indeed, on Fig. 7.6, a Poincaré plot of the magnetic surfaces taken at the time of the rise, it can be seen that when the core has been completely reconnected, the new core has not stabilized yet. Following the principle that when ideal MHD is valid (which should be the case in the newly formed core) the frozen-in-law is valid, a displacement of the magnetic surfaces also implies a displacement of the plasma, and some reorganization of the density occurs at this time.

Nevertheless, we can see that the amount of particles inside the $q = 1$ surface after the crash is small, globally the sawtooth efficiently flushed the impurities away from the core. Fig. 7.7 shows some flux surface averaged profiles during the reconnection phase. The reference time is the same as on Fig. 7.5. The formation of a "hump" at a location close to the mixing radius (see section 7.4) is clearly visible. This happens because the density is mainly advected by the flows, which are dominantly located at the reconnection separatrix. This separatrix moves from the initial $q = 1$ surface until the mixing radius at the end of the reconnection phase, and the density follows.

No post-crash crescent-shaped structure can be observed in this case, as seen on Fig. 7.8. It does not seem to be due to some physics missing in the model since the same model obtains crescent with the profiles of Fig. 7.3. So it seems to indicate that the crescent structure is dependent on the details of the pre-crash profiles.

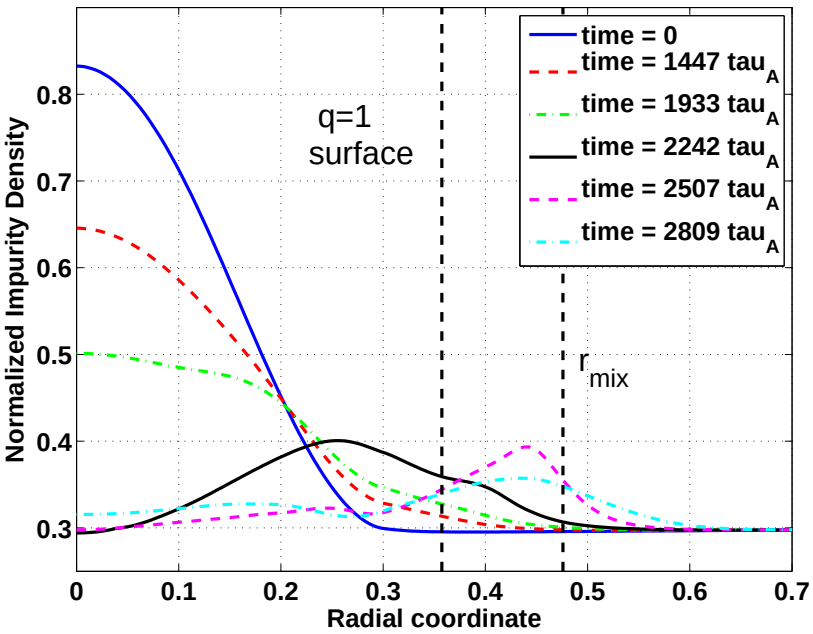


Figure 7.7: Flux surface averaged impurity density profiles before, during and after the sawtooth crash for Case 1. The initial $q = 1$ surface and mixing radius are represented by the vertical dashed lines.

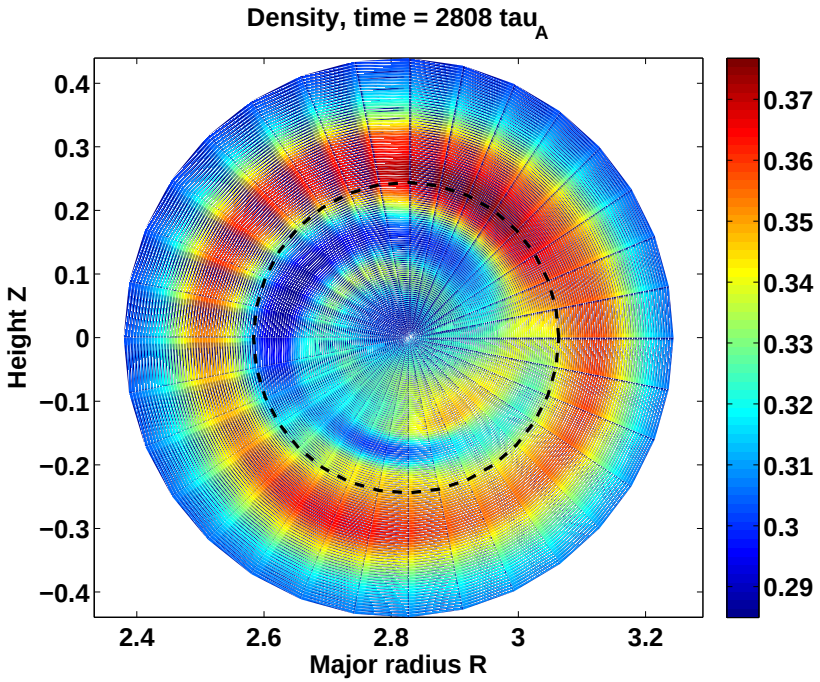


Figure 7.8: Post-crash poloidal density profile obtained in Case 1. The dashed circle is the position of the pre-crash $q = 1$ surface. There is no trace of a crescent-shaped structure.

### 7.3.2 Case 2 (W-like)

We now come to case 2. Following the methodology of case 1, we compute a quantity $N_{Z2\%}(t)$, where now it is defined by

$$N_{Z2\%}(t) = \frac{100}{A}\int_{\mathcal{V}_{core}} (n_Z(\mathbf{r},t) - N_0)\mathrm{d}^3\mathbf{r}, \tag{7.14}$$

where now $\mathcal{V}_{core}$ is bounded by the magnetic axis and the radius where the equilibrium density starts to increase, $s = 0.3$ ($s = \sqrt{\psi/\psi_a}$). $N_0 = 1$ is the offset value, and $A$ is a normalization constant, such that $A = \int_{\mathcal{V}_{core}} 1\mathrm{d}^3\mathbf{r}$, so that $N_{Z2\%} = 100\%$ when the core impurity density is equal to the external density everywhere. The results are presented on Fig. 7.9. The same kind of behaviour can be observed as in case 1, but inverted. Now the crash leads to a penetration of impurities, indeed the flows connect the external region to the internal region. At the beginning, the penetration is very important, and we observe a spiky behaviour, similar to case 1 but much more pronounced. $N_{Z2\%}$ reaches 50% transiently, then falls rapidly to 30%, and finally decreases diffusively until the following crash. The relevant profile to look at is the profile at the end of the spike phase, the magenta profile on Fig. 7.9 b), with an impurity density approximately flat and equal to 1.3 in the core, compared to 1 initially and 2 in the external region. Thus our simulations indicate that the sawtooth crash efficiently leads to the penetration of impurities up to the magnetic axis. This has been experimentally observed during impurity injection experiments on the JET [Wesson 1997] and ASDEX Upgrade [Dux 1999] tokamaks. This is quite preoccupying because this means that when W is generated at the walls and enters the plasma, if it has an inward pinch velocity and reaches the $q = 1$ surface, it will be rapidly, in a reconnection time, driven to the very core of the tokamak. This can lead to a radiative collapse because the core of a burning fusion plasma is much hotter than the $q = 1$ surface, and a given W concentration can be tolerable at the $q = 1$ surface but intolerable in the hot core.

We now discuss the influence of the parameters $Z$ and $A$ which characterize the impurity species. The charge $Z$ is taken into account in our model in order to model properly the diamagnetic velocity of the impurity, implying the resolution of an additional parallel velocity equation. Obviously, the parameter $A$, which represents the inertia of the impurities, affects the dynamics of the impurity parallel velocity. During the sawtooth crash, when parallel gradients significantly depart from zero, the two first terms on the r.h.s. of *Eq.* (7.8) will lead to parallel acceleration. The first scales as $1/A$ and thus will be small for heavy impurities. The second one scales as $Z/A$ and can remain large even for heavy impurities, providing the plasma is hot enough for the impurity to be fully stripped. Nonetheless, we see that the basic physics is not modified when varying $A$ and $Z$. The only difference will be the relative amplitude of the parallel velocity sheets generated in the vicinity of the $q = 1$ surface, but the dominant effect on the particles during the crash remains the advection by the perpendicular flows (*cf.* chapter 6), so that we do not expect a significant difference on the results for the density. Notice that for this study, we dropped the inertia terms $(\boldsymbol{v}_Z \cdot \nabla \boldsymbol{v}_Z + \boldsymbol{v}_Z^\star \cdot \nabla \boldsymbol{v}_\perp)_\parallel$. It was not expected to play any significant role for the comparison at different values of $A$ and $Z$ and we could check at moderate $A$ and $Z$ that indeed it does not modify the results.

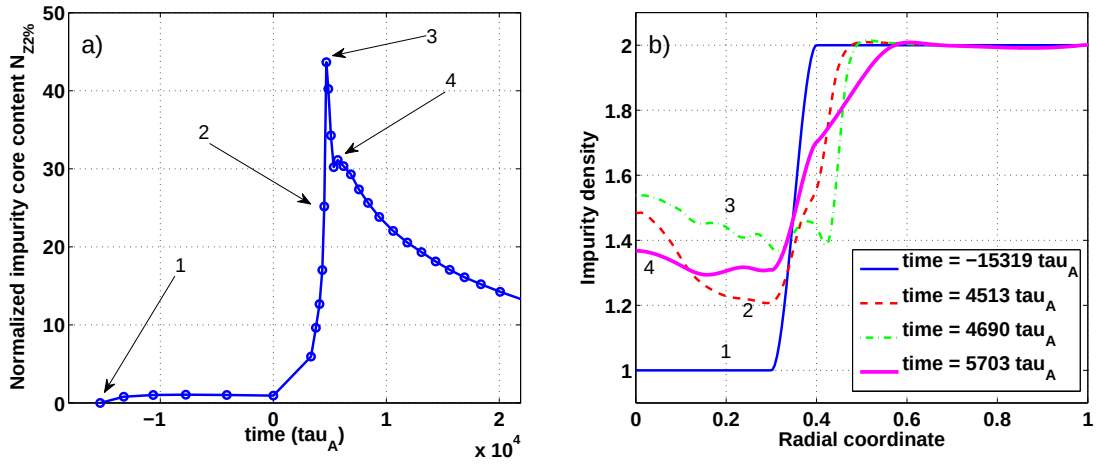


Figure 7.9: Evolution of $N_{Z2\%}$ during a sawtooth crash (a) and impurity core density profiles (b) for Case 2. The numbers on the profiles correspond to the numbers indicating the times on panel (a).

For the benchmark, we have used 4 couples $(A, Z)$. First the value used throughout this chapter, $(A, Z) = (2, 1)$, which is the deuterium value. Then multiplying both by ten, and again by two, the values $(20, 10)$ and $(40, 20)$ are used, keeping the ratio $A/Z = 2$. Finally, a value which is relevant to W has been used, $(A, Z) = (184, 40)$. The mass number of W is 183.84 and $Z = 40$ is a typical order of magnitude for W at temperatures of a few keV (see figure 6 of Ref. [Pütterich 2008]). The results are presented on Fig. 7.10. It is seen that there are virtually no quantitative differences between the four cases, as expected. This shows that the mass and charge numbers of the impurities have very little influence on their dynamics during the crash. This is of course, however, not true at all during the quiescent MHD free evolution of the plasma, where strong dependence of the neoclassical and turbulent transport coefficients are found theoretically and numerically, and observed experimentally [Wenzel 1990, Angioni 2006, Barnes 2012].

### 7.3.3 Case 3 (He-like)

We now present the results for case 3. Recall that this corresponds to a He source from fusion reactions. The reader should keep in mind that what matters is the long term average He density profile in the core. If it is too large and there is no efficient way to extract the Helium ash after it has delivered its heat to the plasma, it may choke the fusion reactions by diluting the D-T mix. For instance, for a 500 MW machine like ITER, a sawtooth period $\tau_{ST}$ larger than 10 s, as predicted by Ref. [Porcelli 1996], leads to a He buildup comparable to the density of the mixture, which starts reducing the fusion power. Indeed, considering that $\langle \sigma v \rangle (T_i) > 10^{-21}$ m$^3$.s$^{-1}$ for $T_i > 10$ keV[Huba 2007], and with Deuterium and Tritium densities $n_D \sim n_T \sim 10^{20}$ m$^{-3}$, the ratio $\mathcal{R}$ between the He density resulting from the fusion reactions between two sawtooth crashes (assuming

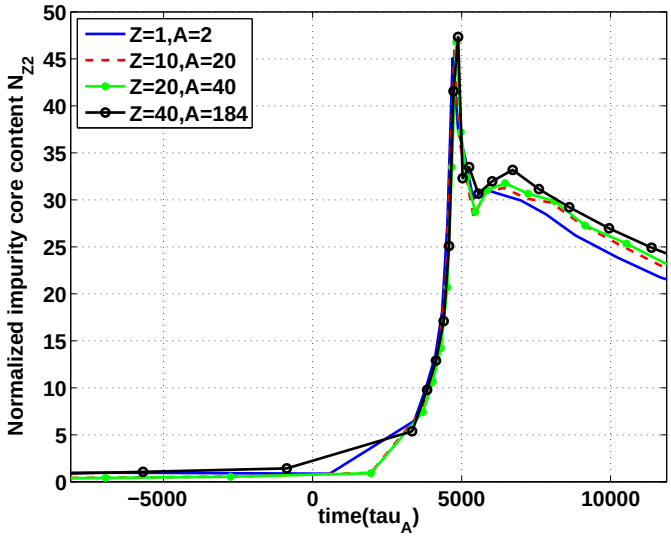


Figure 7.10: Comparison between different values of $A$ and $Z$ for a hollow profile.

no transport) and the Deuterium density, $\mathcal{R} = n_D n_T \langle\sigma v\rangle \tau_{ST}/n_D = n_T \langle\sigma v\rangle \tau_{ST}$, can easily reach unity, which leads to a decrease of the D-T mixture density unless the $\alpha$ particles are adequately evacuated and D-T efficiently replaced in the core. Thus, if the sawtooth crash does not flush the core efficiently enough, the impurity content can be increased, leading to dilution for the case of He ash, and possibly to radiative collapse in the case of W.

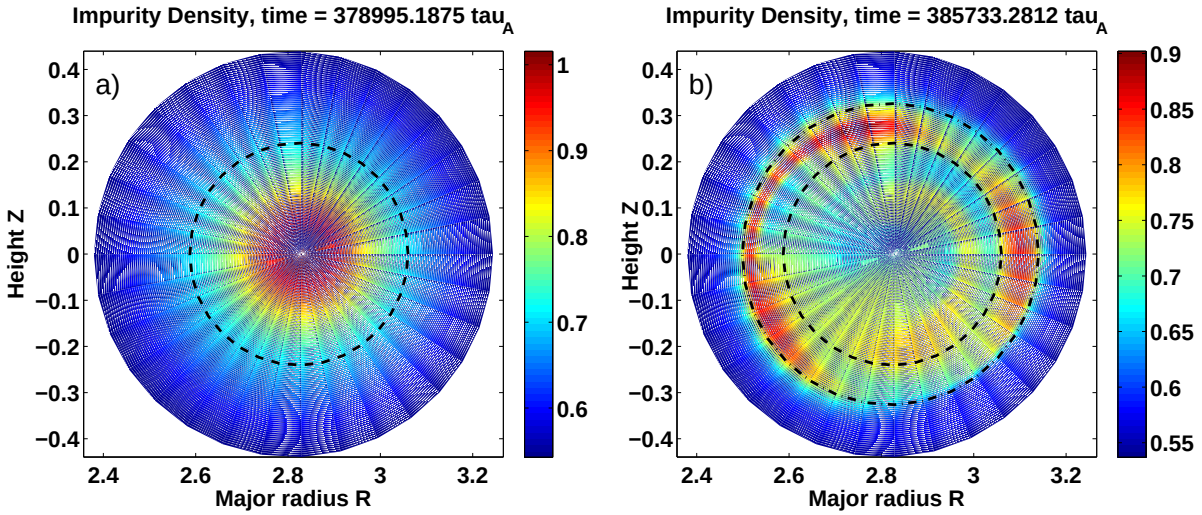


Figure 7.11: Surface plots of the pre-crash (a) and post-crash (b) 2D density profiles in the poloidal plane for Case 3 (He-like). The dashed circle represents the initial $q = 1$ surface and the dot-dashed circle on panel (b) represents the position of the mixing radius.

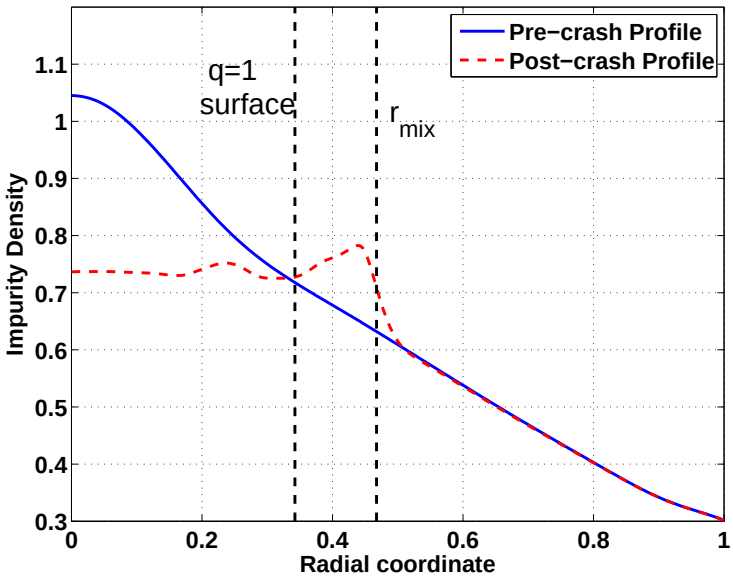


Figure 7.12: Flux surface averaged profiles corresponding to Fig. 7.11.

Obviously, the average impurity content of the core will be highly dependent on the sawtooth period $\tau_{ST}$, or more precisely to the ratio between $\tau_{ST}$ to the diffusive time $a^2/D_{Z\perp}$. $\tau_{ST}$ is fixed by our equilibrium and our choice of $S$ and $\alpha$, and $D_{Z\perp}$ can be quite easily modified. However an extensive numerical study would have required an excessive amount of computational time, hence we did only two simulations, one with the diffusion of Fig. 7.2, one with the same profile scaled up by a factor of three. We will focus on the first case, with the profile of Fig. 7.2, and it will be seen that the other case confirms the results. Even though we will compute an average density over a sawtooth cycle after reaching stationarity, we will not discuss in detail this mere result directly, but rather we will focus on the comparison with the 1-D model derived from Kadomtsev's rules in section 7.4.

Fig. 7.11 shows the pre-crash and post-crash 2D poloidal He profiles for case 3. The corresponding flux surface averaged profiles are represented on Fig. 7.12. It is seen how the density has been dominantly remapped on a ring located outside the $q = 1$ surface. This location corresponds to the mixing radius. Hence the phenomenology is the same as in case 1. This time, we see a crescent-shaped structure, its amplitude is about 3% of the impurity density. It is much smaller than the external ring, which has an amplitude of about 8%. Compared to the total impurity content inside the $q = 1$ surface (in excess of the density at $q = 1$, see *Eq.* (7.13)), the amount of particles contained in the small crescent is slightly less than 10%. Thus it seems rather unimportant and not a source of concern regarding the impurity flushing during the sawtooth crash. We do not develop further the analysis, which is mainly done in the next section, together with the comparison to the Kadomtsev model.

## 7.4 Comparison with Kadomtsev model

It is instructive to compare the post-crash profiles produced by XTOR-2F with those predicted by Kadomtsev model because the latter model is often used to model the sawteeth. Thus its validity must be assessed. Notice that here, when we refer to the Kadomtsev model, we refer only to the basic geometrical and flux conservation constraints of the model, and not to the predicted resistive time scale, which has been shown to be too slow. This approach makes sense since here only the post-crash profile matters, not the time it took to get there. Refer to section 4.1 for details on the Kadomtsev model. Also, notice that chapter 6 suggests that the model should fail in predicting the post-crash profiles. Indeed, first the density redistribution mechanism underlying the Kadomtsev model, fast parallel transport along field lines, has been shown to be different from the actual redistribution mechanism in XTOR-2F, which involves the fast perpendicular flows at the reconnection layer. Second, the post crash crescent-shaped structure obtained seems incompatible with Kadomstev's redistribution, which in general predicts monotonic post-crash profiles, from the core to the mixing radius (see Fig. 6.18). However we will see that Kadomtsev model is quantitatively in good agreement with XTOR-2F simulations in the He-like case, and we will give a reason for that.

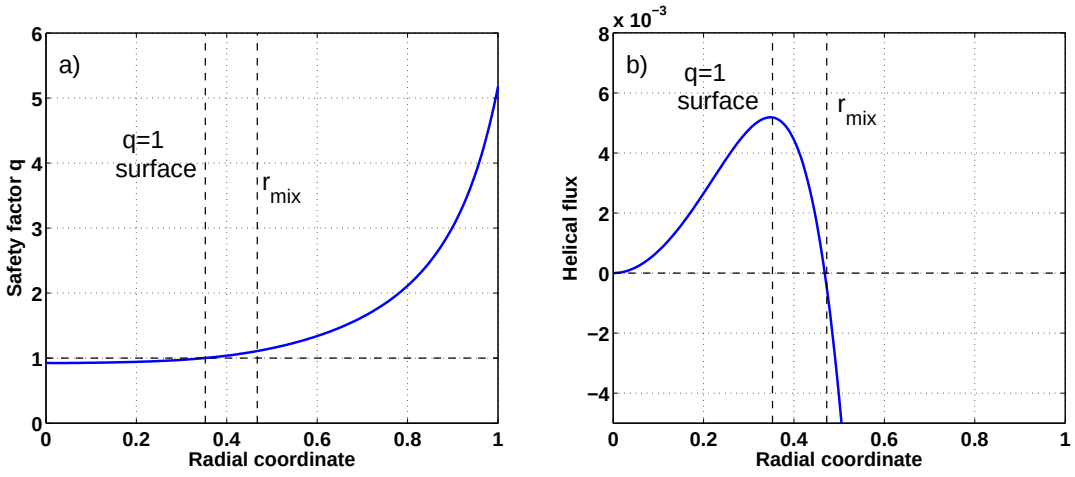


Figure 7.13: Pre-crash safety factor profile (a) and corresponding helical flux (b) in the XTOR-2F simulations. The central value of the safety factor is $q_0 = 0.93$.

To compare the redistribution model with the results of XTOR-2F, we used the code in an MHD stable situation with exactly the same source and diffusion for the impurity, and we applied the profile redistribution described above every time there is a sawtooth crash. To obtain a stable MHD equilibrium, we raised the $q$ profile above unity in the core. This modifies the equilibrium however the operation is done without modifying the metrics, so that in both cases the source computed from $-\nabla \cdot D_Z \nabla n_{Z0}$ is identical and the comparison meaningful. The safety factor profile used in the redistribution model is the profile taken from the full XTOR-2F simulation, just before the sawtooth crash is

triggered.

Fig. 7.14 shows the initial and post-crash profiles corresponding to case 3, obtained with this model (black) and with the full non-linear bifluid MHD code (red) after a typical crash. In contrast with chapter 6, the profiles are quite similar. They both present a

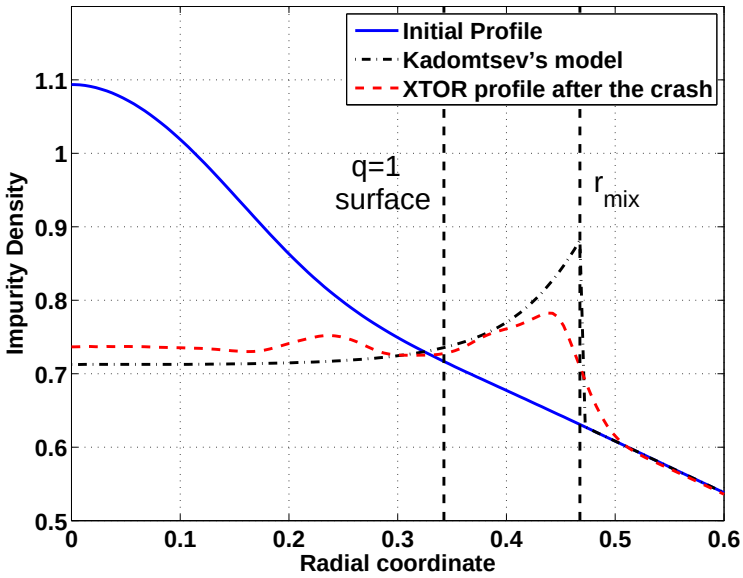


Figure 7.14: Initial (blue) and post-crash (green dash-dot) profile for the peaked He profile of section 7.3, case 3. The red dashed curve shows the post-crash profile given by XTOR-2F.

hump close to $r_{mix}$ and the core values are similar. In the case of the Kadomtsev model, it is even a spike with a sharp discontinuity at $r_{mix}$. This discontinuity is rapidly smoothed away by the subsequent diffusive evolution. The origin of this spike is that the toroidal flux (or volume) increments on both sides of the separatrix tend to have very similar values, hence the final density is merely the mean of the density in $r_l(\Psi^\star)$ and $r_r(\Psi^\star)$. The final density on the new magnetic axis is equal to $n_i(r_s)$ while the density at $r_{mix}$ is the mean between the initial density on the magnetic axis and the initial density at $r_{mix}$. Since $r_{mix}$ is close to $r_s$, we obtain that the final density at the mixing radius is of the order of $(n_i(r_s) + n_i(0))/2 > n_i(r_s)$.

The XTOR-2F profile has also a sharp transition to the external unaffected profile centered around $r_{mix}$. It is striking that the model derived from mere transport along the field lines agrees well with the XTOR-2F results, despite completely different mechanisms. In the XTOR-2F case, the density transport is due to advection by the kink and reconnection flows, which overall have a double convection cell structure. Since kinetic energy is located dominantly behind the reconnection site, that is, on the separatrix, density accumulates there and leads to the formation of the observed hump. At the end of the reconnection, the separatrix is at $r_{mix}$, hence the observed agreement between the 1-D model and XTOR-2F results in Fig. 7.14.

Fig. 7.15 shows the central density for both models. It is seen that the bottom value

after the crash is well predicted by the Kadomtsev model. This is the value of the density at the initial $q = 1$ surface. The top value is higher in the Kadomtsev model case. This is because the crash is instantaneous in the model, whereas it actually takes a few thousands $\tau_A$ for the flux to reconnect in XTOR-2F. Thus when the core is initially displaced by the kink, the core value starts to drop, while in the 1-D model it continues to rise diffusively until the crash is triggered. Overall the profiles are very close in the evolution, which is not surprising since in between crashes, the evolution is dominated by diffusion, which is identical in both cases. A last comparison is obtained by plotting the time-averaged

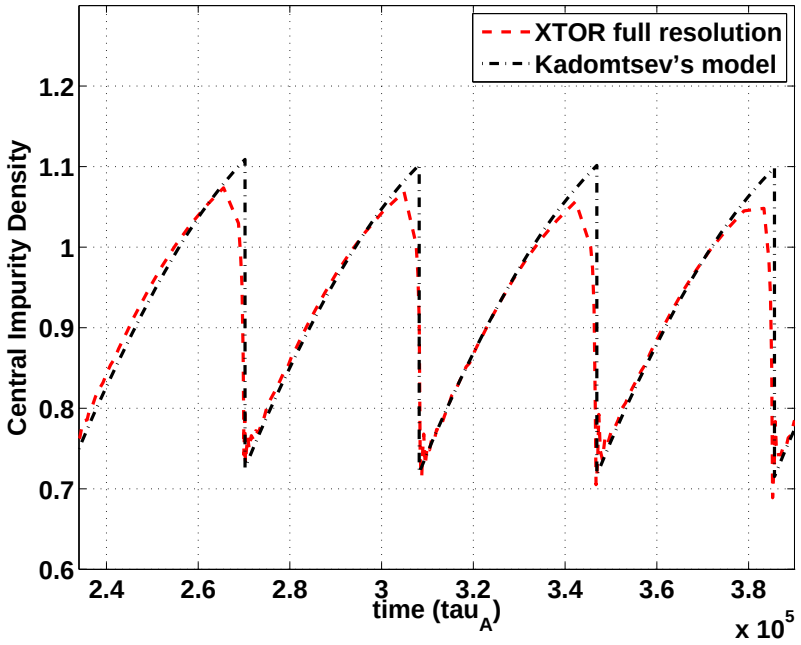


Figure 7.15: Central impurity density in the XTOR-2F case (red) and computed with Kadomtsev model (green).

profile over a sawtooth cycle. The result is shown on Fig. 7.16 a), where the agreement is observed once again. Fig. 7.16 b) shows the same analysis for the case with the increased diffusion coefficient, which clearly confirms the results. As expected, the central value in the Kadomtsev model case is slightly higher because the crash is instantaneous and thus triggered a bit later. However the overall agreement is good, within 2%. The profile at the maximum of the ramp is also plotted in blue.

It is also interesting to perform the comparison on the hollow profile. The results can be seen on Fig. 7.17. The redistributed profile is very similar to the XTOR-2F profile obtained at the top of the spike on Fig. 7.9 a), as shown with the red profile. However it has been mentioned that the remaining flows at the end of the reconnection phase reduce the value of the impurity content obtained at the top of the spike down to a smaller value. The relevant profile is the magenta profile of Fig. 7.9 (number 4), reported on Fig. 7.9 as well. Thus the Kadomtsev model slightly overestimates the impurity penetration.

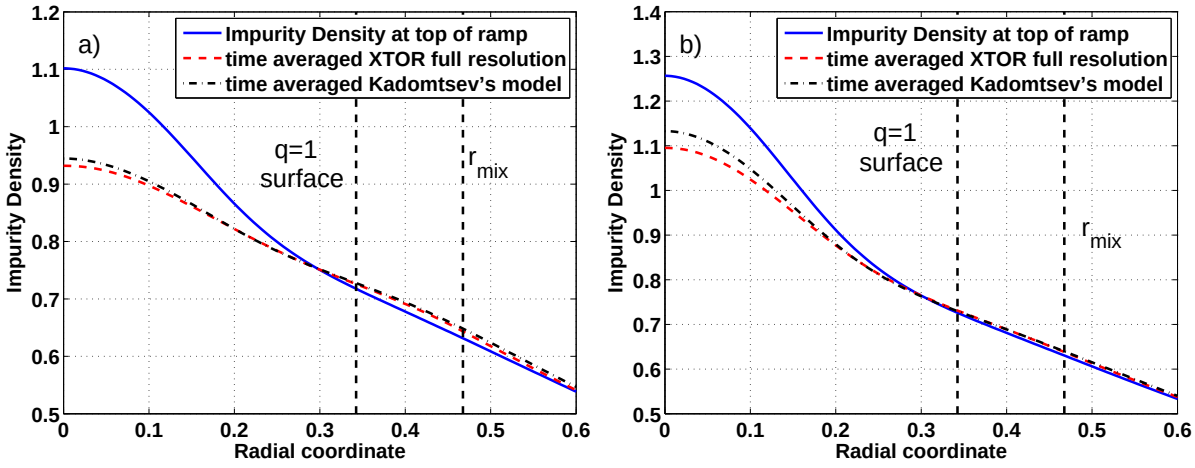


Figure 7.16: Time-averaged density for the XTOR-2F case (red) and Kadomtsev model case (green). In blue, the impurity density at the maximum of a sawtooth ramp is plotted (a). Same figure in (b) for a diffusion coefficient scaled up by a factor of three.

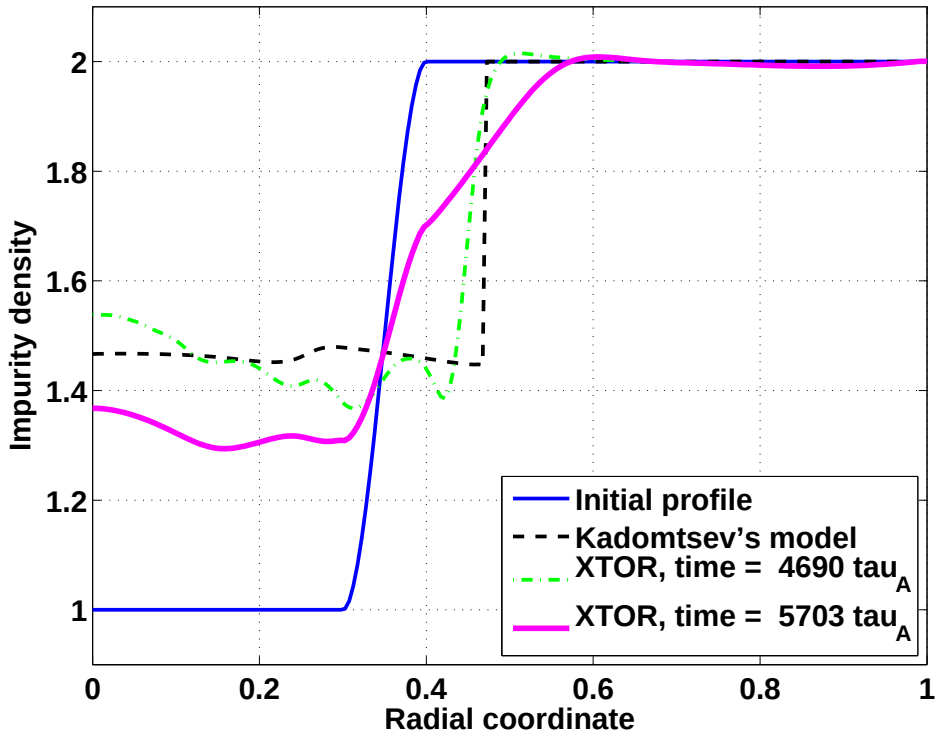


Figure 7.17: Comparison between XTOR-2F and Kadomtsev model for the hollow case (case 2).

## 7.5 Discussion

Going back to the motivation in section 7.1, it appears that the detail of the pre-crash peaking matters for the formation of the crescent-shaped structure, which is the result of a complex interaction between the initial gradients, the advecting flows and the compressibility. When they are visible, their amplitude is small and they should finally not be considered as a source of concern regarding the sawtooth flushing mechanism. Notice that contrary to the electron density results, these results cannot be easily compared to the experiment, because impurity density measurements are not available yet with sufficient precision. Only density estimates and rough structures can be inferred from soft X-ray tomography and spectroscopic measurements coupled to temperature and electron density measurements [Asmussen 1998, Pütterich 2008, Pütterich 2010, Vezinet 2013].

The main *caveat* of this study is the full reconnection observed in XTOR-2F. Indeed most experimental evidence point to the relevance of incomplete reconnection in most cases. Up to now, no self-consistent MHD model has been able to simulate sawteeth with incomplete reconnection. Hence we chose to use full reconnection also with Kadomtsev model. This constraint could be easily released, and the reader can refer to Ref. [Furno 2001] for an interesting example. However the agreement between such models and full MHD models like XTOR-2F cannot be guaranteed in the case of incomplete reconnection. It would be ideal to possess an MHD code able to simulate incomplete reconnection together with self-consistent sawteeth, but this is currently not available.

The agreement between XTOR-2F and Kadomtsev model seems unexpected because of the inherently different redistribution mechanisms discussed in the preceding chapter, however as mentioned above, in the case of a quite peaked profile like the He-like case studied here, we expect both models to yield similar core values after the crash ($n_{Z0}(r_s)$), and to display a hump around $r_{mix}$, in the one case because of pure volume element matters, in the XTOR-2F case because the flow is most important on the separatrix, which ends on $r_{mix}$ at the end of the reconnection phase.

To make things as clear as possible, we could say the following: after seeing the crescent-shaped structure on the electron density case, where it represents a very small fraction of the total density but a significant fraction of the central density peak, we were concerned that it could become an important part of the total density in more peaked cases. In this chapter, we have studied this possibility on peaked impurity profiles, and we conclude that the post-crash structures remain small (in other words they are not proportional to the amplitude of the pre-crash density peak in the core). As a result, the profiles obtained with XTOR-2F and the one predicted by the Kadomtsev model look very similar. The quantitative difference between the two can be seen only when the perturbations are very small (as was the case in chapter 6, *cf.* Fig. 6.18). We have also studied the case of hollow impurity profiles and we find that in this case, the Kadomtsev model slightly overestimates the penetration.

We have not focused a lot on the mere values obtained in these simulations, because, as mentioned above, they depend on the ratio between diffusive time and sawtooth period. In our simulations, this ratio assumes quite frequent sawteeth, more or less in the range of Tore Supra ohmic sawteeth with periods of the order of 30 ms. We have taken

$D_Z \tau_{ST}/a^2 \sim 4 \times 10^{-3}$, which is consistent with a core particle diffusivity of $5 \times 10^{-2}$ $m^2.s^{-1}$ (measured value for electrons in the core [Guirlet 2010]), a sawtooth period of 30 ms and a plasma radius $a = 0.7$ m. In reactors, the sawtooth period is expected to be much longer, of the order of several seconds, or tens of seconds [Porcelli 1996], reducing by much the usefulness of sawteeth as a means to expel impurities or He ash from the core of the tokamak. This could however be changed if sawtooth control is used on ITER, following the strategy presented in Refs. [Graves 2012, Chapman 2011] for example (see section 2.2.7).

We would also like to point out that the Kadomtsev model is of use only if a convincing triggering threshold is known for the sawtooth crash. There have been several attempts to derive a criterion for sawtooth triggering, or, equivalently, a prediction for the sawtooth period, but this is still an actively discussed subject, see for instance Ref. [Zocco 2013]. At the least, if one wants to simulate the sawtooth induced transport for a real experimental discharge, it is possible to take the experimentally measured sawtooth period.

Considering that the agreement between our nonlinear electron density MHD simulations and the experiment presented in chapter 6 was only qualitative, there may still be some physics missing in XTOR-2F to explain the crescent-shaped structure. Regarding this point, we come back to the model of Biskamp discussed in section 5.2.7. Recall that is was proposed [Kolesnichenko 1992, Biskamp 1994] that the sawtooth crash could happen in two phases: the first, Kadomtsev-like, relaxes the $q$ profile to 1, and the second, due to the remaining kinetic energy accumulated in the core due to the reconnection jets, reconnects the helical flux in a Wesson-like [Wesson 1986] process, leading to $q < 1$. The mechanism invoked and numerically demonstrated in Ref. [Biskamp 1994] is the electron inertia combined with hyperresistivity and flow damping. This Wesson mechanism clearly involves reinjection in the core of a part of the primarily reconnected flux. While it should not affect the temperature, which is usually flattened by Kadomtsev reconnection, this may indeed be a mechanism able to reinject particles from the external denser ring observed on the impurity density (notice that Kadomtsev reconnection flattening the profiles or not depends only on the detail of the pre-crash profile). Electron inertia is not present in the code and we do not observe any Wesson-like second phase. However the observation of the spike on Fig. 7.9 a), which implies a modification of the core particle content after the end of the reconnection phase, was attributed to the flows remaining after the crash. There may be a link with the physics described in this paragraph. The introduction of electron inertia in full MHD sawtooth crash simulations would be very instructive in this regard.

## 7.6 Summary

We can summarize the results of this chapter in four main points:

- The crescent-shaped structures can be observed on the post-crash profiles for some impurity density profiles, although they do not seem to be a universal feature of the post-crash profiles simulated by XTOR-2F's MHD model. In any case, their

amplitude is small and should not be regarded as a source of concern for impurity redistribution by the sawtooth crash.

- Peaked profiles tend to produce large humps at the location of $r_{mix}$, because the separatrix where the flows are located moves from the $q = 1$ surface up to $r_{mix}$. The flow drives the dense core toward the separatrix and maps it to an external ring which ends up close to $r_{mix}$.

- In the case of hollow profiles, there is a significant penetration of the impurities up to the magnetic axis. This has been experimentally seen on the JET tokamak and may be a serious issue for Tungsten operation.

- A 1-D model based on Kadomtsev's principles is seen to reproduce the XTOR-2F results with a very good quantitative agreement in the case of peaked profiles. However, the agreement is less good in the hollow case, and the impurity penetration is slightly overestimated in this case. More simulations will be required to determine if this discrepancy is systematic, and where it comes from. Nonetheless, the model gives the good order of magnitude for the impurity penetration.

- The 1-D model could be easily improved to treat incomplete reconnection, but such a model would lack both experimental and numerical confirmation in the absence of reliable impurity density measurements and MHD codes able to simulate incomplete sawtooth crashes.

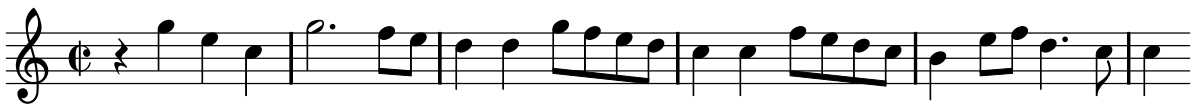

*Chœur des triomphants*
*(David et Jonathas)*
**Marc-Antoine Charpentier**

# Chapter 8
# Conclusion

The realization of sustained electricity production by Deuterium-Tritium is one of the most ambitious scientific and technological challenge ever faced by mankind. In the introduction, we have tried to explain why. There are several still unresolved issues that will have to be addressed and solved in the following decades in order for the project to become a success. Among these issues, particle transport is crucial and different apparently contradictory constraints must be met:

- The transport of electrons must be minimized in order to improve the confinement.
- The transport of fusion born $\alpha$ particles must be maximized in the core to avoid plasma dilution.
- The transport of heavy impurities like W must be maximized in the core and minimized in the edge to avoid large radiative cooling. This point is particularly important since the most widely accepted divertor design involves W plasma facing components.

On long time scales, of the order of the confinement time $\sim 1$ s, the transport is dominated by turbulence and neoclassical physics, which determine the diffusion coefficient and the radial pinch velocity of the different species in the plasma[1]. However transient MHD events crucially affect the radial transport of all plasma quantities on much faster timescales, in the range $0.1 - 10$ ms. The sawtooth instability, which periodically redistributes the core temperature and density, is one of the most crucial of these MHD phenomena, because it is observed on all tokamaks and usually affects a very large part of the plasma. For instance in ITER, it could affect 50% of the minor radius. In this thesis, we tried to elucidate the interactions between the sawtooth instability and particle transport using tridimensional nonlinear MHD simulations with the XTOR-2F code.

The sawtooth instability is also a very interesting phenomenon from the purely physical point of view. Indeed, even if its stability and basic features have been reasonably well understood since soon after its discovery, most experimental and theoretical discoveries taking place in the late 70s, some central features still resist a convincing explanation, such as the fast time scale of the crash and the possibility of incomplete magnetic reconnection. In this thesis, we have also tried to adress these issues, aided, again, by the XTOR-2F code.

[1] Assuming that transport can be considered local.

Thus the objectives of this thesis were:

1. Improve the understanding of sawtooth induced particle transport
2. Test the predictive capabilities of the XTOR-2F code.

We have first presented, in chapter 2, the basic theoretical framework necessary to study the sawtooth instability: MHD and the refinements thereof. The stability of the internal kink mode, which is the fundamental instability at the origin of the sawtooth crash, was studied, in the ideal, resistive and bifluid cases. The corrections due to the toroidal geometry of a tokamak and to the existence of trapped and passing particles were also presented. The fundamental features of magnetic reconnection involved in the nonlinear evolution of the internal kink mode were also drawn. The fast redistribution of particles is made possible by this reconnection process.

The XTOR-2F code and its equilibrium code CHEASE, the indispensable numerical tools of this study, were presented in chapter 3. We emphasized the fact that sawtooth cycling can be obtained only in a certain domain of parameters, namely at low resistivity and large ion skin depth. In order to get a deeper insight in the nonlinear features of the internal kink mode evolution, we then presented, in chapter 4, a few models trying to predict an evolution equation for the magnetic island width. We described Kadomtsev's model, relevant to resistive evolution, and refined by Waelbroeck, as well as Wang's model, relevant to the situation where the crash is dominated by bifluid effects, quantified by the ion skin depth. We have compared these models with XTOR-2F results and found that XTOR-2F is in good agreement with Kadomtsev's model. In particular, the safety factor is always larger than 1 everywhere after the sawtooth crash. However, in the bifluid regime, a very significant acceleration of the sawtooth crash is observed, which is much larger than that predicted by Wang's model. This acceleration is probably part of the answer to the question of the fast crash observed in the experiments.

In chapter 5, we presented experimental observations of sawtooth crashes on Tore Supra and JET. Even if some of these observations are merely curiosities, others show how crucial the sawtooth instability can be in some cases. An example on JET where the confinement of the plasma is lost immediately after a sawtooth crash leads to the penetration of W in the core is particularly instructive. In this chapter, the observations of electron density using fast-sweeping reflectometry, which motivated this work, were also detailed. Indeed, these observations revealed that fine structures are always observed after the sawtooth crash on the electron density, indicating that the sawtooth flushing mechanism implied by Kadomtsev's model may not be as efficient as previously foreseen. This could be related to the observation of impurity accumulation in the experiments. The last two chapters detail the investigations of this issue, and constitute the most part of my personal contribution to the subject.

In chapter 6, we showed that the fine structures observed on the electron density are recovered by the bifluid MHD model of the XTOR-2F code. It was shown that the electron density dynamics is dominated by the fast flows which are generated at the reconnection layer, and not, as is the case for the temperature and as assumed in Kadomtsev's model, by fast transport along field lines. If the post-crash structures are large, it means that

the transport during the sawtooth crash is such that a significant part of the density is not expelled by the crash but reinjected inside the $q < 1$ region. This is good for electron confinement, but bad for impurity evacuation, which is a more restrictive constraint. Hence this preliminary work motivated investigations on the redistribution of impurities by the sawtooth crash.

Chapter 7 starts with justifying the new impurity module implemented in XTOR-2F. The impurities are passive but they have a separate equation for the evolution of their parallel velocity. Then different pre-crash impurity profiles are tested and the amount of redistribution caused by the crash is evaluated. For peaked profiles, structures similar to the ones observed on the electron density are obtained after the crash. However they remain very small even with very peaked profiles and should not be regarded as a source of concern. For hollow pre-crash profiles, the impurity penetration up to the magnetic axis is significant, as expected and observed in the experiments. Finally, these results of the fully 3D nonlinear code are compared with the redistribution obtained using Kadomtsev's model. A very good quantitative agreement is found for the peaked profiles, despite the fact that Kadomtsev's mechanism and the nonlinear evolution of impurity density in XTOR-2F are essentially very different. A probable reason for this unexpected agreement is given.

The general conclusion of this work is that the density evolution at the sawtooth crash obtained with the nonlinear MHD code is in rather good quantitative agreement with the predictions of the much simpler Kadomtsev model, which was not at all evident *a priori*.

**Future work**

Now that the mechanisms of redistribution by the sawtooth crash are much better understood, a more ambitious and delicate task will be to add the feedback of the impurities on the main plasma. The goal is to understand the complex interaction between heavy impurity radiation and the sawtooth dynamics. Namely, the level of radiative cooling implied by, say, W, could be high enough that the sawtooth features (the radius of the $q = 1$ surface, the diamagnetic frequencies related to the pressure gradient, etc...) are significantly modified and cannot lead to sufficient flushing, resulting in radiative collapse of the discharge. A heat sink term proportional to the impurity density will have to be added in order to account for the radiative cooling. This may seem simple, but is actually is not, because the coefficient of proportionality for heavy, not fully stripped impurities, is a rather complex function of temperature, electron density and ionization number of the species. A synthetic Soft X-ray diagnostic will also be implemented to provide satisfying comparisons with experiments. This is the subject of a new PhD work starting about now.

Also, there is much more to say about the fundamental features of the sawtooth crash using the XTOR-2F code. On the one hand, with some patience, larger values of the Lundquist number (lower values of the resistivity) could be explored to approach the experimental values and be conclusive about the need or not of new effects in Ohm's law and/or other Finite Larmor Radius effects in the continuity equation, which determine the time scale of reconnection. Such simulations are extremely long, because they require

a larger resolution to resolve the current sheet, and also because the inter sawtooth time evolution is slower. On the other hand, an upgrade of XTOR-2F, the XTOR-K code, is now ready for use. This code treats the ions kinetically with the numerical technique called Particle-In-Cell (PIC), resulting in a mixed fluid-kinetic description. At each fluid timestep, the particles are evolved in the magnetic field and yield a completely kinetic pressure tensor, which is plugged into the fluid part for the next fluid timestep. This allows to bypass the difficult closure issue and could be very instructive about the fundamental features of the sawtooth instability.

Appendix A

# Vector operators in covariant formulation

The Euclidian space $\mathbb{R}^3$ can be described by any set of generalized coordinates $(\psi(x,y,z), \chi(x,y,z), \zeta(x,y,z))$ provided that the Jacobian $\mathcal{J} \equiv [\nabla\psi \cdot (\nabla\chi \times \nabla\zeta)]^{-1}$ is non singular. This makes the description of complex geometries often much easier. Consider a cylinder of radius 1 centered on the $z$ axis. When the Cartesian coordinates are used, its bondary is defined by the implicit relation $x^2 + y^2 = 1$, while when it is described by cylindrical coordinates, it is simply bounded by $r = 1$. In tokamaks, which are axisymmetric, the coordinates which are used are often the toroidal angle $\varphi$ and in the poloidal plane, the poloidal flux $\psi$ as radial coordinate and an angle $\chi$, which can be either a generalized angle defined such as to make field lines look straight (*cf.* section 2.1.1), or the geometrical angle $\theta$. This system makes the definition of the boundary much easier, since it is a flux surface, and also, as we will see, the operators adopt an elegant form.

For generalized coordinates, there are two distinct basis of "natural" vectors, called the covariant and contravariant basis. The covariant basis is

$$\left(\frac{\partial \boldsymbol{r}}{\partial\psi}, \frac{\partial \boldsymbol{r}}{\partial\chi}, \frac{\partial \boldsymbol{r}}{\partial\zeta}\right), \tag{A.1}$$

and the contravariant basis is

$$(\nabla\psi, \nabla\chi, \nabla\zeta)\,. \tag{A.2}$$

To understand why these two triplets of vectors are natural, Fig. A.1 shows the two sets of vectors, covariant in red, contravariant in blue, for elliptic surfaces labeled by $\psi$ for the "radial" direction and $\chi$ for the polar direction.

When such basis vectors are used, the vectors also have covariant and contravariant components. Using the notation $(x^1, x^2, x^3)$ for $(\psi, \chi, \zeta)$, the contravariant component of a vector $\mathbf{A}$ is noted $A^i$ and is

$$A^i = \mathbf{A} \cdot \nabla x^i, \tag{A.3}$$

while its covariant component $A_i$ is

$$A_i = \mathbf{A} \cdot \frac{\partial \boldsymbol{r}}{\partial x^i}. \tag{A.4}$$

One sees that there are now two ways of writing the vector $\mathbf{A}$:

$$\mathbf{A} = A_i \nabla x^i \tag{A.5}$$

$$\mathbf{A} = A^i \partial_i \boldsymbol{r}, \tag{A.6}$$

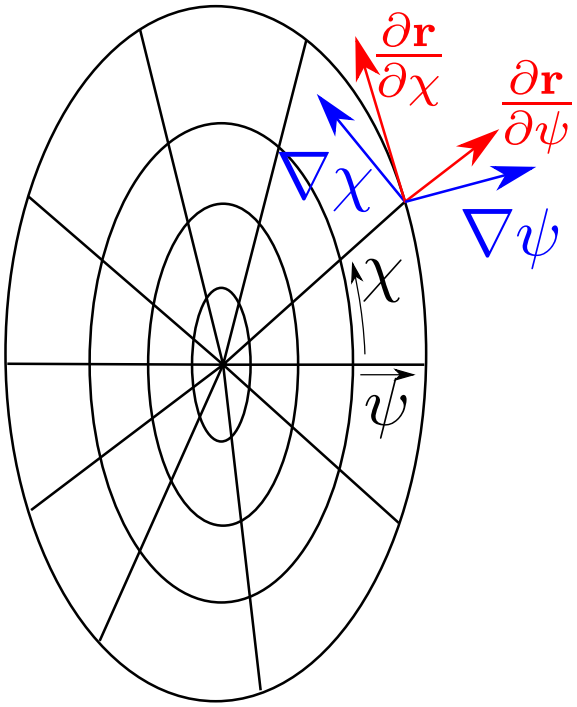


Figure A.1: Covariant (red) and contravariant (blue) basis for a general description of the poloidal plane.

where summation over repeated indices is assumed, and $\partial_i \equiv \frac{\partial}{\partial x^i}$. This is because of the unicity of a decomposition on a basis, and using

$$\nabla x^i \cdot \frac{\partial \boldsymbol{r}}{\partial x^j} = \frac{\partial x^i}{\partial x^j} = \delta^i_j, \tag{A.7}$$

with $\delta^i_j$ the Kronecker delta.

Also note the following very useful relations between the covariant and contravariant basis

$$\nabla x^i = \frac{1}{\mathcal{J}} \left( \partial_j \boldsymbol{r} \times \partial_k \boldsymbol{r} \right) \tag{A.8}$$

$$\partial_i \boldsymbol{r} = \mathcal{J} \left( \nabla x^j \times \nabla x^k \right), \tag{A.9}$$

where $(i, j, k)$ is any permutation of $(1, 2, 3)$. Thus the two identities

$$\nabla \times \nabla f = 0 \tag{A.10}$$

$$\nabla \cdot (\mathbf{A} \times \mathbf{B}) = \mathbf{B} \cdot \nabla \times \mathbf{A} - \mathbf{A} \cdot \nabla \times \mathbf{B}, \tag{A.11}$$

can be used to express the rotational and divergence of the vectors in covariant and contravariant form. Namely, we easily obtain

$$\nabla f = \partial_i f \nabla x^i \tag{A.12}$$

$$\nabla \cdot \mathbf{A} = \frac{1}{\mathcal{J}} \partial_i \left( \mathcal{J} A^i \right) \tag{A.13}$$

$$\nabla \times \mathbf{A} = \frac{1}{\mathcal{J}} \varepsilon^{ijk} \partial_j A_k \partial_i \boldsymbol{r}, \tag{A.14}$$

where $\varepsilon^{ijk}$ is the Levi-Civita completely antisymmetric rank 3 tensor. The latter formula translates into

$$(\nabla \times \mathbf{A})^i = \frac{\partial_j A_k - \partial_k A_j}{\mathcal{J}}, \tag{A.15}$$

where again $(i, j, k)$ is a permutation of $(1, 2, 3)$.

This is the way vector operators are implemented in the XTOR-2F code.

Appendix B

# The frozen-in-law

In this appendix, we show that when ideal Ohm's law is verified, two plasma volume elements initially on the same field line stay on this field line. Let us consider 2 points on a given field line at time $t$, separated by a small curvilinear distance $\delta s$. The distance vector between these two points is

$$\delta\mathbf{l} = \delta s\,\mathbf{t} + \mathcal{O}(\delta s^2), \tag{B.1}$$

where $\mathbf{t}$ is the tangent vector on the field line. During a time $\mathrm{d}t$, the first point moves a distance $\boldsymbol{v}\mathrm{d}t$, and the second one by a distance $(\boldsymbol{v}+\delta\boldsymbol{v})\mathrm{d}t$, and the new distance between the points is $\delta\mathbf{l} + \mathrm{d}\delta\mathbf{l}$. Obviously, in the quadrilateral formed by the two points at $t$ and the two points at $t + \mathrm{d}t$, we have (see Fig. B.1)

$$\delta\mathbf{l} + (\boldsymbol{v} + \delta\boldsymbol{v})\mathrm{d}t = \boldsymbol{v}\mathrm{d}t + (\delta\mathbf{l} + \mathrm{d}\delta\mathbf{l}), \tag{B.2}$$

so that

$$\frac{\mathrm{d}\delta\mathbf{l}}{\mathrm{d}t} = \delta\boldsymbol{v} = \delta\mathbf{l}\cdot\nabla\boldsymbol{v}, \tag{B.3}$$

where the expression for $\delta\boldsymbol{v}$ was deduced from the first term in the Taylor expansion

$$\boldsymbol{v}(\boldsymbol{x} + \delta\mathbf{l}) = \boldsymbol{v}(\boldsymbol{x}) + \delta\mathbf{l}\cdot\nabla\boldsymbol{v} + \mathcal{O}(\delta\mathbf{l}^2). \tag{B.4}$$

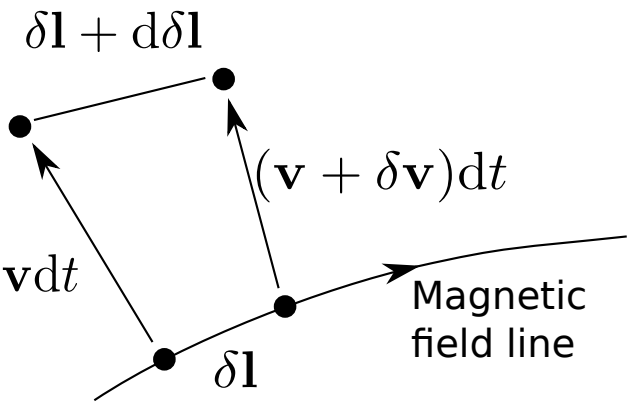


Figure B.1: Quadrilateral formed by the 4 points in the evolution.

Now we must exhibit a quantity proportional to $\mathbf{B}$ which has the same equation of evolution. We see that $\mathbf{B}/\rho$, where $\rho$ is the plasma density ruled by the continuity equation, does the job. Indeed, taking the curl of Ohm's law, $\mathbf{E} + \boldsymbol{v}\times\mathbf{B}$, we have

$$\frac{\partial\mathbf{B}}{\partial t} = \nabla\times(\boldsymbol{v}\times\mathbf{B}) \tag{B.5}$$

$$= -\boldsymbol{v}\cdot\nabla\mathbf{B} + \mathbf{B}\cdot\nabla\boldsymbol{v} - (\nabla\cdot\boldsymbol{v})\,\mathbf{B}, \tag{B.6}$$

so that

$$\frac{\mathrm{d}\mathbf{B}/\rho}{\mathrm{d}t} = \frac{1}{\rho}\frac{\mathrm{d}\mathbf{B}}{\mathrm{d}t} + \frac{\mathbf{B}}{\rho}\nabla\cdot\boldsymbol{v} \tag{B.7}$$

$$= \frac{1}{\rho}\left[\mathbf{B}\cdot\nabla\boldsymbol{v} - (\nabla\cdot\boldsymbol{v})\,\mathbf{B}\right] + \frac{\mathbf{B}}{\rho}\nabla\cdot\boldsymbol{v} \tag{B.8}$$

$$= \frac{\mathbf{B}}{\rho}\cdot\nabla\boldsymbol{v}. \tag{B.9}$$

Finally, $\delta\mathbf{l}$ and $\mathbf{B}/\rho$ are initially parallel and have the same evolution equation, hence they stay parallel throughout their evolution. This means that two points on a given field line will remain on this field line forever. Using the reversibility of time (in the absence of dissipation, which is the case for ideal Ohm's law), this also means that points that are initially not connected by a magnetic field line must stay unconnected in the future. Hence the flow carries the magnetic field rigidly with itself and topologically separated regions remain separated throughout the field's evolution. This is called the frozen-in-law.

Appendix C

# Simplification of the expression for $\delta W$

To simplify the expression of $\delta W$, *Eq.* (2.98), we separate the perturbations $\boldsymbol{\xi}$ and $\delta\mathbf{B}$ into their parallel and perpendicular components

$$\begin{aligned} \boldsymbol{\xi} &= \boldsymbol{\xi}_\perp + \xi_\parallel \mathbf{b} \\ \delta\mathbf{B} &= \delta\mathbf{B}_\perp + \delta B_\parallel \mathbf{b}, \end{aligned} \tag{C.1}$$

and use the following identities

$$\mathbf{J}\times\mathbf{B} = \nabla p \tag{C.2}$$

$$\nabla_\perp\left(p + \frac{B^2}{2\mu_0}\right) = \frac{B^2}{\mu_0}\boldsymbol{\kappa}, \tag{C.3}$$

where $\boldsymbol{\kappa} = \mathbf{b}\cdot\nabla\mathbf{b} = (\nabla\times\mathbf{b})\times\mathbf{b}$ is the magnetic curvature, orthogonal to the magnetic field: $\boldsymbol{\kappa}\cdot\mathbf{b} = 0$. The first equation is the equilibrium condition while the second derives from the first:

$$\begin{aligned} \mu_0\nabla_\perp p &= \mu_0\mathbf{J}\times\mathbf{B} \\ &= -\mathbf{B}\times\nabla\times\mathbf{B} \\ &= \mathbf{B}\cdot\nabla\mathbf{B} - \nabla\frac{B^2}{2} \\ &= B^2\boldsymbol{\kappa} + \mathbf{b}\nabla_\parallel\frac{B^2}{2} - \nabla\frac{B^2}{2} \\ &= B^2\boldsymbol{\kappa} - \nabla_\perp\frac{B^2}{2} \end{aligned} \tag{C.4}$$

A first algebraic simplification is obtained by noting that

$$\begin{aligned} \mathbf{B}\cdot(\mathbf{J}\times\delta\mathbf{B}) &= -\delta\mathbf{B}\cdot\nabla p = -\nabla\times(\boldsymbol{\xi}\times\mathbf{B})\cdot\nabla p \\ &= -\nabla\cdot((\boldsymbol{\xi}\times\mathbf{B})\times\nabla p) \\ &= -\nabla\cdot(\mathbf{B}(\boldsymbol{\xi}\cdot\nabla p)) \\ &= -\mathbf{B}\cdot\nabla(\boldsymbol{\xi}\cdot\nabla p). \end{aligned} \tag{C.5}$$

Therefore $\xi_\parallel\mathbf{b}\cdot(\mathbf{J}\times\delta\mathbf{B} + \nabla(\boldsymbol{\xi}\cdot\nabla p)) = 0$, and $\delta W$ now reads

$$\delta W = \frac{1}{2}\int \mathrm{d}^3\boldsymbol{x}\left[|\delta\mathbf{B}|^2 - \boldsymbol{\xi}_\perp^\star\cdot\nabla(\boldsymbol{\xi}_\perp\cdot\nabla p) + \Gamma p|\nabla\cdot\boldsymbol{\xi}|^2 - \boldsymbol{\xi}_\perp^\star\cdot\mathbf{J}\times\delta\mathbf{B}\right]. \tag{C.6}$$

Next $\delta B_\parallel$ is computed. Developing the curl and using *Eq.* (C.3), we have

$$\delta B_\parallel = \mathbf{b}\cdot\nabla\times(\boldsymbol{\xi}_\perp\times\mathbf{B}) = -B(\nabla\cdot\boldsymbol{\xi}_\perp + 2\boldsymbol{\xi}_\perp\cdot\nabla\boldsymbol{\kappa}) + \frac{\mu_0}{B}\boldsymbol{\xi}_\perp\cdot\nabla p.$$

Finally, replacing $\mathbf{J}_\perp$ with $\mathbf{B}\times\nabla p/(\mu_0 B^2)$, developing and simplifying the terms involving $\delta B_\parallel$ in $\delta W$, the following form is obtained:

$$\delta W = \frac{1}{2}\int \mathrm{d}^3\boldsymbol{x}\Big[|\delta\mathbf{B}_\perp|^2 + \frac{B^2}{\mu_0}\,|\nabla\cdot\boldsymbol{\xi}_\perp + 2\boldsymbol{\xi}_\perp\cdot\boldsymbol{\kappa}|^2 + \Gamma p\,|\nabla\cdot\boldsymbol{\xi}|^2 \\ -(\boldsymbol{\xi}_\perp\cdot\nabla p)(2\boldsymbol{\xi}_\perp^\star\cdot\boldsymbol{\kappa}) - J_\parallel(\boldsymbol{\xi}_\perp\times\mathbf{B})\cdot\delta\mathbf{B}_\perp\Big]. \qquad \text{(C.7)}$$

Appendix D

# Derivation of the bifluid layer equations

Here we derive the layer equations valid in the layer with the cylindrical approximation. The two equations for the flux and the MHD displacement are the momentum equation and the Ohm's law, respectively.

In our cylindrical approximation, the diamagnetic drifts are

$$\boldsymbol{v}_s^\star = \frac{\hat{\mathbf{z}} \times \nabla p_s}{n_e e_s B_0}. \tag{D.1}$$

Projecting the bifluid Ohm's law, *Eq.* (2.76), on $\hat{\mathbf{z}}$ and again using the expression of the parallel gradient, *Eq.* (2.145), Ohm's law is written

$$\partial_t \Psi^\star + (\boldsymbol{v}_1 + \boldsymbol{v}_e^\star) \cdot \nabla \Psi^\star = \bar{\eta} \nabla_\perp^2 \psi_1. \tag{D.2}$$

The $\boldsymbol{v}_e^\star \cdot \nabla \Psi^\star$ term is decomposed in its equilibrium and linearized perturbed parts:

$$\boldsymbol{v}_e^\star \cdot \nabla \Psi^\star = \boldsymbol{v}_{e0}^\star \cdot \nabla \Psi_0^\star + \boldsymbol{v}_{e1}^\star \cdot \nabla \Psi_0^\star + \boldsymbol{v}_{e0}^\star \cdot \nabla \psi_1. \tag{D.3}$$

The first term vanishes because $p_0$ and $\Psi_0^\star$ depend only on $r$. The second term is

$$\boldsymbol{v}_{e1}^\star \cdot \nabla \Psi_0^\star = \frac{\partial_\theta p_{e1}}{n_e e r B_0} \frac{\mathrm{d}\Psi_0^\star}{\mathrm{d}r}. \tag{D.4}$$

To express the perturbed diamagnetic velocities, we still use the pressure equation for a given species, *Eq.* (2.23). Within our cylindrical approximation, we have $p_{e1} = -\xi_r p'_{e0}$, so defining the electron diamagnetic frequency,

$$\omega_e^\star = -\frac{p'_{e0}(r_s)}{n_e e B_0 r_s} > 0, \tag{D.5}$$

we have $\boldsymbol{v}_{e1}^\star \cdot \nabla \Psi_0^\star = i\omega_e^\star \xi_r \frac{\mathrm{d}\Psi_0^\star}{\mathrm{d}r}$.

The third term in *Eq.* (D.3) is also proportional to $\omega_e^\star$:

$$\boldsymbol{v}_{e0}^\star \cdot \nabla \psi_1 = i\omega_e^\star \psi_1. \tag{D.6}$$

Thus Ohm's law is now

$$(\gamma + i\omega_e^\star)\, \psi_1 + (\gamma + i\omega_e^\star)\, \frac{r_s B_0}{Rq}(q-1)\xi_r = \bar{\eta} \nabla_\perp^2 \psi_1. \tag{D.7}$$

Regarding the momentum equation, we will adopt an alternative method using the quasi-neutrality condition $\nabla \cdot \mathbf{J} = 0$. We use *Eq.* (2.84) and drop the non-linear inertia term to obtain:

$$\mathbf{J}_\perp = \frac{\mathbf{B} \times \nabla p}{B^2} + \rho_0 \frac{\mathbf{B} \times (\partial_t \boldsymbol{v}_1 + \boldsymbol{v}_{i0}^\star \cdot \nabla \boldsymbol{v}_{\perp 1})}{B^2}, \tag{D.8}$$

which in our ordering should rather be written

$$\mathbf{J}_\perp = \frac{\hat{\mathbf{z}}\times\nabla p}{B_0} + \rho_0\frac{\hat{\mathbf{z}}\times(\partial_t \boldsymbol{v}_1 + \boldsymbol{v}^\star_{i0}\cdot\nabla\boldsymbol{v}_{\perp 1})}{B_0}. \tag{D.9}$$

The divergence of the first term vanishes since $\nabla\times\hat{\mathbf{z}}=0$ and $\nabla\times\nabla p=0$. The second term can be developed:

$$\rho_0\frac{\hat{\mathbf{z}}\times\partial_t\boldsymbol{v}}{B_0} = -\frac{\rho_0\gamma}{B_0^2}\nabla_\perp\phi \tag{D.10}$$

We must also detail the term $\hat{\mathbf{z}}\times(\boldsymbol{v}^\star_{i0}\cdot\nabla\boldsymbol{v}_{\perp 1})$. We first define the ion diamagnetic frequency[1]

$$\omega_i^\star = \frac{p'_{i0}(r_s)}{n_e e B_0 r_s} < 0. \tag{D.11}$$

Using this definition, and $\hat{\boldsymbol{\theta}}\cdot\nabla\hat{\boldsymbol{r}} = \hat{\boldsymbol{\theta}}/r$, $\hat{\boldsymbol{\theta}}\cdot\nabla\hat{\boldsymbol{\theta}} = -\hat{\boldsymbol{r}}/r$, we obtain

$$\boldsymbol{v}^\star_{i0}\cdot\nabla\boldsymbol{v}_{\perp 1} = -\frac{\omega_i^\star}{B_0}\left[\nabla_\perp\phi_1 - \frac{\phi_1}{r}\hat{\boldsymbol{r}} - i\partial_r\phi_1\hat{\boldsymbol{\theta}}\right]. \tag{D.12}$$

Given that radial derivative of perturbed quantities dominate over poloidal derivatives in the layer, $\partial_r \gg 1/r$, it is correct to write that

$$B_0\hat{\mathbf{z}}\times(\boldsymbol{v}^\star_{i0}\cdot\nabla\boldsymbol{v}_{\perp 1}) \simeq -\omega_i^\star\left(\hat{\mathbf{z}}\times\nabla_\perp\phi_1 + i\nabla_\perp\phi_1\right). \tag{D.13}$$

Taking the divergence, the first term will vanish and the second term will remain, so that

$$\nabla\cdot\mathbf{J}_\perp = -\frac{\rho_0}{B_0^2}\left(\gamma + i\omega_i^\star\right)\frac{\mathrm{d}^2\phi_1}{\mathrm{d}r^2}. \tag{D.14}$$

Using again, $p_{i1} = -\xi_r p'_{i0}$, and the relation between $\phi_1$ and $\xi_r$, $\nabla\cdot\mathbf{J} = \nabla\cdot\mathbf{J}_\perp + \nabla\cdot\mathbf{J}_\parallel = 0$ writes, neglecting $\nabla\cdot\mathbf{b}$,

$$i\frac{\rho_0 r_s}{B_0^2}\gamma\left(\gamma + i\omega_i^\star\right)\frac{\mathrm{d}^2\xi_r}{\mathrm{d}r^2} = \nabla_\parallel j_{\parallel 1}, \tag{D.15}$$

where

$$\nabla_\parallel j_{\parallel 1} \simeq \frac{\mathbf{B}}{B_0}\cdot\nabla j_{z1} = -\frac{i}{Rq}(q-1)\frac{\mathrm{d}^2\psi_1}{\mathrm{d}r^2}, \tag{D.16}$$

since the perturbed parallel current is essentially equal to the perturbed axial current, and where we used *Eq.* (2.152). Thus

$$\frac{\rho_0 r_s}{B_0^2}\gamma\left(\gamma + i\omega_i^\star\right)\frac{\mathrm{d}^2\xi_r}{\mathrm{d}r^2} = -\frac{q-1}{Rq}\frac{\mathrm{d}^2\psi_1}{\mathrm{d}r^2} \tag{D.17}$$

is our equation of motion valid in the layer. Note that the $\gamma + i\omega_i^\star$ factor can also be interpreted as the fact that the perturbed ion radial velocity is $(\boldsymbol{v}_{i1})_r = (\boldsymbol{v}_1 + \boldsymbol{v}^\star_{i1})_r = (\gamma + i\omega_i^\star)\xi_r$.

[1] Our sign conventions for $\omega_e^\star$ and $\omega_i^\star$, different from Ref. [Ara 1978], take into account the fact that with the definitions of Fig. 2.2 and $\mathbf{B}$ in the $+\hat{\boldsymbol{\varphi}}$ direction, the ion diamagnetic direction is in the $-\hat{\boldsymbol{\theta}}$ direction, whereas the electron diamagnetic direction is the $+\hat{\boldsymbol{\theta}}$ direction.

Combining *Eq.* (D.7) and (D.17) together, one obtains after the usual Taylor expansion $(q-1)/q \simeq \hat{s}x$ in the layer,

$$\begin{cases} \psi = -x\xi_r + \dfrac{\hat{\eta}}{\lambda - i\lambda_e}\dfrac{\mathrm{d}^2\psi}{\mathrm{d}x^2} \\ \\ \lambda\left(\lambda - i\lambda_i\right)\dfrac{\mathrm{d}^2\xi_r}{\mathrm{d}x^2} = x\dfrac{\mathrm{d}^2\psi}{\mathrm{d}x^2}, \end{cases} \tag{D.18}$$

with the same normalizations as before, and $\lambda_i = -\omega_e^\star\tau_I$, $\lambda_e = -\omega_i^\star\tau_I$.

Appendix E

# The Ware pinch

The Ware pinch is a neoclassical effect. At the most fundamental level, neoclassical effects are caused by a collisional friction between trapped and passing particles. Namely, because of their bounce motion, trapped particles do not carry any parallel momentum (or a very small one related to their secular slow toroidal motion, see section 2.2.6), contrary to the passing particles which carry a momentum determined by the mean fluid parallel velocity $v_\parallel$. This induces a discontinuity in the distribution function in the velocity space at the trapped/passing boundary, which can be regularized only by collisions, resulting in a friction force. Because of axisymmetry, this force vanishes in the toroidal direction. The neoclassical calculations give this friction in the form of the divergence of a neoclassical pressure tensor $\mathbf{\Pi}_{neo}$ such that the force in the parallel direction for the species $s$, $F_{s\parallel}$, is of the form

$$F_{s\parallel} \equiv -\langle \mathbf{b} \cdot \nabla \cdot \mathbf{\Pi}_{s,neo} \rangle = -n_s m_s \mu_s \left( v_{s\theta} - k_s \frac{\partial_r T_s}{e_s B} \right), \tag{E.1}$$

where in the low collisionality regime (banana regime), $\mu_s \propto \nu_s$, $\nu_s$ being the collision frequency of the species $s$, $k_s$ is a coefficient of order unity, and $\langle \cdot \rangle$ denotes flux surface average. We can get a grasp of the neoclassical physics by writing the force balance equation, projected in the radial, parallel and toroidal directions. In this sort appendix, we restrict ourselves to the case where there are only two species: ions and electrons, with a circular plasma in the high aspect ratio approximation. We use the following equation of motion:

$$n_s m_s \partial_t \boldsymbol{v}_s = n_s e_s \left( \mathbf{E} + \boldsymbol{v}_s \times \mathbf{B} \right) - \nabla \cdot \mathbf{\Pi}_{s,neo} - n_s m_s \sum_{s'} \nu_{ss'} \left( \boldsymbol{v}_s - \boldsymbol{v}_{s'} \right) \tag{E.2}$$

We thus have, in steady state, given that $\langle \hat{\boldsymbol{\varphi}} \cdot \nabla \cdot \mathbf{\Pi}_{s,neo} \rangle = 0$, and $E_\parallel \simeq E_\varphi \equiv E_{ind}$ in the high aspect ratio approximation:

$$E_r + v_{s\theta} B_\varphi - v_{s\varphi} B_\theta - \frac{\partial_r p_s}{n_s e_s} = 0, \tag{E.3}$$

$$n_s e_s E_{ind} + F_{s\parallel} - n_s m_s \sum_{s'} \nu_{ss'} \left( V_{s\parallel} - V_{s'\parallel} \right) = 0, \tag{E.4}$$

$$n_s e_s (E_{ind} + v_{sr} B_\theta) - n_s m_s \sum_{s'} \nu_{ss'} \left( V_{s\varphi} - V_{s'\varphi} \right) = 0. \tag{E.5}$$

Here, as usual in neoclassical computations, we are interested in the expression of the radial flux $\Gamma_s \equiv n_s v_{sr}$. The preceding system can be recast using this expression and the

difference between *Eqs.* (E.5) and (E.4):

$$E_r + v_{s\theta} B_\varphi - v_{s\varphi} B_\theta - \frac{\partial_r p_s}{n_s e_s} = 0, \tag{E.6}$$

$$n_s e_s E_{ind} + F_{s\|} - n_s m_s \sum_{s'} \nu_{ss'} \left( V_{s\|} - V_{s'\|} \right) = 0, \tag{E.7}$$

$$e_s \Gamma_s B_\theta - F_{s\|} = 0. \tag{E.8}$$

Carrying the sum of *Eq.* (E.7) over the two species, using the quasineutrality condition $\sum_s n_s e_s = 0$, and the action/reaction principle, we obtain that

$$\sum_s F_{s\|} = 0. \tag{E.9}$$

Plugging this into *Eq.* (E.8), we immediately obtain the so-called *ambipolarity condition*,

$$\sum_s e_s \Gamma_s = 0, \tag{E.10}$$

which is a consequence of axisymmetry.

Now, *Eq.* (E.9) reads

$$\sum_s n_s m_s \mu_s \left( v_{s\theta} - k_s \frac{\partial_r T_s}{e_s B} \right) = 0. \tag{E.11}$$

Since $\mu_s$ is proportional to the collision frequency and $\nu_e/\nu_i \sim (m_i/m_e)^{1/2}$, we have $m_i \mu_i / m_e \nu_e \sim (m_i/m_e)^{1/2}$ and the ion term is dominating *Eq.* (E.11). Hence this equation yields the ion poloidal velocity:

$$v_{i\theta} \simeq k_i \frac{\partial_r T_i}{eB}. \tag{E.12}$$

The ion poloidal velocity can be used to determine the electron velocity, and then the electron flux, which is equal to the ion flux by ambipolarity. We rewrite *Eq.* (E.7) for the electrons, which is nothing but an Ohm's law, and the difference between electrons and ions of *Eqs.* (E.6), in terms of the parallel current $j_\| = n_e e (v_{i_\|} - v_{e\|})$, and using $B_\theta / B_\varphi \simeq \varepsilon / q$, $\varepsilon = r/R$:

$$\frac{n_e e q}{\varepsilon} (v_{e\theta} - v_{i\theta}) + j_\| + q \frac{\partial_r p_e + \partial_r p_i}{\varepsilon B} = 0, \tag{E.13}$$

$$\frac{n_e e^2}{m_e \nu_{ei}} E_{ind} = j_\| - n_e e \frac{\mu_e}{\nu_{ei}} \left( v_{e\theta} + k_e \frac{\partial_r T_e}{eB} \right). \tag{E.14}$$

It is straightforward to eliminate the unknown current to obtain the electron poloidal velocity. The second term on the r.h.s of *Eq.* (E.14) is found to be of order $\varepsilon$ compared to the other terms in *Eq.* (E.13) and thus is neglected. One obtains:

$$v_{e\theta} = -\frac{1}{eB} \left[ (T_i + T_e) \frac{\partial_r n_e}{n_e} + \partial_r T_e + (1 - k_i) \partial_r T_i \right] - \frac{\varepsilon e}{q m_e \nu_{ei}} E_{ind}. \tag{E.15}$$

Finally, the radial flux can be obtained from *Eq.* (E.8) applied to the electrons:

$$\Gamma_e = -\frac{F_{e\parallel}}{eB_\theta} = \frac{q}{\varepsilon eB} n_e m_e \mu_e \left( v_{e\theta} + k_e \frac{\partial_r T_e}{eB} \right) \tag{E.16}$$

One obtains

$$\Gamma_e = -n_e D_e \left[ \left( 1 + \frac{T_i}{T_e} \right) \frac{\partial_r n_e}{n_e} + (1 + k_e) \frac{\partial_r T_e}{T_e} + (1 - k_i) \frac{\partial_r T_i}{T_e} \right] - \frac{n_e \mu_e}{B \nu_{ei}} E_{ind}, \tag{E.17}$$

with

$$D_e = \frac{q}{\varepsilon} \frac{\mu_e}{\omega_{ce}} \frac{T_e}{eB} \tag{E.18}$$

the electron diffusion coefficient in the banana regime, with $\omega_{ce}$ the electron cyclotron pulsation. The part of interest in *Eq.* (E.17) is the last term, proportional to the induction field. We now make explicit the expression of $\mu_e$ given by neoclassical theory. In the banana regime, relevant for the electrons,

$$\mu_e = \frac{C_e \nu_e q}{\varepsilon^{1/2}}, \tag{E.19}$$

where $C_e = 1.46(0.53 + Z_{eff})$ is a quantity of order unity. Thus the last term in *Eq.* (E.17) is a flux of the form $\Gamma_{e,Ware} = n_e v_{Ware}$, with

$$v_{Ware} = -C_e \sqrt{\varepsilon} \frac{E_{ind}}{B_\theta}. \tag{E.20}$$

This velocity is called the Ware pinch. We have used the conventions of Fig. 2.2, so $B_\theta$ is positive when $E_{ind}$ is positive, hence this velocity is directed from the edge toward the core. The $\sqrt{\varepsilon}$ factor is reminiscent of the trapped particle fraction. Notice that there is no dependence in the collision frequency. However the expression will be different when the electrons leave the banana regime, very close to the center.

Note that since the ion flux is equal to the electron flux, it is possible to now obtain the difference between $v_{i\theta}$ and $k_i \frac{\partial_r T_i}{eB}$ in *Eq.* (E.12).

Appendix F

# Waelbroeck's current sheet

We use the cylindrical (or large aspect ratio) approximation, toroidal effects are not retained, thus the parallel current is equivalent to the current in the $\hat{\mathbf{z}} = \hat{\boldsymbol{\varphi}}$ direction. The magnetic field is written using the helical flux[1], as in *Eq.* (2.146):

$$\mathbf{B} = B_0 \left( \hat{\mathbf{z}} + \frac{r}{R} \hat{\boldsymbol{\theta}} \right) - \nabla \Psi^\star \times \hat{\mathbf{z}}. \tag{F.1}$$

Since we describe the evolution as a series of equilibria, we no longer separate the flux in an equilibrium and perturbed part. Since $(\mathbf{A} \cdot \nabla \mathbf{B})_z = \mathbf{A} \cdot \nabla B_z$ for any fields $\mathbf{A}$ and $\mathbf{B}$, and since the toroidal field component is constant, the equilibrium condition (4.29) reduces to $\mathbf{B} \cdot \nabla j_z = 0$, that is, using *Eq.* (2.145):

$$\nabla \Psi^\star \times \nabla j_z = 0. \tag{F.2}$$

This means that when $\nabla \Psi^\star \neq 0$ (everywhere except on resonant field lines), the general solution is that the current must be constant on the field lines:

$$j_z = j_z(\Psi^\star). \tag{F.3}$$

Taking the curl of *Eq.* (F.1) and assuming the island is thin $\nabla^2 \Psi^\star \simeq \partial_r^2 \Psi^\star$, we have

$$\partial_r^2 \Psi^\star = j_z(\Psi^\star) - 2\frac{B_0}{R}. \tag{F.4}$$

This will be our basic equation for assessing the physical behaviour in the island. Note that even though only radial derivatives are retained, $\nabla^2 \Psi^\star$ still depends on the angle $\theta$.

At this point it is good to describe our goal more precisely. The MHD displacement is directed toward, say, the right and flux surfaces reconnect at the resonant surface to form an island on the left. Inside this island as in the unperturbed configuration, the current is constant on flux surfaces and *Eq.* (F.4) can be used to relate the different geometrical quantities together, even though it may not seem straightforward at first glance. The first step is to multiply *Eq.* (F.4) by $\partial_r \Psi^\star$ and to integrate in the radial direction along a radius, from the separatrix to a flux surface labeled with $\Psi^\star$. One obtains

$$\partial_r \Psi^\star = \pm \sqrt{2\left(F(\Psi^\star) - G(\theta)\right)}, \tag{F.5}$$

since $\partial_r \Psi^\star = 0$ at the separatrix. $G$ is an unknown integration constant and

$$F(\Psi^\star) = \int_0^{\Psi^\star} \left( j_z(\psi) - 2\frac{B_0}{R} \right) \mathrm{d}\psi, \tag{F.6}$$

[1] Contrary to the preceding section, we take the magnetic flux to have the dimension of the magnetic potential $\mathbf{A}$.

since $\partial_r \Psi^\star\big|_{r=0} \sim 0$ for a small displacement of the surfaces. Up to now the current is still unknoawn however. The goal is to determine the two unknown functions $F$ (or equivalently $j_z$) and $G$. *Eq.* (F.5) implies that for the flux surfaces such that $F(\Psi^\star) < \max(G(\theta))$, not all angles are allowed, in other words, the flux surface does not encircle the original magnetic axis. Obviously, this corresponds to the flux surfaces of the island. We

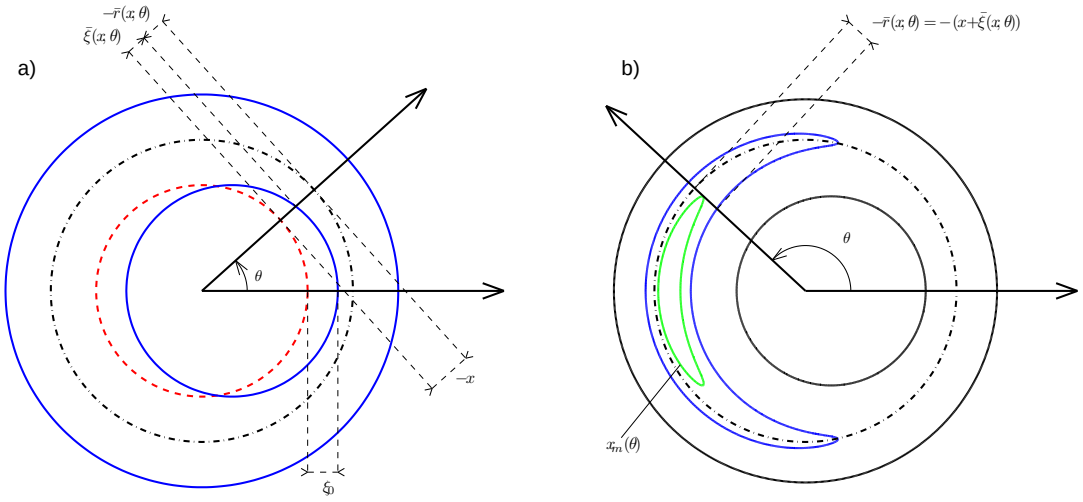


Figure F.1: Geometry for Waelbroeck's model. Definition of the geometrical quantities for the perturbed non reconnected surfaces (a) and for the reconnected surfaces in the island (b). On both cases, the initial $q = 1$ surface is the dot-dashed circle. $x$ is the distance between the red dashed circle and the initial $q = 1$ surface on panel (a). The displayed surfaces have $x < 0$, so that $-x$ and $-\bar{r}$ are indicated on the figure as the positive distances. It is seen that $\bar{\xi}(x,\theta) = r(x,\theta) - x$. The rigid MHD displacement is $\xi_0$. Also shown on panel (b), a green flux surface in the island to which the straight line defined by the angle $\theta$ is tangent. The label of this surface is defined as the quantity $x_m(\theta)$.

first give a few definitions. We define a new distance $\bar{r} = r - r_s$, where $r$ is the polar radius and $r_s$ the resonant surface. The initial helical flux, in the unperturbed configuration, is of the form $\Psi_0^\star = 1/2\Psi_0^{\star\prime\prime}x^2$, where $x$ is the initial distance to the separatrix. It is chosen as the flux surface label. Notice that for thin islands the two surfaces which reconnect have the same absolute value of $x$, so that $|x|$ becomes a good label of the reconnected surfaces. A displacement $\bar{\xi} \equiv \bar{r} - x$ is also defined. Fig. F.1 shows the different quantities. It is meaningful to choose a flux surface labeled by $x$ and to look at the point obtained by the intersection of a given $\theta$ straight line. This defines the two functions $\bar{r}(x,\theta)$ and $\bar{\xi}(x,\theta)$ related by

$$\bar{\xi}(x,\theta) = \bar{r}(x,\theta) - x. \tag{F.7}$$

Notice that $\bar{\xi}$ is different from the MHD displacement $\xi_r$. Again using the negligible $\theta$

derivatives of $\Psi^\star$, we have

$$\frac{\partial \bar{r}}{\partial x} = \frac{\partial_x \Psi^\star}{\partial_r \Psi^\star}, \tag{F.8}$$

where, with respect to the initial configuration, $\partial_x \Psi^\star = \Psi_0^{\star\prime\prime} x$. Defining $f(x) = F(\Psi^\star)/(1/2\Psi_0^{\star\prime\prime})$ and $g(\theta) = G(\theta)/(1/2\Psi_0^{\star\prime\prime})$, one rewrites *Eq.* (F.5) as

$$\frac{\partial \bar{r}(x,\theta)}{\partial x} = \frac{|x|}{\sqrt{f(x) - g(\theta)}}, \tag{F.9}$$

which implicitly determines the relevant signs in *Eq.* (F.5). They are chosen so that $\partial_x \bar{r}(x,\theta)$ is always positive. This is consistent with our conventions. In particular, we see on Fig. F.1 b) that the green surface, which was reconnected before the blue one, has a flux label which is smaller in absolute value. Thus it is larger for the inner branch (the inner branch corresponds to $x < 0$). Hence starting from the inner branch of the blue surface and going toward the green surface, $x$ increases and $\bar{r}(x,\theta)$ also increases, which is consistent with the sign of *Eq.* (F.9).

From *Eq.* (F.9) and *Eq.* (F.7), we can deduce $\bar{\xi}(x,\theta)$ as a function of $f$ and $g$, by integrating between $x_m(\theta)$ and $x$. The function $x_m(\theta)$ is defined as the (positive) label of the flux surface to which the straight line of angle $\theta$ is tangent (see Fig. F.1). One obtains:

$$\bar{\xi}(x,\theta) = \bar{\xi}(x_m(\theta)) + \int_{x_m(\theta)}^{x} \mathrm{d}x \left( \frac{|x|}{\sqrt{f(x) - g(\theta)}} - 1 \right) \tag{F.10}$$

for $x > x_m(\theta) > 0$ and

$$\bar{\xi}(-|x|,\theta) = \bar{\xi}(-x_m(\theta)) + \int_{-x_m(\theta)}^{-|x|} \mathrm{d}x \left( \frac{|x|}{\sqrt{f(x) - g(\theta)}} - 1 \right) \tag{F.11}$$

for $x < x_m(\theta) < 0$.

Now the solution must be matched to the solution valid for large $|x|$, that is, far from the separatrix. For these surfaces, the displacement is equal to the linear solution: $\bar{\xi}(x,\theta) \underset{x\to-\infty}{\longrightarrow} \xi_0 \cos\theta$ and $\bar{\xi}(x,\theta) \underset{x\to-\infty}{\longrightarrow} \xi_0 \cos\theta$ (the external region does not move while the core undergoes a rigid shift). It is possible to let $|x|$ tend to $\infty$ in the integrals of *Eqs.* (F.10) and (F.11) because the integrand tends to 0, thanks to $f \underset{x\to\infty}{\sim} x^2$ according to *Eq.* (F.5). In addition, the unknown function $\bar{\xi}(x_m(\theta),\theta)$ is eliminated by using the fact that $\bar{r}(x_m(\theta),\theta) = \bar{r}(-x_m(\theta),\theta)$, indeed the two branches coming from the outer and inner regions connect at the mirror point $\theta_m(\theta)$. Thus $\bar{\xi}(-x_m(\theta),\theta) - \bar{\xi}(x_m(\theta),\theta) = 2x_m(\theta)$ and $x_m$ is not an unknown once $f$ and $g$ have been found. Using this property, taking the difference of the two limits $x \to \infty$ in *Eq.* (F.10) and $x \to -\infty$ in *Eq.* (F.11) yields

$$\xi_0 \cos\theta = 2x_m(\theta) - 2\int_{x_m(\theta)}^{\infty} \mathrm{d}x \left( \frac{|x|}{\sqrt{f(x) - g(\theta)}} - 1 \right) \tag{F.12}$$

Since there are two unknowns, $f$ and $g$, we need an other equation to close the system. This equation is provided by the constraint of flux conservation during the reconnection

process. We assume that the volume elements are preserved when two flux surfaces reconnect and unfold in the island. In this 2D problem, this amounts to the conservation of the area. Denoting by $\mathrm{d}\mathcal{A}_+$ and $\mathrm{d}\mathcal{A}_-$ the area elements in the outer and inner region separating two flux surfaces labeled by $x$ and $x+\mathrm{d}x$ (and $-x$, $-(x+\mathrm{d}x)$) and $\mathrm{d}V_f$ the final area element, we have $\mathrm{d}\mathcal{A}_f = \mathrm{d}\mathcal{A}_+ + \mathrm{d}\mathcal{A}_-$. Since the flux increments (alternatively the label increment $\mathrm{d}x$) are the same in the unperturbed and reconnection configurations, we have

$$\frac{\mathrm{d}\mathcal{A}_f}{\mathrm{d}\Psi^\star} = \frac{\mathrm{d}\mathcal{A}_+}{\mathrm{d}\Psi^\star} + \frac{\mathrm{d}\mathcal{A}_-}{\mathrm{d}\Psi^\star}. \tag{F.13}$$

Writing the area for general coordinates $(\Psi^\star, \theta)$: $\mathcal{A}(\Psi^\star) = \int^{\Psi^\star} \oint_{\Psi^\star = C^{te}} \mathcal{J}\mathrm{d}\theta\mathrm{d}\Psi^\star$, with $\mathcal{J} = [(\nabla\Psi^\star \times \nabla\theta)\cdot\hat{\mathbf{z}}]^{-1}$, we see that we can write

$$\frac{\mathrm{d}\mathcal{A}}{\mathrm{d}\Psi^\star} = \oint_{\Psi^\star = C^{te}} \frac{r\mathrm{d}\theta}{\partial_r \Psi^\star}. \tag{F.14}$$

Applied to the unperturbed configuration, the sum of the inner and outer branches yields

$$\frac{\mathrm{d}\mathcal{A}_+}{\mathrm{d}\Psi^\star} + \frac{\mathrm{d}\mathcal{A}_-}{\mathrm{d}\Psi^\star} = \frac{4\pi r_s}{\Psi_0^{\star\prime\prime}|x|}. \tag{F.15}$$

For the reconnected surfaces, the integral must be carried out around a reconnected surface. Since these surfaces do not encircle the origin taken for the definition of the angle $\theta$, the integral must be carried out twice between the mirror points located at $\theta_m(x)$ and $2\pi - \theta_m(x)$, where $\theta_m$ is the reciprocal of $x_m$: $x_m(\theta_m(x)) = x$. Using the thin island approximation, here as $r \simeq r_s$, and *Eq.* (F.5), we obtain:

$$\begin{aligned} \frac{\mathrm{d}\mathcal{A}_f}{\mathrm{d}\Psi^\star} &= 2\int_{\theta_m(x)}^{2\pi-\theta_m(x)} \frac{r_s \mathrm{d}\theta}{\partial_r \Psi^\star} \\ &= \frac{2r_s}{\Psi_0^{\star\prime\prime}} \int_{\theta_m(x)}^{2\pi-\theta_m(x)} \frac{\mathrm{d}\theta}{\sqrt{f(x)-g(\theta)}}. \end{aligned} \tag{F.16}$$

Finally the flux conservation can be written

$$\frac{1}{|x|} = \frac{1}{2\pi} \int_{\theta_m(x)}^{2\pi-\theta_m(x)} \frac{\mathrm{d}\theta}{\sqrt{f(x)-g(\theta)}}. \tag{F.17}$$

*Eqs.* (F.12) and (F.17) can be used to numerically determine $f$ and $g$ as a function of $\xi_0$, the MHD displacement. This in turn gives the range of $x$ in which $\max(G(\theta)) > f(x)$, that is, the position $x_s$ of the separatrix and the angle $\theta_0 = \theta_m(x_s)$ gives the angular extension of the island, and also the island width $W$. The results are [Zakharov 1993]

$$\theta_0 \simeq 60^\circ, \quad x_s = 0.4\xi_0, \quad W = 1.84\xi_0. \tag{F.18}$$

Appendix G

# The equilibrium electric field in the bifluid model

In XTOR-2F's toroidal and bifluid plasma, it is obvious to see that $v_{E\theta} = 0$ is not a fixed point of the system. Indeed, the divergence of the diamagnetic term is a large source term in the density and pressure equation. This induces pressure and density fluctuations which relax the system to its equilibrium. A first guess is $v_{E\theta} = -v^{\star}_{i\theta}$ so that $\nabla \cdot (n (\boldsymbol{v}_E + \boldsymbol{v}_i^{\star})) = 0$ . However the parallel compressibility must also be taken into account. By doing so, we will see that starting with $v_{E\theta} = v_{\parallel} = 0$, the electric field $\phi' = B_0 v_{E\theta}$ relaxes to a slightly different equilibrium by emitting GAMs. The GAMs are damped by the parallel diffusion, on a very fast time scale.

We will need of course the momentum equation, projected on the $\theta$ and parallel directions. Then we will write the pressure and density fluctuation equations. We will not write the advection terms, because they do not couple to the same harmonics. Indeed, the relevant toroidal coupling term, the divergence of the diamagnetic flux, is proportional to $\sin\theta$, so the induced fluctuations on the pressure are also $\propto \sin\theta$, whereas advection terms are $\propto \cos\theta$. This will eventually generate a cosine component in the pressure but we expect it to be smaller and we can check in the code that indeed the sine component clearly dominates in the pressure. On the contrary, the parallel velocity is clearly dominated by the cosine component. The scalars are written $f = f_0 + f_1 g(\theta)$, where $g(\theta)$ is $\cos\theta$ for the parallel velocity and $\sin\theta$ for pressure and density fluctuations (and pressure, temperature and density are related by $p = nT$). The poloidal component of the $\mathbf{E} \times \mathbf{B}$ velocity is now written simply $v_\theta$.

The poloidal and parallel momentum equations, the density and temperature equations read:

$$nm\partial_t v_\theta = j_r B_\varphi - \frac{\partial_\theta p}{r} \tag{G.1}$$

$$nm\partial_t v_{\parallel} = -\nabla_{\parallel} p. \tag{G.2}$$

$$\partial_t n = -n\left(\nabla\phi + \frac{\nabla p}{ne}\right) \cdot \nabla \times \frac{\mathbf{B}}{B^2} - n\nabla \cdot v_{\parallel}\mathbf{b} \tag{G.3}$$

$$\partial_t T = -\frac{3}{2}T\left(\nabla\phi + \frac{\nabla p}{ne}\right) \cdot \nabla \times \frac{\mathbf{B}}{B^2} - T\nabla \cdot v_{\parallel}\mathbf{b} - \chi_{\parallel}\nabla_{\parallel}^2 T \tag{G.4}$$

Before going any further, these equations need some remarks. First note that the problem is related to the absence of invariance in the $\theta$ direction, contrary to the $\phi$ direction. Thus the couplings are between poloidal modes. The toroidal derivatives can be omitted even

for the perturbed quantities. Also, the remarks above about which terms to retain become more evident. We are looking for the $\mathsf{m} = 0$ component of the poloidal velocity, thus it is obvious that the curvature term couples to the $\mathsf{m} = 1$ component of the parallel velocity. The parallel velocity also has an $\mathsf{m} = 0$ component but at the next order in aspect ratio, so we will neglect it. In the following we consider only the $\mathsf{m} = 0$ component of $v_\theta$, and the $\mathsf{m} = 1$ component of $v_\parallel$. We have $v_\theta = \phi_0'/B_0$, and the two notations will be used in the following. Notice that we have also neglected the perpendicular diffusion. Neglecting $\nabla \times \mathbf{B}$ in front of $\nabla B$ for low $\beta$ plasmas, the total curvature term can be written

$$\left(\nabla\phi + \frac{\nabla p}{ne}\right) \cdot \nabla \times \frac{\mathbf{B}}{B^2} = -\frac{2}{R_0 B_0}\left(\phi_0' + \frac{p_0'}{ne}\right)\sin\theta. \tag{G.5}$$

The radial current can be eliminated considering that the total radial current crossing a given flux surface vanishes:

$$\oint_{r=C^{te}} j_r R \mathrm{d}\theta = 0. \tag{G.6}$$

Thus using the $1/R$ dependence of $B_\varphi$, we multiply *Eq.* (G.1) by $R^2$ and integrate over $\theta$, which yields:

$$nm \oint \partial_t v_\theta R^2 \mathrm{d}\theta = -\oint \frac{p_1}{r}\cos\theta(R_0 + r\cos\theta)^2 \mathrm{d}\theta, \tag{G.7}$$

so that $n_0 m \partial_t v_\theta = -p_1/R_0$. *Eq.* (G.2), written $nm\partial_t v_\parallel = -\partial_\theta p/qR_0$, together with the condition $v_\theta(t=0) = v_\parallel(t=0) = 0$, thus becomes

$$q v_\parallel = v_\theta = \frac{\phi'}{B_0}. \tag{G.8}$$

Now $v_\parallel$ can be replaced in *Eq.* (G.3) and *Eq.* (G.4), noting that $\nabla_\parallel = \partial_\theta/(qR)$, and the system coupling $n_1$, $T_1$, $p_1$ and $\phi'$ can be written

$$\partial_t n_1 = \frac{2n_0}{R_0 B_0}\left(\sigma\phi_0' + \frac{p_0'}{n_0 e}\right) \tag{G.9}$$

$$\partial_t T_1 = -\frac{3}{2}T_0\left(\sigma\phi_0' + \frac{p_0'}{n_0 e}\right) - \chi_\parallel \nabla_\parallel^2 T_1 \tag{G.10}$$

$$\frac{n_0 m}{B_0}\partial_t \phi' = -\frac{p_1}{R_0} \tag{G.11}$$

$$p_1 = T_0 n_1 + n_0 T_1, \tag{G.12}$$

with $\sigma = 1 + 1/(2q^2)$.

The fixed point of this system of equations can be readily determined as

$$\phi_{0,\mathrm{eq}}' = -\frac{2q^2}{1+2q^2}\frac{p_0'}{n_0 e}, \tag{G.13}$$

or

$$v_{\theta,\mathrm{eq}} = -\frac{2q^2}{1+2q^2} v^\star_{i\theta}. \tag{G.14}$$

Also, the dispersion relation reads

$$\omega^2 = \omega_0^2 - i\frac{\omega_c}{\omega}\left(\omega^2 - \frac{2}{5}\omega_0^2\right), \tag{G.15}$$

with

$$\omega_0^2 = 3\Gamma\frac{T_0}{mR_0^2} \tag{G.16}$$

$$\omega_c = \frac{\chi_\parallel}{q^2 R_0^2}. \tag{G.17}$$

The pulsation $\omega_0$ is the GAM pulsation. Thus in this model the system relaxes toward the equilibrium by emitting GAMs and the dissipation occurs through the parallel diffusivity, which is large. In XTOR-2F, $\omega_c/\omega_0$ is large so that the oscillations have the time to live many cycles but $(\omega_0\tau_A)^{-1} \sim (a/R_0)^{-2} \sim 10$ so that the oscillations are still rapidly damped, after a few hundreds of $\tau_A$. Fig. G.1 displays a comparison between $v_\theta$ and *Eq.* (G.14) after the equilibrium has been reached in XTOR-2F. A very good agreement is found, within 3% everywhere. However considering the aspect ratio expansion carried out, the agreement could be expected to be better for small $r/a$ than for the plasma edge.

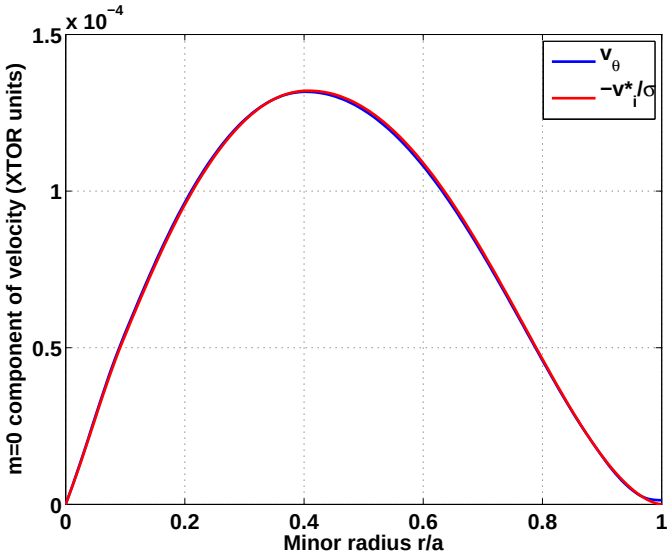


Figure G.1: Radial profiles of $v_{\theta,\mathrm{eq}}$ (blue curve) and $-2q^2/(1+2q^2)v^\star_{i\theta}$ (red curve). The agreement is within 3% everywhere.

Appendix H

# Diamagnetic asymmetry of an impurity

In this appendix, it will be shown how an asymmetry in the density of an impurity with $Z \neq 1$ arises as soon as diamagnetic effects are taken into account. This asymmetry will be found to be small, maximum a few percents. It was shown in appendix G how the system produces a perpendicular flow $v_\theta$ and a parallel flow $v_\parallel = v_\theta/q$ in order to compensate for the toroidal compressibility of the diamagnetic flow. In other words the combination

$$C \equiv \left(\nabla\phi + \frac{\nabla p}{ne}\right) \cdot \nabla \times \frac{\mathbf{B}}{B^2} + \nabla \cdot v_\parallel \mathbf{b} \tag{H.1}$$

must vanish. Now let us write the equation verified by the impurity density and parallel velocity, in physical units. Diffusion and pinch are not taken into account.

$$\partial_t n_Z = -\boldsymbol{v}_\perp \cdot \nabla n_Z - V_{\parallel Z}\nabla_\parallel n_Z - n_Z \left(\nabla\phi + \frac{\nabla p_Z}{Z n_Z e}\right) \cdot \nabla \times \frac{\mathbf{B}}{B^2} - n_Z \nabla \cdot V_{\parallel Z}\mathbf{b} \tag{H.2}$$

$$\partial_t V_{\parallel Z} = -\frac{\nabla_\parallel p_Z}{n_Z m_Z} - \frac{Z\nabla_\parallel p_e}{n m_Z} + \nu\left(v_\parallel - V_{\parallel Z}\right). \tag{H.3}$$

In these equations, $p_Z = n_Z T$ is the impurity pressure, computed with the plasma temperature, since the impurity is assumed to be thermalized. The friction $\nu$ in *Eq.* (H.3) tends to align the impurity parallel velocity on that of the main plasma. However, it is seen that such a process is not viable. Indeed, since the diamagnetic term is divided by $Z$ for the impurity, if $v_\parallel = V_{\parallel Z}$, the impurity compressibility does not vanish anymore if $C = 0$ and $Z \neq 1$. Therefore there is a trade-off between the friction and the asymmetries produced by the compressibility, which we will now investigate in more details. In this case, contrary to appendix G, we must add the advection by the $\mathbf{E}\times\mathbf{B}$ flow, but still the parallel advection is neglected. Indeed we expect the poloidal perturbation to be a sum of sine and cosine functions because of *Eq.* (H.3). However the parallel advection gives $\mathsf{m} = 0$ and $\mathsf{m} = 2$ contributions and thus will be disregarded.

We jump immediately to the search for the equilibrium point of the system. The density perturbation is $n_1 = \Re(\underline{n_Z} e^{i\theta})$ and the parallel velocity is $V_{\parallel Z1} = \Re(\underline{V_{\parallel Z}} e^{i\theta})$, while the initial $\mathsf{m} = 0$ component of the impurity density is denoted $n_{Z0}$. The main plasma quantities are assumed to be given. In particular, $C = 0$ and $v_\parallel = v_\theta/q = \phi'/qB_0$, $\nabla_\parallel p_e = 0$. The algebra is similar to appendix G, except that $\sin\theta$ in the curvature term is written $\Re(-ie^{i\theta})$. Thus after proper linearization, the perturbations verify

$$\frac{\phi'}{rB_0}\underline{n_Z} + \frac{2n_{Z0}}{R_0 B_0}\left(\phi' + \frac{(n_{Z0}T)'}{Z n_{Z0}}\right) + \frac{n_{Z0}}{qR_0}\underline{V_{\parallel Z}} = 0 \tag{H.4}$$

$$\frac{T}{\nu n_{Z0} m_Z q R}\underline{n_Z} = i\left(\underline{V_{\parallel Z}} - \frac{\phi'}{qB_0}\right), \tag{H.5}$$

from which the following result can be driven :

$$\left(1+i\sigma\frac{\omega_0^2}{\nu\omega_i^\star}\right)\frac{n_Z}{n_{Z0}} = -2\sigma\frac{r}{R_0}\left(1-\frac{1}{Z}\frac{(n_{Z0}T)'}{n_{Z0}T'}\frac{\omega_{Ti}^\star}{\omega_i^\star}\right), \tag{H.6}$$

with $\sigma = 1+1/(2q^2)$ as in appendix G, $\omega_0^2 = T/(m_Z q^2 R_0^2)$, and $\omega_{Ti}^\star = T'/(reB_0)$. Obviously the parenthesis in the *r.h.s* of *Eq.* (H.6) is of order $1-1/Z \underset{Z\to\infty}{\longrightarrow} 1$, which makes the result convenient for high $Z$ impurities like Tungsten.

This formula can easily be applied to the two limiting cases depending on the value of the friction.

When $\nu \gg \omega_0^2/\omega_i^\star$, $V_{\|Z} = v_\|$ and the impurity exhibits a significant LFS/HFS asymmetry

$$\left|\frac{\delta n_Z}{n_Z}\right| \simeq -2\sigma\frac{r}{R_0}\cos\theta. \tag{H.7}$$

Thus the density is more important on the HFS.

When $\nu \ll \omega_0^2/\omega_i^\star$, the impurity exhibits a top/bottom asymmetry,

$$\left|\frac{\delta n_Z}{n_Z}\right| \simeq 2\frac{r}{R_0}\frac{\nu\omega_i^\star}{\omega_0^2}\sin\theta \propto \nu A \propto Z^2. \tag{H.8}$$

The density is more important on the top part of the tokamak, and tends to increase with the square of the charge of the impurity.

As we shall see immediately, the latter case is more common given typical collision frequencies. Let us normalize the frequencies to the Alfvén time $\tau_A = R_0\sqrt{\mu_0\rho_0}/B_0$:

$$\begin{aligned} 2\frac{r}{R_0}\frac{\nu\omega_i^\star}{\omega_0^2} &= 2(\nu\tau_A)\frac{r\omega_i^\star}{R_0\omega_0^2\tau_A} \\ &\sim (\nu\tau_A)\frac{2T}{aeB_0}\frac{q^2R_0m_Z}{T\tau_A} \\ &\sim (\nu\tau_A)A\frac{1}{\omega_{ci}\varepsilon\tau_A} \\ &\sim (\nu A\tau_A)\alpha, \end{aligned} \tag{H.9}$$

where $\alpha$ is the quantity used in XTOR-2F to scale diamagnetic effects, typically $\alpha = 0.05-0.1$ and $\varepsilon = a/R_0$. Since obviously $\nu A\tau_A \ll 1$, and $\nu \propto Z^2/A$, it is seen that very high values of $Z$ are required for the effect to be observable. With the friction $\nu$ obtained from NRL formulary [Huba 2007] for Tungsten, $\nu\tau_A \simeq 5\times10^{-4}$, an asymmetry $|\delta n_Z|/n_Z \sim 0.5-1\%$ can be expected. The case of *Eq.* (H.7) is probably never encountered given the typical values of the friction. However other mechanisms are responsible for such HFS/LFS asymmetries.

# Bibliography


[Angioni 2006] C. Angioni and A. G. Peeters. *Direction of Impurity Pinch and Auxiliary Heating in Tokamak Plasmas.* Phys. Rev. Lett., vol. 96, page 095003, Mar 2006. (Cited on page 186.)

[Ara 1978] G. Ara, B. Basu, B. Coppi, G. Laval, M.N. Rosenbluth and B.V. Waddell. *Magnetic reconnection and m = 1 oscillations in current carrying plasmas.* Ann. Phys. (N.Y.), vol. 112, no. 2, pages 443 – 476, 1978. (Cited on pages 19, 51, 53, 56, 99, 152 and 210.)

[Arakawa 1966] A. Arakawa. *Computational design for long-term numerical integration of the equations of fluid motion: Two-dimensional incompressible flow. Part I.* J. Comput. Phys., vol. 1, no. 1, pages 119 – 143, 1966. (Cited on page 84.)

[Asmussen 1998] Knut Asmussen, KB Fournier, JM Laming, R Neu, JF Seely, R Dux, W Engelhardt, JC Fuchs and ASDEX Upgrade Team. *Spectroscopic investigations of tungsten in the EUV region and the determination of its concentration in tokamaks.* Nucl. Fusion, vol. 38, no. 7, page 967, 1998. (Cited on page 193.)

[Aydemir 1992] A.Y. Aydemir. *Nonlinear Studies Of M=1 Modes in High-Temperature Plasmas.* Phys. Fluids B-Plasma, vol. 4, no. 11, pages 3469–3472, NOV 1992. (Cited on pages 20 and 99.)

[Barnes 2012] M. Barnes, F. I. Parra and W. Dorland. *Turbulent Transport and Heating of Trace Heavy Ions in Hot Magnetized Plasmas.* Phys. Rev. Lett., vol. 109, page 185003, Oct 2012. (Cited on page 186.)

[Beidler 2011] Matthew T Beidler and Paul A Cassak. *Model for Incomplete Reconnection in Sawtooth Crashes.* Phys. Rev. Lett., vol. 107, no. 25, page 255002, 2011. (Cited on page 138.)

[Belo 2004] P Belo, V Parail, G Corrigan, D Heading, W Houlberg, P Monier-Garbet, J Ongena and JET EFDA contributors. *Impurity penetration through the edge transport barrier.* Plasma Phys. Contr. F., vol. 46, no. 8, page 1299, 2004. (Cited on pages 94, 175 and 178.)

[Bergerson 2012] W. F. Bergerson, P. Xu, J. H. Irby, D. L. Brower, W. X. Ding and E. S. Marmar. *Far-infrared polarimetry diagnostic for measurement of internal magnetic field dynamics and fluctuations in the C-MOD Tokamak (invited).* Rev. Sci. Instrum., vol. 83, no. 10, page 10E316, 2012. (Cited on page 133.)

[Bernstein 1958] Ira B Bernstein, EA Frieman, MD Kruskal and RM Kulsrud. *An energy principle for hydromagnetic stability problems.* Proceedings of the Royal Society of London. Series A. Mathematical and Physical Sciences, vol. 244, no. 1236, pages 17–40, 1958. (Cited on page 43.)

[Bhatnagar 1989] V P Bhatnagar, A Taroni, J J Ellis, J Jacquinot and D F H Start. *ICRF power-deposition profiles, heating and confinement of monster sawtooth and peaked-density profile discharges in JET*. Plasma Phys. Contr. F., vol. 31, no. 14, page 2111, 1989. (Cited on page 129.)

[Biskamp 1994] D. Biskamp and J. F. Drake. *Dynamics of the Sawtooth Collapse in Tokamak Plasmas*. Phys. Rev. Lett., vol. 73, pages 971–974, Aug 1994. (Cited on pages 20, 31, 139, 148 and 194.)

[Biskamp 2000] D. Biskamp. Magnetic reconnection in plasmas. Cambridge University Press, 2000. (Cited on pages 34, 64 and 67.)

[Braginskii 1965] S. I. Braginskii. *Transport Processes in a Plasma*. Rev. Mod. Phys., vol. 1, page 205, 1965. (Cited on pages 29 and 35.)

[Bussac 1975] M.N. Bussac, R. Pellat, D. Edery and J.L. Soule. *Internal Kink Modes in Toroidal Plasmas with Circular Cross Sections*. Phys. Rev. Lett., vol. 35, pages 1638–1641, Dec 1975. (Cited on pages 19, 42 and 56.)

[Buttery 2004] RJ Buttery, TC Hender, DF Howell, RJ La Haye, S Parris, O Sauter, CG Windsor and JET-EFDA Contributors. *On the form of NTM onset scalings*. Nucl. Fusion, vol. 44, no. 5, page 678, 2004. (Cited on page 20.)

[Campbell 1988] D. J. Campbell, D. F. H. Start, J. A. Wesson, D. V. Bartlett, V. P. Bhatnagar, M. Bures, J. G. Cordey, G. A. Cottrell, P. A. Dupperex, A. W. Edwards, C. D. Challis, C. Gormezano, C. W. Gowers, R. S. Granetz, J. H. Hammen, T. Hellsten, J. Jacquinot, E. Lazzaro, P. J. Lomas, N. Lopes Cardozo, P. Mantica, J. A. Snipes, D. Stork, P. E. Stott, P. R. Thomas, E. Thompson, K. Thomsen and G. Tonetti. *Stabilization of Sawteeth with Additional Heating in the JET Tokamak*. Phys. Rev. Lett., vol. 60, pages 2148–2151, May 1988. (Cited on page 129.)

[Chang 1992] Zuoyang Chang and JD Callen. *Unified fluid/kinetic description of plasma microinstabilities. Part I: Basic equations in a sheared slab geometry*. Phys. Fluids B-Plasma, vol. 4, page 1167, 1992. (Cited on page 29.)

[Chang 1998] S. Chang, G.H. Miley and C.E. Singer. *Controlled sawteeth for helium exhaust*. Fusion Technol., vol. 33, no. 4, pages 387–397, JUL 1998. (Cited on page 176.)

[Chapman 2010a] I.T. Chapman, R.J. Buttery, S. Coda, S. Gerhardt, J.P. Graves, D.F. Howell, A. Isayama, R.J. La Haye, Y. Liu, P. Maget, M. Maraschek, S. Sabbagh, O. Sauter, the ASDEX Upgrade, DIII-D, HL-2A, JT-60U, MAST, NSTX, TCV, Tore Supra Teams and JET-EFDA Contributors. *Empirical scaling of sawtooth period for onset of neoclassical tearing modes*. Nucl. Fusion, vol. 50, no. 10, page 102001, 2010. (Cited on pages 21, 61 and 129.)

[Chapman 2010b] I.T. Chapman, R. Scannell, W.A. Cooper, J.P. Graves, R.J. Hastie, G. Naylor and A. Zocco. *Magnetic Reconnection Triggering Magnetohydrodynamic Instabilities during a Sawtooth Crash in a Tokamak Plasma.* Phys. Rev. Lett., vol. 105, page 255002, Dec 2010. (Cited on page 129.)

[Chapman 2011] I T Chapman. *Controlling sawtooth oscillations in tokamak plasmas.* Plasma Phys. Contr. F., vol. 53, no. 1, page 013001, 2011. (Cited on pages 21, 59 and 194.)

[Chapman 2013] I.T. Chapman, J.P. Graves, O. Sauter, C. Zucca, O. Asunta, R.J. Buttery, S. Coda, T. Goodman, V. Igochine, T. Johnson, M. Jucker, R.J. La Haye, M. Lennholm and JET-EFDA Contributors. *Power requirements for electron cyclotron current drive and ion cyclotron resonance heating for sawtooth control in ITER.* Nucl. Fusion, vol. 53, no. 6, page 066001, 2013. (Cited on page 60.)

[Chen 1984] Liu Chen, R. B. White and M. N. Rosenbluth. *Excitation of Internal Kink Modes by Trapped Energetic Beam Ions.* Phys. Rev. Lett., vol. 52, pages 1122–1125, Mar 1984. (Cited on page 56.)

[Ciric 2011] D. Ciric, A.D. Ash, B. Crowley, I.E. Day, S.J. Gee, L.J. Hackett, D.A. Homfray, I. Jenkins, T.T.C. Jones, D. Keeling, D.B. King, R.F. King, M. Kovari, R. McAdams, E. Surrey, D. Young and J. Zacks. *Performance of upgraded {JET} neutral beam injectors.* Fusion Eng. Des., vol. 86, no. 6–8, pages 509 – 512, 2011. (Cited on page 118.)

[Clairet 2011] F Clairet, B Ricaud, F Briolle, S Heuraux and C Bottereau. *New signal processing technique for density profile reconstruction using reflectometry.* Rev. Sci. Instrum., vol. 82, no. 8, pages 083502–083502, 2011. (Cited on page 113.)

[Connor 1985] JW Connor and RJ Hastie. *The effect of shaped plasma cross sections on the ideal internal kink mode in a tokamak.* Rep. CLM-M-106, Culham Laboratory, Abingdon, Oxfordshire, 1985. (Cited on page 42.)

[Cooper 2011] WA Cooper, JP Graves, O Sauter, J Rossel, M Albergante, S Coda, BP Duval, B Labit, A Pochelon, H Reimerdes*et al.* *Helical core tokamak MHD equilibrium states.* Plasma Phys. Contr. F., vol. 53, no. 12, page 124005, 2011. (Cited on page 138.)

[Coppi 1989] B. Coppi, P. Detragiache, S. Migliuolo, F. Pegoraro and F. Porcelli. *Quiescent window for global plasma modes.* Phys. Rev. Lett., vol. 63, pages 2733–2736, Dec 1989. (Cited on page 56.)

[Coppi 1990] B. Coppi, S. Migliuolo and Y-K. Pu. *Candidate mode for electron thermal energy transport in multi-keV plasmas.* Phys. Fluids B-Plasma, vol. 2, no. 10, pages 2322–2333, 1990. (Cited on page 56.)

[Cristofani 1996] P. Cristofani. *Activité MHD associée à la surface q=1 dans le tokamak Tore Supra.* PhD thesis, 1996. (Cited on page 137.)

[De La Luna 2004] E De La Luna, J Sánchez, V Tribaldos, G Conway, W Suttrop, J Fessey, R Prentice, C Gowers, JM Chareau*et al. Electron cyclotron emission radiometer upgrade on the Joint European Torus (JET) tokamak.* Rev. Sci. Instrum., vol. 75, page 3831, 2004. (Cited on page 116.)

[Deblank 1991] H.J. Deblank and T.J. Schep. *Theory of the m = 1 kink mode in toroidal plasma.* Phys. Fluids B-Plasma, vol. 3, no. 5, pages 1136–1151, MAY 1991. (Cited on pages 19 and 42.)

[Delgado-Aparicio 2013] L. Delgado-Aparicio, L Sugiyama, R. Granetz, D. Gates, J. Rice, M.L. Reinke, W. Bergerson, M. Bitter, D.L. Brower, E. Fredrickson, C. Gao, M. Greenwald, K. Hill, A. Hubbard, J. Irby, J.W. Hughes, E. Marmar, N. Pablant, S. Scott, R. Wilson, S. Wolfe and S. Wukitch. *On the formation and stability of long-lived impurity-ion snakes in Alcator C-Mod.* Nucl. Fusion, vol. 53, no. 4, page 043019, 2013. (Cited on page 136.)

[Drake 1991] J. F. Drake and R. G. Kleva. *Collisionless reconnection and the sawtooth crash.* Phys. Rev. Lett., vol. 66, pages 1458–1461, Mar 1991. (Cited on page 31.)

[Duval 2010] B. P. Duval, A. Bortolon, L. Federspiel, F. Felici, I. Furno, A. Karpushov, J. Paley, F. Piras and the TCV team. *Momentum Transport in TCV Across Sawteeth Events.* In $23^{rd}$ IAEA Fusion Energy Conf., Daejon (Rep. of Korea), October 2010. (Cited on page 132.)

[Dux 1999] R. Dux, A.G. Peeters, A. Gude, A. Kallenbach, R. Neu and ASDEX Upgrade Team. *Z dependence of the core impurity transport in ASDEX Upgrade H mode discharges.* Nucl. Fusion, vol. 39, no. 11, page 1509, 1999. (Cited on page 185.)

[Dux 2005] R. Dux, V. Bobkov, A. Kallenbach, K. Krieger, R. Neu, T. Pütterich, V. Petrzilka, V. Rohde, J. Stober and ASDEX Upgrade Team. *Tungsten Erosion at the Auxiliary Limiters in ASDEX Upgrade.* In $32^{nd}$ EPS Conf. on Plasma Phys., 2005. (Cited on page 142.)

[Dux 2007] R. Dux, V. Bobkov, N. Fedorczak, K. Iraschko, A. Kallenbach, R. Neu, T. Pütterich and V. Rohde. *Tungsten erosion at the ICRH limiters in ASDEX Upgrade.* J. Nucl. Mater., vol. 363–365, no. 0, pages 112 – 116, 2007. (Cited on page 142.)

[Edwards 1986] A. W. Edwards, D. J. Campbell, W. W. Engelhardt, H. U. Fahrbach, R. D. Gill, R. S. Granetz, S. Tsuji, B. J. D. Tubbing, A. Weller, J. Wesson and D. Zasche. *Rapid Collapse of a Plasma Sawtooth Oscillation in the JET Tokamak.* Phys. Rev. Lett., vol. 57, pages 210–213, Jul 1986. (Cited on pages 19, 123 and 124.)

[Fenzi 2011] C. Fenzi, X. Garbet, E. Trier, P. Hennequin, C. Bourdelle, T. Aniel, G. Colledani, P. Devynck, C. Gil, Oe. Guercan, L. Manenc, M. Schneider, J.-L. Segui and Tore Supra Team. *On plasma rotation with toroidal magnetic field*

*ripple and no external momentum input.* Nucl. Fusion, vol. 51, no. 10, OCT 2011. (Cited on page 159.)

[Fitzpatrick 1991] R. Fitzpatrick and T. C. Hender. *The interaction of resonant magnetic perturbations with rotating plasmas.* Phys. Fluids B-Plasma, vol. 3, no. 3, pages 644–673, 1991. (Cited on page 131.)

[Fitzpatrick 1995a] R. Fitzpatrick. *Driven Reconnection in Magnetic Fusion Experiments*, August 1995 (`http://farside.ph.utexas.edu/papers/error1.pdf`) (Cited on page 131.)

[Fitzpatrick 1995b] Richard Fitzpatrick. *Helical temperature perturbations associated with tearing modes in tokamak plasmas.* Phys. Plasmas, vol. 2, no. 3, pages 825–838, 1995. (Cited on page 131.)

[Furno 2001] I. Furno, C. Angioni, F. Porcelli, H. Weisen, R. Behn, T.P. Goodman, M.A. Henderson, Z.A. Pietrzyk, A. Pochelon, H. Reimerdes and E. Rossi. *Understanding sawtooth activity during intense electron cyclotron heating experiments on TCV.* Nucl. Fusion, vol. 41, no. 4, page 403, 2001. (Cited on pages 85, 176 and 193.)

[Garbet 2004] X. Garbet, P. Mantica, F. Ryter, G. Cordey, F. Imbeaux, C. Sozzi, A. Manini, E. Asp, V. Parail, R. Wolf and the JET EFDA Contributors. *Profile stiffness and global confinement.* Plasma Phys. Contr. F., vol. 46, no. 9, page 1351, 2004. (Cited on page 180.)

[Garbet 2009] X. Garbet, G. Dif-Pradalier, C. Nguyen, Y. Sarazin, V. Grandgirard and Ph. Ghendrih. *Neoclassical equilibrium in gyrokinetic simulations.* Phys. Plasmas, vol. 16, no. 6, JUN 2009. (Cited on page 158.)

[Garbet 2010] X. Garbet, J. Abiteboul, E. Trier, O. Gurcan, Y. Sarazin, A. Smolyakov, S. Allfrey, C. Bourdelle, C. Fenzi, V. Grandgirard, P. Ghendrih and P. Hennequin. *Entropy production rate in tokamaks with nonaxisymmetric magnetic fields.* Phys. Plasmas, vol. 17, no. 7, JUL 2010. (Cited on page 158.)

[Graves 2004] Jonathan P. Graves. *Influence of Asymmetric Energetic Ion Distributions on Sawtooth Stabilization.* Phys. Rev. Lett., vol. 92, page 185003, May 2004. (Cited on page 59.)

[Graves 2009] J. P. Graves, I. Chapman, S. Coda, L.-G. Eriksson and T. Johnson. *Sawtooth-Control Mechanism using Toroidally Propagating Ion-Cyclotron-Resonance Waves in Tokamaks.* Phys. Rev. Lett., vol. 102, page 065005, Feb 2009. (Cited on page 59.)

[Graves 2010] J. P. Graves, I. T. Chapman, S. Coda, T. Johnson, M. Lennholm and JET-EFDA Contributors. *A new sawtooth control mechanism relying on toroidally propagating ion cyclotron resonance frequency waves: Theory and Joint European*

*Torus tokamak experimental evidence.* Phys. Plasmas, vol. 17, no. 5, page 056118, 2010. (Cited on page 59.)

[Graves 2012] J.P. Graves, I.T. Chapman, S. Coda, M. Lennholm, M. Albergante and M. Jucker. *Control of magnetohydrodynamic stability by phase space engineering of energetic ions in tokamak plasmas.* Nat. Commun., vol. 3, Jan 2012. (Cited on pages 21, 61, 129 and 194.)

[Guirlet 2009] R. Guirlet, D. Villegas, T. Parisot, C. Bourdelle, X. Garbet, F. Imbeaux, D. Mazon and D. Pacella. *Anomalous transport of light and heavy impurities in Tore Supra ohmic, weakly sawtoothing plasmas.* Nucl. Fusion, vol. 49, no. 5, page 055007, 2009. (Cited on page 178.)

[Guirlet 2010] R. Guirlet, A. Sirinelli, T. Parisot, R. Sabot, J. F. Artaud, C. Bourdelle, X. Garbet, P. Hennequin, G. T. Hoang, F. Imbeaux, J. L. Segui, D. Mazon and D. Villegas. *Particle transport in low core turbulence Tore-Supra plasmas.* Nucl. Fusion, vol. 50, no. 9, page 095009, SEP 2010. (Cited on pages 149, 150, 151, 152, 171, 180 and 194.)

[Halpern 2011a] F.D. Halpern, D. Leblond, H. Lütjens and J.-F. Luciani. *Oscillation regimes of the internal kink mode in tokamak plasmas.* Plasma Phys. Contr. F., vol. 53, no. 1, page 015011, 2011. (Cited on pages 82 and 83.)

[Halpern 2011b] F.D. Halpern, H. Lütjens and J.-F. Luciani. *Diamagnetic thresholds for sawtooth cycling in tokamak plasmas.* Phys. Plasmas, vol. 18, no. 10, page 102501, OCT 2011. (Cited on pages 20, 82 and 83.)

[Hazeltine 2003] R. D. Hazeltine and J. D. Meiss. Plasma confinement. Dover Publications, Inc, Mineola (New York), 2003. (Cited on pages 32 and 40.)

[Hornig 1996] G. Hornig and K. Schindler. *Magnetic topology and the problem of its invariant definition.* Phys. Plasmas, vol. 3, no. 3, pages 781–791, 1996. (Cited on page 63.)

[Hornung 2013] G. Hornung. *Etude de la turbulence plasma par réflectometrie a balayage ultra rapide.* PhD thesis, 2013. (Cited on page 113.)

[Houlberg 1997] W.A. Houlberg, K.C. Shaing, S.P. Hirshman and M.C. Zarnstorff. *Bootstrap current and neoclassical transport in tokamaks of arbitrary collisionality and aspect ratio.* Phys. Plasmas, vol. 4, no. 9, pages 3230–3242, SEP 1997. (Cited on pages 150 and 151.)

[Huba 2007] J. D. Huba. *NRL Plasma Formulary.* Washington DC: Naval Research Laboratory, 2007. (Cited on pages 4, 6, 178, 186 and 226.)

[Hutchinson 1987] I. H. Hutchinson. Principles of plasma diagnostics. Cambridge university press, 1987. (Cited on page 116.)

[ITER 1999a] Physics Basis Editors ITER. *Chapter 1: Overview and summary.* Nucl. Fusion, vol. 39, no. 12, page 2137, 1999. (Cited on pages 12 and 178.)

[ITER 1999b] Physics Basis Editors ITER. *Chapter 2: Plasma confinement and transport.* Nucl. Fusion, vol. 39, no. 12, page 2175, 1999. (Cited on page 16.)

[Kadomtsev 1975] BB Kadomtsev. *On disruptive instability in tokamaks.* Sov. J. Plasma Phys., vol. 1, pages 710–715, 1975. (Cited on page 19.)

[Kadomtsev 1987] B.B. Kadomtsev. *Magnetic-Field Line Reconnection.* Rep. Prog. Phys., vol. 50, no. 2, pages 115–143, FEB 1987. (Cited on pages 24 and 176.)

[Knoll 2004] D.A. Knoll and D.E. Keyes. *Jacobian-free Newton–Krylov methods: a survey of approaches and applications.* J. Comput. Phys., vol. 193, no. 2, pages 357 – 397, 2004. (Cited on page 73.)

[Kolesnichenko 1992] Ya. I. Kolesnichenko, Yu. V. Yakovenko, D. Anderson, M. Lisak and F. Wising. *Sawtooth oscillations with the central safety factor, $q_0$, below unity.* Phys. Rev. Lett., vol. 68, pages 3881–3884, Jun 1992. (Cited on pages 138, 139 and 194.)

[Krieger 2011] K. Krieger, T. Lunt, R. Dux, A. Janzer, A. Kallenbach, H.W. Müller, R. Neu, T. Pütterich and V. Rohde. *Induced tungsten melting events in the divertor of ASDEX Upgrade and their influence on plasma performance.* J. Nucl. Mater., vol. 415, no. 1, Supplement, pages S297 – S300, 2011. (Cited on page 178.)

[Kruskal 1958] M. D. Kruskal and C. R. Oberman. *On the Stability of Plasma in Static Equilibrium.* Phys. Fluids, vol. 1, no. 4, pages 275–280, 1958. (Cited on page 56.)

[Lao 1985] L.L. Lao, H. St. John, R.D. Stambaugh, A.G. Kellman and W. Pfeiffer. *Reconstruction of current profile parameters and plasma shapes in tokamaks.* Nucl. Fusion, vol. 25, no. 11, page 1611, 1985. (Cited on page 70.)

[Levinton 1989] F. M. Levinton, R. J. Fonck, G. M. Gammel, R. Kaita, H. W. Kugel, E. T. Powell and D. W. Roberts. *Magnetic field pitch-angle measurments in the PBX-M tokamak using the motional Stark effect.* Phys. Rev. Lett., vol. 63, pages 2060–2063, Nov 1989. (Cited on pages 133 and 135.)

[Levinton 1993] F. M. Levinton, S. H. Batha, M. Yamada and M. C. Zarnstorff. *q-profile measurements in the Tokamak Fusion Test Reactor.* Phys. Fluids B-Plasma, vol. 5, no. 7, pages 2554–2561, 1993. (Cited on page 135.)

[Lichtenberg 1984] A.J. Lichtenberg. *Stochasticity as the mechanism for the disruptive phase of the m = 1 tokamak oscillations.* Nucl. Fusion, vol. 24, no. 10, page 1277, 1984. (Cited on page 140.)

[Lutjens 1996] H. Lutjens, A. Bondeson and O. Sauter. *The CHEASE code for toroidal MHD equilibria.* Comput. Phys. Commun., vol. 97, no. 3, pages 219–260, SEP 1996. (Cited on pages 27 and 69.)

[Lütjens 2009] H Lütjens, JF Luciani, D Leblond, F Halpern and P Maget. *Non-linear modeling of core MHD in tokamaks.* Plasma Phys. Contr. F., vol. 51, no. 12, page 124038, 2009. (Cited on page 20.)

[Lütjens 2010] H. Lütjens and J.-F. Luciani. *XTOR-2F: A fully implicit Newton-Krylov solver applied to nonlinear 3D extended MHD in tokamaks.* J. Comput. Phys., vol. 229, no. 21, pages 8130–8143, OCT 20 2010. (Cited on pages 69 and 73.)

[Maget 2005] P Maget, J-F Artaud, L-G Eriksson, G Huysmans, A Lazaros, P Moreau, M Ottaviani, J-L Segui and W Zwingmann. *MHD activity triggered by monster sawtooth crashes on Tore Supra.* Plasma Phys. Contr. F., vol. 47, no. 2, page 357, 2005. (Cited on page 129.)

[Malamud 1965] H. Malamud. *Measurement of Low Electron Density in Plasmas Using Laser Interferometry.* Rev. Sci. Instrum., vol. 36, no. 10, pages 1507–1508, 1965. (Cited on page 110.)

[Mattioli 1998] M. Mattioli, C. De Michelis and A.L. Pecquet. *Laser blow-off injected impurity transport in L mode Tore Supra plasmas.* Nucl. Fusion, vol. 38, no. 11, page 1629, 1998. (Cited on page 178.)

[Mazzucato 1998] E Mazzucato. *Microwave reflectometry for magnetically confined plasmas.* Rev. Sci. Instrum., vol. 69, no. 6, pages 2201–2217, 1998. (Cited on page 112.)

[Moreau 2000] Ph Moreau, F Clairet, JM Chareau, M Paume and C Laviron. *Ultrafast frequency sweep heterodyne reflectometer on the Tore Supra tokamak.* Rev. Sci. Instrum., vol. 71, no. 1, pages 74–81, 2000. (Cited on page 113.)

[Mukhovatov 2003] V Mukhovatov, M Shimada, A N Chudnovskiy, A E Costley, Y Gribov, G Federici, O Kardaun, A S Kukushkin, A Polevoi, V D Pustovitov, Y Shimomura, T Sugie, M Sugihara and G Vayakis. *Overview of physics basis for ITER.* Plasma Phys. Contr. F., vol. 45, no. 12A, page A235, 2003. (Cited on page 8.)

[Nagayama 1990] Y. Nagayama, R. Buchse, A. Cavallo, E.D. Fredrickson, A Janos, KM Mcguire, GK Petravic, C Sule and G Taylor. *Image Reconstructions of ECE and X-Ray Signals For High Beta-Plasmas on TFTR.* Rev. Sci. Instrum., vol. 61, no. 10, Part 2, pages 3265–3267, OCT 1990. (Cited on page 114.)

[Nakano 2009] T. Nakano, N. Asakura, H. Kubo, J. Yanagibayashi and Y. Ueda. *Tungsten accumulation in H-mode plasmas of JT-60U.* Nucl. Fusion, vol. 49, no. 11, page 115024, 2009. (Cited on pages 94 and 175.)

[Nave 2003] M.F.F. Nave, J. Rapp, T. Bolzonella, R. Dux, M.J. Mantsinen, R. Budny, P. Dumortier, M. von Hellermann, S. Jachmich, H.R. Koslowski, G. Maddison, A. Messiaen, P. Monier-Garbet, J. Ongena, M.E. Puiatti, J. Strachan, G. Telesca, B. Unterberg, M. Valisa, P. de Vries and contributors to the JET-EFDA Workprogramme. *Role of sawtooth in avoiding impurity accumulation and maintaining*

*good confinement in JET radiative mantle discharges.* Nucl. Fusion, vol. 43, no. 10, page 1204, 2003. (Cited on pages 94, 175 and 178.)

[Nicolas 2012] T. Nicolas, R. Sabot, X. Garbet, H. Lutjens, J.-F. Luciani, Z. Guimaraes-Filho, J. Decker and A. Merle. *Non-linear magnetohydrodynamic simulations of density evolution in Tore Supra sawtoothing plasmas.* Phys. Plasmas, vol. 19, no. 11, page 112305, 2012. (Cited on page 149.)

[Nicolas 2013] T. Nicolas, R. Sabot, X. Garbet, H. Lutjens, J.-F. Luciani, Z. Guimaraes-Filho, J. Decker and A. Merle. *Non-linear magnetohydrodynamic simulations of density evolution in Tore Supra sawtoothing plasmas,* accepted in Plasma and Fusion Research. 2013. (Cited on page 149.)

[O'Rourke 1991] J O'Rourke. *The change in the safety factor profile at a sawtooth collapse.* Plasma Phys. Contr. F., vol. 33, no. 4, page 289, 1991. (Cited on page 134.)

[Parker 1963] E. N. Parker. *The Solar-Flare Phenomenon and the Theory of Reconnection and Annihiliation of Magnetic Fields.* Astrophys. J. Suppl. Ser., vol. 8, page 177, July 1963. (Cited on pages 24 and 65.)

[Pecquet 1997] A-L Pecquet, P Cristofani, M Mattioli, X Garbet, L Laurent, A Geraud, C Gil, E Joffrin and R Sabot. *Snake-like phenomena in Tore Supra following pellet injection.* Nucl. Fusion, vol. 37, no. 4, page 451, 1997. (Cited on page 136.)

[Pegoraro 1989] F. Pegoraro, F. Porcelli and T. J. Schep. *Internal kink modes in the ion-kinetic regime.* Phys. Fluids B-Plasma, vol. 1, no. 2, pages 364–374, 1989. (Cited on page 58.)

[Pernice 1998] M Pernice and HF Walker. *NITSOL: A Newton iterative solver for nonlinear systems.* Siam J. Sci. Comput., vol. 19, no. 1, pages 302–318, JAN 1998. (Cited on page 73.)

[Pitts 2011] R.A. Pitts, S. Carpentier, F. Escourbiac, T. Hirai, V. Komarov, A.S. Kukushkin, S. Lisgo, A. Loarte, M. Merola, R. Mitteau, A.R. Raffray, M. Shimada and P.C. Stangeby. *Physics basis and design of the {ITER} plasma-facing components.* J. Nucl. Mater., vol. 415, no. 1, Supplement, pages S957 – S964, 2011. <ce:title>Proceedings of the 19th International Conference on Plasma-Surface Interactions in Controlled Fusion</ce:title>. (Cited on page 15.)

[Porcelli 1991] F Porcelli. *Fast particle stabilisation.* Plasma Phys. Contr. F., vol. 33, no. 13, page 1601, 1991. (Cited on pages 56 and 57.)

[Porcelli 1996] F. Porcelli, D. Boucher and M.N. Rosenbluth. *Model for the sawtooth period and amplitude.* Plasma Phys. Contr. F., vol. 38, no. 12, page 2163, 1996. (Cited on pages 19, 58, 168, 170, 186 and 194.)

[Porcelli 1999] F. Porcelli, E. Rossi, G. Cima and A. Wootton. *Macroscopic Magnetic Islands and Plasma Energy Transport.* Phys. Rev. Lett., vol. 82, pages 1458–1461, Feb 1999. (Cited on pages 85 and 176.)

[Priest 2000] E Priest and T. Forbes. Magnetic reconnection. Cambridge University Press, 2000. (Cited on page 39.)

[Puiatti 2003] M E Puiatti, M Valisa, M Mattioli, T Bolzonella, A Bortolon, I Coffey, R Dux, M von Hellermann, P Monier-Garbet, M F F Nave, J Ongena and contributors to the EFDA-JET Workprogramme. *Simulation of the time behaviour of impurities in JET Ar-seeded discharges and its relation with sawtoothing and RF heating.* Plasma Phys. Contr. F., vol. 45, no. 12, page 2011, 2003. (Cited on page 178.)

[Pütterich 2008] T Pütterich, R Neu, R Dux, AD Whiteford, MG O'Mullane*et al. Modelling of measured tungsten spectra from ASDEX Upgrade and predictions for ITER.* Plasma Phys. Contr. F., vol. 50, no. 8, page 085016, 2008. (Cited on pages 186 and 193.)

[Pütterich 2010] T. Pütterich, R. Neu, R. Dux, A.D. Whiteford, M.G. O'Mullane, H.P. Summers and the ASDEX Upgrade Team. *Calculation and experimental test of the cooling factor of tungsten.* Nucl. Fusion, vol. 50, no. 2, page 025012, 2010. (Cited on pages 17, 141, 175 and 193.)

[Pütterich 2012] T. Pütterich, R. Dux, M. N. A. Beurskens, V. Bobkov, S. Brezinsek, J. Bucalossi, J. W. Coenen, I. Coffey, A. Czarnecka, C. Giroud, E. Joffrin, K. D. Lawson, M. Lehnen, E. de la Luna, J. Mailloux, S. Marsen, M.-L. Mayoral, A. Meigs, R. Neu, F. Rimini, M. Sertoli, M. Stamp, G. van Rooij and JET EFDA Contributors. *Tungsten screening and impurity control in JET.* In $24^{th}$ IAEA Fusion Energy Conf., San Diego (USA), October 2012. (Cited on pages 143, 145 and 175.)

[Ramos 2005] Jesus J Ramos. *General expression of the gyroviscous force.* Phys. Plasmas, vol. 12, page 112301, 2005. (Cited on page 40.)

[Redi 1991] M.H. Redi, S.A. Cohen and E.J. Synakowski. *Transport simulations of helium exhaust in ITER using recent data from TFTR, TEXTOR and JT-60.* Nucl. Fusion, vol. 31, no. 9, page 1689, 1991. (Cited on page 176.)

[Rogers 1995] B. Rogers and L. Zakharov. *Nonlinear omega$^\star$-stabilization of the m=1 mode in tokamaks.* Phys. Plasmas, vol. 2, no. 9, pages 3420–3428, 1995. (Cited on pages 20 and 99.)

[Rosenbluth 1973] M.N. Rosenbluth, R.Y. Dagazian and P.H. Rutherford. *Nonlinear Properties Of Internal M = 1 Kink Instability in Cylindrical Tokamak.* Phys. Fluids, vol. 16, no. 11, pages 1894–1902, 1973. (Cited on page 20.)

[Sabot 2006] R. Sabot, A. Sirinelli, J.-M. Chareau and J.-C. Giacalone. *A dual source D-band reflectometer for density profile and fluctuations measurements in Tore-Supra.* Nucl. Fusion, vol. 46, no. 9, pages S685–S692, SEP 2006. 7th International Reflectometry Workshop for Fusion Plasma Diagnostics (IRW7), Max Plank Inst Plasmaphys, Garching, GERMANY, MAY 09-12, 2005. (Cited on page 113.)

[Sabot 2010] R. Sabot, F. Halpern, T. Ristorcelli, Z. O. Guimaraes-Filho, H. Lütjens, D. Elbeze, P. Maget, X. Garbet and J.-C. Giacalone. *Tomographic reconstruction of the core density profile during sawtooth oscillations.* In $37^{th}$ EPS Conf. on Plasma Phys., Dublin (Ireland), 2010. (Cited on page 145.)

[Sauter 2002] O. Sauter, E. Westerhof, M. L. Mayoral, B. Alper, P. A. Belo, R. J. Buttery, A. Gondhalekar, T. Hellsten, T. C. Hender, D. F. Howell, T. Johnson, P. Lamalle, M. J. Mantsinen, F. Milani, M. F. F. Nave, F. Nguyen, A. L. Pecquet, S. D. Pinches, S. Podda and J. Rapp. *Control of Neoclassical Tearing Modes by Sawtooth Control.* Phys. Rev. Lett., vol. 88, page 105001, Feb 2002. (Cited on page 129.)

[Ségui 2005] JL Ségui, D Molina, G Giruzzi, M Goniche, G Huysmans, P Maget and M Ottaviani. *An upgraded 32-channel heterodyne electron cyclotron emission radiometer on Tore Supra.* Rev. Sci. Instrum., vol. 76, no. 12, pages 123501–123501, 2005. (Cited on page 116.)

[Simonet 1985] F. Simonet. *Measurement of electron density profile by microwave reflectometry on tokamaks.* Rev. Sci. Instrum., vol. 56, no. 5, pages 664–669, 1985. (Cited on page 110.)

[Soltwisch 1988] H. Soltwisch. *Measurement of current density changes during sawtooth activity in a tokamak by far-infrared polarimetry (invited).* Rev. Sci. Instrum., vol. 59, no. 8, pages 1599–1604, 1988. (Cited on pages 134 and 135.)

[Sweet 1958] P.A. Sweet. *The production of high energy particles in solar flares.* Il Nuovo Cimento, vol. 8, no. 2, pages 188–196, 1958. (Cited on pages 24 and 65.)

[Swisdak 2003] M Swisdak, BN Rogers, JF Drake and MA Shay. *Diamagnetic suppression of component magnetic reconnection at the magnetopause.* J. Geophys. Res.-Space., vol. 108, no. A5, 2003. (Cited on page 138.)

[Tomabechi 1991] K. Tomabechi, J.R. Gilleland, Yu.A. Sokolov, R. Toschi and ITER Team. *ITER conceptual design.* Nucl. Fusion, vol. 31, no. 6, page 1135, 1991. (Cited on page 175.)

[Udintsev 2005] V.S. Udintsev, M. Ottaviani, P. Maget, G. Giruzzi, J.-L. Ségui, T. Aniel, J.-F. Artaud, F. Clairet, M. Goniche, G. T. Hoang, G. T. A. Huysmans, F. Imbeaux, E. Joffrin, D. Mazon, A.-L. Pecquet, R. Sabot, A. Sirinelli, L. Vermare, Tore Supra Team, A. Krämer-Flecken, H. R. Koslowski, TEXTOR Team, A. J. H. Donné, F. C. Schüller, C. W. Domier, N. C. Jr Luhmann and S. V. Mirnov. *Experimental observation of m/n = 1/1 mode behaviour during sawtooth activity and*

*its manifestations in tokamak plasmas.* Plasma Phys. Contr. F., vol. 47, no. 8, page 1111, 2005. (Cited on pages 119, 120 and 121.)

[Vezinet 2013] D. Vezinet, D. Mazon, R. Guirlet, J. Decker and Y. Peysson. *Domain of validity of the robustness of an impurity Soft X-Ray cooling factor versus impurity transport in Tokamak plasma.* submitted to Europhys. Lett., 2013. (Cited on page 193.)

[von Goeler 1974] S. von Goeler, W. Stodiek and N. Sauthoff. *Studies of Internal Disruptions and $m = 1$ Oscillations in Tokamak Discharges with Soft X-Ray Tecniques.* Phys. Rev. Lett., vol. 33, pages 1201–1203, Nov 1974. (Cited on pages 19, 20 and 117.)

[Waelbroeck 1989] F.L. Waelbroeck. *Current Sheets And Nonlinear Growth Of The M=1 Kink-Tearing Mode.* Phys. Fluids B-Plasma, vol. 1, no. 12, pages 2372–2380, DEC 1989. (Cited on pages 20 and 95.)

[Wagner 1982] F. Wagner, G. Becker, K. Behringer, D. Campbell, A. Eberhagen, W. Engelhardt, G. Fussmann, O. Gehre, J. Gernhardt, G. v. Gierke, G. Haas, M. Huang, F. Karger, M. Keilhacker, O. Klüber, M. Kornherr, K. Lackner, G. Lisitano, G. G. Lister, H. M. Mayer, D. Meisel, E. R. Müller, H. Murmann, H. Niedermeyer, W. Poschenrieder, H. Rapp, H. Röhr, F. Schneider, G. Siller, E. Speth, A. Stäbler, K. H. Steuer, G. Venus, O. Vollmer and Z. Yü. *Regime of Improved Confinement and High Beta in Neutral-Beam-Heated Divertor Discharges of the ASDEX Tokamak.* Phys. Rev. Lett., vol. 49, pages 1408–1412, Nov 1982. (Cited on page 12.)

[Wang 1993] X. Wang and A. Bhattacharjee. *Nonlinear dynamics of the m =1 instability and fast sawtooth collapse in high-temperature plasmas.* Phys. Rev. Lett., vol. 70, pages 1627–1630, Mar 1993. (Cited on pages 20, 40 and 99.)

[Wang 1997] Xiaogang Wang and A. Bhattacharjee. *Forced reconnection and mode locking in rotating cylindrical plasmas.* Phys. Plasmas, vol. 4, no. 3, pages 748–754, 1997. (Cited on page 131.)

[Ware 1970] A.A. Ware. *Pinch Effect for Trapped Particles in a Tokamak.* Phys. Rev. Lett., vol. 25, pages 15–17, Jul 1970. (Cited on pages 10 and 149.)

[Weller 1987] A. Weller, A. D. Cheetham, A. W. Edwards, R. D. Gill, A. Gondhalekar, R. S. Granetz, J. Snipes and J. A. Wesson. *Persistent density perturbations at rational- q surfaces following pellet injection in the Joint European Torus.* Phys. Rev. Lett., vol. 59, pages 2303–2306, Nov 1987. (Cited on pages 135, 136 and 137.)

[Wenzel 1990] K.W. Wenzel and D.J. Sigmar. *Neoclassical analysis of impurity transport following transition to improved particle confinement.* Nucl. Fusion, vol. 30, no. 6, page 1117, 1990. (Cited on page 186.)

[Wesson 1986] JA Wesson. *Sawtooth Oscillations.* Plasma Phys. Contr. F., vol. 28, no. 1A, pages 243–248, JAN 1986. (Cited on pages 94 and 194.)

[Wesson 1989] J.A. Wesson, R.D. Gill, M. Hugon, F.C. Schüller, J.A. Snipes, D.J. Ward, D.V. Bartlett, D.J. Campbell, P.A. Duperrex, A.W. Edwards, R.S. Granetz, N.A.O. Gottardi, T.C. Hender, E. Lazzaro, P.J. Lomas, N. Lopes Cardozo, K.F. Mast, M.F.F. Nave, N.A. Salmon, P. Smeulders, P.R. Thomas, B.J.D. Tubbing, M.F. Turner and A. Weller. *Disruptions in JET.* Nucl. Fusion, vol. 29, no. 4, page 641, 1989. (Cited on page 59.)

[Wesson 1997] J. A. Wesson, B. Alper, A. W. Edwards and R. D. Gill. *Transport in the Sawtooth Collapse.* Phys. Rev. Lett., vol. 79, pages 5018–5021, Dec 1997. (Cited on page 185.)

[White 1989] R. B. White, M. N. Bussac and F. Romanelli. *High-$\beta$, Sawtooth-Free Tokamak Operation Using Energetic Trapped Particles.* Phys. Rev. Lett., vol. 62, pages 539–542, Jan 1989. (Cited on page 56.)

[White 2006] R. B. White. The theory of toroidally confined plasmas. Imperial College Press, 2006. (Cited on page 24.)

[Wróblewski 1993] D. Wróblewski and R.T. Snider. *Evidence of the complete magnetic reconnection during a sawtooth collapse in a tokamak.* Phys. Rev. Lett., vol. 71, pages 859–862, Aug 1993. (Cited on pages 134 and 135.)

[Yamada 1994] M. Yamada, F. M. Levinton, N. Pomphrey, R. Budny, J. Manickam and Y. Nagayama. *Investigation of magnetic reconnection during a sawtooth crash in a high-temperature tokamak plasma.* Phys. Plasmas, vol. 1, no. 10, pages 3269–3276, 1994. (Cited on page 135.)

[Zakharov 1992] L. Zakharov and B. Rogers. *Two-fluid magnetohydrodynamic description of the internal kink mode in tokamaks.* Phys. Fluids B-Plasma, vol. 4, no. 10, pages 3285–3301, 1992. (Cited on page 99.)

[Zakharov 1993] L. Zakharov, B. Rogers and S. Migliuolo. *The Theory Of The Early Nonlinear Stage Of M=1 Reconnection In Tokamaks.* Phys. Fluids B-Plasma, vol. 5, no. 7, Part 2, pages 2498–2505, JUL 1993. (Cited on pages 20, 95, 99 and 220.)

[Zocco 2013] A Zocco, J W Connor, C G Gimblett and R J Hastie. *Improved criterion for sawtooth trigger and modelling.* Plasma Phys. Contr. F., vol. 55, no. 7, page 074005, 2013. (Cited on page 194.)